ANDREEV BOUND STATES IN SUPERCONDUCTOR-QUANTUM DOT CHAINS

by

Zhaoen Su

Bachelor of Science, Lanzhou University, 2011

Submitted to the Graduate Faculty of
the Kenneth P. Dietrich School of Arts and Sciences in partial
fulfillment
of the requirements for the degree of

Doctor of Philosophy in Physics

University of Pittsburgh

2017

UNIVERSITY OF PITTSBURGH

KENNETH P. DIETRICH SCHOOL OF ARTS AND SCIENCES

This dissertation was presented

by

Zhaoen Su

It was defended on

Sept 15th 2017

and approved by

Sergey M. Frolov, Assistant Professor, Department of Physics and Astronomy

M. V. Gurudev Dutt, Associate Professor, Department of Physics and Astronomy

W. Vincent Liu, Professor, Department of Physics and Astronomy

Vladimir Savinov, Professor, Department of Physics and Astronomy

Di Xiao, Associate Professor, Department of Physics, Carnegie Mellon University

Dissertation Director: Sergey M. Frolov, Assistant Professor, Department of Physics and Astronomy

ANDREEV BOUND STATES IN SUPERCONDUCTOR-QUANTUM DOT CHAINS

Zhaoen Su, PhD

University of Pittsburgh, 2017

Andreev bound states in superconductor-quantum dot chains can provide a platform for quantum simulation and topologically protected quantum computation. This thesis focuses on quantum transport in superconductor-semiconductor nanowire hybrid structures. With InSb nanowires, we study Andreev bound states in single, double and triple dot chains. We first implement highly tunable single quantum dots in nanowires coupled to superconductors facilitated by local gates and transparent contacts. We explore the tunneling resonance of Andreev bound states in a wide parameter regime: from co-tunneling regime to spinfull singlet Andreev bound states, and find simultaneous transitions of superconducting and normal transports as the dot is tuned to be strongly coupled to the superconductor. In the open dot regime we investigate the zero bias feature that is strongly relevant to Majorana zero modes based on continuous nanowire sections. With two copies of this superconductor-quantum dot structure, we study the hybridization of Andreev bound states in a double dot. We observe tunneling spectra of the hybridized Andreev bound states and resolve their spin structure. Finally we implement a chain made of three superconductors and three quantum dots in series. Each dot is strongly coupled to a superconductor and has a single electron near the superconductor chemical potential. Spectroscopy measurement demonstrates resonances through Andreev bound states in the triple dot. A zero-bias peak is observed when a magnetic field is applied and it sustains in magnetic fields for a wide range, which can provide a signature of Majorana zero modes in this chain structure. We also evaluate the potential of Ge/Si core/shell nanowires for the realization of Majorana zero modes. To that end we establish three of the necessary ingredients for realizing Majorana zero modes based in nanowires: we achieve induced superconductivity from NbTiN, we estimate spin-orbit coupling ($l_{\mathrm{SO}} \approx 100 - 500$ nm) based on spin blockade, and we measure g-factors (up to 8) in Ge/Si double dots.

TABLE OF CONTENTS

LIST OF FIGURES

1.0 INTRODUCTION

This thesis is about combining semiconductor quantum dots and superconductors to provide platforms for topological quantum computation and quantum simulation. In this chapter, we introduce these two materials, their combination, and potential applications in quantum computation and quantum simulation.

1.1 TOPOLOGICAL QUANTUM COMPUTATION AND QUANTUM SIMULATION WITH QUANTUM DOTS AND SUPERCONDUCTORS

Semiconductors are among the most versatile materials in modern technology and science [1]. Their conductivity can be engineered over a huge range by either doping or gating. One can utilize spin-orbit interaction and the Zeeman effect in the semiconductors to engineer the electron spins. Low-dimensional semiconductors can be grown in film, wire and dot form. This thesis focuses on quantum dots created in nanowires. A quantum dot is a semiconductor island of sub-micrometer scale. Their small sizes lead to strong Coulomb interaction and discrete quantum dot energy levels, which makes them atom-like. After fast development of fabrication in the past years, currently quantum dots can be created by well controllable semiconductor growth, fabrication or gating. Quantum dot parameters such as charging energy, discrete levels, and coupling to the environment can be engineered experimentally, and the quantum dots can be described by models characterized by these parameters. The high versatility and controllability make quantum dots promising building blocks for implementing more advanced quantum devices.

In recent years, "adding" superconductivity in low-dimensional semiconductors has drawn a lot of attentions in the search for robust quantum computation [2, 3, 4]. Superconductivity originates from microscopic interaction, i.e., although electrons in superconductors are fermions and all have negative charge, some of them trend to be bind pairwise. Fortunately, introducing superconductivity into semiconductor can be achieved, which is known as superconducting proximity effect: when a normal conductor, a semiconductor in our case, makes a good electrical contact to a superconductor, the superconductivity "leaks" into the normal conductor. Close to the interface, the semiconductor behaves like a superconductor. By inducing the desired superconductivity into the versatile semiconductors, elaborated engineering can be performed to realize important physical systems, such as transmon qubits, topological quantum computers and quantum simulators [5, 3, 4, 6].

Specifically, inducing superconductivity in quantum dots leads to a number of remarkable quantum phenomena [7, 8, 9]. Even in a single quantum dot coupled to a superconductor, rich physics takes place due to the interplay between several important interactions such as

Coulomb interaction, superconductivity, the Zeeman effect and spin-orbit interaction. One of the most remarkable phenomena is the formation of Andreev bound states. Andreev bound states in single dots have been studied extensively. Recently they attract great attention because of their strong connection to Majorana zero modes in superconductor-nanowire hybrid structures, because both share great similarities in experimental observations and device structures. [10, 11, 12, 13].

A Majorana fermion is a fermion that is its own antiparticle [14]. In condensed matter, they are quasiparticles that are predicted to exhibit non-abelian exchange statistics, i.e., exchanging two Majorana zero modes twice ends up with a state different from the initial state. This differs from the exchange statistics of bosons and fermions. Importantly, by exchanging Majorana zero modes in a process called "braiding" in 2+1 space-time dimensions, robust quantum computation operations can be performed [15]. This leads to the so-called "topological quantum computation" where robust quantum computation can be achieved using quantum levels based on Majorana zero modes instead of using physical properties such as electron spins [16]. Majorana zero modes have been predicted to be created in superconductor-ballistic semiconductor nanowires containing the following ingredients: induced superconductivity, the Zeeman effect and strong spin-orbit interaction [3, 4].

In this thesis, we realize and study superconductor-single dots in a new superconductor-semiconductor combination (NbTiN-InSb nanowire). In addition to exploring the connection between Andreev bound states in single dots and Majorana zero modes, we gain a number of new physical insights into the hybrid systems. We then scale the structure to superconductor-quantum dot chains, motivated by the following.

First, scaling the superconductor-quantum dot structure to chains provides an alternative approach to realize robust Majorana zero modes other than that based on the superconductor-nanowire structures [2, 17, 18, 19]. Moreover, it is suggested that Majorana zero modes generated in the chain structure are insensitive to disorder which, in contrast, can be a dominating destructive factor for the implementation of Majorana zero modes based in nanowires.

More generally, we suggest that when the superconductor-quantum dot structure is scaled to chains or arrays, quantum simulation might be performed. The chains or arrays can work as quantum simulators whose state basis is formed with electron states near the highest occupied quantum dot levels. Quantum simulators enable us to explore Hamiltonians of important quantum systems in condensed-matter physics, atomic physics, quantum chemistry [6]. Modeling these quantum systems can advance our knowledge and bring breakthroughs to physics such as room temperature superconductivity. These systems, however, can be impossible to model with classical computers as they are beyond the computation power of supercomputers. Quantum simulation makes the modeling of these systems realizable by mapping them onto the assemblies of well-understood quantum systems. Such simulation has been achieved with ultracold atoms in optical lattices [20], trapped ions [21] and superconducting circuits [22]. As mentioned previously, quantum dots provide high controllability and can be well-understood. Besides, integrated circuits have shown the accessibility of integrating billions of semiconductor devices. Therefore, with multiple semiconductor quantum dots, the quantum simulators might be realized using quantum dot chains and arrays as seen in other physical systems. At last, in the solid state implementation, intrinsic properties such as superconductivity, large g-factors, and strong spin-orbit interactions can be incorporated into the modeled Hamiltonians naturally.

1.2 OUTLINE OF THE THESIS

The content of this thesis is as follow:

Chapter 2 introduces the theory and background of Andreev bound states.

Chapter 3 describes the materials, device fabrication techniques and measurement setup used in this thesis.

Chapter 4 shows the realization of single dots in InSb nanowires coupled to superconductors (NbTiN), and the measurements of single dot Andreev bound states in the hybrid structures.

Chapter 5 demonstrates the hybridization of Andreev bound states in an InSb double quantum dot where each dot is coupled to a superconducting reservoir.

Chapter 6 studies quantum transport through a chain made of three superconductor-InSb quantum dots.

Chapter 7 shows the observation of induced superconductivity in Ge/Si core/shell nanowires.

Chapter 8 implements double quantum dots in Ge/Si nanowires and uses them to measure the spin-orbit interaction and g-factors in Ge/Si nanowires. These properties, together with the induced superconductivity studied in Chapter 7, are the ingredients to evaluate the potential of Ge/Si-based devices for the study of Majorana zero modes.

Chapter 9 includes concluding remarks and outlook.

2.0 THEORY AND BACKGROUND

This chapter introduces the theories and background to quantum dots, Andreev bound states in superconductor-quantum dot hybrid structures and the Kitaev model.

2.1 INTRODUCTION

We first introduce the physics of electrons in small semiconductor islands: quantum dots. Quantum dots in semiconductors have been studied intensively in the past years. Since it is one of the experimental backbone components in this thesis, some of the most iconic phenomena in quantum transport through quantum dots are discussed, such as Coulomb blockade due to Coulomb interaction and spin blockade due to the Pauli exclusion principle [23]. In Section 2.2, they are introduced without considering superconductivity in the dots. These transport features are crucial even in measurements where superconductivity is present, because they can be used to trace quantum dot occupations and parities.

We then describe the quantum states in the dots when superconductivity is introduced. Superconductivity competes with Coulomb interaction because it favors pairing of electrons while Coulomb interaction in these systems makes electrons repeal. One of the most important results is the formation of Andreev bound states. I will explain them in two steps. (1) In Section 2.3, we introduce the superconductor-single quantum dot structures and the Hamiltonian of a minimum model. Instead of presenting comprehensive theoretical approaches immediately, we summarize the most significant properties of Andreev bound states in single dots which will be the foundation to understanding the experimental chapters. (2) In Section 2.4, we then present technical details of the models of our specific experimental systems, numerical approaches to solve the Hamiltonians and simulation of transport. Importantly, these theoretical approaches solve hybridized Andreev bound states in double dots with soft gap superconductivity, which had not been developed before.

Finally, superconductor-nanowire structure and chains made of superconductors and quantum dots have been proposed to realize the Kitaev chain model [2, 17, 18, 19]. This model is thus introduced and possible experimental realizations are discussed. Although both InSb and Ge/Si nanowires where electrons as well as holes as charge carriers are studied in this thesis, they share generic theoretical models. Unless specified, the description and discussion are based on electron systems.

2.2 QUANTUM DOTS

2.2.1 Single quantum dots

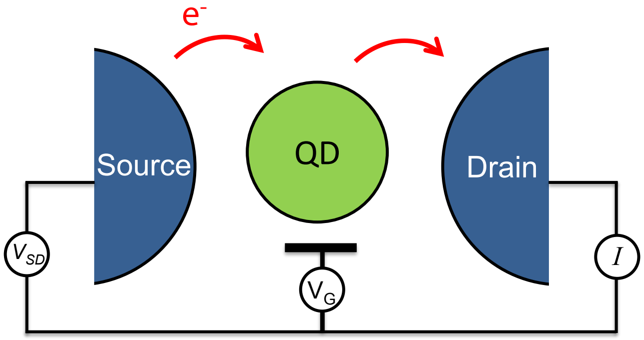

Figure 2.1: Illustration of a weakly coupled quantum dot. A quantum dot is weakly coupled to the left lead (source) and right lead (drain) via tunnel couplings. The chemical potential of states in the dot is tuned by the gate voltage (V_G). A bias voltage (V_{SD}) can be applied to the source lead and current through the quantum dot is measured on the drain side.

We start with a single quantum dot with two normal leads. As shown by the illustration of a weakly coupled system (Fig.2.1), the quantum dot is a semiconductor island that can be connected to leads. The minimal model describing the system takes two factors into account: Coulomb charging effect and discrete quantum levels. Coulomb interactions between electrons in the dot, and between electrons in the dot and in the environment, are often characterized by a single parameter that is the sum of capacitances (C) between the quantum dot and gate (C_G), source (C_S) and drain (C_D). Secondly, due to quantum confinement, there is a single-particle spectrum. Together, the total energy of a quantum dot at ground state having N electrons with voltages V_G, V_S and V_D on the gate, source and drain, respectively, is

$$U_{QD}(N) = \frac{1}{2C}\left[-|e|(N-N_0) + C_S V_S + C_D V_D + C_G V_G\right]^2 + \sum_{n=1}^{N} E_n, \tag{2.1}$$

where $-|e|$ is electron charge, N_0 describes the background charge, E_n is the single particle energy level of the n-th electron, $C = C_S + C_D + C_G$, and V_S, V_D and V_G can be tuned continuously in measurements [23]. The electrochemical potential that will be called chemical potential for short, defined as the energy required to add the N-th electron, is

$$\mu(N) = U_{QD}(N) - U_{QD}(N-1) = \left(N - N_0 - \frac{1}{2}\right) U - (C_S V_S + C_D V_D + C_G V_G) \frac{U}{|e|} + E_N, \tag{2.2}$$

where $U = e^2/C$ is charging energy. One can see from Eq.2.2 that the energy cost of adding the N-th electron to the dot consists of two parts: energy to overcome the charging effect and discrete level energy.

In electrical transport experiments, a bias voltage, $V_{SD} = V_S - V_D$ can be applied across the dot and the current through the dot can be measured to analyze the quantum states in the dot. The bias voltage opens an electron transport window ($|e|V_{SD}$). When a quantum dot chemical potential is tuned to be inside the window, one electron moves from source to the dot resulting in $N+1$ electrons in the dot, then leaves the dot to drain (Fig.2.2a). Note that this is a successive process and only one electron is transferred at a time. In contrast, when there are no quantum dot levels within the source-drain bias window, electron transport stops and the dot has a fixed electron occupation (Fig.2.2b). When the charging effect is involved, this phenomenon is called Coulomb blockade [24]. As seen in Eq.2.2, the chemical potential in the dot can be tuned by V_G such that it can be shifted into the source-drain bias window and Coulomb blockade is lifted. Within the source-drain bias window, if there are chemical potentials associated with excited quantum dot levels, there can also be resonant transport through the dots. Fig.2.2c depicts electron transport via resonant tunneling when the Fermi level of the source is aligned with a chemical potential associated with an excited level. Experimentally, current or differential conductance (dI/dV) is often measured as a function of the source-drain voltage and gate voltage, which gives rise to a bias vs. gate diagram. An example is shown in Fig.2.2d where the current is zero inside the diamond-shape regimes (Coulomb diamonds) and the quantum dot has a fixed electron number. By increasing V_G the dot undergoes from one diamond to another with increasing electron number. Outside the Coulomb diamonds, current flows. Transport via dot excited states are observed as current increments (or conductance peaks) outside Coulomb diamonds and the directions are parallel to the diamond edges (If the leads are superconducting, they are

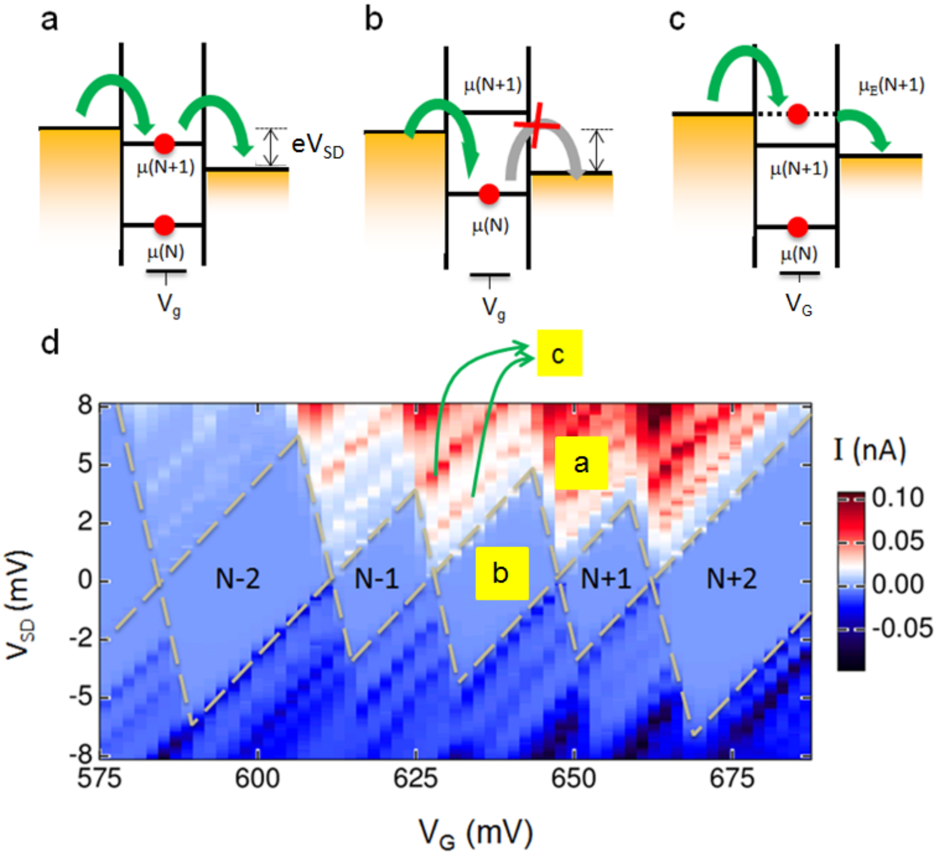

Figure 2.2: Electron transport though a quantum dot in InSb nanowire. **a,** Coulomb blockade is lifted when a level is shifted into the bias window by tuning the chemical potential level ladder using the gate voltage (V_G). **b,** Coulomb blockade. No quantum dot levels are within the source-drain bias window (eV_{SD}) and no electrons flow through the quantum dot. **c,** Resonant tunneling via an excited level in the dot. **d,** Bias vs. gate diagram of a quantum dot in InSb weakly coupled to two NbTiN leads. Current through a quantum dot as a function of source-drain voltage (V_{SD}) and gate voltage (V_G) is measured. Electron numbers in Coulomb diamonds are N-2, N-1, N etc, where N is an integer. The three scenarios depicted in **a,** **b** and **c** are marked in the corresponding positions in **d**.

observed as current peaks or conductance peaks of opposite signs such as Fig.2.2d. Here, the superconductors are weakly coupled to the dot and do not change the quantum dot states. However, transport features can be different because the density of states in superconductors differs from that in normal leads. Detailed discussion is presented in section 4.7.). Later in Chapter 4, where single dots are studied, we will use Coulomb blockade to trace quantum dot occupations and study the evolution of quantum states formed due to the presence of superconductivity.

We shall end this section by discussing spin states of single dot systems. When there is a single electron (or electrons of odd numbers) in the dot, the spin state is either spin-up ($|\uparrow\rangle$) or spin-down ($|\downarrow\rangle$). These two spin states are degenerate at zero magnetic field, and are thus called spin doublets. Their energies split in magnetic field, following the relation of Zeeman effect; when there are two electrons (or electrons of even numbers), the spin state is a singlet ($|\downarrow\uparrow\rangle$) due to the Pauli exclusion principle. The energy of a spin singlet single dot remains under a finite magnetic field.

2.2.2 Double quantum dots

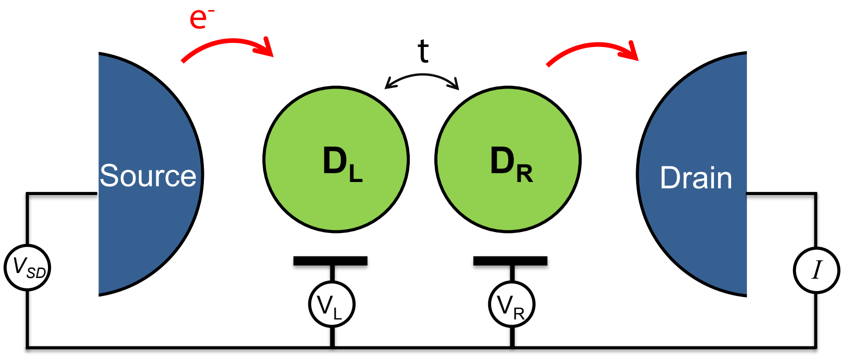

Figure 2.3: Illustration of a double quantum dot in series. Each dot is coupled to a lead. Electrochemical potential of each dot is tuned by its gate separately. Two dots are coupled via a tunneling barrier, allowing electrons to tunnel from one dot to the other. The system configuration can be controlled by the gate voltages (V_L, V_R). Current is measured to probe the double dot states.

A double quantum dot, in this thesis, consists of two quantum dots in series [25]. Each of the dots is connected to a lead and they are coupled via a tunneling barrier, as schematically shown in Fig.2.3. The chemical potential of each dot can be controlled separately by changing the voltages on the gates (V_L and V_R) under the dots. Like in single dots, Coulomb interaction forbids transport in some regimes and in these regimes the electron occupations are definite. To describe a double dot configuration, the notation (N_L, N_R) is used to denote the dot occupations on the left dot (N_L) and right dot (N_R). At a low source-drain bias, the transfer of an electron from the left source to the right drain is accomplished via the following transport cycle: $(N_L,\, N_R) \rightarrow (N_L+1,\, N_R) \rightarrow (N_L,\, N_R+1) \rightarrow (N_L,\, N_R)$. The transport is allowed only when all of the three transitions involved are allowed. At a bias close to zero, it means the initial and final states of every transition should have the same chemical potentials in the leads or dots. These conditions give rise to a V_L vs. V_R stability diagram where the transport is blocked except at points where all of the three conditions are met. These points are called triple points. The triple points form a honeycomb structure in the stability diagram (See Fig.2.4) where each blockade regime of the honeycomb structure has a fixed double dot configuration, $(N_L,\, N_R)$. Note that the triple points grow into triangles as the bias is increased.

Besides Coulomb interaction, the transport can be blocked due to the Pauli exclusion principle [26]. This is illustrated in Fig.2.5a, where, at a forward bias, the double dot is initialized in the (0,1) configuration whose single electron is either spin-up or spin-down. An electron can enter the left dot and form a spin-singlet (S(1,1)) or spin-triplet (T(1,1)) with the electron in the right dot. When a T(1, 1) forms, the electron in the left dot cannot continue to the right dot as it would form a T(0,2) state whose level would be higher than T(1,1). At the same time, the electron cannot go back to the source, as its chemical potential is lower than the Fermi level of the source. In other words, the electron is trapped in the left dot. As long as this event, called spin blockade, occurs, the current stops flowing. In experimental systems, the electron spin flips after some time so weak but non-zero current can be observed in a DC measurement. Note that although we use 0, 1 and 2 to denote the dot occupations, spin blockade can occur at transitions between configurations of higher occupations. What matters are the parities of the dot configurations and typical spin blockade occurs at the (odd, odd) → (even, even) transitions. At the opposite bias, spin blockade does not happen at the (0,2) → (1,1) transition, because the new electron can only form S(0,2) with the electron that is already in the right dot. As a result, it continues to the left dot and forms a S(1,1) (Fig.2.5b).

Spin blockade has practical importance for state initialization and readout in quantum computation based on semiconductor spins [27]. In our experiments, we use it to determine

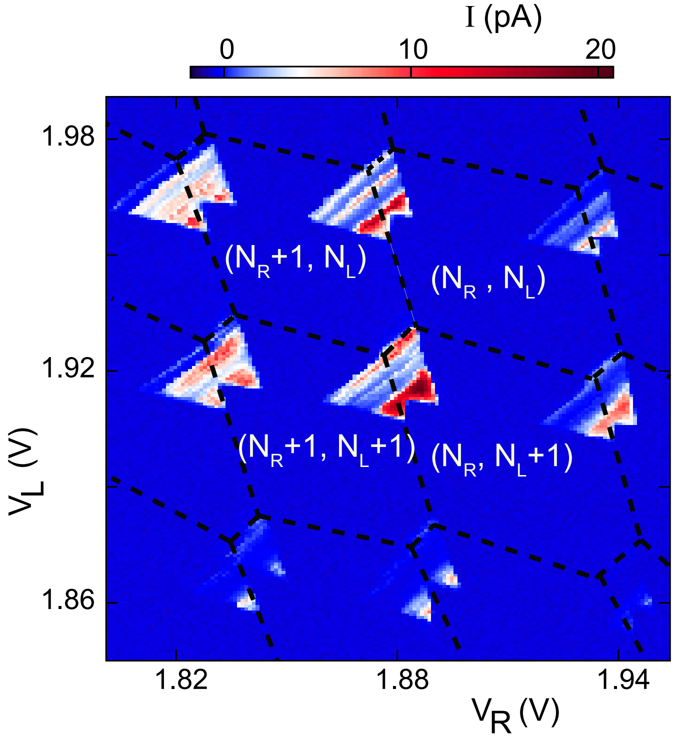

Figure 2.4: Stability diagram of a double dot. At a fixed bias of 5 mV, current is measured as a function of plunger gate voltages of left and right dots (V_L and V_R) via a double dot in a Ge/Si core/shell nanowire. The dashed lines connect the triple points and define a honeycomb structure. Inside each honeycomb cell there is a definite double dot configuration (N_L, N_R). At this finite bias (5 mV), the triple points are shown as triangles. Note that the dot occupations increase as the gate voltages are decreased because it is a hole double dot in a Ge/Si nanowire.

the parities in the quantum dots (Chapter 5) and to extract spin-orbit coupling in Ge/Si core/shell nanowires (Chapter 8). In semiconductor nanowires, the spins and momenta of electrons are coupled due to bulk-induced-asymmetry (Dresselhaus type) such as in InSb whose crystal structure is zinc-blende, and surface-induced-asymmetry (Rashba type) [28]. Spin-orbit coupling is one of the mechanisms that can cause the spin of the trapped electron to flip [29].

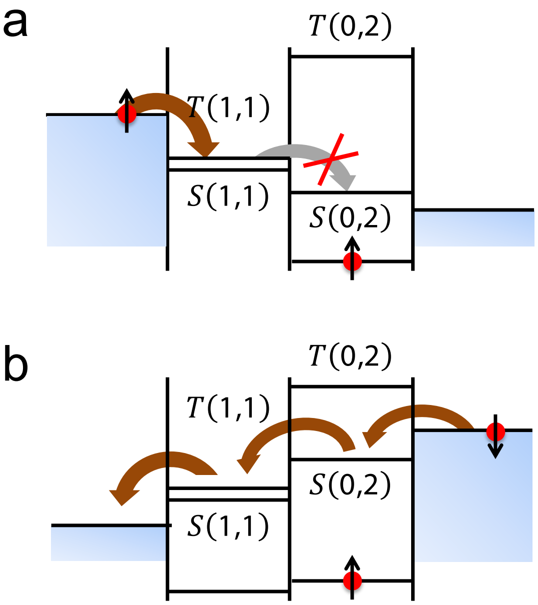

Figure 2.5: Spin blockade in a double dot. a, Spin blockade at a positive bias for the (1,1) → (0,2) transition. It occurs when an electron in the left dot fills T(1,1). Moving forward to the right dot is forbidden, because forming a T(0, 2) requires energy that is not accessible and forming a S(0,2) that would require a spin flip. Moving backward to the source is not allowed either. **b,** No spin blockade at the opposite bias. A spin-down electron is transferred via S(0,2) then S(1,1).

2.3 ANDREEV BOUND STATES: PROPERTIES

The Anderson impurity model has been widely used to describe a single quantum dot coupled to metallic leads [30]. Only a single spin-degenerate level is considered in the model. This single level approximation is valid for the Andreev bound states that we are interested in here, because the discrete quantum level spacing is on the order of meV, whereas the NbTiN-InSb hybrid structures studied in this thesis have induced superconducting gaps on the order of 100 μeV. As we shall discuss later, the energy difference between the ground and first excited states is within superconducting gap, which validates the single level approximation. The Hamiltonian for our systems consists of several terms:

$$H = H_{\mathrm{L}} + H_{\mathrm{R}} + H_{\mathrm{QD}} + H_{\mathrm{t}}, \tag{2.3}$$

where H_{QD} corresponds to a single uncoupled quantum dot. It is given by

$$H_{\mathrm{QD}} = \sum_{\sigma=\{\uparrow,\downarrow\}} \epsilon c_\sigma^\dagger c_\sigma + U n_\uparrow n_\downarrow, \tag{2.4}$$

where $c_\sigma^\dagger$ creates an electron with spin σ on the level of ϵ in the quantum dot and U is the Coulomb interaction between two electrons of opposite spin in the dot.

$H_{L(R)}$ represents the left (right) lead. In our case, they are superconducting electrodes. The theory describing the conventional superconductivity, the Bardeen-Cooper-Schrieffer (BCS) theory, is well explained in *Introduction to Superconductivity* by M. Tinkham [31]. The superconducting lead Hamiltonian can be written as:

$$H_{v=\{L,R\}} = \sum_{k\sigma} \xi_{k,v} d_{k,\sigma v}^\dagger d_{k,\sigma v} + \sum_{k} \left(\Delta_v d_{k\uparrow,v}^\dagger d_{-k\downarrow,v}^\dagger + \mathrm{H.C.} \right), \tag{2.5}$$

where $d_\sigma^\dagger$ creates an electron (quasiparticle) with spin σ and momentum k on the level of $\xi_{k,v}$ in the superconducting lead and Δ_v is the superconducting order parameter on lead v.

Finally H_t expresses the coupling between the dot and the leads,

$$H_{\mathrm{t}} = \sum_{k\sigma,v} \left(V_{k,v} d_{k\sigma,v}^\dagger c_\sigma + H.C. \right). \tag{2.6}$$

The hopping parameter $V_{k,v}$ can be simplified by assuming a constant normal density of states (ρ_v) in the leads near the Fermi level around superconducting gap and its momentum dependence is neglected. As a result, the lead-dot coupling can be characterized with a single parameter:

$$\Gamma_v = \pi \rho_v |V_v|^2. \tag{2.7}$$

The system Hamiltonian involves the interplay of two interactions in the dot: Coulomb interaction and superconductivity. We first provide a qualitative discussion in two limits. (1) When the superconductivity is dominated by the charging effect completely, we can equivalently set Δ_v to zero such that only the first term in Eq.2.5 is kept. Furthermore, if we consider the case where Γ's are small, the system is what we have discussed previously: a quantum dot weakly coupled to normal leads. (2) Whereas in the limit where $\Gamma_v \gg U$, the quantum dot is strongly coupled to the leads and is called an open quantum dot. It is dominated by the induced superconductivity from the superconductor by the proximity effect (also called Holm-Meissner effect). The proximity effect occurs when a superconductor makes good contact with a normal conductor. It results in superconductivity in the normal material over mesoscopic distances. In this case, the quantum dot becomes effectively an extension of the superconductor. If the dot is coupled to two superconductors strongly, it serves as a weak link between the two superconductors and Josephson supercurrent can flow through it [7].

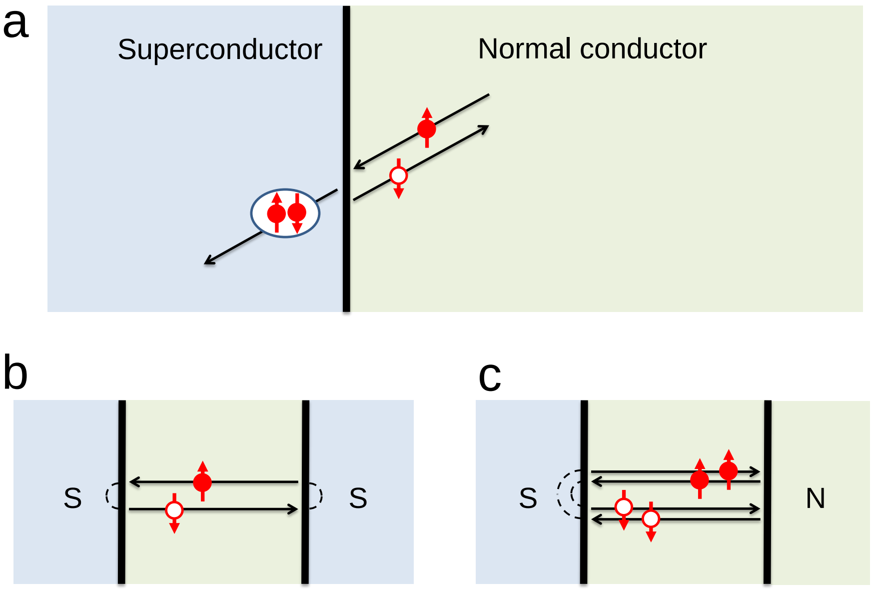

Figure 2.6: Andreev reflection. a, Schematics of Andreev reflection at a superconductor-normal conductor (S-N) interface. An electron (solid dot) in the normal conductor meets the interface, which produces a Cooper pair (ellipse) in the superconductor and a reflected hole (circle) in the normal conductor. Note the electron and reflected hole have opposite spins and momentums. **b,** Andreev reflections in a 1D S-N-S structure whose normal conductor has a finite size. Andreev reflection occurs at two S-N interfaces. The dashed semicircles depict the two Andreev reflections. **c,** Andreev reflection and normal reflection in a 1D S-N-N structure whose normal conductor in the middle has a finite size. Andreev reflection and normal reflection occur at the S-N interface, and N-N interface with a barrier, respectively. The dashed semicircles depict the Andreev reflections.

Theoretical studies of this simplified Hamiltonian fascilitate the explaintion of a number of interesting physical phenomena. Various theoretical approaches have been applied to solve this single dot Hamiltonian, such as the co-tunneling approach [32], diagrammatic approaches [33], diagonalization by numerical methods [34], functional renormalization group [35] and quantum Monte-Carlo [36]. Ref.[37] provides a complete review of these approaches. Note that without superconductivity, analytical results such as the Kondo effect can be obtained [38], which will be mentioned later as well. Superconductivity brings additional complexity to the problem [37]. As a result, numerical approaches, such as numerical renormalization group and exact diagonalization [39, 40, 41, 42], have been currently developed to the specific tunneling regime explored in this thesis. We also develop numerical approaches to model single dot systems and extend it to double dot systems (and in principle systems containing an arbitrary number of dots). This will be presented in Section 2.4.

In this section, we focus on the properties of Andreev bound states in single dots which are the results of an interplay between Coulomb interaction and superconductivity. The origin of Andreev bound states comes from a process called Andreev reflection at superconductor-normal conductor interfaces where an electron in the normal conductor is converted into a Cooper pair in the superconductor necessitating a reflected hole (See Fig.2.6a). When the normal conductor has a finite size, Andreev reflection and normal reflection can occur at multiple interfaces in the normal conductor. Andreev bound states form as a result of coherent superposition of all possible Andreev reflection and normal reflection processes (See Fig.2.6b and c). When the size of the normal conductor is small, such as a quantum dot, Coulomb interaction becomes important in determining how Andreev bound states (also called Yu-Shiba-Rusinov states or Shiba states [43]) form. Experimentally, Andreev bound states in single dots have been studied in InAs nanowires by the Tarucha Group [41], Franceschi Group [8, 40, 42], Marcus Group [44], Xu Group [45], Shtrikman Group[46], in carbon nanotubes by the Joyez Group[47], Martín-Rodero Group [48], Strunk Group [49], and in graphene by the Nadya Group [50].

Here we summarize the most significant properties of Andreev bound states in a single dot found in the experiments listed above. The spectrum of the single dot system in the Andreev bound state regime consist of spin-singlets ($|S\rangle$) ($|0\rangle + |\uparrow\downarrow\rangle$ and $|0\rangle - |\uparrow\downarrow\rangle$) and spin-doublets ($|D\rangle$) ($|\uparrow\rangle$ and $|\downarrow\rangle$). Without considering the effect of magnetic field, the ground and first excited states have different parities as they differ by one electron. The transitions between these states of different parities, are associated with the so-called Andreev bound states. First we consider the regime where the coupling to the superconductor, Γ_S, is small

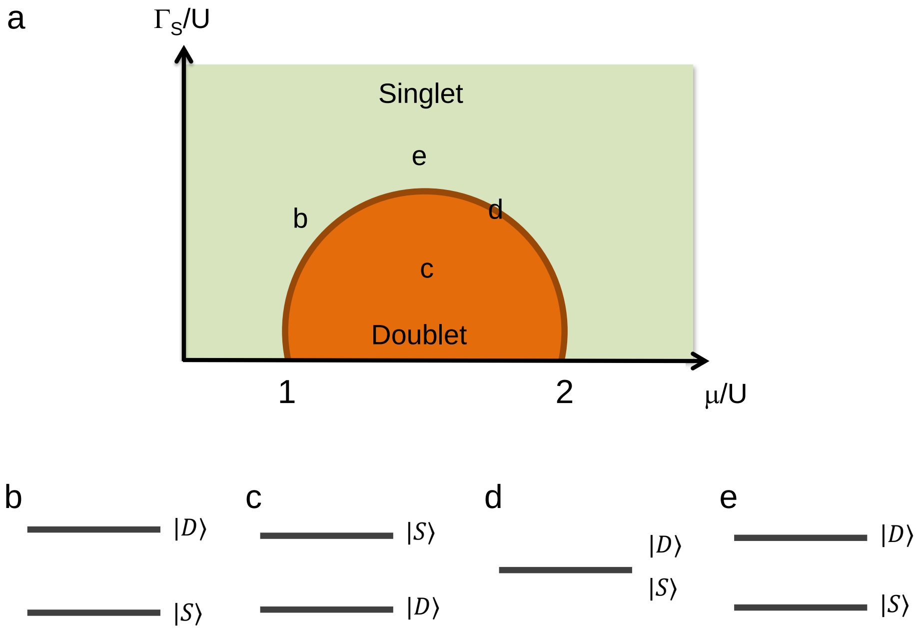

Figure 2.7: Phase diagram of spin states in a single dot. a, Phase diagram of spin states in a single dot coupled to a superconductor, as a function of μ/U and Γ_S/U, where μ is chemical potential, U is charging energy and Γ_S is superconductor-dot coupling. The green regime has $|S\rangle$ ground state while the orange regime has $|D\rangle$ ground state. When the dot occupation is even, i.e., $\mu/U < 1$ or $\mu/U > 2$, the phase is always spin singlet. Whereas when the dot occupation is odd, i.e., $1 < \mu/U < 2$, the ground state can be either a spin singlet or a doublet. The singlet-doublet phases are separated by a arc-like boundary. **b-e,** The spectra in different regimes of the phase diagram denoted in **a** respectively. In regimes **b** and **e**, the ground states are singlets; in regime **c** the ground state is $|D\rangle$; spot **d** is on the phase boundary and the ground state is singlet-doublet degenerate.

(close to the x-axis of the phase diagram in Fig.2.7a). The ground state is $|D\rangle$ when the dot occupation is odd and the ground state is $|S\rangle$, meaning $|0\rangle$ if the dot occupation is 0, and $|\uparrow\downarrow\rangle$ if the dot occupation is 2. As Γ_S/U is increased, the range of chemical potential, where the ground state is $|D\rangle$, shrinks. The ground state can be $|S\rangle$ even when the dot occupation is odd and the singlet is a superposition of $|0\rangle$ and $|\uparrow\downarrow\rangle$. This is indeed the effect of the induced superconductivity as superconductivity favors electron pairs and therefore it partially screens the single electron spin. As Γ_S/U is further increased, the ground state and the first excited states move close to each other and at some point they are degenerate (See Fig.2.7d). Finally, the ground state becomes $|S\rangle$ over the entire μ/U range (See Fig.2.7e). Fig.2.7a depicts the phase boundary between the singlet and doublet as a function of μ/U and Γ_S/U. The exact shape of the phase boundary is determined by more than charging energy and induced superconductivity. The Kondo effect can also screen a single spin in a spin-full quantum dot as the electron is coupled to conductance electrons in the normal lead or quasiparticles in the superconducting leads [51, 52]. Thus, both superconductivity and the Kondo effect can make the ground state $|S\rangle$ in a spinfull dot. Although the Kondo effect is not directly observed in our experiments, probably because it is suppressed in the superconductor-quantum dot structures as the energies of the quasiparticles are gapped by Δ_v (Although we notice that our NbTiN-InSb hybrid structures have finite subgap density of states thus the single electron can also be coupled to the subgap quasiparticles.). On the other hand, no practical methods have been found to separate the effect by superconducting pairing from the Kondo effect [8]. In this thesis, although the Kondo effect is a suppressed effect, we are aware that it cannot be excluded in our experiments.

2.3.1 Transport cycle through Andreev bound states

Experimentally, we observe the transitions between the eigenstates of the superconductor-dot systems, i.e., Andreev bound states, by electrical transport. Each transport cycle through Andreev bound states transfers two quasiparticles from the probe that is either a normal conductor, a superconductor or a semiconductor with induced superconductivity, and results in a Cooper pair in the superconducting reservoir. In Fig.2.8, we depict the transport cycle in 4 steps for a normal conductor probe at positive bias. (1) The system starts in a ground state (Fig.2.8a). (2) When the energy level (ζ) associated with the transition energy between the ground and excited states is aligned with the chemical potential of the probe, an electron enters the dot on level ζ and changes its spin state (i.e., from $|S\rangle$ to $|D\rangle$ or the other way around) (Fig.2.8b). (3) Andreev reflection at the superconductor-quantum dot interface generates a Cooper pair in the superconductor and reflects a hole (Fig.2.8c). (4) Finally, the hole enters the probe and the system is relaxed back to the ground state (Fig.2.8d). The

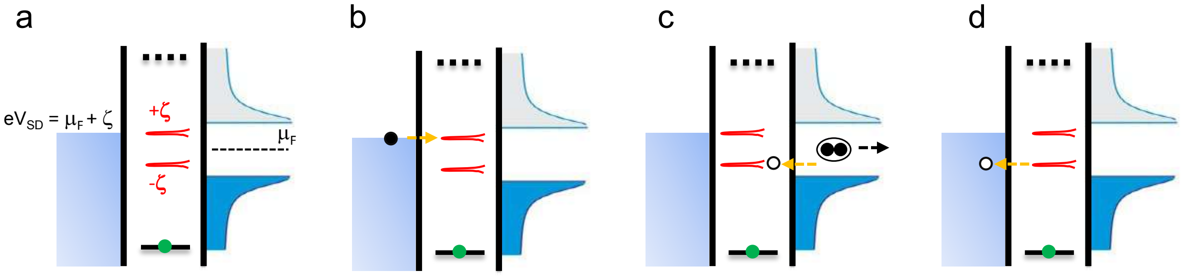

Figure 2.8: Transport cycle through single dot Andreev bound states. Schematics of transport cycle for a normal conductor probe. **a,** The transport starts with a ground state. The quantum dot level below the Fermi level of the probe (solid-line level in the dot) is filled and the quantum dot level above (dashed-line level in the dot) is unfilled. **b,** The chemical potential of the probe is aligned with the resonance level that are associated with Andreev bound states. An electron enters the resonance level. **c,** The electron undergoes Andreev reflection at the superconductor-quantum dot interface. A Cooper pair is formed in the superconductor and a hole is reflected. **d,** The hole enters the probe and the system is relaxed back to **a**.

complete transport cycle ends up with two electrons less in the probe, an extra Cooper pair in the superconducting reservoir, and 2ζ of energy dissipated. The resonance occurs when the dissipated energy is compensated by the bias $|V_{bias}|$, i.e, $|eV_{\text{bias}}| = \zeta$. The resonance at $V_{\text{bias}} = -\zeta/e$ involves a similar transport cycle. When the Fermi level of the probe is aligned with the $-\zeta$ level, a hole enters the level. At the superconductor-dot interface, an electron is reflected and a Cooper pair is annihilated in the superconductor. Finally, the reflected electron enters the probes and the system is relaxed back to the initial state. A complete cycle ends up with a Cooper pair annihilated in the superconductor and two extra electrons in the probe.

The energies of Andreev bound states, $\pm\zeta$, can be tuned by the dot chemical potential (μ). Their relation is revealed in terms of resonances in differential conductance (dI/dV) in bias vs. gate spectroscopies. In Fig.2.9 we simulate the transport through Andreev bound states numerically and plot differential conductance as a function of bias and μ. They are obtained using the theoretical approaches that will be described in Section 2.4. In Fig.2.9a, a small value is chosen for Γ_S such that the ground state is $|D\rangle$ in the spinful dot. Effectively,

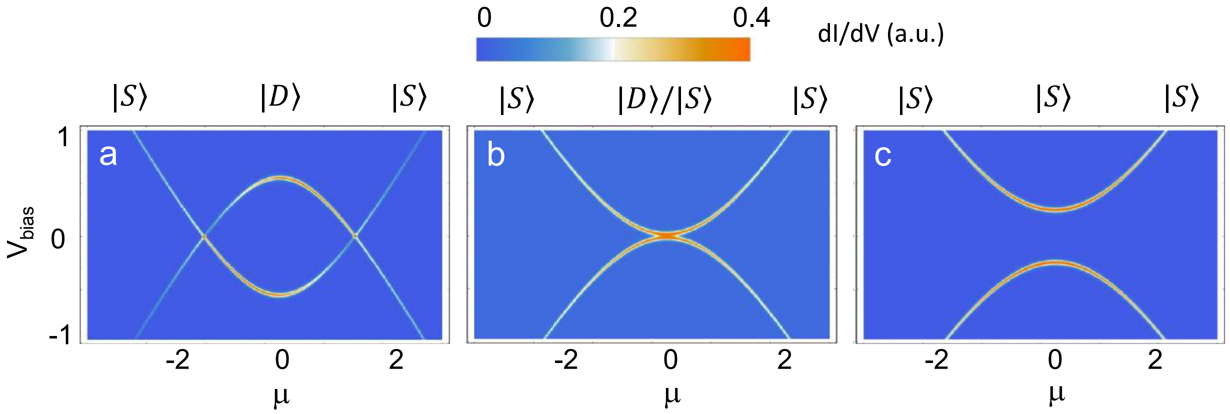

Figure 2.9: Theoretical simulation of transport through Andreev bound states. Transport simulation in three regimes obtained using the theoretical approaches described in Section 2.4. **a,** In the regime where the odd occupation has $|D\rangle$ ground state. $\Gamma_S = 1.2$. **b,** Close to the $|D\rangle\,/\,|S\rangle$ phase transition. $\Gamma_S = 1.77$. **c,** In the regime where the ground state is $|S\rangle$ over entire μ range. $\Gamma_S = 2.0$. Other simulation parameters are the same for **a**, **b** and **c**: $U = 3.5$, $\varepsilon = 1.75$, $t = 0.1$, where ε is quantum dot level spacing. All parameters and V_{bias} have the same unit, $\hbar$.

this is transport shown along a horizontal line cut through the arc-like boundary shown in Fig.2.7a. The ground states from left to right are $|S\rangle$, $|D\rangle$, $|S\rangle$ respectively, separated by the two zero bias crossings. At the center of the closed loop, $|\zeta|$ is maximum, which is associated with a quantum dot level arrangement where the filled and unfilled quantum dot levels are equally apart from the superconductor chemical potential (See Fig.2.8). As the dot chemical potential is tuned off from this arrangement, either tuned up or down, $|\zeta|$ is decreased. Importantly, the resonances have non-linear gate dependence due to the interplay between superconductivity and Coulomb interaction.

As Γ_S is increased to some value, 1.77, the system is at the phase transition point (Fig.2.9b), which corresponds to the horizontal line cut that is tangent to the arc-like boundary in Fig.2.7a. The ground states are $|S\rangle$, except at the degenerate point. This $|\zeta| = 0$ point is associated with the same quantum dot level arrangement depicted in Fig.2.8 but with a larger Γ_S. As the dot chemical potential is tuned off from this spot, either tuned up or down, $|\zeta|$ is increased. Finally, when a large value is chosen for Γ_S in Fig.2.9c where the ground state is $|S\rangle$ for the entire μ range, i.e., this is transport along a horizontal line cut above the arc-like boundary in Fig.2.7a. The simulation displays anti-crossing-like resonances with one branch at positive bias and the other at negative bias. Similarly, the minimum gap, $2|\zeta|$, is associated with the same quantum dot level arrangement depicted in Fig.2.8. Tuning the dot chemical potential away from this spot increases $|\zeta|$. These simulation results are found to be consistent with the experimental observations in Chapter 4.

2.3.2 Magnetic field dependence of Andreev bound states

Spin structure of Andreev bound states can be resolved by measuring the transitions as a function of magnetic field [8]. In the case where the ground state is $|S\rangle$, the excited state is $|D\rangle$. When a magnetic field is applied, the two doublets, $|\uparrow\rangle$ and $|\downarrow\rangle$, gain Zeeman energies of $\pm\,\frac{1}{2}g\mu_B B$ respectively, where g is the Landé g-factor and μ_B is the Bohr magneton, and the ground state which is a singlet remains (See Fig.2.10a). As a result, two transitions take place. One has increasing transition energy whereas the other has decreasing energy. In other words, the two transitions which are degenerate at zero field evolve into two branches in magnetic field. On the other hand, when the ground state is $|D\rangle$, one of the doublets becomes the ground states at finite fields (say $|\uparrow\rangle$). The only allowed transition is from it to the excited $|S\rangle$. The transition between the two doublets is not allowed, because a transition involves adding or removing one electron (See Fig.2.10b). Therefore for the doublet phase, resonances of increasing values are observed as magnetic field. This provides an experimental approach to resolve the spin structure. Note the illustrations in Fig.2.10 do not take the effect that the induced gap is decreased in magnetic field into account. Because of the decreasing induced gap, the linear field dependences in Fig.2.10 can be absent [8]. This effect is particularly pronounced with hybrid structures where low critical magnetic field superconductors such as evaporated Al are involved. Besides, the linearity can be missing when the transition energy is close to the induced gap, because the transition energy cannot exceed the induced gap [13].

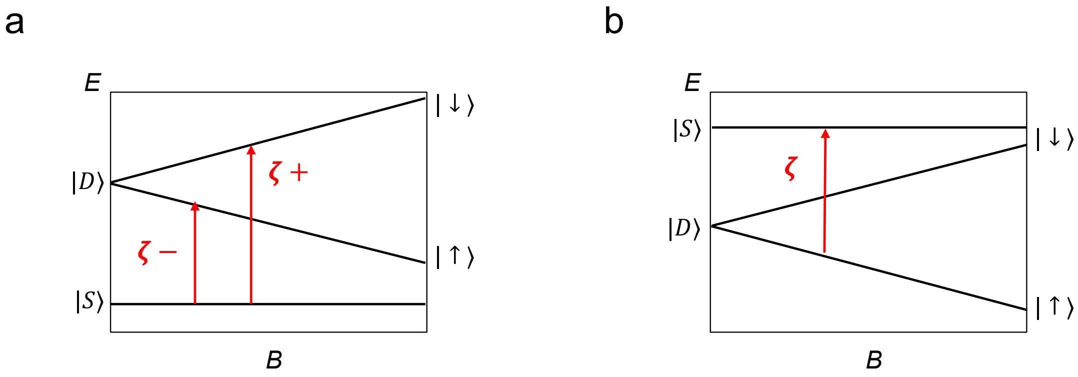

Figure 2.10: Illustrative magnetic field dependence of Andreev bound states in a single dot. a, The transition between the ground state $|S\rangle$ and excited state $|D\rangle$, as a function of magnetic field. Two transitions from the ground states to the $|\uparrow\rangle$ and $|\downarrow\rangle$ excited take place. **b,** The transition between the ground state $|D\rangle$ and excited state $|S\rangle$. Only the transition from the ground $|D\rangle$ states to the excited $|S\rangle$ is allowed.

2.4 ANDREEV BOUND STATES: THEORETICAL APPROACHES[1]

We model our superconductor-quantum dot systems with finite subgap density of states to approximate the soft gap induced superconductivity. In this section we focus on the double dot systems. The results, energy spectra and transport simulation, will be presented together with the experimental observation in the Chapter 5 for convenient comparison.

2.4.1 Hamiltonians

We first simplify the Hamiltonian of a single dot coupled to a single superconductor by assuming an infinite superconducting gap. Instead, we use a single parameter, τ, to describe the strength of Andreev reflection of electrons from the superconductor. The model thus yields

$$H_{\text{S-QD}} = \sum_{\sigma=\{\uparrow,\downarrow\}} \varepsilon_\sigma n_\sigma + U n_\uparrow n_\downarrow - \left(\tau d_\uparrow^\dagger d_\downarrow^\dagger + \text{H.c.}\right), \tag{2.8}$$

---

[1] THIS SECTION IS ADAPTED FROM REF.[61].

where ε_σ is the energy of an electron with spin σ on the quantum dot which is set by the gate voltage and the magnetic field, $n_\sigma = d_\sigma^\dagger d_\sigma$ is the number operator for electrons with spin σ on the dot, U is the charging energy for double occupancy of the dot, and $d_\sigma^\dagger$ and d_σ are the electron creation and annihilation operators. The spectrum of this Hamiltonian consists of two spin-singlets ($\sin(\theta)|0\rangle + \cos(\theta)|\uparrow\downarrow\rangle$ and $\cos(\theta)|0\rangle - \sin(\theta)|\uparrow\downarrow\rangle$) and a spin-doublet ($|\uparrow\rangle$ and $|\downarrow\rangle$). The parity of the ground state, as well as the angle θ, is determined by the coupling constants and can be tuned from even to odd to even by varying $\varepsilon_\uparrow$ and $\varepsilon_\downarrow$.

As we will see, this simplified Hamiltonian preserves the essence of Andreev bound states and will lead to less computation when to numerically compute systems of two or more dots. On the other hand, we are fully aware that it would fail to capture the following effects. (1) The Kondo effect. Because the quasiparticles have infinity energy so that the coupling between the electron in the dot and the quasiparticles in the leads is zero; (2) Multiple Andreev reflection. Multiple Andreev reflection can occur in a quantum dot strongly coupled to two superconducting leads. A particle undergoes Andreev reflections for multiple time and each time gains energy of $|e|V_{SD}$ where V_{SD} is the bias across the dot. It results in transport resonances at $V_{SD} = 2\Delta/|e|n$ where n's are integers. Thus the assumption ($\Delta = \inf$) eliminates multiple Andreev reflection. This does not cause issues because in our experiments, the quantum dots are strongly coupled to only a superconductor and thus multiple Andreev reflection is not explored and observed.

To describe the hybridization of Andreev bound states in double dots that we call Andreev molecular states at zero bias we need to couple two atomic Andreev bound states. The corresponding Hamiltonian becomes

$$H_{\text{S-QD-QD-S}} = \sum_{i=\{L,R\}} \left[\sum_{\sigma=\{\uparrow,\downarrow\}} \varepsilon_{i,\sigma} n_{i,\sigma} + U_i n_{i,\uparrow} n_{i,\downarrow} - \left(\tau_i d_{i,\uparrow}^\dagger d_{i,\downarrow}^\dagger + \text{H.c.} \right) \right] \tag{2.9}$$

$$- t \sum_{\sigma=\{\uparrow,\downarrow\}} \left(d_{L,\sigma}^\dagger d_{R,\sigma} + \text{H.c.} \right), \tag{2.10}$$

where the subscripts L and R stand for the left and the right quantum dots and t is the interdot tunneling matrix element. The eigenstates of $H_{\text{S-QD-QD-S}}$ are the Andreev molecular states plotted in Fig.5.1c.

In the following section, we discuss a more detailed model of Andreev molecular states at nonzero bias voltages, which describes both Andreev reflections and interdot coupling while keeping track of the charging energy of the two superconducting leads.

2.4.2 "Two-fluid" model

In the experiment presented in Chapter 5, the structure of the device is superconductor-single dot-single-dot-superconductor. In the experiment, we measure the resonance through the Andreev molecular states and clearly it is probed by the superconducting leads. The reason that the superconducting leads can serve as probes are the presence of subgap quasi-particles in the so-called "soft gap" induced superconductivity in the nanowires. To account for the presence of sub-gap quasi-particles, we model each lead as having a superconducting component and a normal metal component (see Fig. 2.11). The superconducting component is a conventional BCS superconductor with a hard gap Δ, which provides a condensate of Cooper pairs and drives Andreev reflection processes. The normal component, which we model as a non-interacting Fermi gas with a low density of states at the Fermi surface, provides the low energy electronic excitations that are necessary for sub-gap transport. Finally, to model the application of bias, V_{bias}, we tie the electro-chemical potentials of the two components together and fix them to the applied bias voltage [see Fig. 2.11].

One of the key features observed in the experimental data are discrete and narrow Andreev bound state-like features. As the strong resonant tunneling of electrons from the normal component of the leads to the quantum dot sub-system tends to broaden the discrete levels of the quantum dot sub-system, we restrict our modeling to the regime where single-electron tunneling (between the quantum dot system and the normal metal component of the leads) is the weakest coupling in the system.

Our transport model is encoded by the Hamiltonian

$$H = H_{\text{QD}} + H_{\text{S}} + H_{T,S} + H_N + H_{T,N}, \tag{2.11}$$

where H_{QD} describes the double-dot subsystem, H_{S} describes the electro-chemical potential energy of the Cooper pairs in the superconducting leads, $H_{T,S}$ describes Andreev reflection, H_N is the Hamiltonian of the normal component of the leads, and $H_{T,N}$ describes the

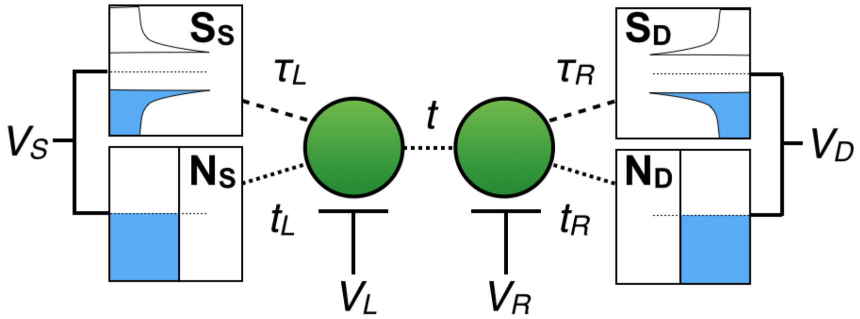

Figure 2.11: Theoretical schematic of the system. Hybrid superconductor-double dot-superconductor system, consisting of an array of two quantum dots tunnel-coupled to superconducting leads. Each lead is modeled as having a standard BCS superconducting (**S**) component and a normal metal (**N**) component. The coupling to the BCS components give rise to Andreev reflection processes, whereas the coupling to the normal components provide low-energy electronic excitations which are responsible for sub-gap transport. The strength of the interdot tunneling is set by t, while τ_L and τ_R (t_L and t_R) control the coupling of the left and right dots to the superconducting (normal) components of the left and right leads. The leads are biased by the source (drain) voltages $V_{S(D)}$ and the chemical potential on the left (right) dot is controlled by the side-gate voltage $V_{L(R)}$.

tunneling between the QDs and the normal components of the leads. H_{QD} is given by

$$H_{\mathrm{QD}} = \sum_{j\sigma} \varepsilon_{j\sigma} n_{j\sigma} + U \sum_{j} n_{j\uparrow} n_{j\downarrow} - t \sum_{\sigma} \left(d^{\dagger}_{R,\sigma} d_{L\sigma} + d^{\dagger}_{L\sigma} d_{R,\sigma} \right), \tag{2.12}$$

where $n_{j\sigma} = d^{\dagger}_{j\sigma} d_{j\sigma}$ is the number operator of the electrons on QD $j = \{L, R\}$ with spin σ, energy $\varepsilon_{j\sigma}$ (controlled by the electro-chemical potential in quantum dot j). The strength of the Coulomb repulsion and of the interdot coupling is set by U and t, respectively. The model Hamiltonian for the leads is a combination of the superconducting component

$$H_{\mathrm{S}} = \sum_{j \in \{S,D\}} eV_j N_j, \tag{2.13}$$

and the normal component

$$H_N = \sum_{j \in \{S,D\}} \sum_{\mathbf{k}\sigma} \left(\xi_{\mathbf{k}} + eV_j \right) c^{\dagger}_{j\mathbf{k}\sigma} c_{j\mathbf{k}\sigma}, \tag{2.14}$$

where $j = \{S, D\}$ indicates the source and drain leads, N_j represents the electron number operator for the superconducting component, $c^\dagger_{j\mathbf{k}\sigma}$ ($c_{j\mathbf{k}\sigma}$) creates (annihilates) an electron with momentum $\mathbf{k}$ and spin σ with energy $\xi_\mathbf{k}$ in the normal component of lead j, and both components are biased by the same voltages V_j. The Andreev reflection (i.e. pair tunneling) is described by the Hamiltonian

$$H_{T,S} = -\tau_L S^+_S d_{L\downarrow} d_{L\uparrow} - \tau_R S^+_D d_{R\downarrow} d_{R\uparrow} + \text{H.c.}, \tag{2.15}$$

where the operator S^+_j increases the number of electrons in the superconducting condensate of the j-th superconducting lead by two: $N_j \to N_j + 2$. Keeping track of the number of electrons in the superconducting condensates in the two leads is an essential feature of the model that allows us to describe Andreev reflection between the QDs and both leads when there is a voltage difference between the leads [53]. The coupling between the QDs and the normal leads is given by the conventional tunneling Hamiltonian

$$H_{T,N} = -t_L \sum_{\mathbf{k}\sigma} c^\dagger_{S\mathbf{k}\sigma} d_{L\sigma} - t_R \sum_{\mathbf{k}\sigma} c^\dagger_{D\mathbf{k}\sigma} d_{R\sigma} + \text{H.c.}. \tag{2.16}$$

Here τ_j and t_j (taken to be real) set the strength of the pair (Andreev reflection) and single-electron tunneling between QD and lead j.

As t_L and t_R are the weakest couplings in the system, we call $H_{\text{AMH}} = H_{\text{QD}} + H_{\text{S}} + H_{T,S}$ the Andreev molecular Hamiltonian and treat $H_{T,N}$ as a perturbation to H_{AMH}. That is, the Andreev molecular Hamiltonian gives rise to the Andreev molecular states, and $H_{T,N}$ drives transitions between these states.

2.4.3 Eigenstates of the Andreev molecular Hamiltonian at finite bias

The Andreev molecular Hamiltonian preserves the total electron number N_T, total parity, total spin S_T, and spin projection S_z. Therefore, the Andreev molecular states of the S-QD-QD-S system can be split into subspaces of even and odd parity; the even subspace consists of singlet (S) and triplet ($T_{0,\pm}$) Andreev molecular states, whereas the odd parity subspace consists of doublet ($D_\pm$) Andreev molecular states.

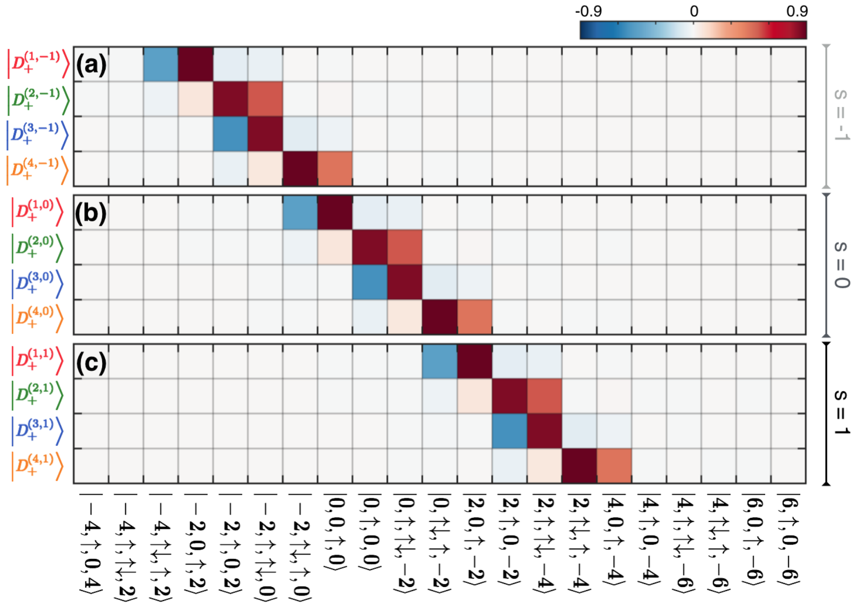

Figure 2.12: Ladder of Andreev molecular states. Ladder of Andreev molecular states for the doublet subspace $|D_+^{(c,s)}\rangle \equiv |N_T = 2N+1, S = 1/2, S_z = 1/2, c, s\rangle$ for $V_{\text{bias}} = V_D - V_S = 0.2\Delta/e$, $\tau_{L(R)} = 0.8\Delta, t = 0.01\Delta$. We show the set of four color eigenstates corresponding to three shifts (a) $s = -1$, (b) $s = 0$, and (c) $s = 1$. The $s = 0$ reference shift corresponds to the set of color states whose maximum components have minimum Cooper pair imbalance between the leads. From those states, we generate the set of states for the subsequent $s = 1$ ($s = -1$) shift by transferring one Cooper pair from the drain (source) lead to the source (drain) lead. For convenience, we choose to count electrons relative to N, which is equivalent to set $N = 0$.

In terms of the number of Cooper pairs in the source and drain leads, N_L and N_R, what do eigenstates of the Andreev molecular Hamiltonian look like at finite bias? A good analogy is the spatially localized eigenstates of a quantum particle in a tilted washboard potential. Although the ground state corresponds to the particle at the "bottom" of the washboard, there is a whole ladder of eigenstates ψ_i, one eigenstate for each lattice site, that lead to Bloch oscillations. Given the eigenstate ψ_i we can find the state ψ_{i+1} by shifting the wavefunction one lattice site down. Hence the eigenstates can be thought of as forming a ladder, with the rungs labeled by the expectation value for position $\langle x\rangle_i$. Similarly, Andreev molecular states "live" on ladders, with rungs corresponding to the "shift" $s \approx N_L - N_R$ [which will be precisely defined in the next paragraph]. Given an eigenstate on a particular rung, we can obtain the eigenstate on the next rung by shifting a Cooper pair from the left lead to the right lead. For the case of the double quantum dot system there are 16 ladders (4 spin up doublets, 4 spin down doublets, 3 triplets and 5 singlets), which we label by the spin state and "color".

Consider, for example, the singlet Andreev molecular subspace with $N_T = 2N$ electrons. Due to Pauli blockade, there are only five possible ways of electrons occupying the double-dot orbitals, namely $|0,0\rangle, |0,\uparrow\downarrow\rangle, |\uparrow\downarrow,0\rangle, |\uparrow\downarrow,\uparrow\downarrow\rangle$ and $(|\uparrow,\downarrow\rangle - |\downarrow,\uparrow\rangle)/\sqrt{2}$. When coupled to the superconducting leads via Andreev reflection, those five double-dot, singlet states hybridize with the bare states of the superconductors $|N_S, N_D\rangle$, which represent a given distribution of Cooper pairs between the leads. Thus, we can generate any state in this subspace from five reference states of the S-QD-QD-S system, such as $|N,0,0,N\rangle, |N,0,\uparrow\downarrow,N-2\rangle, |N-2,\uparrow\downarrow,0,N\rangle, |N-2,\uparrow\downarrow,\uparrow\downarrow,N-2\rangle$ and $(|N,\uparrow,\downarrow,N-2\rangle - |N,\downarrow,\uparrow,N-2\rangle)/\sqrt{2}$, by transferring Cooper pairs from one lead to the other using the transfer operators $T^{\pm}|N_S, \mathrm{QD_L}, \mathrm{QD_R}, N_D\rangle = |N_1 \pm 2, \mathrm{QD_L}, \mathrm{QD_R}, N_2 \mp 2\rangle$. This is possible since all remaining states of the span correspond to one of the reference states, but with a different Cooper pair configuration. By linearity, the same considerations apply to the eigenstates. Hence, the whole ladder of singlet Andreev molecular states $|S^{(c,s)}\rangle \equiv |N_T = 2N, S_T = 0, S_z = 0, c, s\rangle$ can be constructed from the five reference eigenstates, which we refer to by the "color" quantum number ($c = 1, 2, \ldots, 5$). The number of unique color eigenstates corresponds to the number of unique Andreev molecular states. As a result, the triplet and doublet subspaces can be generated from sets of three and eight color eigenstates, respectively. Here we also introduce the "shift" quantum number ($s = 0, \pm 1, \pm 2, \ldots$), defined as the number of times one needs to apply $T^{\pm}$ to a reference eigenstate to generate an eigenstate with a different Cooper pair configuration.

We define the $s = 0$ reference shift as the eigenstates whose maximum components show minimum Cooper pair imbalance between the leads. We remark that this definition is arbitrary, and alternative definitions should not physical results. Note that the eigenenergies for non-zero shifts ($s \neq 0$) can then be easily obtained from the relation

$$E^{c,s}_{N_T,S_z} = E^{c,0}_{N_T,S_z} + 2s\, e(V_S - V_D). \tag{2.17}$$

As an example, we show in Fig. 2.12 the $s = 0$ color states for the D_+ subspace for different bias voltages. At larger bias voltages, the eigenstates are well localized in Hilbert space, showing a narrow distribution of Cooper pairs. As the bias voltage decreases towards zero, the number of Cooper pairs is allowed to fluctuate and, as a result, the eigenstates spread.

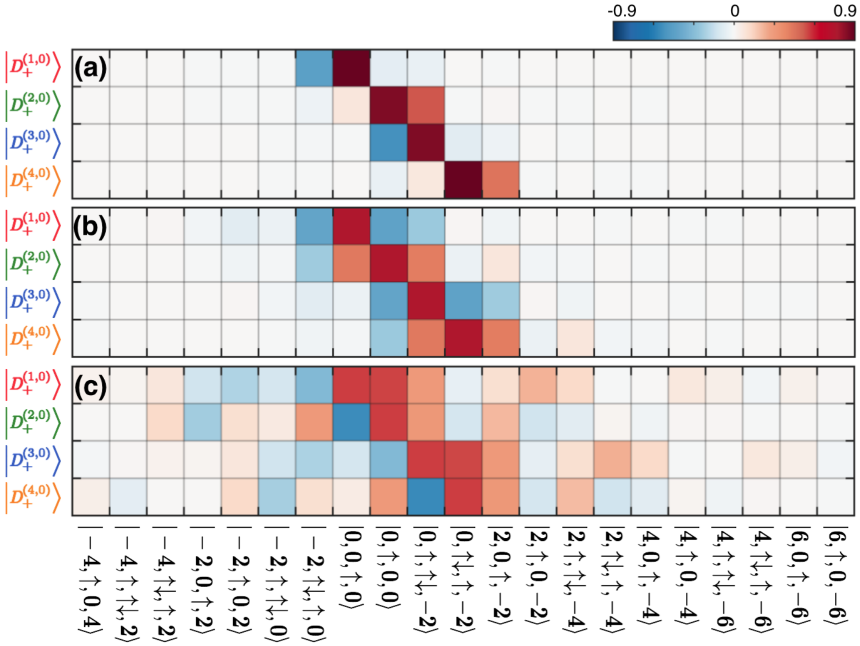

Figure 2.13: Ladder of $s = 0$ color Andreev states. Reference $s = 0$ color states for the doublet Andreev molecular subspace $|D_+^{(c,0)}\rangle \equiv |N_T = 2N + 1, S = 1/2, S_z = 1/2, c, s = 0\rangle$ for (a)–(c) $eV_{\text{bias}}/\Delta = 0.2, 0.02, 0.002$, showing the spreading of the probability amplitudes at low bias voltages.

2.4.4 Classical master equation

To describe the experimentally observed sub-gap transport through the S-QD-QD-S device, we now consider the effects of the coupling to the normal component of the leads. We describe the state of the S-QD-QD-S device by the probability distribution P, which gives the probability of finding the system in a particular eigenstate $|N_T, S_T, S_z, c, s\rangle$ of the Andreev molecular Hamiltonian. The S-QD-QD-S system is pushed out of equilibrium by a nonzero source-drain bias voltage. Energy is dissipated by single electrons tunneling from the quantum dots to the normal components of the leads. Such incoherent processes drive transitions between Andreev molecular subspaces of different parity, as illustrated in Fig. 2.14.

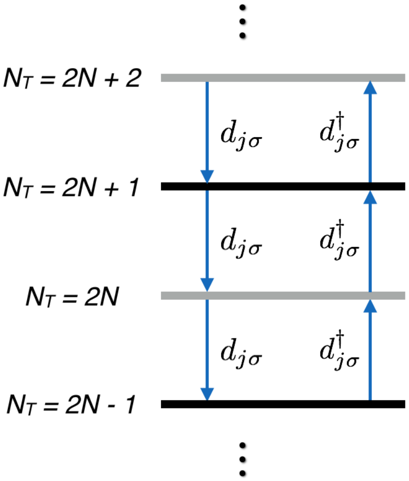

Figure 2.14: Schematic diagram of the transitions between Andreev bound states of different parities. Transitions between the even and odd Andreev molecular subspaces of the S-QD-QD-S system driven by single electron tunneling between the normal leads and the double dot subsystem. Depending on the spin of the exchanged electron, these transitions couple doublet states to either singlet or triplet states.

We write a classical master equation that accounts for the transitions between the various Andreev molecular levels. Depending on the spin of the exchanged electron, these transitions couple doublet states to either singlets or triplets. As we are interested in describing the transport dynamics in the long time limit, the non-equilibrium probability distribution P is given by the steady state solution of the rate equation

$$\frac{\mathrm{d}P(\mathbf{n})}{\mathrm{dt}} = \sum_{\mathbf{m}} \Big(\Gamma_{\mathbf{n}\leftarrow\mathbf{m}} P(\mathbf{m}) - \Gamma_{\mathbf{m}\leftarrow\mathbf{n}} P(\mathbf{n}) \Big), \tag{2.18}$$

where the first (second) term represents the probability of tunneling into (out of) state $|\mathbf{n}\rangle \equiv |N_T, S_T, S_z, c, s\rangle$ and $\Gamma_{\mathbf{n}\leftarrow\mathbf{m}}$ are the transition rates between levels $\mathbf{m}$ and $\mathbf{n}$ due to the exchange of one electron with the normal leads [54]. Specifically, if the transition rate $\Gamma_{\mathbf{n}\leftarrow\mathbf{m}}$ results from the addition of an electron to the S-QD-QD-S system, it is given by

$$\Gamma^{(\mathrm{gain})}_{\mathbf{n}\leftarrow\mathbf{m}} = 2\pi \sum_{j,\sigma} t_j^2 |\langle\mathbf{n}|\, d^\dagger_{j,\sigma}\, |\mathbf{m}\rangle|^2 n_F(E_{\mathbf{n}} - E_{\mathbf{m}} - eV_j), \tag{2.19}$$

whereas if it results in the loss of an electron to the normal leads, we have

$$\Gamma^{(\text{loss})}_{\mathbf{n}\leftarrow\mathbf{m}} = 2\pi \sum_{j,\sigma} t_j^2 |\langle \mathbf{n}| d_{j,\sigma} |\mathbf{m}\rangle|^2 \big(1 - n_F(E_{\mathbf{m}} - E_{\mathbf{n}} - eV_j)\big). \tag{2.20}$$

Here n_F represents the Fermi-Dirac distribution, which gives the probability to find an electron in the normal leads, and $\{E_{\mathbf{m}}\}$ represent the eigenenergies of the S-QD-QD-S system. The rate equation Eq.2.18 takes into account all possible single-electron transitions between Andreev molecular states. However, as we show below, we can use the symmetries of the Andreev molecular Hamiltonian to effectively reduce Eq.2.18 to involve only transitions between two subspaces of opposite parity, containing a total of $2N$ and $2N+1$ electrons ($N \gg 1$).

As shown in Fig. 2.14, the $2N$ and $2N+1$ subspaces are directly coupled by transitions involving either the addition of an electron to the $2N$ subspace or the removal of an electron from the $2N+1$ subspace. Using Eqs. (2.19) and (2.20), those rates are given by

$$\Gamma^{(\text{gain})}_{\alpha_O\leftarrow\beta_E} = 2\pi \sum_{j,\sigma} t_j^2 |\langle 2N+1, \alpha_O, c', s'| d^\dagger_{j\sigma} |2N, \beta_E, c, s\rangle|^2 n_F\big(E^{c',s'}_{2N+1,\alpha_O} - E^{c,s}_{2N,\beta_E} - eV_j\big), \tag{2.21}$$

$$\Gamma^{(\text{loss})}_{\alpha_E\leftarrow\beta_O} = 2\pi \sum_{j,\sigma} t_j^2 |\langle 2N, \alpha_E, c', s'| d_{j\sigma} |2N+1, \beta_O, c, s\rangle|^2 \Big(1 - n_F\big(E^{c,s}_{2N+1,\beta_O} - E^{c',s'}_{2N,\alpha_E} - eV_j\big)\Big). \tag{2.22}$$

For simplicity of notation, here and henceforth we label the spin subspaces by $\alpha_{E(O)}, \beta_{E(O)} = S, T_{0,\pm}(D_\pm)$, where the E, O subscripts emphasize that these are transitions between the $N_T = 2N$ (even) and $N_T = 2N+1$ (odd) Andreev molecular subspaces of the S-QD-QD-S system.

We refer to transitions described by Eqs. (2.21) and (2.22) as type 1 transitions. Type 2 transitions connect the $2N$ and $2N+1$ subspaces to the $2N-1$ and $2N+2$ subspaces (see Fig. 2.14). Type 2 transitions can be mapped back onto the $2N$ and $2N+1$ subspaces because when the number of Cooper pairs is changed by one on a lead at fixed bias voltage, within our model, the eigenenergies are trivially shifted according to the change in electrochemical potential energy, i.e., $E^{c,s}_{N_T\pm 2,\alpha} = E^{c,s}_{N_T,\alpha} \pm 2eV_j$. Thus, by using this relation and the operators S^+ and S^-, we can write the following identities:

$$\begin{aligned}
&|\langle 2N+1,\alpha',c',s'|\, d_{j\sigma}\, |2N+2,\alpha,c,s\rangle|^2\Big(1-n_F\big(E^{c,s}_{2N+2,\alpha}-E^{c',s'}_{2N+1,\alpha'}-eV_j\big)\Big)\\
&\qquad = |\langle 2N+1,\alpha',c',s'|\, d_{j\sigma}S^+\, |2N,\alpha,c,s\rangle|^2\Big(1-n_F\big(E^{c,s}_{2N,\alpha}-E^{c',s'}_{2N+1,\alpha'}+eV_j\big)\Big), \qquad (2.23)\\
&|\langle 2N+2,\alpha,c',s'|\, d^\dagger_{j\sigma}\, |2N+1,\beta,c,s\rangle|^2 n_F\big(E^{c',s'}_{2N+2,\alpha}-E^{c,s}_{2N+1,\beta}-eV_j\big)\\
&\qquad = |\langle 2N,\alpha,c',s'|\, S^- d^\dagger_{j\sigma}\, |2N+1,\beta,c,s\rangle|^2 n_F\big(E^{c',s'}_{2N,\alpha}-E^{c,s}_{2N+1,\beta}+eV_j\big), \qquad (2.24)
\end{aligned}$$

Eq.2.23 and Eq.2.24 thus show how transitions of type 2 can be effectively mapped onto a transition between the $2N$ and $2N+1$ subspaces. Note that those transitions are driven by the exchange of a single electron with the normal leads together with the creation or annihilation of a Cooper pair on the superconducting component of the same lead. The rates for type-2 transitions are then given by

$$\tilde{\Gamma}^{(\text{gain})}_{\alpha_E\leftarrow\beta_O} = 2\pi\sum_{j,\sigma} t_j^2 |\langle 2N,\alpha_E,c',s'|\, S^- d^\dagger_{j\sigma}\, |2N+1,\beta_O,c,s\rangle|^2 n_F\big(E^{c',s'}_{2N,\alpha_E}-E^{c,s}_{2N+1,\beta_O}+eV_j\big), \qquad (2.25)$$

$$\tilde{\Gamma}^{(\text{loss})}_{\alpha_O\leftarrow\beta_E} = 2\pi\sum_{j,\sigma} t_j^2 |\langle 2N+1,\alpha_O,c',s'|\, S^+ d_{j\sigma}\, |2N,\beta_E,c,s\rangle|^2\Big(1-n_F\big(E^{c,s}_{2N,\beta_E}-E^{c',s'}_{2N+1,\alpha_O}+eV_j\big)\Big), \qquad (2.26)$$

which describe either the removal of an electron from an even parity state or the addition of an electron to an odd eigenstate.

It is easy to generalize this mapping to all other N_T subspaces and show that any single-electron transition rate are of type 1 or 2 and, hence, can be calculated from Eqs. (2.21), (2.22), (2.25), or (2.26). Those effective transitions between the $2N$ and $2N+1$ subspaces are illustrated in Fig. 2.15. In this way, we reduce Eq.2.18 to a single even ($2N$) and odd ($2N+1$) subspaces. From now on, we simply refer to those subspaces as even and odd.

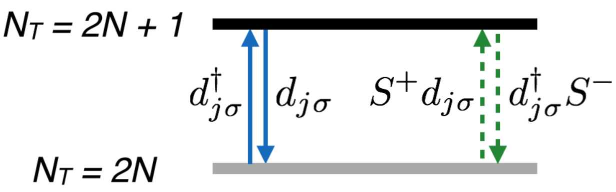

Figure 2.15: Allowed transitions between the states of even and odd parities. Effective transitions between the even ($N_T = 2N$) and odd ($N_T = 2N + 1$) Andreev molecular subspaces of the S-QD-QD-S system. The solid, blue arrows represent transitions of type 1, which involve the exchange of an electron between the normal leads and the quantum dots (see Eqs. (2.21) and (2.22)). Transitions of type 2 (dashed, green arrows), on the other hand, are driven by the exchange of an electron between the dots and the normal lead, but followed by the creation or annihilation of a Cooper pair in the superconducting component of the same lead (see Eqs. (2.25) and (2.26)).

We obtain the steady-state solution of Eq.2.18 from the eigenvalue equation

$$\begin{pmatrix} M^{\text{out}}_{S} & M^{\text{in}}_{S\leftarrow D_+} & M^{\text{in}}_{S\leftarrow D_-} & 0 & 0 & 0 \\ M^{\text{in}}_{D_+\leftarrow S} & M^{\text{out}}_{D_+} & 0 & M^{\text{in}}_{D_+\leftarrow T_+} & M^{\text{in}}_{D_+\leftarrow T_0} & M^{\text{in}}_{D_+\leftarrow T_-} \\ M^{\text{in}}_{D_-\leftarrow S} & 0 & M^{\text{out}}_{D_-} & M^{\text{in}}_{D_-\leftarrow T_+} & M^{\text{in}}_{D_-\leftarrow T_0} & M^{\text{in}}_{D_-\leftarrow T_-} \\ 0 & M^{\text{in}}_{T_+\leftarrow D_+} & M^{\text{in}}_{T_+\leftarrow D_-} & M^{\text{out}}_{T_+} & 0 & 0 \\ 0 & M^{\text{in}}_{T_0\leftarrow D_+} & M^{\text{in}}_{T_0\leftarrow D_-} & 0 & M^{\text{out}}_{T_0} & 0 \\ 0 & M^{\text{in}}_{T_-\leftarrow D_+} & M^{\text{in}}_{T_-\leftarrow D_-} & 0 & 0 & M^{\text{out}}_{T_-} \end{pmatrix} \begin{pmatrix} \vec{P}_S \\ \vec{P}_{D_+} \\ \vec{P}_{D_-} \\ \vec{P}_{T_+} \\ \vec{P}_{T_0} \\ \vec{P}_{T_-} \end{pmatrix} = 0, \qquad (2.27)$$

where the matrices $M^{\text{in}}_{\alpha\leftarrow\beta} = \Gamma_{\alpha\leftarrow\beta} + \tilde{\Gamma}_{\alpha\leftarrow\beta}$ and $M^{\text{out}}_{\alpha} = -\sum_\beta \left(\Gamma_{\beta\leftarrow\alpha} + \tilde{\Gamma}_{\beta\leftarrow\alpha}\right)$ describe the influx and outflux of probability of subspace α (with $\alpha, \beta = S, D_\pm, T_{0,\pm}$). Note that the vectors $\vec{P}_\alpha$ have dimension $d^\alpha_c d^\alpha_s$, where d^α_c (d^α_s) is the number of color (shift) states in subspace α. Similarly, M^{out}_α and $M^{\text{in}}_{\alpha\leftarrow\beta}$ are matrices of dimension equal to $d^\alpha_c d^\alpha_s \times d^\alpha_c d^\alpha_s$ and $d^\alpha_c d^\alpha_s \times d^\beta_c d^\beta_s$.

2.4.5 Steady-state Current

The steady-state current is obtained from the rate at which electrons go through the S-QD-QD-S device and is given by

$$I = -e \sum_{\alpha,\beta} \left(\gamma^{(\text{gain})}_{R,\alpha\leftarrow\beta} - \gamma^{(\text{loss})}_{R,\alpha\leftarrow\beta} \right) \vec{P}_\beta \qquad (2.28)$$

where the matrices $\gamma^{(\text{gain})}_{R,\alpha\leftarrow\beta}$ and $\gamma^{(\text{loss})}_{R,\alpha\leftarrow\beta}$ (of dimension $d_c^\alpha d_s^\alpha \times d_c^\beta d_s^\beta$) provide the current rates for transitions to the odd subspace, which are given by

$$\gamma^{(\text{gain})}_{R,\alpha_O\leftarrow\beta_E} = 2\pi t_j^2 |\langle \alpha_O^{(c',s')}|\, d^\dagger_{j\sigma}\, |\beta_E^{(c,s)}\rangle|^2 n_F\big(E^{c',s'}_{\alpha_O} - E^{c,s}_{\beta_E} - eV_j\big)(2s'-2s-1), \tag{2.29}$$

$$\gamma^{(\text{loss})}_{R,\alpha_O\leftarrow\beta_E} = 2\pi t_j^2 |\langle \alpha_O^{(c',s')}|\, S^+ d_{j\sigma}\, |\beta_E^{(c,s)}\rangle|^2 \Big(1 - n_F\big(E^{c,s}_{\beta_E} - E^{c',s'}_{\alpha_O} + eV_j\big)\Big)(2s'-2s-1), \tag{2.30}$$

and for transitions to the even subspace, which are given by

$$\gamma^{(\text{gain})}_{R,\alpha_E\leftarrow\beta_O} = 2\pi t_j^2 |\langle \alpha_E^{(c',s')}|\, S^- d^\dagger_{j\sigma}\, |\beta_O^{(c,s)}\rangle|^2 n_F\big(E^{c',s'}_{\alpha_E} - E^{c,s}_{\beta_O} + eV_j\big)(2s'-2s-1), \tag{2.31}$$

$$\gamma^{(\text{loss})}_{R,\alpha_E\leftarrow\beta_O} = 2\pi t_j^2 |\langle \alpha_E^{(c',s')}|\, d_{j\sigma}\, |\beta_O^{(c,s)}\rangle|^2 \Big(1 - n_F\big(E^{c,s}_{\beta_O} - E^{c',s'}_{\alpha_E} - eV_j\big)\Big)(2s'-2s-1). \tag{2.32}$$

We solve the master equation Eq.2.27 and compute the current with Eq.2.28 numerically, by first finding the set of even and odd eigenstates of the S-QD-QD-S Hamiltonian (2.11) via exact diagonalization. As discussed above, we restrict this calculation to even and odd subspaces with a total of $2N$ and $2N+1$ electrons. Note that because of the conservation of the total electron number, the exact value of N only sets an overall offset and, hence, N can be taken as an arbitrary parameter. After diagonalizing H, we select the reference color eigenstates and eigenenergies for each subspace. Together with the Cooper pair transfer operators $T^{\pm}$, we then construct the ladders of Andreev molecular states, whose energies are calculated from Eq. (2.17). We use the ladders of Andreev states to compute the transition probabilities between the even and odd subspaces and their respective Fermi electron (hole) occupation probabilities on the normal leads. Finally, this allow us to calculate the transition rates (2.21), (2.22), (2.25), (2.26), and (2.29)–(2.32) and then to construct and solve both the master equation Eq.2.27 and the current equation Eq.2.28.

2.5 KITAEV MODEL

In 2000, A. Y. Kitaev studied a quantum wire made of L ($L \gg 1$) fermionic sites with the following Hamiltonian [2]:

$$H_{\text{Kitaev}} = \sum_j \left(-t(c_j^\dagger c_{j+1} + c_{j+1}^\dagger c_j) - \mu(c_j^\dagger c_j - \frac{1}{2}) + (\Delta c_j c_{j+1} + H.C.) \right), \tag{2.33}$$

where j is the number of the site, t is the inter-site hopping amplitude, μ is the chemical potential and $\Delta = |\Delta| e^{i\theta}$ is the superconducting gap. Notice that no spin subindices are present because it is assumed that the quantum wire has only one spin component. As a result, Δ pairs particles of same spin and favors the triplet form, i.e., the paring is p-wave or f-wave type.

By rewriting the fermion operators in terms of Majorana operators:

$$a_{2j-1} = e^{i\frac{\theta}{2}} c_j + e^{-i\frac{\theta}{2}} c_j^\dagger, \tag{2.34}$$

and

$$a_{2j} = -ie^{i\frac{\theta}{2}} c_j + ie^{-i\frac{\theta}{2}} c_j^\dagger, \tag{2.35}$$

the Hamiltonian becomes

$$H_{\text{Kitaev}} = \frac{i}{2} \sum_j \left(-\mu a_{2j-1} a_{2j} + (t + |\Delta|) a_{2j} a_{2j+1} + (-t + |\Delta|) a_{2j-1} a_{2j+2} \right). \tag{2.36}$$

Note that the conjugate of either Majorana operator is itself, i.e., $a_{2j-1}^\dagger = e^{-i\frac{\theta}{2}} c_j^\dagger + e^{i\frac{\theta}{2}} c_j = a_{2j-1}$ and $a_{2j}^\dagger = ie^{-i\frac{\theta}{2}} c_j^\dagger - ie^{i\frac{\theta}{2}} c_j = a_{2j}$. The study of the Hamiltonian is presented comprehensively in the paper [2]. Here, just by considering two very special cases, we can already unveil two dramatically different results:

- $|\Delta| = t = 0$ and $\mu < 0$. The Hamiltonian becomes

$$H_{\text{Kitaev}} = \frac{i}{2} \sum_j \left(-\mu a_{2j-1} a_{2j}\right), \tag{2.37}$$

  where only the first term remains. The Majorana operators, a_{2j+1} and a_{2j+2} are paired within same site (See Fig.2.16a). It is a trivial case where fermionic sites build the quantum wire.

- $|\Delta| = t > 0$ and $\mu = 0$. The Hamiltonian becomes

$$H_{\text{Kitaev}} = i \sum_j \left(|\Delta| a_{2j} a_{2j+1}\right), \tag{2.38}$$

  where only the second term survives. The Majorana operators, a_{2j} and a_{2j+1} from neighboring sites are paired (See Fig.2.16b). Importantly, two Majorana operators, a_1 and a_{2L} at the two ends of the quantum wire are not included in the Hamiltonian. They are left unpaired. These quasiparticle modes with zero energy are called Majorana zero modes.

The parameter regime where unpaired Majorana zero modes are present is called the topological regime. Note that $|\Delta| = t > 0$ and $\mu = 0$ are the conditions to create Majorana zero modes completely localized at the two end sites of the wire. More relaxed conditions of the topological regime are given by the following: $2|t| > |\mu|$ and $|\Delta| > 0$ [2].

A great amount of experimental [10, 46, 45, 55, 56, 11, 13, 12] and theoretical [3, 4] works have been devoted to implementing the Kitaev model. Except for the chains of iron atoms formed on the surface of superconducting leads [55], most of them are based on one-dimensional nanowires. These works are based on the arguments in Ref. [3, 4] that the Kitaev model can be realized in superconductor-nanowire hybrid structures, given the following ingredients: nanowires that have strong spin-orbit coupling and facilitate ballistic transport, induced superconductivity in the nanowires from s-wave superconductors that sustains at sufficiently high magnetic fields, and a sufficiently strong magnetic field.

The experimental study of Majorana zero modes based in nanowires, one direction, has gained significant developments by demonstrating the prime feature of Majorana zero modes — the zero bias peak — in various experiments [10, 46, 45, 56, 11, 13, 12]. More

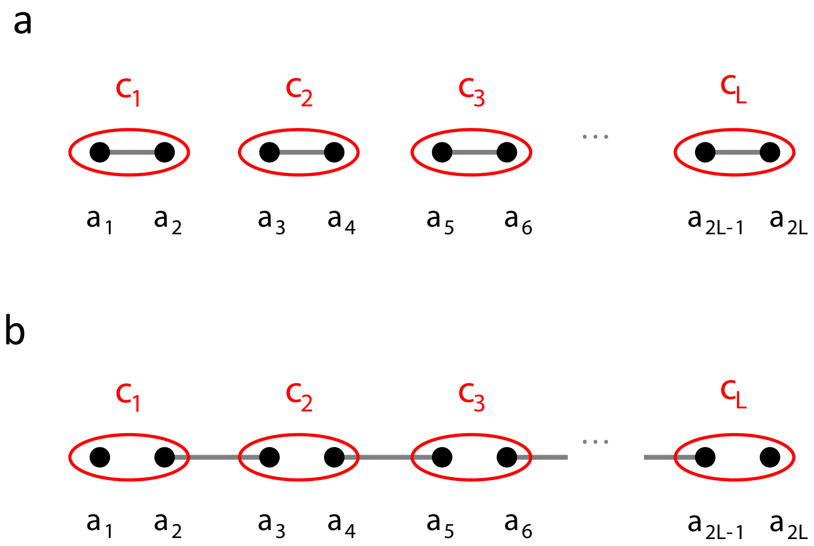

Figure 2.16: Two types of pairing in the Kitaev model. Schematics of the Kitaev model in two parameter regimes. The quantum wire has L sites. Each site, enclosed with a red ellipse, is a fermion (c_j) that can be expressed as superposition of two Majorana operators, a_{2j-1} and a_{2j}. **a,** $|\Delta| = t = 0$ and $\mu < 0$. The Majorana operators are paired within each site. **b,** $|\Delta| = t > 0$ and $\mu = 0$. The Majorana operators of neighboring sites are paired, i.e, a_{2j} and a_{2j+1}, where $j = 1, 2, ..., L$, are paired except for a_1 and a_{2L}.

fundamental properties of Majorana zero modes beside the zero bias feature, however, remain to be observed before the existence of Majorana zero modes in solid states can be concluded.

Another direction, the implementation of the Kitaev chain model in terms of the literal chain structure, has been less explored. More recently, theoretical proposals have detailed the chain geometry and necessary ingredients to create Majorana zero modes [17, 18, 19], i.e., strong spin-orbit interaction, a high g-factor in the semiconductor dots and induced superconductivity. Notice that the necessary ingredients remain the same, except that ballistic transport is no longer necessary. Actually, in the experimental realization of Majorana zero modes based on nanowires, realizing ballistic transport is challenging because of disorder and variation of chemical potential generated by gating. Indeed, as suggested by these theoretical works [17, 18, 19], more robust realization of Majorana zero modes can be realized with chain structures, because ensuring ballistic transport is no longer necessary. Further discussion in this direction will be continued in Chapter 6.

We shall end the discussion of the Kitaev model by connecting these two directions, continuous and chain implementations, to our experiments. The former, is explored in Chapter 4 based on NbTiN-InSb single dots in the open dot regime. The latter, is explored by studying the Andreev bound states in single dots (Chapter 4), double dots (Chapter 5) and triple dots (Chapter 6). Also, in Chapter 7 and Chapter 8 we explore the experimental feasibility of realizing Majorana zero modes based on a different type of nanowires, Ge/Si nanowires, by exploring the individual ingredients: induced superconductivity, spin-orbit coupling and g-factors.

3.0 FABRICATION AND MEASUREMENT SETUP

This chapter describes the InSb nanowires used in Chapter 4, Chapter 5 and Chapter 6, and the Ge/Si core/shell nanowires used in Chapter 7 and Chapter 8; the nanofabrication techniques involved in making the superconductor-semiconductor nanowire hybrid devices based on InSb and Ge/Si nanowires, and the measurement setup used to perform low-temperature electrical quantum transport measurements on these devices.

3.1 SEMICONDUCTOR NANOWIRES

Semiconductor nanowires are a versatile platform for studying quantum systems. The dimensions and crystal direction of nanowires can be precisely controlled during growth. Also, thanks to the quasi-one-dimensional structure, heterostructures of various material combinations can be realized, because the area of interface can be much smaller than those in film or bulk. As a result, the strain accumulated due to lattice constant mismatch at the interface can be much lower, giving access to a broader range of material combinations. The 1D nature also enables studies of interesting physics in one and zero dimensional systems, such as one-dimensional diffusive and ballistic transport [57], quantum point contacts [58], field effect transistors [59] and Josephson junctions [60]. In this thesis, the nanowires particularly facilitate the implementation of highly tunable quantum dots and quantum dot chains using local electrode gates [61].

The InSb nanowires used in this thesis are grown by Diana Car, Sébastien R. Plissard and Erik P.A.M. Bakkers at Eindhoven University of Technology. The Ge/Si core/shell nanowires are grown by Binh-Minh Nguyen, Jinkyoung Yoo and Shadi A. Dayeh in Los Alamos National Laboratory. These nanowires are then sent to the University of Pittsburgh, where further device fabrication and quantum transport measurements are performed.

3.1.1 InSb nanowires

The InSb nanowires used in this thesis have zinc blende lattice structure. The nanowire axis is along [111] direction, which yields a hexagonal cross section. They are 80-120 nm in diameter and 2-4 μm in length. They are grown using a technique called metalorganic vapor phase epitaxy (MOVPE) [62]. After the growth, the nanowire chip (also called the mother chip) is taken out from the growth reactor and native oxide quickly grows on the nanowire surface. Careful removal of the native oxide will be an important step of device fabrication later.

InSb nanowires have recently attracted interest because of several properties. The small bandgap (0.17 meV in bulk at room temperature) of InSb facilitates bipolar transistor oper-

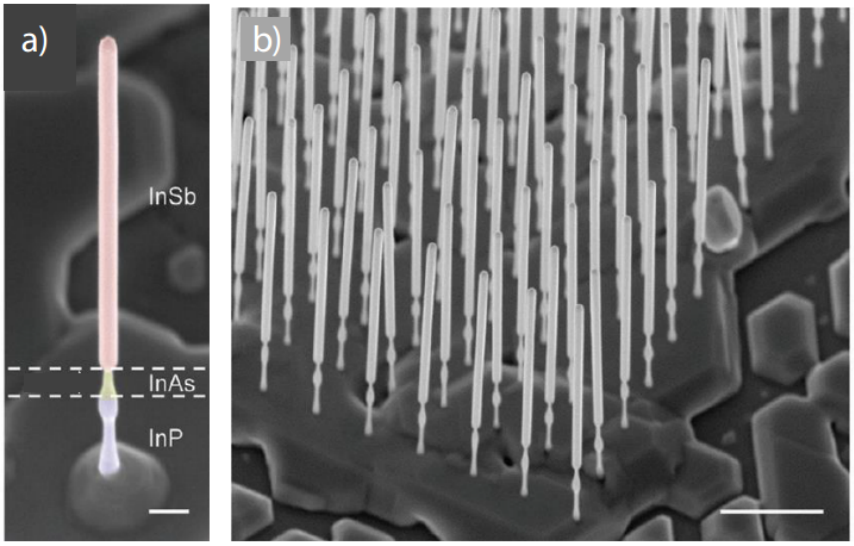

Figure 3.1: InSb nanowires on mother chips. **a,** Scanning electron micrograph (SEM) of an InSb nanowire consisting of several sections: InP stem, InAs stem, InSb nanowire and gold particle. The nanowire is grown using randomly deposited gold catalyst particles. **b,** SEM of arrays of nanowires grown by patterning the substrate with Au catalyst particles with electron beam lithography (EBL). Panels are adapted from Ref.[63]. The scale bars are 200 nm and 1 μm, respectively.

ations in conduction and valance bands [64]. The g-factor is impressively large ($\sim 30-50$) [60, 10], which facilitates a large Zeeman energy using a low magnetic field. The electron mobility in InSb nanowires is high — up to 10^4 cm^2 V^{-1} s^1 — and the signatures of ballistic transport can be observed in the nanowire channels [63, 58]. Also, the spin-orbit interaction is strong (spin-orbit length is $\sim$ 200 nm)[29]. Finally, transparent contacts of various normal metals and superconductors have been developed to InSb nanowires [60, 10, 13]. Particularly because of the latter four merits, InSb nanowires are among the prime materials for the study of Majorana zero modes based on nanowires [10, 11, 13].

3.1.2 Ge/Si core/shell nanowires

The Ge/Si core/shell nanowires used in this thesis have pure Ge core of 30-50 nm in diameter and Si shell of 1 - 4 nm in thickness. The core has diamond cubic lattice structure and its nanowire axis is along [111] direction. The nanowires are grown in a low pressure, cold wall chemical vapor deposition (CVD) [65]. Similarly, when the nanowires leave the growth reactor, native oxide grows on the surface.

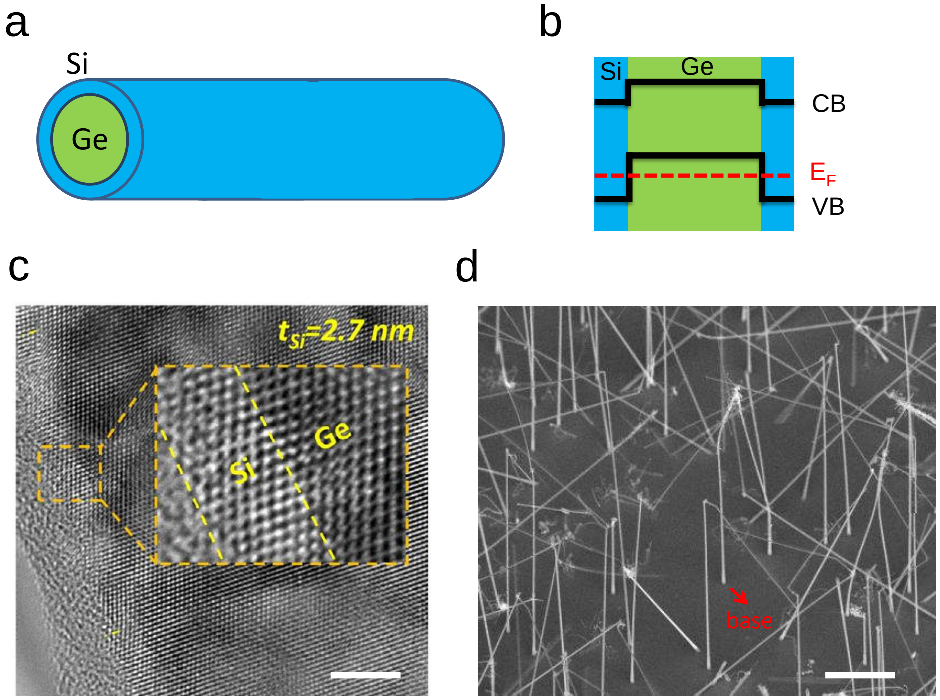

Figure 3.2: Ge/Si core/shell nanowire schematics and images. **a,** Schematic of the core/shell structure whose core is pure Ge and shell is Si. **b,** Schematic of the band structure of the core/shell heterostructure where the Fermi level lies in the valance band (VB) of Ge core. **c,** Transmission electron micrograph (TEM) near the surface. Crystal structure without disorder and impurities is displayed. The inset shows the atomically sharp boundary between Ge and Si. **d,** Tilted SEM image of dense Ge/Si nanowires grown on a mother chip. The thicker ends of the nanowires are the bases on the substrate. The scale bars are 5 nm and 2 μm in **c** and **d**, respectively. Panel **c** is adapted from Ref.[65].

Ge/Si core/shell nanowires exhibit promising properties for further applications. First, with sufficiently small lattice constant mismatch (4.1%) between Ge and Si, Ge/Si is a suitable combination for 1D heterostructure (Lattice matching is better in GeSi/Si heterostructure such that 2D materials can be made [66]). Also, the band structure of the heterostructure has a type II band mismatch. The large valance band offset (500 meV) between the Ge core and Si shell in this heterostructure enables accumulation of free holes in the Ge channel, as shown in Fig.3.2b. In this way, the hole gas is formed without doping with acceptors which would reduce the mean free path. Besides, the Si shell serves as a passivation layer that suppresses surface scattering. Scattering caused by surface roughness is one of the most critical factors that prevent ballistic transport in low dimensional materials. Finally, rich electronic properties are predicted for the hole carriers: first the angular moment of holes in Ge/Si nanowires is a mixture of 3/2 and 1/2 and the spin-orbit interaction is expected to be larger than that of electrons in the conductance band [67]; the spin-orbit interaction of holes is predicted to be enhanced by an order of magnitude using external electric fields [67].

3.2 DEVICE FABRICATION

3.2.1 General fabrication process

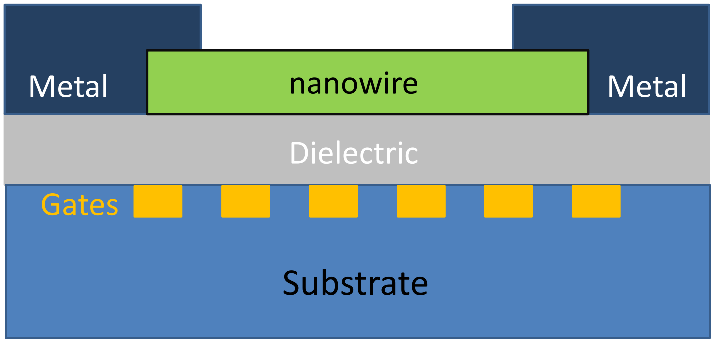

Figure 3.3: Illustration of nanowire device fabrication. Nanowire device fabrication consists of making metal-nanowire contacts such that electrons can flow through the nanowire, and gate fabrication. The latter is necessary to define and tuned quantum stats in the nanowires, using local gates (orange rectangles). The dielectric layer between gates and the metal-nanowire structure prevent current flowing from gates to meta-nanowire structure.

Many successive nano-fabrication steps are necessary to create a device. The parts of a full nanowire device are outlined in Fig.3.3. First, metal-nanowire contacts are fabricated to facilitate current through the device such that electrical measurements can be performed. Besides, gate fabrication is necessary as gates provide on-chip control knobs that can define and tune the quantum states in the device. In InSb nanowires in which we study electron charge carriers, a local gate below a nanowire section with a positive voltage attracts electrons to the section, while a gate with a negative voltage repels electrons. These local gates will be introduced in subsection 3.2.2 in detail. These gates can be used to define and control quantum dots along the nanowire, which is widely used in the later chapters. The tuning is reversed for Ge/Si nanowires, i.e., gates with positive (negative) voltages repel (attract) charge carriers, because the charge carriers are holes.

Next, we go through the general fabrication steps of a full device from scratch chronologically. Some of the processes are experiment-specific techniques and will be discussed further in subsections 3.2.2 - 3.2.6 separately.

1. Fabrication of markers. Since fabrication begins with an empty Si/SiO$_2$ chip, a coordinate system must be fabricated on the chip for alignment during the following steps. We fabricate a coordinate system, four encoded locating markers for each local device field, and large metal pads for later wire-bonding. Their fabrication follows the standard electron-beam (e-beam) lithography with metals Ti/Au (5/60 nm). Steps 5 - 9, 11, and 12, described below, introduce e-beam lithography for nanowire contact fabrication, which is also the process to fabricate the markers in this step.
2. Gate fabrication. Two types of gates are used for experiments: global and local gates. Global gate chips have a doped Si layer on the back of the chip. The gate dielectric is a thermally grown, 285 nm, SiO$_2$ layer on the doped Si layer. For this reason these type of global gates are also called backgates. Backgates are simple and often used for nanowire characterization, contact recipe development, and for simple devices like the Josephson junctions of Chapter 7. Local gates will be discussed in subsection 3.2.2.
3. Transfer of nanowires onto substrates. Each time only a small number of nanowires are transferred to the sample substrate (Fig.3.4a). Two transfer methods are used: (I) Random deposition. A cleanroom tissue tip is wiped on the surface of the mother chip and wiped across the substrate. This scatters wires randomly across the surface of the chip. It is suitable for backgate devices since precise nanowire placement is not necessary. (II) Micromanipulation. Under an optical microscope, a micromanipulator equipped with a sharp indium tip (a few hundred nanometers) is used to break a single nanowire off of

the mother chip and then accurately place the nanowire onto the sample substrate. This method is often used for local gate devices where nanowires need to be put exactly on top of local gates with a certain orientation.

4. Elimination of ill-attached nanowires. A small proportion of nanowires may be not well attached to the substrate by Van der Waals force. They can move or simply leave substrate in the later fabrication steps. A solution to this problem is to submerge the sample in isopropyl alcohol (IPA) and manually shake it gently, which would adjust those nanowire be well attached, or remove them.
5. Nanowire location and device computer aided design (CAD). To know the location of the placed nanowires, we take SEM images of the nanowires with location markers nearby. The images are then inserted into a CAD program like Klayout or AutoCAD by aligning the markers. Finally, we draw the contacts to the nanowires and gates in the CAD layout. The drawn patterns will be metalized later by lithography.
6. Resist coating. One or multiple layers of electron-beam (e-beam) lithography resist called poly(methyl methacrylate) (PMMA) are spin coated on the substrate. The PMMA coating is followed by baking at 175 °C for 15 - 30 min.
7. E-beam exposure (Fig.3.4b). With an electron-beam lithograph (EBL) setup, the PMMA coated chip is now exposed with a focused electron beam, but only on areas designated by the CAD pattern. The e-beam exposure increases the solubility of the resist.
8. Development (Fig.3.4c). The sample is immersed in the developer (MIBK:IPA = 1:3) that dissolves the areas where e-beam exposure has taken place while leaving the rest of the PMMA surface intact. This results in voids in the PMMA coating.
9. Removal of resist residue. Even given proper e-beam exposure and development, resist residue is commonly left on the substrate. This residue can lead to poor adhesion between the metal film and the substrate. More importantly, in the subsequent wet etch, the resist residue on the surface of nanowires prevents the etchant from reacting with native oxide. Gentle oxygen plasma cleaning is used to remove the residue efficiently.
10. Removal of surface oxide (Fig.3.4d). Surface cleaning can be done by physical or chemical methods. In this thesis, we will explore the technique of using argon plasma to physically mill the surface oxide and two chemical etching approaches. Surface cleaning techniques

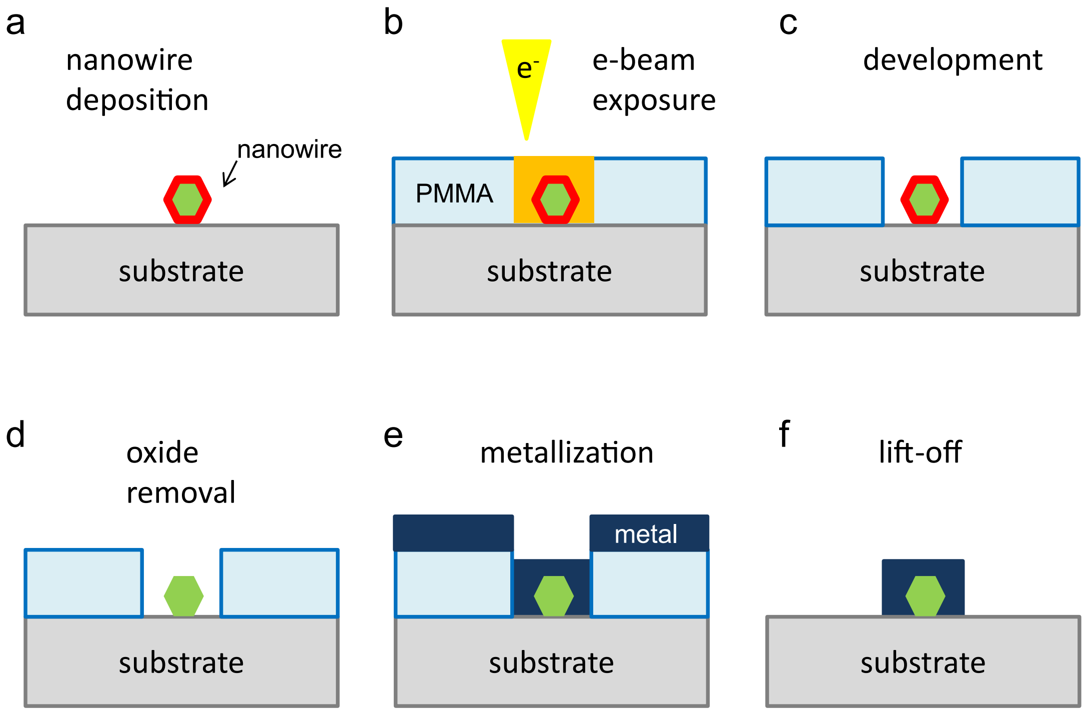

Figure 3.4: Successive e-beam lithography steps to fabricate contacts to nanowires. a, A nanowire (green) covered with native oxide (red) is deposited on top of substrate. **b,** PMMA is coated over the entire sample surface and e-beam exposes the designed area (orange). **c,** The exposed PMMA is removed by development. **d,** The native oxide on the surface of nanowire is removed with an etch method. **e,** Metal is deposited to the entire sample surface. **f,** The lift-off process removes the unexposed PMMA together with the metal on top of the unexposed PMMA, and leaves the nanowire covered with contacts in the designed area.

are often material specific. The approaches for InSb and Ge/Si nanowires are individually described in subsection 3.2.3.

11. Metalization (Fig.3.4e). Standard electron-beam evaporation and magnetron sputtering are used. Various normal metals (Au, Pd and Ni) and superconductors (NbTiN, NbTi, Al, Ti and V) are explored.
12. Lift-off (Fig.3.4f). After metalization, the sample surface is covered with metal. When it is immersed in the lift-off agent (acetone in our case), the resist is dissolved in the remover. As a result, the metal on top of the resist is lifted off the substrate while the metal in the developed area remains.

13. Post-deposition treatment. Some operations can be performed after lift-off to improve device quality such as contact transparency and device charge stability. In Section 3.2.4, I will describe the effect of annealing on Al-Ge/Si contacts.

For nanodevice-based quantum transport experiments, device fabrication is often the most headache inducing but also important processes. I will discuss some aspects in dealing with superconductor-nanowire devices based on InSb and Ge/Si in detail in the following sections.

3.2.2 Bottomgates

Local gates provide the ability to define and tune quantum dots in the nanowires. In our experiments, using the e-beam lithography described above in steps 5 - 9, 11, and 12, they are fabricated at the bottom the nanowire devices, thus they are called bottomgates. In this way, they can be fabricated directly on the flat substrate. The center-to-center distance between neighboring gates (pitch) can be as small as 60 nm. We achieve bottomgates whose pitch can be as low as 100 nm at University of Pittsburgh (see Fig.3.5a) with an EBL setup whose maximum e-beam accelerating voltage is 30 kV. The bottomgates used in the experiments in this thesis have a smaller pitch (60 nm, see Fig.3.5b), and are fabricated by Moïra Hocevar in Centre Nationnal de la Recherche Scientifique (CNRS) Grenoble, using an EBL setup whose e-beam accelerating voltage can be above 100 kV. A higher accelerating voltage facilitates higher e-beam exposure resolutions and finer gates.

E-beam lithography of dense gate electrodes is technically difficult. To work well, each gate should have no breaks and neighboring gates should not be shorted. The former requires sufficient e-beam exposure while the latter would fail given too high dose. Besides, the e-beam exposure proximity effect, i.e., exposure of neighboring area, plays an important role in defining these dense patterns. For these reasons, the following parameters need to be fine tuned: (1) dose. Only a small range of dose is suitable and the doses for parts of different dimensions differ. For example, the “extended arms” need a higher dose than the center horizontal dense electrodes because they are far apart whereas the later needs a lower dose due to proximity effect (See Fig.3.5b). (2) e-beam. The e-beam exposure should have

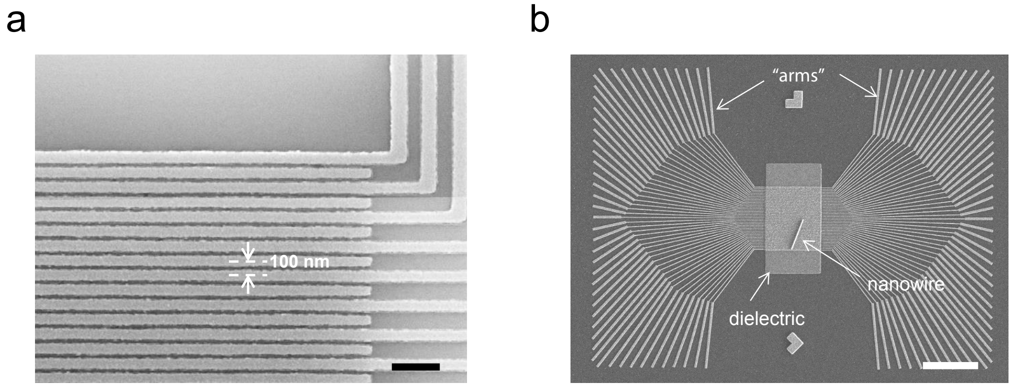

Figure 3.5: Bottomgates. a, A zoom-in SEM of bottomgates without dielectric. The pitch, depicted as the distance between centers of two neighboring gates, is 100 nm. The electrodes are closely arranged but not connected. They are fabricated at University of Pittsburgh. **b,** An overview SEM of a bottomgate set with dielectric. The center area is patterned with horizontal electrodes with pitch of 60 nm. Away from the center, they spread out as "arms" for easier alignment of the contacts to them. The center area is covered with a rectangular HfO_2 film. A nanowire is placed on top. These bottomgates are fabricated in CNRS. The scale bars are 5 um and 200 nm in **a** and **b**, respectively.

the smallest spot size, i.e., maximum accelerating voltage, minimum working distance and minimum aperture are preferred. (3) PMMA structure. Tall PMMA structures are unstable so thin PMMA films are desired (950 PMMA A2, 80 nm). After development, the PMMA structures have to be preserved, meaning there should be no heating and metalization should be performed as soon as possible. (4) metal deposition. Because the PMMA layers are thin, the gate metal has to be thin as well. Ti/Au (5/10 nm) are used for our bottomgates.

A dielectric layer is deposited on the gate electrodes. Charge leakage can occur in a dielectric when the voltage across the dielectric exceeds its breakdown voltage. It can even occur starting from zero voltage at dielectric defects (pinholes). Two bottomgate dielectrics are tested. HfO_2 of 30 nm grown by atomic layer deposition (ALD) at Carnegie Mellon University is observed to have an average breakdown voltage of 22 V. Si_3N_4 of the same thickness grown by sputtering at University of Pittsburgh is found to break-down at 11 V on average. Pinhole density is also found to be lower in HfO_2 than in Si_3N_4. The dielectric used in the experiments, HfO_2 of 10 nm, is grown in CNRS and has an average breakdown voltage that is higher than 10 V.

3.2.3 Superconducting contacts

In experiments studying Andreev bound states, elaborate superconductor-semiconductor contacts are required. As explained by the Blonder-Tinkham-Klapwijk model [68], the transparency of superconducting contacts directly determines the ratio of Andreev reflection to normal reflection. This necessitates a clean nanowire surface without oxides or impurities introduced during contact fabrication. Smooth nanowire-superconductor interface, and matching between superconductors and semiconductors are also necessary to ensure high transparency.

Superconducting contacts to InSb nanowires. With proper surface oxide cleaning, InSb nanowires are found to make good contacts to various superconductors such as Ti, Al, NbTi, NbTiN and V. Ti/NbTi/NbTiN is used in most of the experiments presented. The following two surface oxide cleaning approaches are used and the discussion is based on Ti/NbTi/NbTiN contacts:

- *In-situ* argon plasma cleaning. The bombardment by argon ions removes the atoms on the nanowire surface. This approach yields junction devices with low saturation resistances (a few kΩ) at low temperature. A saturation resistance of a nanowire device is the resistance when the device is tuned to be as open as possible.
- *Ex-situ* sulfur passivation. Wet etch removes the oxide by a chemical reaction using a recipe developed based on Ref.[69]. (1) Mix and stir ammonia solvent with sulfur powder with a ratio of 10 mL/g for 30 minutes. (2) Dilute the resulted ammonium polysulfide $(NH_4)_2S_x$ solution with water (1:400). (3) Immerse the sample in the diluted ammonium polysulfide solution at 55 °C for 30 min. (4) Wash away sulfur residue on the sample substrate before metalization. Sulfur passivation can yield junction devices of low saturation resistances at low temperature as well.

In our experiments, tunneling transport demonstrates that induced superconductivity in plasma-cleaned devices have a higher subgap density of states than that measured in devices cleaned with sulfur passivation. This is probably due to surface roughness after argon bombardment. Combining these two approaches, by performing sulfur passivation followed by gentle argon cleaning for a short period, yields better induced superconducting gap than either of them alone. Probably because although sulfur passivation does not cause surface roughness, sulfur residue can be left on the nanowire surface. This residue can be removed by the gentle plasma cleaning.

Superconducting contacts to Ge/Si nanowires. We explore contacts using various superconductors such as Ti, Al, NbTi and NbTiN to Ge/Si nanowires intensively. Regarding contacts based on NbTiN, it is found that depositing a thin interlayer of Ti or Al prior to NbTiN improves contact transparency. Surface oxide cleaning also plays an important role in determining the contact quality. Two surface oxide cleaning approaches are tested:

- *In-situ* argon plasma etch is tested with various cleaning time and powers. The optimized recipe yields uniform but relatively high saturation resistances (a few tens kΩ) and contact interface barriers at low temperature. They might be a result of interface roughness caused by argon ion bombardment.
- Alternatively, a more gentle etch method by buffered hydrofluoric acid (BHF) is found to produce transparent contacts, although the yield of devices with low junction resistance ($<$10 k Ω) is low ($\sim$ 10%). Varying etch time is found to have little effect on the junction resistance, although long etches ($>$ 1 min) are not suggested because it can remove the lithography resist from substrate. With the same BHF etch method, we also test the contact qualities of nanowires with Si shell thicknesses varying from $\sim$ 0.5 to $\sim$ 4 nm. No statistical difference is found. Note that in our test, chemical vapor deposited (CVD) Si_3N_4 dielectric is grown on top of the substrate to protect SiO_2 from being etched quickly by BHF solution.

3.2.4 Annealing effects of Al-Ge/Si contacts[1]

To improve the yield of transparent contacts we explore contact annealing in the presence of forming gas (5% H_2 and 95% N_2) at 1 bar. For NbTiN contacts with thin Al or Ti interlayers

---

[1] This section is adapted from Ref.[135].

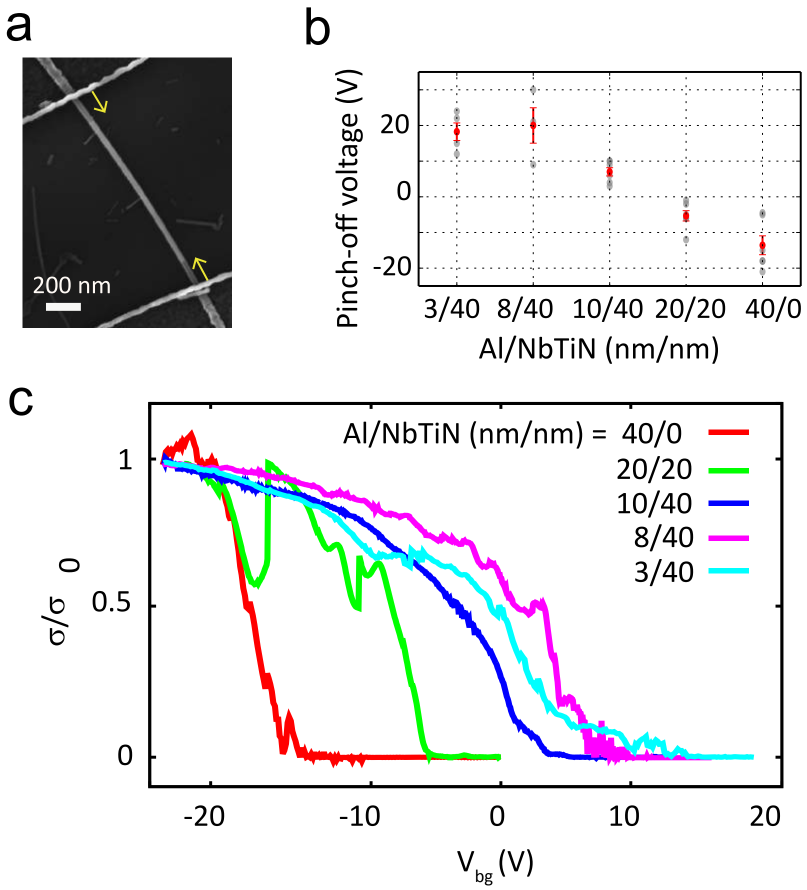

Figure 3.6: Annealing effect of Al-Ge/Si contacts and effect of Al interlayer thickness on device pinch-off. **a,** Al-Ge/Si-Al device after a rapid annealing at 180 °C. The arrows indicate alloyed regions of the nanowire. **b,** Pinch-off voltages of 21 devices with various Al/NbTiN thicknesses. The average value for each Al/NbTiN thickness combination is indicated by the red dot. **c,** Typical pinch-off traces of devices for various Al/NbTiN thickness combinations. The conductance is normalized by conductance σ_0 measured for each device at backgate voltage, $V_{bg} = -24$ V.

(3 nm), no measurable change in the saturation resistance is observed after annealing at temperatures up to 400 °C for a few minutes. However, we observe that pure Al contacts alloy rapidly, within seconds, at temperatures as low as 180 °C. Fig.3.6a displays the alloying of 200 nm regions next to each contact. Saturation junction resistances are reduced by more than one order of magnitude after the annealing in some devices. Low resistance ($\leq 10\ k\Omega$) devices are obtained with a high yield of $\sim 1/4$ for pure Al contacts. It is important

to be aware of the Al-alloying effect because such low annealing temperature is close to the temperature used during standard nanofabrication. For example, electron beam resist PMMA is commonly baked at 175 °C, so if following fabrication steps such as top gate fabrication are performed after pure Al contacts, those contacts are going to be annealed with the nanowires.

3.2.5 The effect of Al interlayer thickness on Ge/Si device pinch-off[2]

Besides that depositing a thin interlayer of Ti or Al prior to NbTiN improves contact transparency, we observe a dramatic and systematic change in the device pinch-off voltages with aluminum thickness.

With increasing thickness of the Al interlayer, we find that the pinch-off voltages of the junctions can be modified. Fig.3.6b,c show the low temperature pinch-off voltage data from many unannealed devices with different Al and NbTiN layer thicknesses. Devices based on NbTiN with a thin Al interlayer have large positive pinch-off voltages. The increase of Al thickness reduces the average pinch-off voltages, which become negative for pure Al contacts. We argue that the pinch-off shift is due to remote doping of the nanowire that is a result of workfunction mismatch between the Ge core and the metal contacts. The workfunction of Ge (5.15 eV) [70] exceeds that of Al (4.06 - 4.26 eV) [71] consistent with n-doping. The workfunction of NbTiN alloy is not known; however the workfunctions of Nb (3.95 - 4.87 eV) [71] and TiN (4.5 eV) [72] are in between those of Ge and Al, which suggests lower n-doping with NbTiN than with Al. For thinner interlayers, no continuous Al film is formed and the contact is dominated by NbTiN. As Al thickness is increased, the doping of the nanowire is increasingly determined by the properties of the Al/Ge interface. The pinch-off voltages can also be affected by the interface between the nanowire and the gate dielectric. We observe that the pinch-off voltages tend to shift positively when HfO_2 is used instead of Si_3N_4. Interfacial charges at the semiconductor/dielectric interfaces are likely responsible for this effect [73]. Combined, the effects of dielectric and interlayer thickness on pinch-off allow for the device working point to be set to zero gate voltage, which is expected to minimize

---

[2] This section is adapted from Ref.[135].

charge instabilities and gate leakage.

3.2.6 Sputtered NbTiN

NbTiN alloy is used in most of the experiments in this thesis. This superconductor has a critical temperature of up to 14 K and a critical magnetic field beyond 10 T. Furthermore, it does not oxidize, thus no cap layers are necessary to protect it.

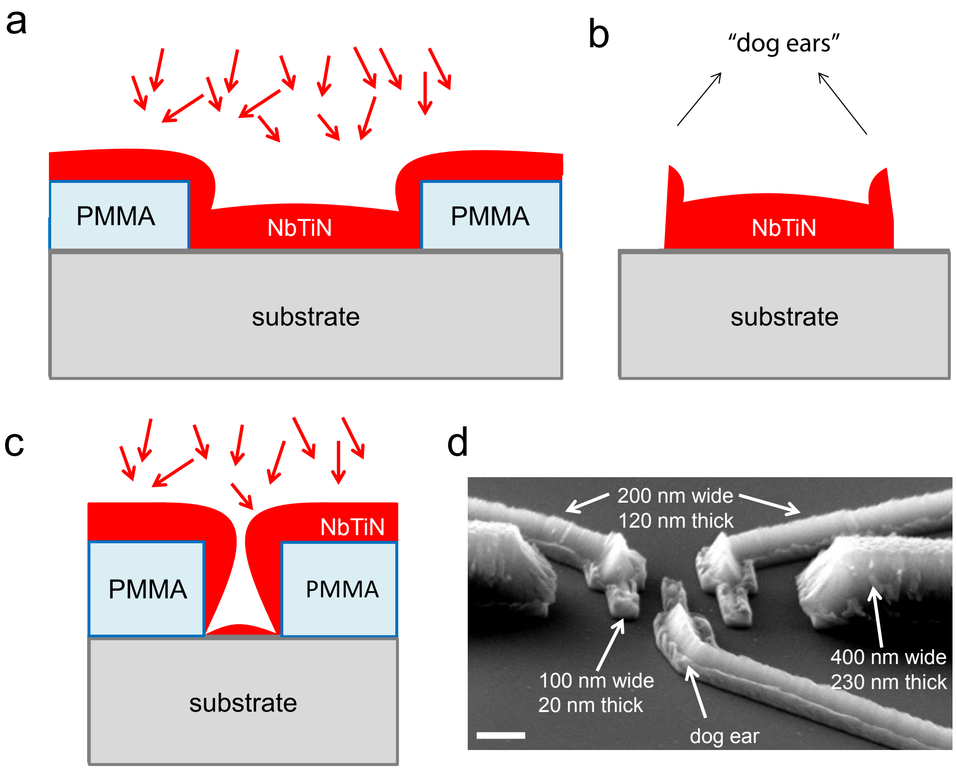

Figure 3.7: Sputtering process and sputtered structures. a, Illustration of sputtering deposition on a wide PMMA void. **b,** The resulted structure of **a** after lift-off. "Dog ears" at the edges of sputtered patterns are caused by the non-directional deposition on the PMMA walls. **c,** Deposition on a narrow PMMA void by sputtering. Little material arrives at the substrate. **d,** SEM of structures of three widths (400, 200 and 100 nm) after sputtering NbTiN (250 nm) on PMMA (160 nm). The narrower patterns result in thinner deposition. The scale bar is 200 nm.

NbTiN is deposited by DC sputtering of NbTi alloy (7:3) in the argon-nitrogen mixed-gas plasma. Sputtering enables depositions of materials with high melting points and chemical compounds from multiple sources, such as NbTiN. However, it can also give rise to fabrication difficulties.

First, because of the scattering in the plasma during sputtering, the deposition is not directional. Fig.3.7a depicts a profile of a sputtered film near a developed area. The central regime of the developed area receives materials from more directions and gains a higher thickness than those near the the walls of the PMMA void. Non-directional deposition can also take place on the walls of the PMMA void. After lift-off, the film often breaks near some sharp corners on the walls, which results in vertical structures at the edges called "dog ears". They are depicted in Fig.3.7b and can be also seen in the SEM (Fig.3.7d). The non-directional deposition gives rise to a severe problem for thin patterns. Fig.3.7c depicts sputtered structure near a narrow PMMA void: the sputtering process deposits material on the walls of the void much faster than to the bottom of the gap. As a result, little material is deposited on the bottom of the void before the material building on the walls closes the narrow void. Fig.3.7d shows structures after sputtering NbTiN (250 nm) on patterns of PMMA (160 nm). The patterns that are 400 nm wide (two horizontal large parts in the SEM) are closer to 230 nm thick. The patterns that are 200 nm wide (the three lines with turns) are 120 nm thick. At last, the narrowest patterns (100 nm, the tips of the three lines) are very thinly coated ($\sim$ 20 nm). This causes narrow contacts to fail to make contact to nanowires. Several methods have been explored to solve the problem, however, they cause new problems. For instance, decreasing the PMMA thickness helps alleviate the issue, but, to cover the nanowires, the PMMA film should be thicker than the nanowires ($\sim$ 100 nm). Sputtering at high temperatures would make the material fill the PMMA voids however high temperature sputtered films fail to lift-off. Using a sputtering collimator improves the directional uniformity of the plasma significantly, however, it also increases the stress of NbTiN film which aggravates another issue discussed below. For three-terminal devices developed in Chapter 6, we achieve narrow NbTiN contacts by tilting the sample during deposition and depositing only 40 nm from one side of the nanowires.

Sputtered films often have stress that can cause damage to thin nanostructures. For simple designs such as two-terminal devices whose two contacts are close in space, the nanowires are more resistant to stress as the torque is small. For devices with large contact spacings and/or side contacts, the stress can bend or break the nanowires. In Fig.3.8a, the nanowire in a NbTiN-Ge/Si-NbTiN device with a large contact separation ($\sim$ 600 nm) is bent; in

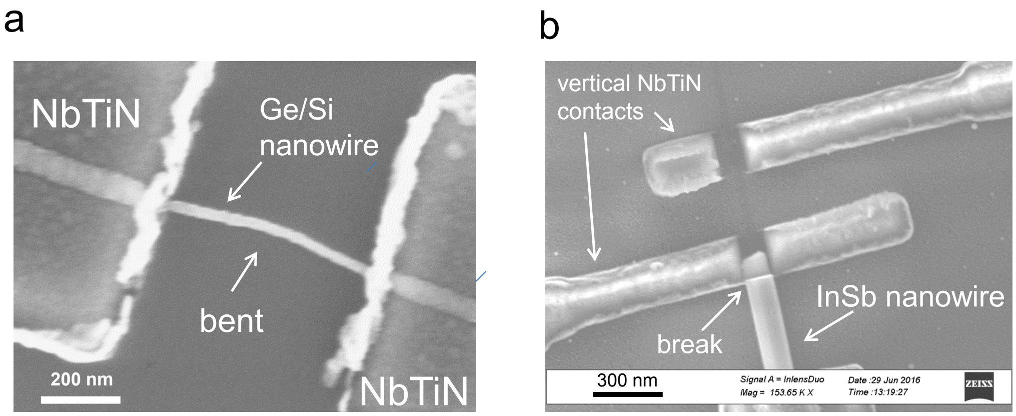

Figure 3.8: Damage to nanowires caused by NbTiN stress. a, SEM of a bent Ge/Si nanowire in a NbTiN-Ge/Si-NbTiN junction. The long Ge/Si channel ($\sim$ 500 nm) is bent by the stress in NbTiN film. **b,** SEM of a broken InSb nanowire connected to three NbTiN contacts. The nanowire is broken by the torque of the stress.

Fig.3.8b, the InSb nanowire is broken by the torque with the vertical contacts. The stress in sputtered films is attributed to bombardment of high energy neutral argon atoms on the film [74]. To mitigate the effects of the bombardment, sputtering power can be lowered; argon pressure in sputtering process can also be increased to thermalize the neural argon atoms before they reach the film. As mentioned, plasma can be adjusted to be more directional by using a collimator. Although this can solve the difficulty in depositing on narrow structures, it is found to generate larger stress. In control experiments, the damage to NbTiN-InSb-NbTiN devices fabricated with a collimator is found to be more severe than that without a collimator. This is because using a collimator reduces the thermalization, which leads to stronger bombardment of neutral argon atoms on the film and stronger stress [74].

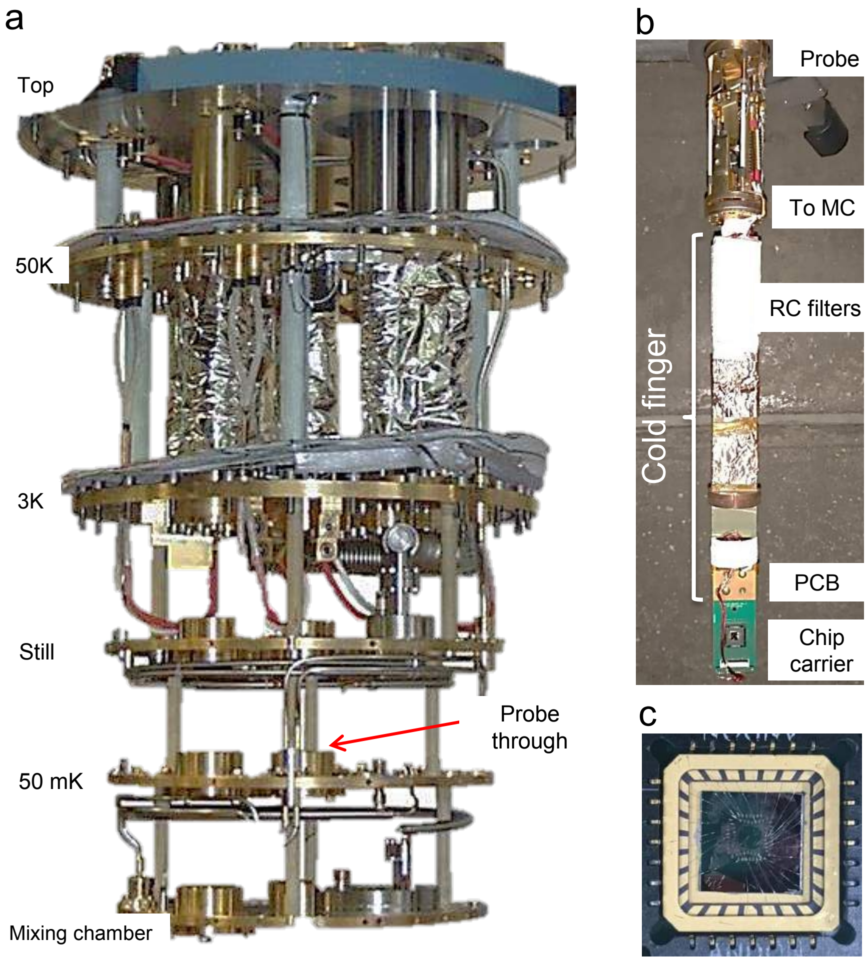

Figure 3.9: Low temperature electrical measurement setup. a, An internal photo of a ^{3}He/^{4}He dilution refrigerator (Leiden Cryogenics). The plates from top to bottom and their typical working temperatures in parenthesis are the following: top-plate (room temperature), 50K-plate (50 K), 3K-plate (3-4 K), still (100-200 mK), 50mK-plate (50-60 mK) and mixing chamber (20-40 mK). At the center of each plate, there is a hole for the measurement probe to pass through. **b,** Probe and cold finger. This lowest part of the probe (marked as "To MC") is thermally connected to mixing chamber (MC) of the fridge during measurements such that it is the coldest part. Cold finger is connected to this coldest part. Low-temperature RC-filters are installed on the cold finger (covered by teflon in the photo). **c,** Chip carrier. The sample is loaded into the carrier embedded in a PCB and devices are connected to measurement wires via bonding pads.

3.3 MEASUREMENT SETUP

Low temperature is critical to perform the quantum transport measurements, to see the charging effect of quantum dots, to keep the devices leads superconducting, to suppress thermal excitation and quasiparticles in the superconductors, and to resolve the tunneling spectroscopy of Andreev bound states whose broadening must be at least one order of magnitude lower than the induced superconducting gap (a few hundred micro-electron volts).

These low temperature measurements are performed at 20 - 40 mK (base temperature) in ^{3}He/^{4}He dilution refrigerators (Fig.3.9a). The coldest part of a refrigerator is called mixing chamber where ^{3}He-rich mixture is diluted in ^{4}He-rich mixture and heat is absorbed from the environment. This is where the measurement chips are thermally attached to. The dilution refrigerators used for the measurements in this thesis are “top loading” type, meaning the body of a dilution refrigerator can keep cold, and cooling down a measurement chip is done by mounting it to a cold-insertable probe (Fig.3.9b) and inserting the probe into the fridge body. After the insertion, the lowest part of the probe, the cold finger, is attached the mixing chamber of the refrigerator such that it can have a same lowest temperature. The cold finger is where we mount the measurement chip.

The measurement chip thermally connected to the mixing chamber can reach the same lattice temperature of mixing chamber. However, in order to perform electrical measurements, wires have to be used to connect the devices (source, drain and gates) to room temperature setups, which introduces heat load to the mixing chamber and leads to a higher base temperature. Moreover, the effective electron temperature in the device can be much higher than the lattice temperature in the devices, because the devices are directly connected to room temperature setups and the electrical noise increases the effective electron temperature significantly. Next we shall describe the wiring from the room temperature setup to the measurement chip and the techniques we apply to reduce the effect of electrical noise.

Digital-to-analog converters (DACs) controlled by computer are used to apply a bias to the device leads, and voltages to gates. The signal of the device is measured with a DC amplifier and a standard lock-in amplifier. The former allows us to measure DC signals such as current, while the latter allows us to measure differential conductance with suppressed noise. To avoid interference from city electricity and computers, all measurement setups except the lock-in amplifier are powered by DC batteries, and the DACs are controlled by computers via optical fiber connection. In addition, each wire is passed through a π filter at room temperature which filters noise in the range of 10 MHz - 100 MHz.

The wires are then passed through plates of various temperatures in the measurement probe. These plates have thermal connection to the corresponding plates in the refrigerator (See 3K-plate, still and 50mK-plate in Fig.3.9a). When the wires are passed through each plate, they are thermally well attached to the plate, which is called thermal anchoring. This reduces the heat load on mixing chamber and lowers the effective electron temperature. Before the measurement chip, the wires are passed through copper powder filters which filter high frequency noise (up to a few GHz) and RC-filters with a cut-off frequency around 10 kHz. These two types of filters are equipped right before the measurement chip to avoid extra noise between room temperature and mixing chamber. Together with the π-filters at room temperature, non-low frequency noise is filtered and effective electron temperature can be efficiently reduced (The lock-in amplifier frequency is 77 Hz in the experiments thus lock-in signals are not filtered by them.). Finally, these wires are connected to a polychlorinated biphenyl board (PCB) where a chip carrier is loaded. The measurement chip is mounted in the chip carrier (Fig.3.9c) and the quantum devices are connected to the pins on the chip carrier by wire bounding.

Magnetic fields are generated by superconducting magnets in the dilution refrigerators. A solenoid magnet capable of producing magnetic fields up to 9 T is used in all experiments. A vector magnet which enables rotating fields in two-dimensions is used in the experiments in Chapter 8.

4.0 ANDREEV BOUND STATES IN INSB SINGLE QUANTUM DOTS

Here we implement highly tunable single quantum dots coupled to superconductors and study Andreev bound states comprehensively in a large parameter space.

4.1 INTRODUCTION

In this chapter we realize Andreev bound states in NbTiN-InSb single dot structures and demonstrate quantum transport through these states in this chapter. This is technically important. On the one hand, the double dot and triple dot chains, in the later chapters, will be built upon a number of such building blocks: NbTiN-InSb single dot structures. On the other hand, although Andreev bound states have been observed in hybrid structures using InAs nanowires, carbon nanotubes or graphene, and superconductors like Al, V or Nb [47, 41, 44, 8, 46], neither InSb nor NbTiN has been reported for the study of Andreev bound states.

In addition, there is a broader interest in the exploration of quantum transport through low-dimensional structures involving semiconductors and superconductors. First of all, these hybrid structures, such as NbTiN-InSb nanowire and Al-InAs nanowire structures, have been used for the study of Majorana zero modes [10, 75, 11, 13]. In those experiments, nanowire sections of finite lengths, ranging from a few tens nanometers to a few micrometers, are used. The superconductor-single quantum dot structures used to study Andreev bound states in this chapter have similarities to those devices, particularly in the open quantum dot regime. Indeed, theories suggest that Andreev bound states in a single quantum dot can be precursors for Majorana zero modes [76, 77, 78, 79]. Furthermore, the same superconductor (NbTiN) and semiconductor (InSb nanowires) combination is used both in the study of Andreev bound states in this thesis, and in the studies of Majorana zero modes [10, 11, 13]. Thus studying Andreev bound states in NbTiN-InSb single dot structures can contribute to the experimental studies of Majorana zero modes. Finally, as will be shown in this chapter, although superconductor-single dots has been studied previously, a number of new physical insights into the system are obtained in our study, such as the simultaneous transitions of superconducting and normal transport as the dot is tuned to be open to a superconducting reservoir, and complexities in the probe and superconducting reservoir.

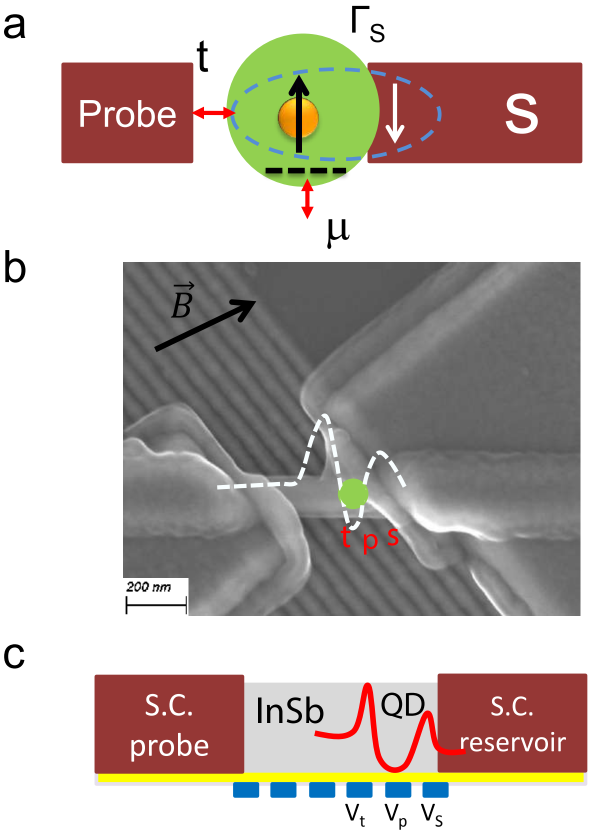

Figure 4.1: Design and SEM image of a highly controllable superconductor-quantum dot system. a, A building block of a chain consists of a superconductor and a quantum dot. In the quantum dot, the chemical potential is μ, the coupling to the superconductor is Γ_S and the tunnel coupling to a probe is t. **b,** SEM image of the device used to create a single dot coupled to the right superconducting lead. The quantum dot, depicted by the green dot, is confined and tuned by three fine gates below the nanowire: V_t, V_p, and V_S. The probe is a nanowire section coupled to the left superconducting lead. **c,** The side-view schematic. The red line depicts a potential well controlled by the gates to confine the quantum dot.

As explained in Chapter 2, to tune Andreev bound states in a superconductor-quantum dot hybrid structure, three parameters should be controlled in sufficiently large ranges and quasi-independently, i.e., Γ_S is the coupling between the dot and the superconducting reservoir, μ is the dot chemical potential, and t is the tunnel coupling to a probe (See Fig.4.1a). Quantum dots can be partially defined by contact barriers or disorder [47, 41, 44, 8, 46]. This limits degree to which Γ_S, μ and t can be tuned. Also, if there are not enough gates, independent control is not possible. The randomness and low controllability determine that spontaneously formed quantum dots by contact barriers or disorder are not applicable to build complex devices like chains.

We facilitate the high and independent controllability of the three parameters by two key techniques. First, we elaborate three local fine gates whose center-to-center distance is 60 nm for a single dot (See the three gates marked as t, p and S in Fig.4.1b) and apply gate voltages V_t, V_p and V_S to them separately. They can be used to control t, μ and Γ_S, respectively and quasi-independently. For instance, by decreasing V_S we effectively reduce Γ_S, and by changing V_p we tune μ. Note that a thin and high-κ gate dielectric (HfO_2, 10 nm) is used to maximize locality of the gate effect. Indeed, cross capacitance coupling from a nearest neighboring gate is only $\sim 1/3$ of that from V_p, and this effect can be compensated by tuning V_p in the opposite direction. In this way, all three parameters can be controlled independently by a combination of three gates. The second key technique to facilitate the controllability is highly transparent superconductor-nanowire contacts. With such contacts, Γ_S can be tuned from a sufficiently high regime where singlet ground states form in spinfull dots, to as low as required by decreasing V_S. High transparency of the probe contact is also important to prevent undesired dots from forming near the superconductor-nanowire interfaces. The device studied in this chapter has resistance of 4 kΩ when the device is tuned to the most open at low temperature, which implies low contact resistance. No unintentional dots are observed either. Finally, the same device can also be used to form a single dot that is strongly coupled to left superconductor (See Supplementary information), or form a double dot where each dot is strongly coupled to a superconducting lead (See Chapter 5).

With these techniques, a single device can demonstrate rich transport phenomena of a superconductor-quantum dot structure in a number of regimes. Here we summarize these phenomena in prior to detailing them in individual sections. At first we shall demonstrate the transition from co-tunneling regime to Andreev bound state regime. Specifically, in Section 4.3 we focus on the evolution of the lowest conductance peaks from horizontal peaks into loop-like peaks within superconducting gap; in Section 4.4 we study the transition of transport where quantized charging effect is removed above the superconducting gap. The relation of these two transitions, within and above the gap, is then discussed. Next, in

Section 4.5, we study zero bias peaks generated by Andreev bound states in the open dot regime and map out the spin state phase diagram of Andreev bound states as a function of magnetic field and chemical potential. Besides these phenomena that can be explained with the theory in Chapter 2, there are some features that require additional discussions which we call "anomalies". They are discussed in sections 4.6 and 4.7.

Note that the couplings to the leads are intentionally tuned to be highly asymmetric such that the left lead is weakly coupled to the dot and only serves as a tunneling probe (i.e., $\Gamma_S \gg t$). This is done by setting V_t around the pinch-off voltage and V_S in a more open regime, and is further verified by the $|D\rangle/|S\rangle$ phase transition that is controlled by V_S. Also, for better comparison, while we vary Γ_S and t, we also tune V_p to maintain the same dot occupations. A black arrow on top of each plot is used to denote the same dot occupation.

4.3 FROM CO-TUNNELING REGIME TO ANDREEV BOUND STATE REGIME

We first look at the transport in the co-tunneling regime. Fig.4.2a measures the differential conductance, dI/dV, as a function of bias and V_p. Besides the Coulomb diamonds from which we can extract charging energy ($U \sim 2.5$meV) and quantum dot level spacing ($\Delta E \sim 1$ mV), there are bias symmetric and gate independent conductance peaks inside the Coulomb diamonds. The absolute bias of the lowest resonances is 600 ± 200 μV. Similar features have been observed and explained in terms of co-tunneling theory where co-tunneling of quasiparticles from one superconducting lead to the other through virtual states in the quantum dot is enhanced at the singularities of density of states at superconducting gap edges in the leads (See Fig.4.3a) [80] . By assuming equal gap values in the leads and symmetric tunnel couplings, the authors estimate that the horizontal peaks correspond to $2\Delta_{\text{induced}}$, where Δ_{induced} is the induced gap [80], following the energy diagram shown in Fig.4.3a. Applying the same argument yields $\Delta_{\text{induced}} = 300 \pm 100$ μeV for our NbTiN-InSb structure.

Horizontal resonances at higher biases appear to be extensions of the diagonal resonance

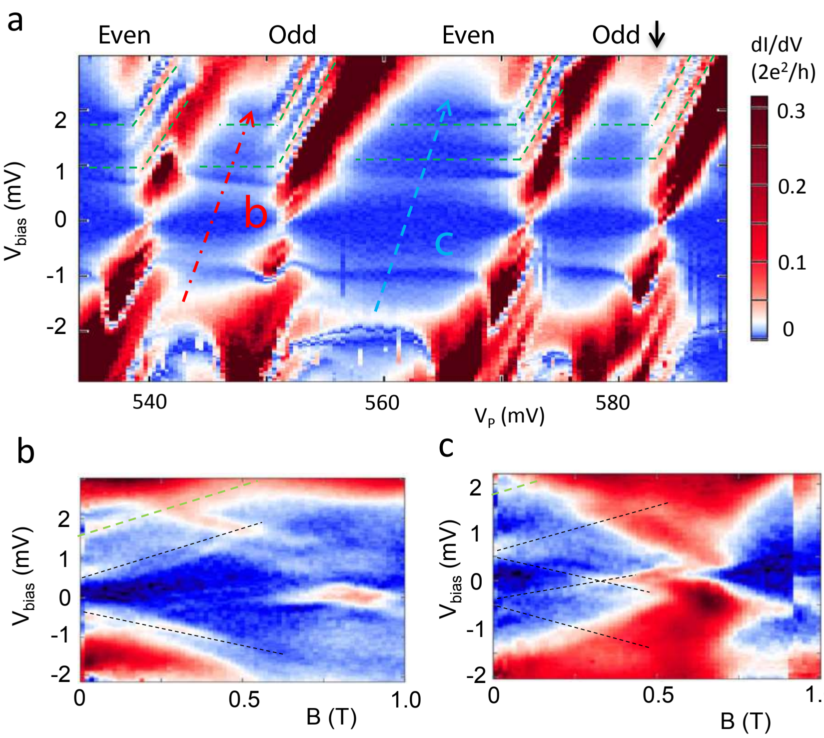

Figure 4.2: Horizontal resonances. a, Bias vs. gate measurement in the co-tunneling regime. V_S = 50 mV and V_t = -500 mV. Horizontal resonances at multiple biases are observed. They seem to be extensions of the diagonal line in the Coulomb peak triangles, depicted by the green dashed lines. "Even" and "Odd" mark the parities of dot occupations. The black arrow is used to track dot occupations. **b** (**c,**) Magnetic field dependence of the resonance peaks in an odd (even) occupation diamond, along the red (blue) dash-dotted arrow in **a**. Black dashed lines track the field evolution of the lowest resonances while green dashed lines track the field evolution of the high bias resonances.

peaks outside the Coulomb diamonds (depicted by the green dashed lines). These diagonal resonance peaks can be associated with transitions through excited quantum dot states or due to nonuniform density of states in the leads [80].

In Fig.4.2b we scan a combination of V_{bias} and V_p along the dash-dotted arrow depicted in a Coulomb diamond of odd occupation in Fig.4.2a as magnetic field is stepped. The lowest resonance at positive (negative) bias goes up (down) as magnetic field with a slope of 2.5 mV/T. The resonances at high biases display the same magnetic field dependence

(Fig.4.2b). A scan of similar manner along the dash-dotted arrow in a Coulomb diamond of even occupation demonstrates different magnetic field evolution (Fig.4.2c), i.e., the lowest resonances appear to split as field with a slope of 1.9 mV/T and meet at zero bias at $\sim$ 0.3 - 0.4 T. No clear splitting behaviors are observed for the high bias resonances. Soon we will see that it is not surprising that Fig.4.2b and c demonstrate different types of magnetic field behaviors, as they are associated with Andreev bound states of doublet and singlet ground states, respectively.

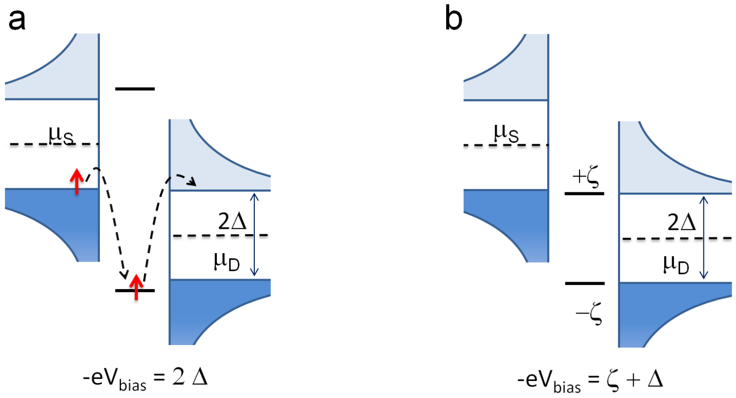

Figure 4.3: Two pictures for the horizontal conductance peaks. a, Co-tunneling picture. Co-tunneling of quasiparticles from the left superconducting lead to the right superconducting lead through virtual states in the quantum dot is enhanced at the singularities of density of states at superconducting gap edges in the leads. The solid lines in the dot depict quantum dot levels. **b,** Andreev bound state picture. The levels associated with Andreev bound states are $\pm\zeta$. In the weak superconductor-dot coupling limit, $\zeta \approx \Delta$. Note that here we consider transport of quasiparticles from the probe gap edge.

Next, starting from this co-tunneling regime, we present a transition to Andreev bound state regime. Note that although it is mainly accomplished by increasing V_S, V_t is also fine tuned to balance broadening and strength of the resonances. From Fig.4.4a (V_S = -25 mV, V_t = -600 mV) that shows the horizontal resonances, we gradually increase Γ_S by tuning V_S to 50 mV. We observe that near the Coulomb peaks, the horizontal resonances start to grow round, move closer to zero bias (Fig.4.4b). As V_S is increased to 220 mV, the resonances develop into loop-like resonances with nonlinear gate dependence (Fig.4.4c). These nonlinear features are the transport resonances through Andreev bound states introduced in Chapter 2. This evolution, in the opposite direction from V_S = 220 mV to -25 mV, demonstrates that when Γ_S is low, the levels associated with Andreev bound states (ζ) have a gate-independent value, except at the charge degeneracies. This provides a different picture explaining the horizontal resonances where the resonances are through levels of Andreev bound states that are close to $\pm\Delta_{\text{induced}}$ (See Fig.4.3b).

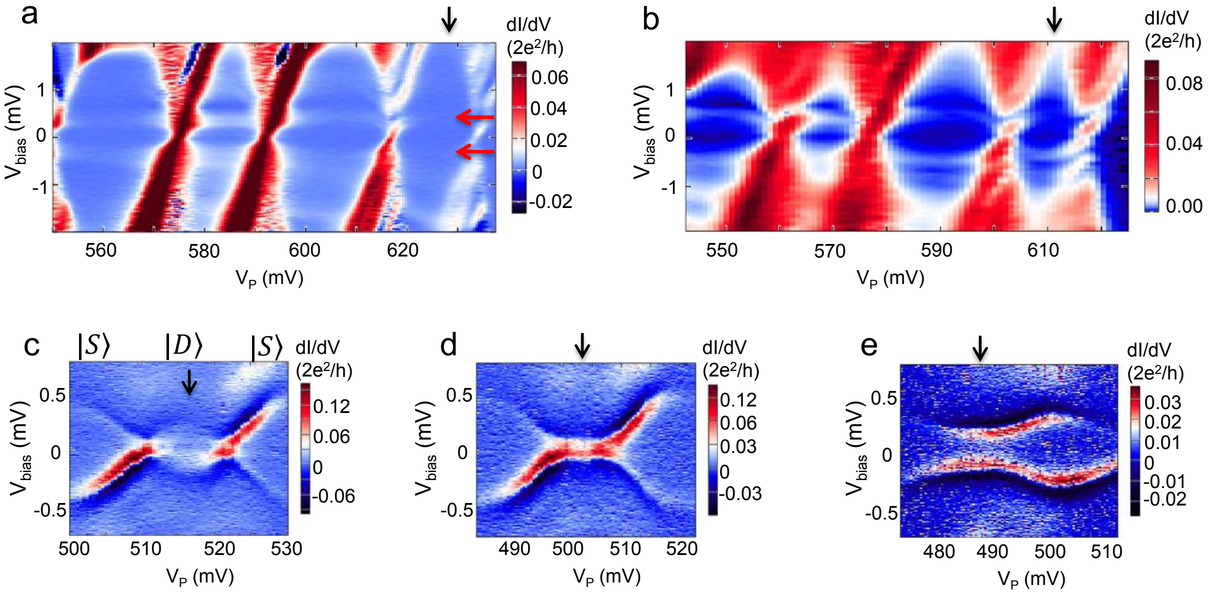

Figure 4.4: From co-tunneling regime to Andreev bound state regime. a-e, Bias vs. gate measurements of subgap resonances through Andreev bound states at various V_S respectively (V_S = -25, 50, 220, 240, 260 mV for **a-e**, respectively). The arrows mark the same quantum dot occupation. Note that V_t = -600 mV for **a-b**, and V_t = -685 mV for panels **c-e**, as V_t is tuned to balance broadening and strength of the resonances.

Next we look at the spin state phase transition in the Andreev bound state regime. The resonances in Fig.4.4c exhibit a closed-loop with two zero bias crossings. The ground states are doublets ($|D\rangle$) between the two zero bias crossings, and singlets ($|S\rangle$) otherwise, which is verified by: (1) magnetospectroscopy measurements in Section 4.6; (2) the $|D\rangle/|S\rangle$ phase transition. As we continue increasing Γ_S, the loop keeps shrinking and the two zero bias crossings move closer. A phase transition is reached when the two zero bias crossings merge ($V_S \approx 240$ mV, Fig.4.4d). Here, the ground state of the system is $|D\rangle/|S\rangle$ degenerate at this touch-point and $|S\rangle$ otherwise. With a larger V_S, the system enters a phase where the ground state is $|S\rangle$ regardless of quantum dot occupation and the resonances through Andreev bound states evolve into anti-crossing-like structures in bias vs. gate scans (Fig.4.4e).

The decrement of differential conductance from Fig.4.4c to e is at first sight counter-intuitive. The maximum strength in Fig.4.4c-e decreases ($\sim$ $0.17, 0.14, 0.035$ G_0, where $G_0 = 2e^2/h$). while the superconductor-dot coupling is increased (V_S = 220, 240, 260 mV). This phenomenon can be explained by tunneling coupling asymmetry, i.e., the maximum conductance (G) through a normal probe-quantum dot-superconductor follows the relation: $G/2G_0 = 4\Gamma_S^2 t^2/(\epsilon + \Gamma_S^2 + t^2)^2$ where ϵ is the quantum dot level [81]. The maximum conductance is reached at quantum dot degenerate points ($\epsilon = 0$) and can be up to $2G_0$ when the barriers are symmetric, where the factor of 2 comes from transferring Cooper pairs. The relation provides an naive explanation: given t fixed, increasing Γ_S enhances the asymmetries thus the conductance decreases (Plugging the maximum conductance values of the resonances in the three plots into the relation yields $t/\Gamma_S \approx$ 0.15, 0.13, 0.07, respectively.).

4.4 TRANSITIONS OF SUPERCONDUCTING AND NORMAL TRANSPORT FROM CLOSED TO OPEN DOT REGIMES

Having seen the transition of the subgap (superconducting) transport as a function of Γ_S, in this section we shall discuss the transition of above-gap (normal) transport as the same parameter, Γ_S. At the end of the section, we will show the relation between these two transitions.

Through a quantum dot coupled to normal leads, current is carried by sequential tunneling, in the closed dot regime; while in the regime where the dot is strongly coupled to contacting reservoirs, Fabry-Perot interferences can be observed [82]. Here we study a single quantum dot strongly coupled to one reservoir. What is new is that the reservoir is a superconductor such that both normal and superconducting couplings are involved.

As an example in the closed dot regime, Fig.4.5a shows Coulomb peaks (1 to 6 in yellow) and Coulomb diamonds (Odd occupations are marked as I, II and III in black) above gap. After increasing V_S from 75 mV to 150 mV, every two Coulomb peaks, for example peaks 5 and 6 in Fig.4.5a, merge together and become one single broadened resonance marked as III in white in Fig.4.5b (A series of scans in Supplementary Figure 4.13 with smaller step

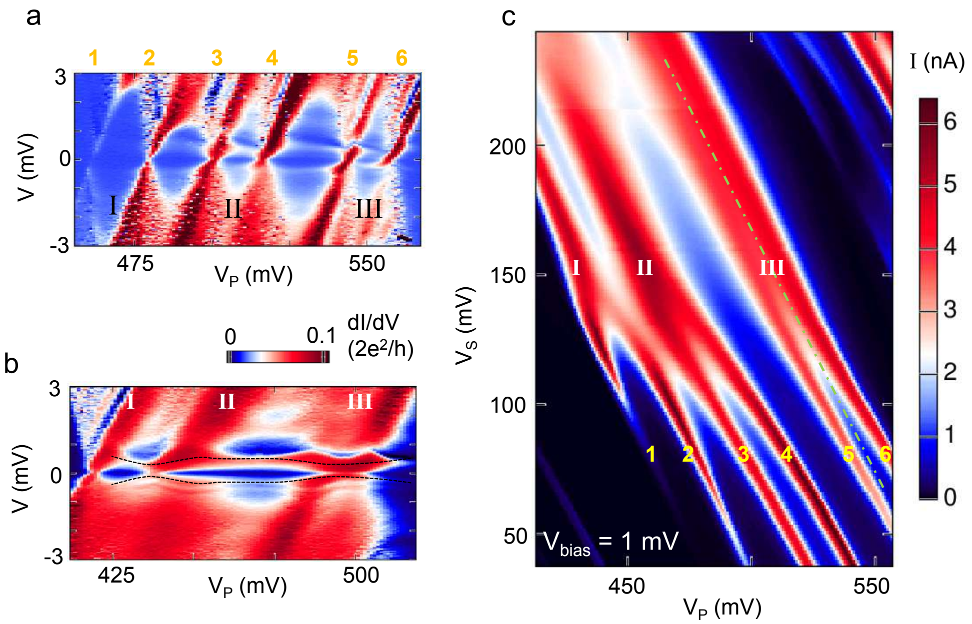

Figure 4.5: Superconducting and normal transport through the closed and open quantum dot coupled to a superconducting reservoir. a, Bias vs. gate measurement in a large bias range at V_S = 75 mV (closed dot regime). Six sharp broadened Coulomb peaks are marked as 1 to 6 in yellow. Three odd occupations are marked as I, II, and III in black. **b,** Bias vs. gate measurement in a large bias range at V_S = 150 mV (open dot regime). Three broadened peaks are marked as I, II, and III in white. **c,** Transport current as a function of V_p and V_S at V_{bias} = 1 mV. V_t = -555 mV in this figure and Fig.4.13.

size in the change of V_S show that the Coulomb diamonds smear gradually from Fig.4.5a to Fig.4.5b). As a result, only three broadened resonances, marked as I, II and III in white in Fig.4.5b, are present eventually. Periodicity of the conductance oscillations changes from one peak per electron added to one peak for every two electrons added.

In Fig.4.5c we measure current in the V_p range studied in Fig.4.5a-b at a fixed bias (1 mV), as V_S is increased continuously. In the closed dot regime (V_S < 100 mV), the parallel thin lines marked from 1 to 6 are associated with the Coulomb peaks marked in Fig.4.5a (V_S = 75 mV). In a large range of V_S (35 mV < V_S < 100 mV), widths of the Coulomb peaks do not undergo significant change. When V_S is close to ∼ 100 mV, the current in odd diamonds (marked as I, II, and III in Fig.4.5a), starts to grow. When V_S is increased to ∼125 mV, Coulomb peaks 1-2, 3-4, and 5-6, merge pairwise and form three broadened peaks, which exhibits the same change of periodicity from one to two electrons per conductance peak discussed with Fig.4.5a-b.

This change of periodicity is associated with decreasing quantized charging energy. In the closed dot regime, each quantum dot orbital is associated with two Coulomb peaks, corresponding to filling the orbital with electrons of spin-up and spin-down. In the open quantum dot regime, there is only one conductance peak, occurring when the orbital level is aligned with the Fermi level in the probe, meaning orbital quantization remains, but quantized charging effect is removed. On the other hand, the average gate voltage required to add an electron changes little: extracting charging energy from V_p values of neighboring above-gap resonances yields 2.7 ± 0.5 meV, assuming gate-dot coupling and quantum dot level spacing unchanged; while the quantized charging energy is the closed dot regime is close to it (~ 2.5 meV).

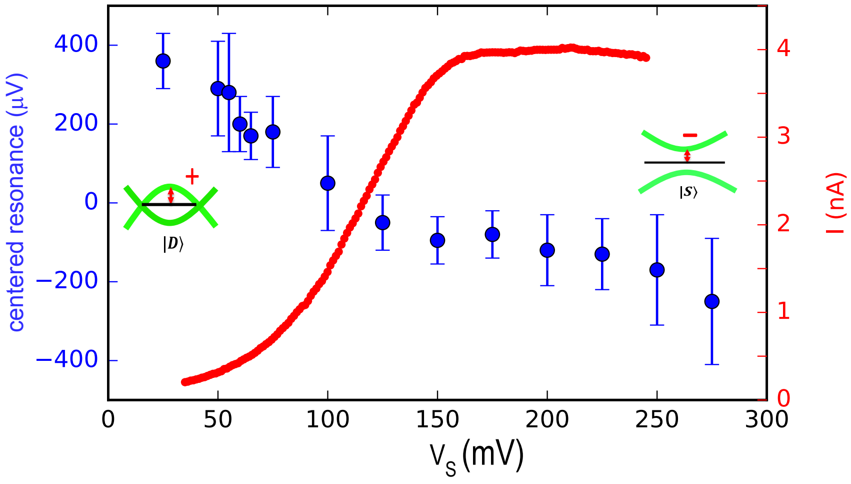

Figure 4.6: Andreev bound state phase transition and smearing of Coulomb blockade. Left (blue), Bias values of the subgap resonances at the center of "III" odd occupation in Fig.4.5. Positive signs are assigned to crossing-type resonances (left cartoon) while negative signs are assigned to anti-crossing-type resonances (right cartoon). The error bars are half-width-at-half-high of the resonances. **Right (red),** Current along the center of "III" odd occupation at 1 mV as a function of V_S. It is taken along the line cut depicted in Fig.4.5c in green.

Having analyzed the transitions of superconducting and normal transport as a same parameter, Γ_S, we now examine their relation. To clarify discussion, we take the Coulomb diamond of odd occupation marked as III in Fig.4.5a as an example, and extract the information of normal and superconducting transport. First, we extract current through this diamond (along the green dashed line cut depicted in Fig.4.5c), and plot it in red as a function of V_S in Fig.4.6. When V_S is low, the current is near zero because of Coulomb blockade. As V_S is increased, the dot becomes open and the current starts to increase and finally reaches 4 nA.

Following the same odd occupation in the superconducting state, we then extract the bias values of the subgap resonances (ζ) at the center of the occupation. We extract data points from fourteen bias vs. gate plots in Fig.4.5a-b and Fig.4.13 corresponding to a number of V_S values, and plot them in blue in Fig.4.6. To distinguish the two spin states, we adopt the convention that $\zeta > 0$ for $|D\rangle$ ground states and $\zeta < 0$ for $|S\rangle$ ground states (See cartoons in Fig.4.6). One can see that the value decreases from positive to negative as a function of V_S. Interestingly, the phase transition point (centered resonance = 0) occurs at $V_S \approx 22$ mV where the current of above-gap transport is also around the middle value (≈ 2.4 nA) between the saturated current (≈ 4.2 nA) and zero (Another way to visualize the $|D\rangle\,/\,|S\rangle$ transition is to follow the zero bias crossings which denote the degeneracies between $|D\rangle$ and $|S\rangle$ as a function of V_S. See supplementary Figure 4.16 from a different device.).

Qualitatively, the simultaneous transitions seem to be natural, because both transitions can be characterized by a same parameter, Γ_S/U [42]. Whether the simultaneous transition are governed by some fundamental mechanism, however, requires theoretical modeling of the system, which is in progress. A comprehensive understanding of the phenomenon is important, because as we shall see in Chapter 6, low charging energy is favored when implementing the Kitaev model in term of superconductor-quantum dots, and it can be achieved by increasing the superconductor-dot coupling, just like what has been performed here. In addition, in fusion experiments, manipulation of Majorana zero modes are accomplished exactly by tuning the dots closed and open to superconducting reservoirs [75].

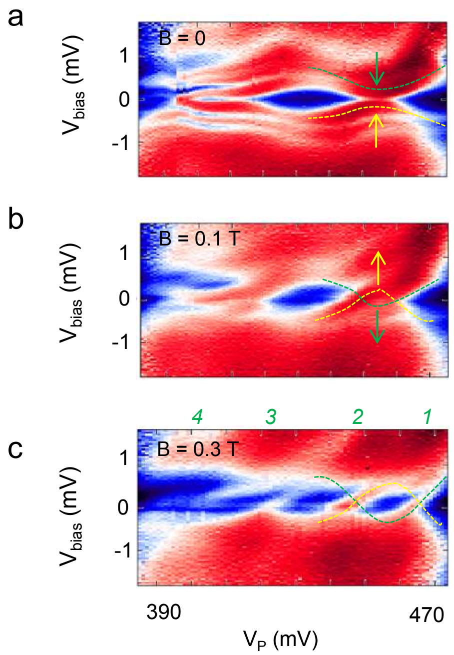

Figure 4.7: Spectroscopies at various magnetic fields in the open quantum dot regime. a-c, Subgap resonances as a function of V_p and bias V_{bias} at 0, 0.1, and 0.3 T, respectively. They have the same dot occupations. The green (yellow) dashed line depicts the branch at positive (negative) bias in **a**. The green and yellow arrows illustrate the directions of the evolutions of resonances as the magnetic field is increased. The numbers, 1 - 4, on top of **c** denotes the four zero bias crossings.

4.5 ZERO BIAS PEAKS IN THE OPEN DOT REGIME

Theories suggest connections between Andreev bound states in superconductor-quantum dot structures and Majorana zero modes in superconductor-nanowire of finite lengths [77, 78]. Furthermore, all components required to realize Majorana zero modes, i.e., strong spin-orbit coupling, a large g-factor and induced superconductivity from a high critical field superconductor, are present in our NbTiN-InSb structure. In this section, we demonstrate zero bias peaks produced by Andreev bound states at finite magnetic fields in our superconductor-dot structure. Zero bias peaks are the prime feature in the study of Majorana zero modes states [10, 56, 11, 13, 12]. We then discuss the similarities and differences between zero bias peaks associated with Andreev bound states and Majorana zero modes.

We tune the system to the open dot regime where the ground states are $|S\rangle$ regardless of dot occupations and then monitor the evolution of the subgap resonances as a function of magnetic field (Fig.4.7). At zero magnetic field, the transport resonances are anti-crossing-like with one branch at positive bias and the other at negative bias, as depicted by the dashed lines in Fig.4.7a. Thus no resonances are across zero bias. Note that the conductance at zero bias is not precisely zero due to resonance broadness and that the anticrossings are not far from zero bias. As an in-plane magnetic field (field-nanowire axis angle $\approx 30°$) is applied, a split resonance at positive (negative) bias marches to zero bias, illustrated by the green (yellow) arrow at positive (negative) bias. At some magnetic field, the resonances depicted by the green and yellow dashed lines touch at zero bias and form a single zero bias peak. At higher magnetic fields, the resonance depicted by green (yellow) dashed line marches further to the negative (positive) bias. They form a loop-like structure with two crossings at zero bias, as demonstrated in Fig.4.7b and c.

This magnetic field behavior is further investigated by measuring the resonances at zero bias as a function of V_p and magnetic field. In Fig.4.8a, two zero bias differential conductance structures appear to be round-V-shape-like. The V-shape structures can be explained by Fig.4.8b and Fig.4.7. Take the V-shape structure on the right as an example: (1) at zero magnetic field, the V-shape structure has not started. That is because the ground states are $|S\rangle$ in the entire V_p range. The associated bias vs. gate plot is Fig.4.7a where no resonances are through zero bias. (2) At ~ 50 mT, the V-shape structures starts to appear. That is when the lower $|D\rangle$, say $|\uparrow\rangle$, crosses the $|S\rangle$ ground state (marked by the vertical dashed line in Fig.4.8b) and the two branches of the anticrossing meet. (3) Afterwards, the structure grows into two branches. This is when $|\uparrow\rangle$ becomes the ground state where the resonances are loop-like in bias vs. gate scans (See Fig.4.7b,c). Each loop gives rise to two zero bias crossings (marked as 1 and 2 in Fig.4.7c) which exhibit as two branches (1 and 2 denoted in Fig.4.8a).

We thus map out the spin state phase diagram of Andreev bound states as a function of magnetic field and V_p: above the V-shape structures, the ground state is $|D\rangle$ and outside the V-shape structure, the ground state is $|S\rangle$. Notice that the branches do not have linear

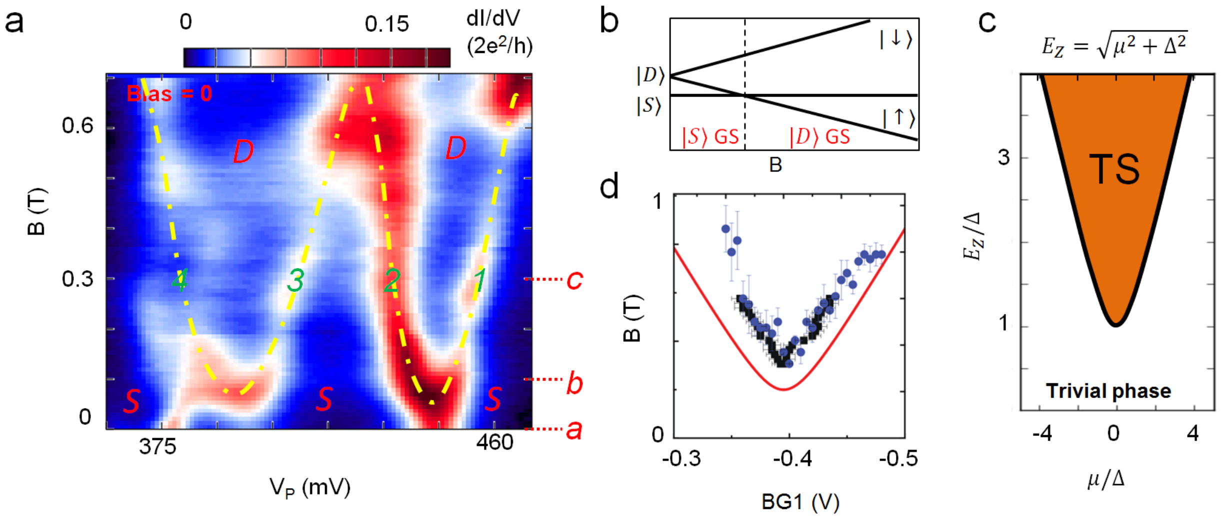

Figure 4.8: Magnetic field evolution of the resonances in open quantum dot regime. **a,** The differential conductance as a function of V_p and magnetic field (B) at zero bias. This plot is taken with the same dot occupations as in Fig.4.7. The fixed field line cuts denoted in a, b and c in red on the right are associated with Fig.4.7a-c, and the four branches marked with numbers, 1-4, correspond to the four zero bias crossings in Fig.4.7c. The V-shape structures are outlined by the yellow dash-dotted lines. D (doublet) and S (singlet) mark the spin states. **b,** Schematic of Andreev bound states as magnetic field. **c,** Topological phase boundary (in black), $E_Z = \sqrt{\mu^2 + \Delta^2}$, where E_Z is Zeeman energy. TS marks the topological supercondcuting phase (in orange) while out of the V-shape boundary the phase is trivial. **d,** Experimental measurement of the phase diagram of zero bias peaks in Ref.[13]. The data points are onsets of zero bias peaks. The red line plotted theoretical prediction of topological phase boundary, i.e., $E_Z = \sqrt{\mu^2 + \Delta^2}$. Panel **d** is adapted from Ref.[13].

dependence on magnetic field, particularly near the bases of the V-shape structures thus "V-shape" is actually not precise description. (Far away from the base of the V-shape structures, slopes of 15 ± 10 mV/T (absolute value) can be estimated by assuming linear magnetic field dependence. With a gate coupling factor ($\sim$1/4) extracted from Fig.4.4a, one can estimate a energy/magnetic field ratio of 4 ± 2 mV/T and a g-factor of $(13 \pm 9) * 10$.).

The spin state phase diagram of Andreev bound states as a function of magnetic field and chemical potential shares similarities with that of Majorana zero modes. Theories predict that Majorana zero modes exist in the following topological superconducting (TS) regime: $E_Z > \sqrt{\mu^2 + \Delta^2}$, where E_Z is Zeeman energy (Fig.4.8c) [3, 4] (This relation has been ex-

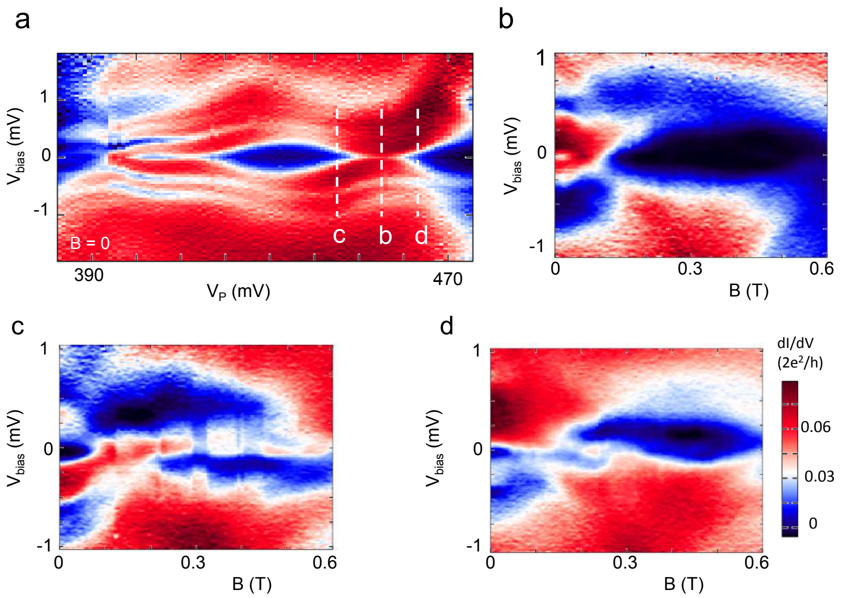

Figure 4.9: Bias vs. field measurements at various V_p in the open quantum dot regime. **a,** Bias vs. gate measurement in the strong Γ_S regime. Dashed lines depict the line cuts vs. field scans in **b-d**. **b-d,** Bias vs. field scans at the center, on the left and one the right of the anti-crossing resonances.

perimentally explored with NbTiN-InSb nanowire structures [13], which yields a boundary between regimes with and without zero bias peaks (Fig.4.8d).). This topological regime is where a zero bias peak is expected, meaning, Majorana zero modes exhibit as a zero bias conductance peak that starts from a finite magnetic field and sustains for a magnetic field range in a bias vs. field scan. Also, in the topological regime, the zero bias conductance peak is present over a chemical potential range at a finite field in a bias vs. gate scan.

The $|S\rangle/|D\rangle$ spin state boundary (yellow dashed lines in Fig.4.8a) shows some resemblance to that of a TS boundary (Fig.4.8c), i.e., both are round-V-shape and start at some finite fields (E_{Z0}), however, a few differences are found. (1) In the case of Majorana zero modes, E_{Z0} is fixed to Δ; while in the case of Andreev bound states, E_{Z0} is determined by Γ_S and is tunable. (2) The zero bias resonances due to Andreev bound states are only present at the phase boundary while the zero bias resonances due to Majorana zero modes (in the unpaired limit) fill the parameter space inside the V-shape boundary. This is further supported by tracking the subgap resonances as a function of bias and magnetic field at different V_p values in Fig.4.9, where the zero energy peaks are crossings of resonances at finite fields.

Then can one be confident that a zero bias peak is associated with Majorana zero modes when E_{Z0} is Δ and zero bias conductance fills the parameter space above the V-shape boundary? Probably no. The first difference can be not applicable to distinguish the two types of boundaries, because in devices for the study of Majorana zero modes, if the zero bias peaks are associated with Andreev bound states, E_{Z0} can be close to Δ given large Γ_S, and cannot be varied as Γ_S is not tunable because the nanowire sections are directly covered by superconductors with transparent contacts [10, 56, 13, 11, 12]. The second difference might be absent as well: the zero bias crossings can be "stretched" into long peaks in bias vs. field scans due to suppression of induced gaps or interactions of extra states [8]. Therefore, in practice, these two differences might not be sufficient to distinguish Andreev bound states from Majorana zero modes. Considering the zero bias peaks are the prime feature to signal Majorana zero modes, extra caution should be taken to distinguish them from zero bias peaks due to Andreev bound states.

4.6 ANOMALY I: REPLICAS AT HIGH BIAS

In the NbTiN-InSb quantum dot-NbTiN structures, some transport features can be well-understood by the theory in Chapter 2, while others require additional discussions. We call them "anomalies".

In this section, we discuss the first anomaly, i.e., high bias resonances may appear as replicas of the resonances around zero bias. In Fig.4.10a, the replicas at positive (negative) bias repeat the positive (negative) half of the lowest loop-like structure. The biases of the resonances at the center of odd occupations are $\sim$ 3.42, 1.93, 1.33, 0.76 and 0.19 mV, marked as 1, 2, 3, 4 and L in Fig.4.10a, where L denotes the lowest resonance. Notice that the highest bias can be 2 times of the superconducting gap in bulk NbTiN (1.76 mV). Also, negative differential conductance can accompany these high bias replicas as well. With V_p fixed in the

$|S\rangle$ regime, we step magnetic field in Fig.4.10b. The lowest resonances display splitting field behavior with an absolute slope of 0.18 mV/T (The plot only exhibits the branch at negative bias clearly because of asymmetric dot barriers.). No obvious splitting, however, is observed with the replicas at high bias, although they shift by the same energy in field, implying same g-factors. Fig.4.10c displays the magnetic field behavior with V_p fixed at the center of the loop structure ($|D\rangle$), splitting is observed with neither the lowest bias resonances nor the high bias replicas. They share a slope of 0.42 mV/T. Resonances at high bias are also present when system is in the open dot regime where the ground states are always $|S\rangle$ regardless of V_p (See Fig.4.10d). These high bias resonances appear to be replicas of the lowest resonances as well.

We first discuss the origin of the high bias replicas by comparing them to known phenomena that also show multiple copies. First, fitting these values except for the lowest resonances with the following relation: $V_{\text{bias}} = 2\Delta/\text{en}$ where e is electron charge, Δ is bulk gap in NbTiN (1.76 meV) and n are integers, yields $n \approx 1.0, 1.8, 2.6$ and 4.6. These values suggest possible connection to multiple Andreev reflections which would yield n values of increasing integers (1, 2, 3, 4, ...). Multiple Andreev reflections can take place in superconductor-normal conductor-superconductor (S-N-S) hybrid structures where quasiparticles are transferred from the lower gap edge of the source to the upper gap edge of the drain after multiple Andreev reflections at the two S-N interfaces. Every process involving an Andreev reflection increases the energy of the particle by $|eV_{\text{bias}}|$. The energy gained after n reflections, compensates the energy required to transfer the quasiparticle, which yields $eV_{\text{bias}} = 2\Delta/\text{n}$. Thus, multiple Andreev reflection requires Andreev reflection at both the left and right side of the dot. With highly asymmetric barriers and in such a low conductance regime ($\sim 0.04\ (2e^2/h)$), however, multiple Andreev reflections are supposed to be greatly suppressed [83]. Besides, supercurrent that usually accompanied with multiple Andreev reflections in InAs and InSb nanowires [40, 60] is not present here. Another phenomenon predicted to exhibit resonances of multiple copies is multiple Andreev bound states in the dot [84]. When there are multiple discrete quantum levels within the superconducting gap, multiple Andreev bound states can form, which is predicted to produce complex features in spectroscopy measurements (See Ref.[84]). In contrast, in our measurements, the replicas at

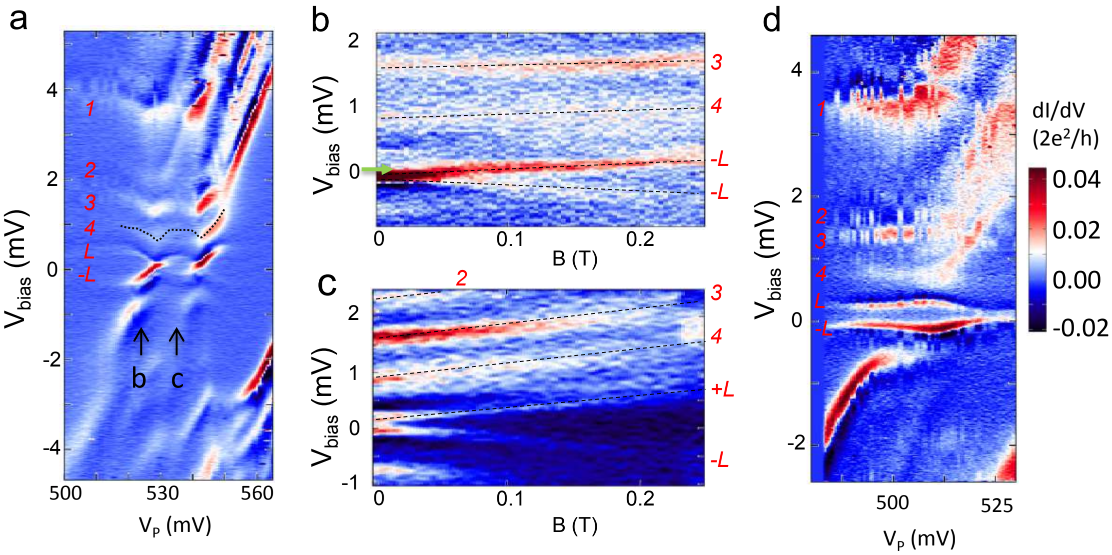

Figure 4.10: Replicas of subgap resonance at high bias. **a,** Bias vs. gate resonance measurement in a large bias range in the closed dot regimes. V_S and V_t are the same as in Fig.4.4c. The numbers, 1 - 4, depicts the replicas from high to low biases. "L" and "-L" denote the lowest resonances centered at zero bias. As an example, replica-4 is depicted by the dotted line. **b,** Magnetic field dependence of the resonances (3, 4 and $-L$) at the gate position marked with **b** in panel **a**. Zero bias is denoted by the green arrow. Note that at this gate position, only the negative bias branch of the lowest resonance has high conductance due to asymmetric dot barriers. **c,** Magnetic field dependence of the resonances (2, 3, 4 and $\pm L$) at the gate position marked with **c** in panel **a**. **d,** Bias vs. gate resonance measurement in a large bias range in the open dot regime. V_S and V_t are the same as in Fig.4.4e. The numbers, 1 - 4, depicts the replicas from high to low biases. "L" and "-L" denotes the lowest resonances centered at zero bias. Note that the position (and existence) of replica-2 is not clearly shown in the data.

positive (negative) bias simply repeat the positive (negative) half-loop structure at lowest bias. In addition, the discrete quantum dot levels have spacing of ∼ 1 meV, which is larger than Δ_{induced} thus multiple Andreev bound states are not expected in this dot [84].

The replicas might come from states in the nanowire probe on the left of the dot, and nanowire section on the right of the dot. Here we propose a minimum model that can explain most of the observed features. This model considers multiple Andreev bound states in the nanowire probe. As illustrated by Fig.4.11a, on the right side, the quantum dot is coupled to a NbTiN-covered nanowire section that has a induced gap (Δ_{induced}); on the left side, it

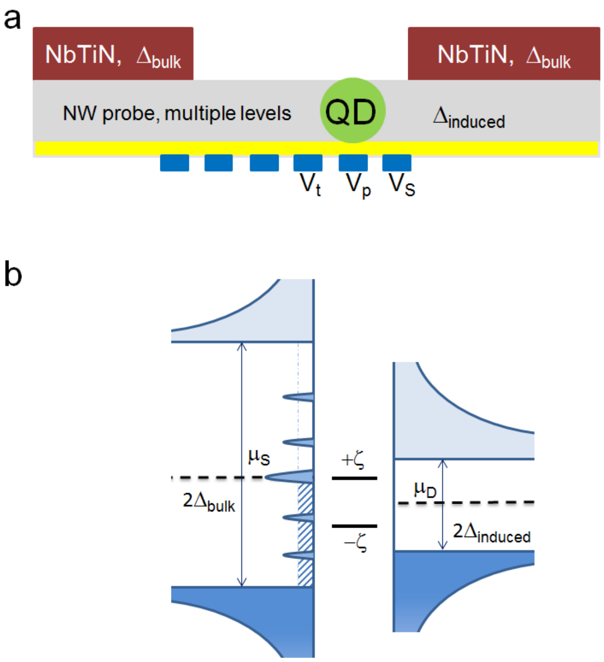

Figure 4.11: Schematic of high bias transport. **a,** Schematic of device structure. The quantum dot (QD) is probed by the nanowire probe (NW probe) with multiple levels; it is coupled to a nanowire (Δ_{induced}) covered by NbTiN (Δ_{bulk}) on the right. **b,** Schematic transport diagram. The nanowire probe has multiple levels associated with multiple Andreev bound states within Δ_{bulk}. The dot is coupled to a superconducting reservoir with Δ_{induced}, and it has two levels ($\pm\zeta$) associated with dot Andreev bound states due to Δ_{induced}. The dashed bar is used to approximate subgap density of states. The level at the probe chemical potential can be used to explain the anomaly in Section 4.7.

is connected to a nanowire probe. Because this nanowire probe has a finite size in length and diameter, and it is strongly coupled to the left NbTiN lead (Δ_{bulk}), Andreev bound states can form in it, which has been observed in Al-InAs nanowire section hybrid structures [56, 75]. On the other hand, this nanowire probe has a large length ($> 1\ \mu$m), which can give rise to a dense discrete quantum level spectrum. When there are multiple discrete quantum levels below Δ_{bulk}, multiple Andreev bound states can form [84]. As a result, each of these levels can give rise to an extra copy of resonance in bias vs. gate scans when it is aligned with the levels ($\pm\zeta$) in the dot. Theoretical modeling of transport through the dot Andreev bound states and multiple Andreev bound states in the nanowire probe is in progress.

4.7 ANOMALY II: SUBGAP NEGATIVE DIFFERENTIAL CONDUCTANCE

Another anomaly has been displayed in Fig.4.4: subgap negative differential conductance. Note that this feature is observed in most of scans in our experiments, although the negative differential conductance is more pronounced in the Andreev bound state regime (See Fig.4.4c-e) than in the co-tunneling regime (See Fig.4.4a). To clarify the discussion, we take Fig.4.4c as an example where the ground state is $|D\rangle$ within some gate range. The bias vs. gate plot shows loop-like resonances of positive differential conductance accompanied by sharp negative differential conductance resonances within the gap (300 - 500 μV). Different features, such as resonances without negative differential conductance below gap [47], and resonances with negative differential conductance above gap [40], have been observed in experiments and can be explained with the following transport diagrams (Fig.4.12).

Fig.4.12a illustrates resonances through a superconductor-dot structure probed by a normal lead. The Fermi level of the probe can map out the position of the levels, $\pm\zeta$, as a function of V_p (Fig.4.12b). The resulting resonances have only positive differential conductances (depicted in red in Fig.4.12a) within $\pm\Delta$ and can cross zero bias [8]. In Fig.4.12c, a hard gap superconducting lead serves as the probe and transport resonances are observed when the lower (upper) gap edge is aligned with $+\zeta$ ($-\zeta$) in the dot. The resulting resonance in a bias vs. gate diagram is a loop gapped by 2Δ (Fig.4.12c). The conductance resonance at each bias consists of a positive conductance peak followed by a negative conductance dip because current through the system spikes on resonance due to the singularities of density of states (DOS) at the edges, and a derivative of the current spike produces two peaks of opposite signs [47]. In superconductors with finite subgap DOS, a Fermi level is pinned to the center of the gap in the probe. This leads to a resonance copy when this chemical potential in the probe is aligned with $\pm\zeta$ in the dot. As a result, both features in Fig.4.12a and c are present (Fig.4.12e) [40]. Note that, importantly, the loop centered at zero bias has only positive differential conductance, assuming constant subgap density of states.

The features observed in our experiments, however, differ from all of the three scenarios (Fig.4.12a-f) and experimental observations. Although we are aware that the induced su-

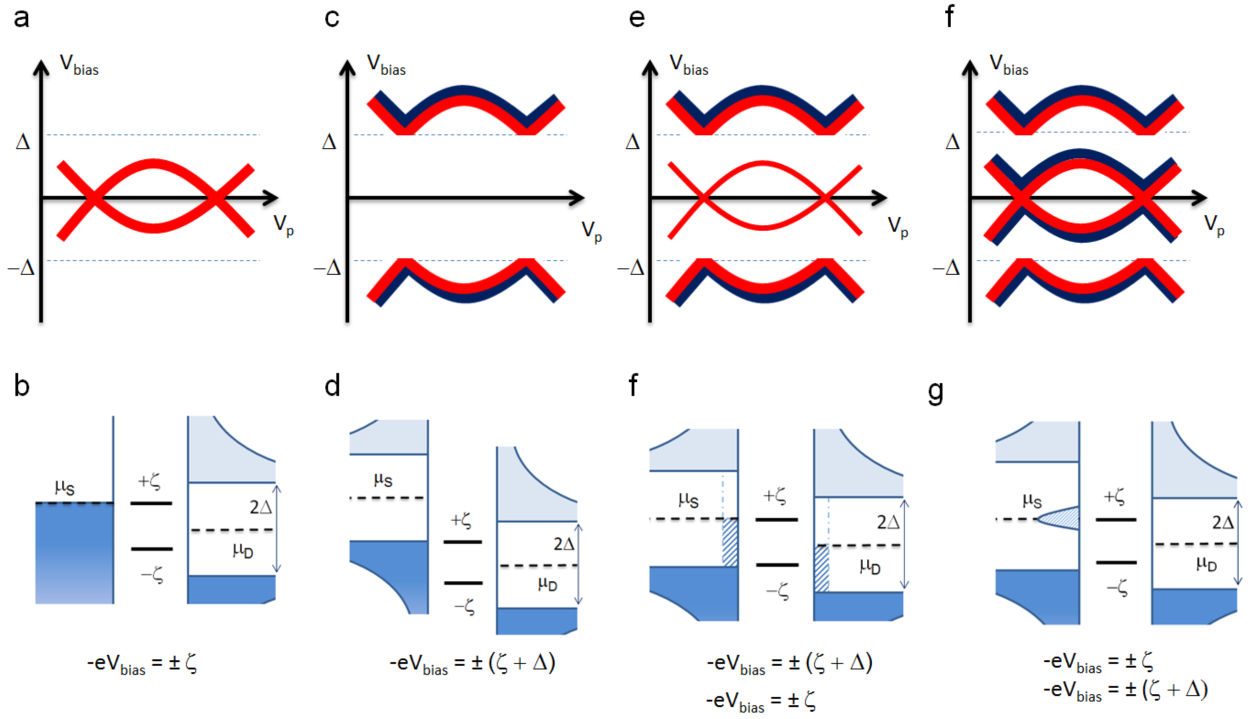

Figure 4.12: Illustrative bias vs. gate plots with different tunneling probes. a, Illustrative bias vs. gate plot with a normal conductor probe. Positive dI/dV resonances are depicted in red. **b,** Schematic energy diagram at resonance with the normal probe. **c-d,** Illustrative bias vs. gate plot and energy diagram with a hard gap superconducting probe. The blue curves in **c** depict negative dI/dV resonances. **e-f,** Illustrative bias vs. gate plot and energy diagram with a soft gap superconducting probe whose subgap density of states (dashed) is approximated as a Fermi level pinned at the center of the gap. **g,** Illustrative bias vs. gate plot of transport through a NbTiN-InSb quantum dot-NbTiN structure. **h,** Proposed schematic energy diagram to explain the experimental measurements. The probe has an energy level near the probe chemical potential, which serves to produce the subgap negative dI/dV feature in **g**.

perconductivity in our hybrid structure has a soft gap which can explain the loop centered at zero bias, the transport picture based on tunneling resonance illustrated by Fig.4.12e and f, fails to explain the negative dI/dV resonances centered at zero bias (The origin of soft gap can be non-uniformity of superconducting gap in NbTiN leads and/or non-uniformity of induced superconductivity in the nanowires.). The subgap negative differential conductance implies a level or DOS peak around the chemical potential of the nanowire probe (Fig.4.12h). In this way, similar to the singularities at superconducting gap edges, current from this level or DOS peak through the dot can spike on resonance and lead to positive dI/dV peaks followed by negative dI/dV peaks.

Importantly, one can rule out the possibility that the level or DOS peak around zero chemical potential in the probe is a Majorana zero mode, because the subgap negative differential conductance is observed regardless the presence of magnetic field that is a necessary ingredient for Majorana zero modes. Instead, the origin of the near-chemical potential level or DOS peak in the probe can be, like the case in Section 4.6, levels associated with multiple Andreev bound states in the nanowire probe (See Fig.4.1b).

Finally, we comment that the anomalies observed in sections 4.7 and 4.7 not only demonstrate rich transport features, but also can provide insights into the study of Majorana zero modes based on superconductor-nanowires. At first, in a superconductor-nanowire device, all quantum states are probed by the nanowire section. As shown here, the probe can be much more complex than a Fermi level or BCS DOS, as quantum states can form in the nanowire section that has confinement. The same applies to the nanowire section covered by the superconductor. Thus, incorporating the complexities in the probe and superconducting reservoir can be necessary for the understanding of some experimental observations.

4.8 SUPPLEMENTARY INFORMATION

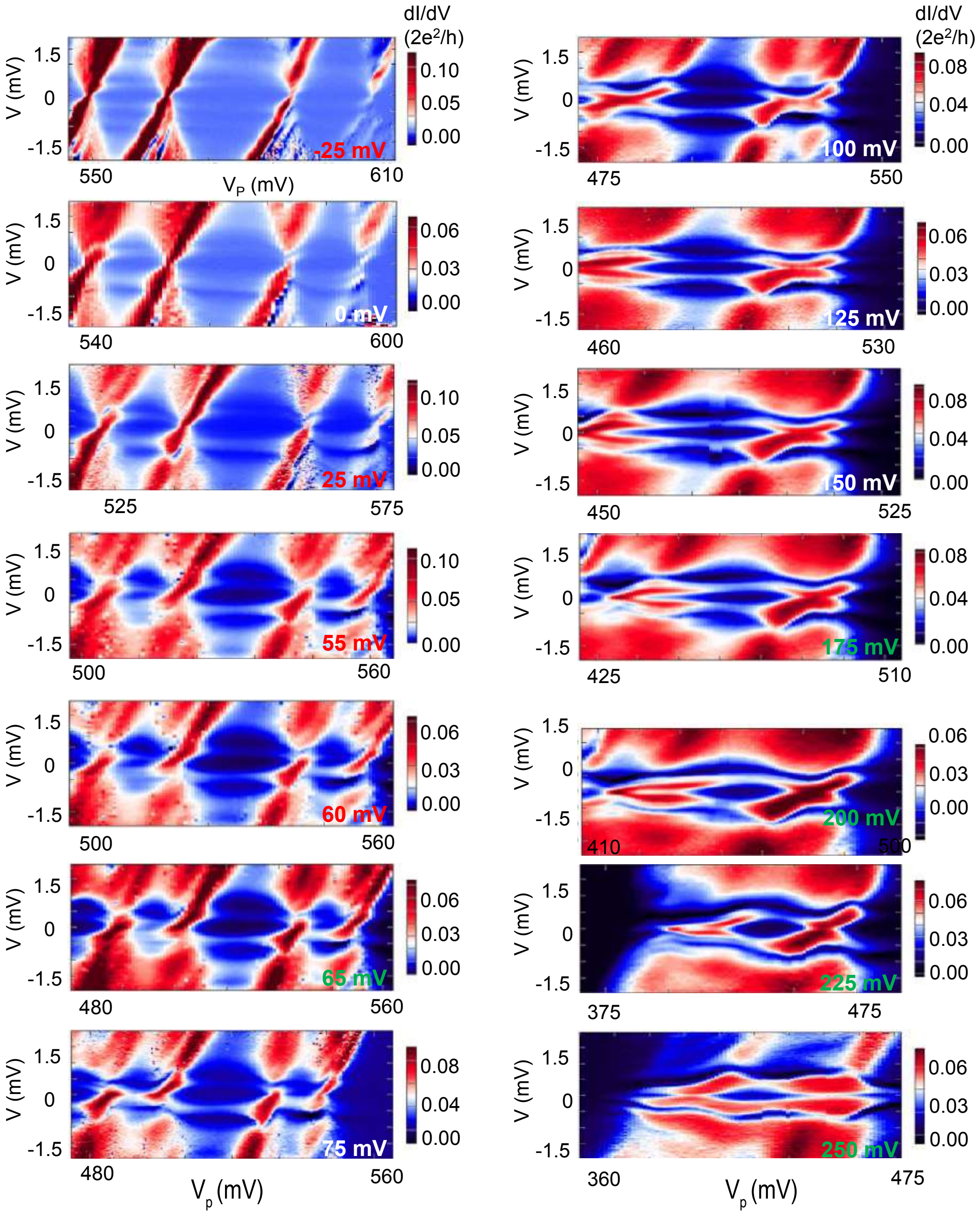

Figure 4.13: Bias vs. gate normal and superconducting spectroscopies at various V_S values. V_S = -25, 0, 25, 55, 60, 65, 75, 100, 125, 150, 175, 200, 225, 250 mV. V_t = -555 mV. Note that in each plot V_p is tuned to compensate the change to maintain same dot occupations.

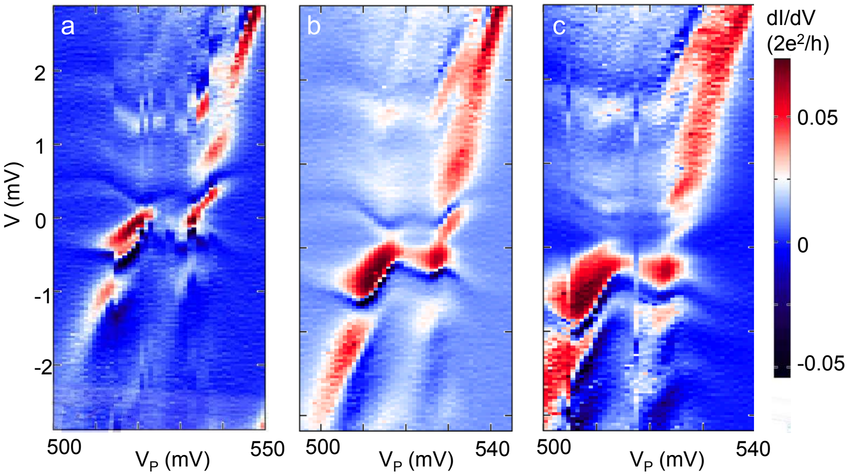

Figure 4.14: The effect of V_t in the closed dot regime. dI/dV as a function of bias and V_p. V_S = 220 mV. **a,** V_t = -685 mV. **b,** V_t = -670 mV. **c,** V_t = -655 mV.

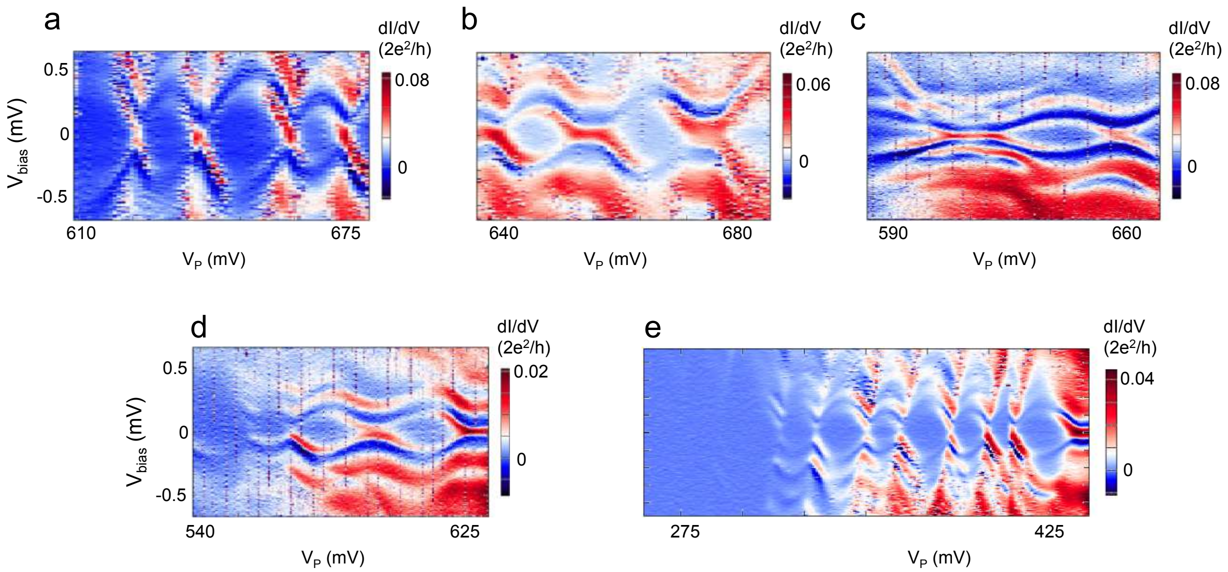

Figure 4.15: Another dot created with the same device. Another quantum dot is created on the other side of the same device. The dot is strongly coupled to left superconducting lead. dI/dV scans as a function of bias and V_p at various V_S and V_t. **a,** V_S = 50 mV and V_t = -700 mV. **b,** V_S = 150 mV and V_t = -700 mV. **c,** V_S = 225 mV and V_t = -700 mV. **d,** V_S = 300 mV and V_t = -700 mV. **e,** V_S = 150 mV and V_t = -600 mV.

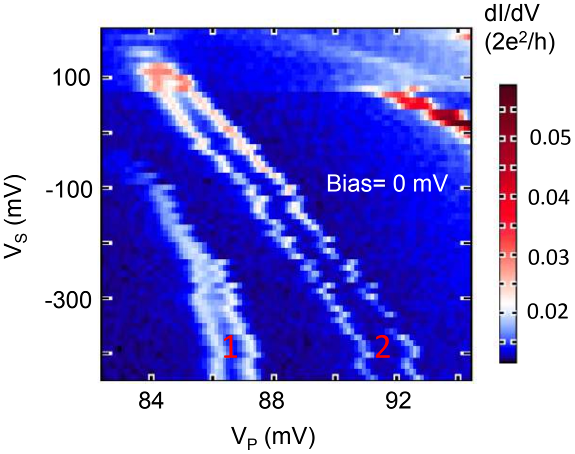

Figure 4.16: Zero bias peaks as a function of V_S. dI/dV as a function of V_S and V_p at zero bias. When $V_S < 50$ (150) mV, the resonances of structure 1 (2) in bias vs. gate plots are loop-like and each loop has two zero bias crossings. When $V_S > 50$ (150) mV, the resonances are anti-crossing-like and there is no zero bias peak. The data is taken in a NbTiN-InSb quantum dot device probed by a normal probe (Pd) by Jun Chen at University of Pittsburgh.

5.0 ANDREEV BOUND STATES IN DOUBLE QUANTUM DOTS[1]

In this chapter we present the hybridization of Andreev bound states in a double dot coupled to two superconductors.

---

[1] THIS CHAPTER IS ADAPTED FROM REF.[61].

5.1 INTRODUCTION

Quantum simulation is a way to study unexplored Hamiltonians by mapping them onto assemblies of well-understood quantum systems [6] such as ultracold atoms in optical lattices [20], trapped ions [21] or superconducting circuits [22]. Semiconductor nanostructures which form the backbone of classical computing hold largely untapped potential for quantum simulation [85, 86, 87]. In particular, chains of quantum dots in semiconductor nanowires can be used to emulate the ground states of one-dimensional Hamiltonians such as the toy model of a topological p-wave superconductor [2, 17, 18, 19]. Here we realize a building block of this model, a double quantum dot with superconducting contacts, in an indium antimonide nanowire [63]. In each dot, tunnel-coupling to a superconductor induces Andreev bound states [48, 88, 41, 47, 50, 44, 8]. We demonstrate that these states hybridize to form the double-dot Andreev molecular states. We establish the parity and the spin structure of Andreev molecular levels by monitoring their evolution in electrostatic potential and magnetic field. Understanding Andreev molecules is a step towards building longer chains which are predicted to generate Majorana bound states at the end sites [10, 55]. Two superconducting quantum dots are already sufficient to test the fusion rules of Majorana bound states, a milestone towards fault-tolerant topological quantum computing [75, 89, 90, 91].

5.2 DOUBLE DOT CONFIGURATIONS AND SUBGAP RESONANCES

In order to realize Andreev molecules we fabricate a device depicted in Fig.5.1a. Superconductivity in the InSb nanowire is induced by two NbTiN contacts placed on top of the nanowire [11], the segments of the wire below the contacts labeled S_L and S_R act as superconducting reservoirs for the left and right dots. The reservoirs are characterized by the induced gap $\Delta \sim 400$ μeV. We use voltages on five electrostatic gate electrodes placed under the nanowire to define the two quantum dots. Voltages on the two outer gates set the couplings Γ_L and Γ_R to the superconducting reservoirs. Gate voltages V_L and V_R control the chemical potentials on the left and right dots. The middle gate labeled V_t controls the cou-

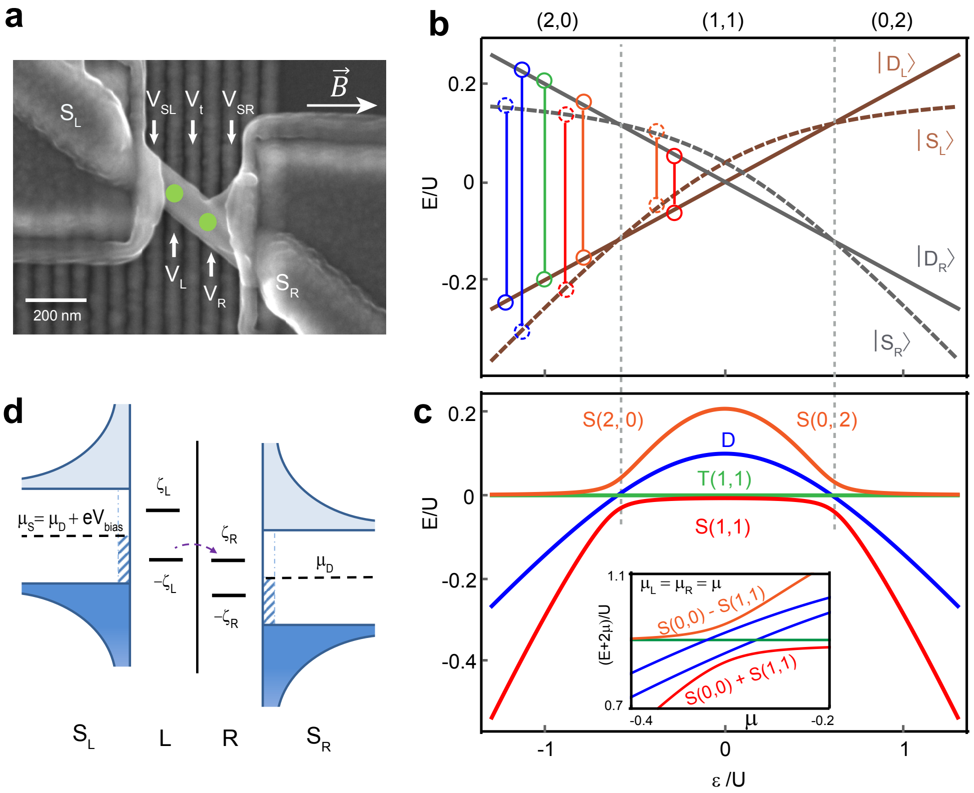

Figure 5.1: Double dot coupled to superconductors and spectra. **a,** Scanning electron micrograph of the InSb nanowire device, green circles indicate positions of the two quantum dots. The direction of magnetic field $\boldsymbol{B}$ is indicated by arrow. **b,** Spectrum of Andreev states in two quantum dots separated by a large barrier as a function of detuning ϵ. On the left(right) dot, the ground states are $|S_{L(R)}\rangle$, $|D_{L(R)}\rangle$ and $|S_{L(R)}\rangle$ with dot occupations 2, 1, 0 (0, 1, 2) respectively. Vertical lines connect levels that hybridize to form molecular states plotted in **d**. **c,** Molecular Andreev spectrum of a double quantum dot as a function of detuning (main panel) and energy level shift (inset). Charge configurations in **b** and **c** are labeled in **b** and separated by dashed lines. **d,** Transport resonance at positive bias occurs when Andreev chemical potentials $-\zeta_L(V_L, \mu_S)$ and $\zeta_R(V_R, \mu_D)$ are aligned. The hashed bars depict subgap states included in the numerical model.

pling t between the dots. While all couplings are tunable in a wide range, here we focus on the regime where the system is approximately left/right symmetric, and with $\Gamma_L, \Gamma_R >$ t. In this regime the two dots are strongly coupled to their respective superconducting reservoirs and weakly coupled to each other. The charging energy on each dot $U \sim 1-2$ meV $> \Delta$ thus the dots can be filled by electrons one at a time rather than in Cooper pairs.

In superconductor-semiconductor hybrid structures, electrons arriving from a semicon-

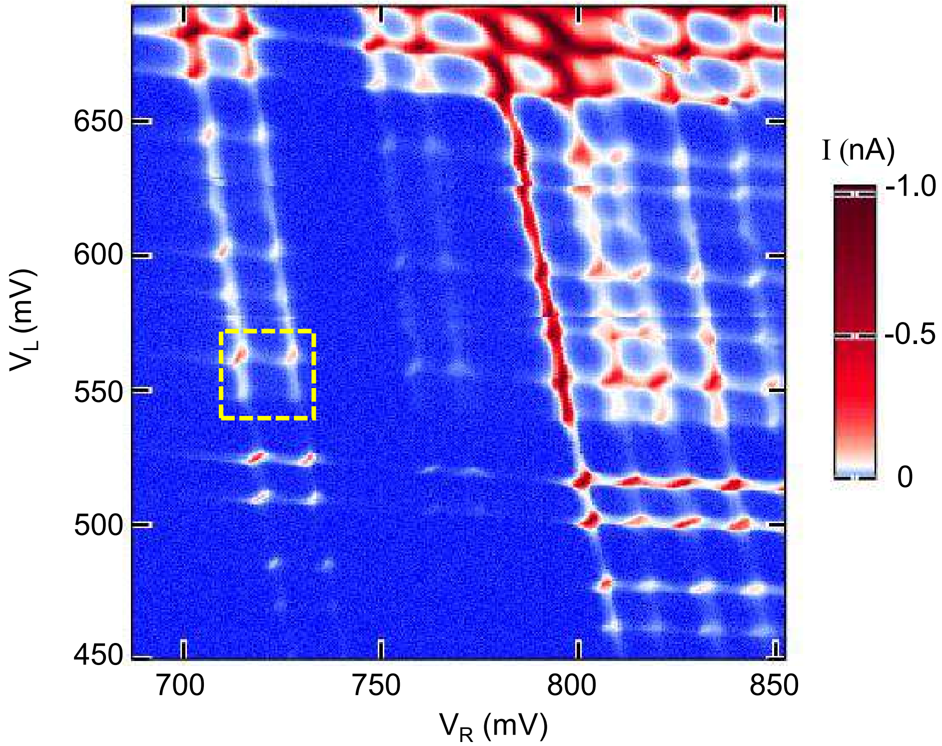

Figure 5.2: Double dot stability diagram in a large gate voltage range. Charge stability diagram at the bias of -200 μV and at zero magnetic field. The measurements in chis chapter focus on a 3x3 configuration window enclosed by the yellow square.

ductor with energies below the superconducting gap are prohibited from entering the superconductor and are reflected back into the semiconductor as quasiholes via Andreev reflection [68]. Through this mechanism, an electron-hole standing wave, known as an Andreev bound state, can form in the semiconductor. In a single quantum dot, Andreev bound state spectrum consists of a spin-singlet state (S) which is a superposition of 0 and 2 electrons on the quantum dot, and two doublet states $D_\uparrow$ and $D_\downarrow$, both of which correspond to a single electron on a quantum dot either in the spin up or spin down state. In Fig. 5.1b, we depict the Andreev spectra of two decoupled quantum dots along the energy level detuning axis, meaning that the electrostatic energies on the two dots are changed in the opposite directions. From negative to positive detuning, the left dot is occupied with 2, 1 and 0 electrons, while the right dot is occupied with 0, 1, and 2. In the (2,0) and (0,2) double dot configurations, singlet states on both dots are lower in energy than doublets. In the (1,1) configuration, doublets are the ground states. We note that in the experimental system the charge occupations of the dot are unknown but the discussion is provided in terms of 0,1,2 electrons on each dot for clarity and because in superconducting systems properties most strongly depend on parity (even or odd) of the charge occupations.

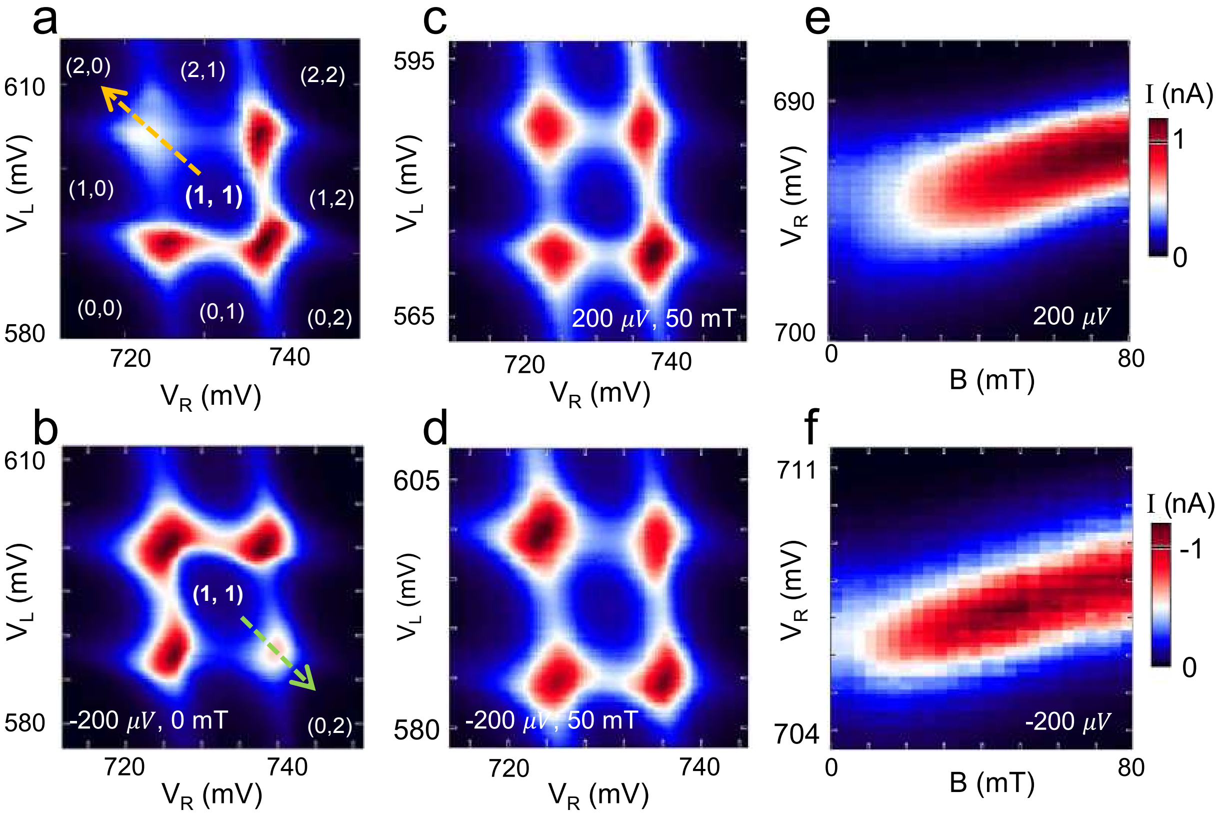

Figure 5.3: Spin blockade and parities. **a**, At bias of 200 μV the (1, 1)↔(2,0) degeneracy point has smaller current. Parities of double dot configurations are indicated in brackets. **b**, At the reverse bias the (1, 1)↔(0,2) degeneracy point has suppressed current. **c, d**, Spin blockade is lifted by a magnetic field of 50 mT, with all four degeneracy points showing similar current. In **e, f**, gates are swept through the spin blockade region (arrows in **a** and in **b**) as magnetic field is stepped. The current has a zero-field dip, consistent with magnetic field behaviors of spin blockade reported previously in InSb nanowires [29].

When the two dots are tunnel-coupled, each of the states on one dot will hybridize with each of the states on the other dot (Fig.5.1c). The new singlet states are S(0,2), S(2,0) and S(1,1): these three states hybridize at their degeneracy points due to tunnel coupling. The four doublet states hybridized of D(0,1) and D(1,0), D(2,1) and D(1,2) are nearly degenerate at zero field and are designated as D in Fig.5.1c and are always the excited states. When the chemical potentials μ_L and μ_R on the left and right dots are tuned along the energy shift axis, such that $\mu_L = \mu_R = \mu$ the double dot can transition from (0,0) to (1,1) configuration. In this case, S(0,0) and S(1,1) are hybridized by superconducting correlations (Fig. 1c(inset)). A new type of levels appears below the gap in a double quantum dot: the three triplet states $T_+(1,1)=(\uparrow,\uparrow)$, $T_-(1,1)=(\downarrow,\downarrow)$ and $T_0(1,1)=(\uparrow,\downarrow)+(\downarrow,\uparrow)$ trace back to the symmetric combinations of single-dot doublet states. T(0,2) and T(2,0) are above the induced gap due to the large orbital energy and thus they do not correspond to bound Andreev states.

In experiment, source-drain voltage bias V_{bias} is applied between S_L and S_R to tune the chemical potentials in the source and drain superconductors μ_S and μ_D (Fig.5.1d). On the left and right quantum dots, chemical potentials that correspond to transitions between ground and excited Andreev bound states, $\pm\zeta_L$ and $\pm\zeta_R$, are arranged symmetrically around the chemical potential of the left(right) superconductor. The splitting between particle-like and hole-like Andreev resonances $+\zeta$ and $-\zeta$ on each dot is tunable with gate voltages on that dot. A resonance in conductance through the double dot occurs when $\mu_S - \mu_D = \zeta_L + \zeta_R$, and thus for each setting of gates V_L and V_R the transport resonance corresponds to a unique value of V_{bias}. In Fig.5.2 we plot the overview the device in terms of a charge stability diagram of the double dot in large gate voltage ranges.

Measurements below are focused on a double dot stability diagram presented in Fig.5.3a. Four degeneracy points are observed at which the current has a local maximum. The upper-left maximum of current is lower than the other three. In reverse V_{bias}, the lower-right maximum has the lowest current (See Fig.5.3b). This is due to spin blockade which occurs between (1,1) and (0,2) or (2,0) double dot states due to Pauli exclusion [29]. Further evidence is provided by magnetic field evolution of the blockade. The blockade is lifted at a finite magnetic field, as shown in Fig.5.3c where 50 mT is applied and the strength of the current at the upper-left maximum is no longer suppressed. In Fig.5.3e, a line cut depicted by the yellow arrow in Fig.5.3a is scanned while magnetic field is stepped, the current shows a dip at zero field and the suppression is removed. Same behaviors are observed at the opposite bias (See Fig.5.3d,f). Spin blockade is a manifestation of hybridized quantum states on the two

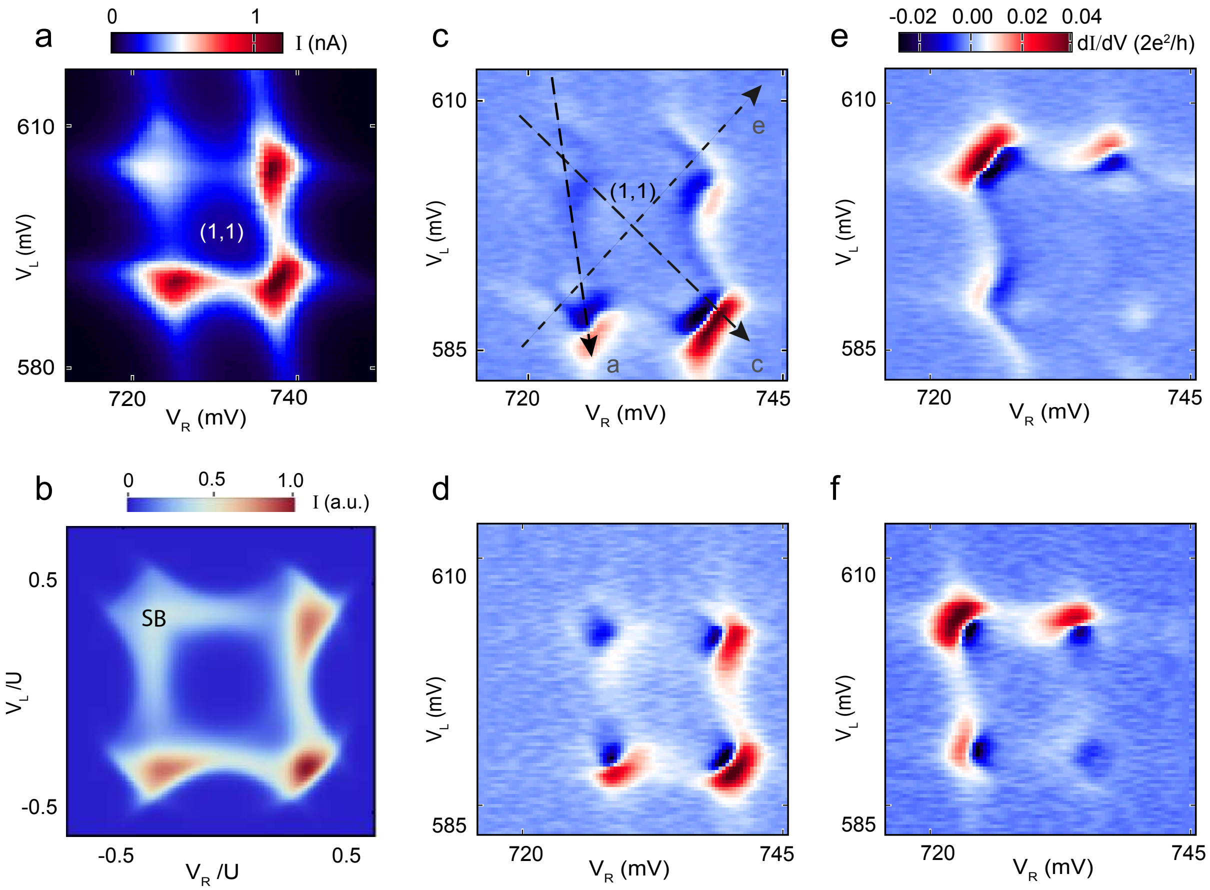

Figure 5.4: Stability diagrams. a, Current at V_{bias} = 200 μV. The plot is repeated for a better comparison with the theoretical plot (**b**). **b,** Numerically computed current at low interdot tunneling as a function of chemical potentials of left and right dots. "SB" marks the corner with numerically reproduced spin blockade. **c,** Differential conductance dI/dV at V_{bias} = 200 μV over the same gate voltage range as in **a**. Dashed lines indicate the cuts that correspond to panels in Fig. 5.5. **d-f,** Differential conductance dI/dV at V_{bias} = -200, 50, -50 μV over the same gate voltage range as in **a**.

dots, and it allows us to identify and label the parity of nine configurations in Fig.5.3a. The regime is closely reproduced by a numerical model of the superconducting double dot discussed below, including the spin blockade regime (Fig.5.4b). In differential conductance the double dot stability diagram is defined by arc-shaped resonances that connect the degeneracy points (Fig.5.4c-f).

The arcs in double dot stability diagrams originate from loop-like resonances in gate vs. bias scans (Fig.5.5). The loop resonances appear most clearly when one dot is fixed at a degeneracy point and the other dot is swept (Fig.5.5a-b). Loop-like resonances are also observed when the energy levels on the two dots are tuned simultaneously (Fig.5.5c-d), though deep within the (1,1) region the interdot tunnel coupling is reduced and the current is suppressed. The loop resonances are accompanied by copies in negative differential conductance. This is because on resonance (Fig.5.1d) current has a maximum, hence differential conductance changes from positive to negative. The origin of arcs in Figure 2 can now be understood: indeed, if Andreev resonances are loop-like in V_{bias} for any cut through the double dot stability diagram, a scan at fixed V_{bias} would reveal arc resonances when V_{bias} matches the interdot Andreev resonance condition.

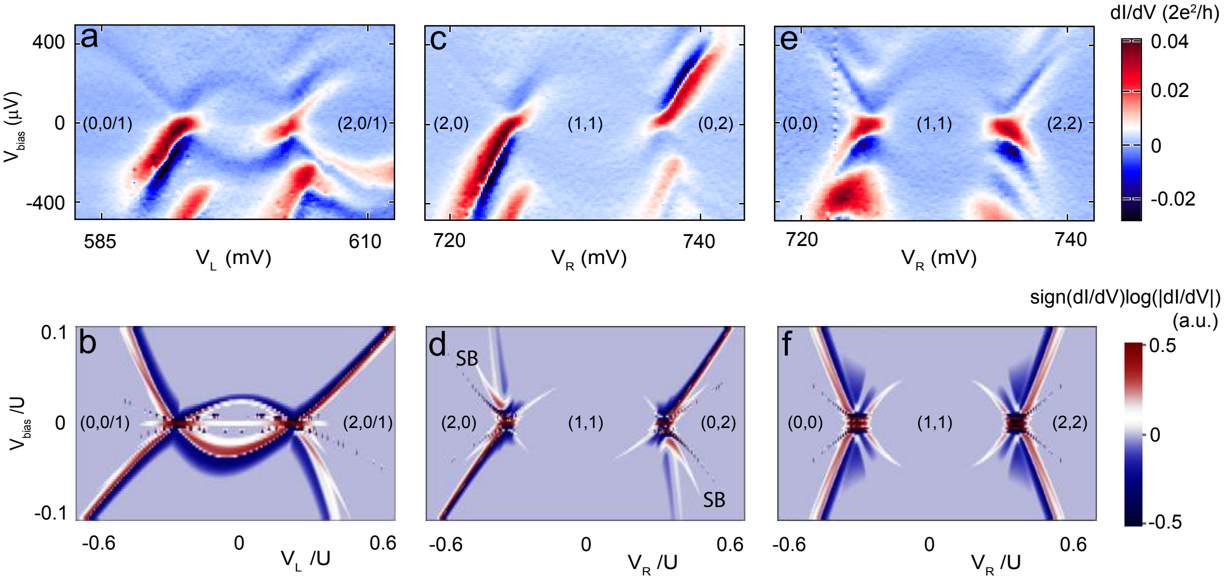

Figure 5.5: Bias spectroscopy of Andreev molecular states. **a, c, e,** Source-drain bias spectroscopy along various cuts depicted by the dashed-line arrows in Fig. 5.4c, i.e., right dot is fixed to 0/1 degeneracy point and left dot is swept in **a**, along detuning in **c**, and along energy level shift axis in **e** (see additional complementary data in the supplementary information). Both V_L and V_R are tuned in each panel, but either V_R or V_L is used to denote the x-axis. Parity configurations indicated in brackets in each region. **b**, **d** and **f**, Corresponding numerically computed differential conductance as function of left dot chemical potential with fixed right dot chemical potential (**b**), along detuning (**d**) and energy level shift axis (**f**). “SB”s in **d** mark the numerically reproduced spin blockade corners at positive and negative biases.

The observed Andreev loops are closed, i.e. the conductance resonances reach zero bias. This is counter-intuitive given that both leads of the system are superconductors and thus an energy gap is expected around zero bias [47, 88]. We ascribe this to sub-gap quasi-particles that enable single-particle transport through the Andreev molecular states. When this effect is included in the numerical model, simulations reproduce the closed loops and negative differential conductance, as well as bias asymmetries due to spin blockade (Figs.5.5b, d, f). We model each lead as being composed of two parts: a conventional superconductor with a hard superconducting gap and a normal Fermi gas with gapless excitations. The electrochemical potentials of the normal and the superconducting parts are pinned together at the value set by the voltage applied to the physical lead. In our model, Andreev reflection off the superconducting part results in the formation of Andreev molecules. The normal part induces transitions between the Andreev molecular states (see supplementary information for details). For simplicity, the model assumes leads with a superconducting gap much larger than the single dot energy U [92].

5.3 SPIN STRUCTURE

We investigate the spin structure of Andreev molecular states by monitoring the evolution of subgap transport features in magnetic field. In Fig. 5.6a we plot differential conductance as a function of magnetic field and source drain bias for a double quantum dot in the (2,2) configuration. At zero magnetic field we observe two peaks, one at positive bias and one at negative bias. The application of magnetic field results in the splitting of both peaks. Two of the peaks move to higher bias towards the gap edge, while the other pair meets at zero bias. The two merged resonances stick to zero bias at finite field. This effect has been investigated as a signature of Majorana fermions [10]. Here, given the narrow range of field over which the zero-bias peak is observed, we associate it with level repulsion from the gap edge or from other subgap states [8]. By comparing measurements to numerical spectra and transport calculations, we assign the peaks to the transitions between the $S(2,2)$ ground state and the $D(\uparrow,2)$ and the $D(\downarrow,2)$ excited states (Fig.5.6b,c). Magneto-transport of the double quantum dot system in the (0,0), (0,2) and (2,0) configurations is qualitatively the same as in the (2,2) configuration (see supplementary information).

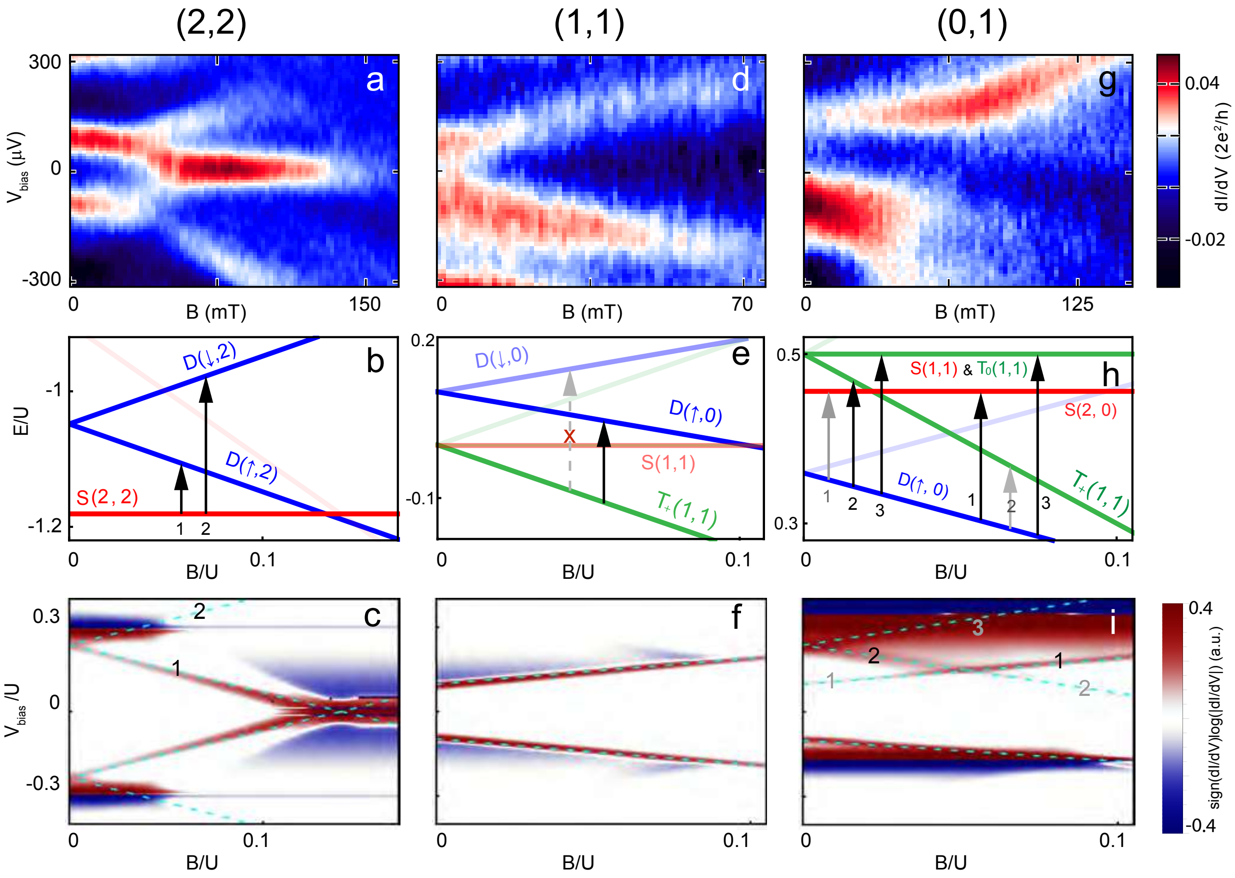

Figure 5.6: Magnetic field evolution of Andreev molecular states. a, d, g, Bias spectroscopy of Andreev resonances as a function of magnetic field for $(2,2)$, $(1,1)$ and $(1,0)$ double dot configurations. **b, e, h**, Numerically computed spectra of Andreev molecular states as a function magnetic field for $V_{\text{bias}} = 0$. The black (gray) arrows and numbers label the allowed transitions in the simulated spectra (**b, e, h**) and the associated high (low) conductance resonances in the numerical dI/dV transport plots (**c, f, i**). In **e** the crossed dashed arrow labels the forbidden transition between $T_+(1,1)$ and $D(\downarrow,0)$. The light blue dashed lines in **c, f, i** plot the bias voltage at which the levels on the dots come into resonance. The dI/dV plots use the same model parameters as in the spectrum plots.

In the (1,1) configuration only a single pair of differential conductance peaks is observed at all fields, one at positive and one at negative bias (Fig.5.6d). Both peaks shift to higher bias at higher magnetic fields. The explanation for this behavior originates in the Andreev molecular level structure depicted in Fig.5.6e. The low energy manifold consists of $S(1,1)$ ground state that is almost degenerate with the three triplet states T_+, T_0, T_-. At finite field T_+ plunges below the $S(1,1)$ and becomes the ground state. Transitions from this triplet state are allowed only to the doublet states $D(\uparrow,0)$, while transitions to $D(\downarrow,0)$ are strongly suppressed because they involve an additional spin flip. Both states T_+ and $D(\uparrow,0)$ shift to lower energies with magnetic field, but the triplet states shifts with $g\mu_B B$ while the doublet states shifts with $g\mu_B B/2$, thus the energy difference between them grows with field. Transport calculations using our detailed model confirm this picture (Fig.5.6f).

Odd total parity configurations (0,1), (1,0), (2,1) and (1,2) offer a richer variety of transport behavior (Fig.5.6g, and supplementary information). The common features include asymmetry with respect to bias and kinks in the conductance peaks at which the effective g-factor increases. In some regimes we also observe the magnetic-field induced splitting of conductance peaks into as many as three sub-peaks. In Fig.5.6h we plot the Andreev molecular spectrum in the (0,1) configuration as a function of magnetic field at zero bias. While $D(0,\uparrow)$ is the well-separated ground state at finite field, there are two singlet states ($S(0,2)$ and $S(1,1)$) and two triplet states (T_+ and T_0) that can contribute to transport (transport via the state T_- requires a spin flip and is therefore suppressed). Numerically computed transport demonstrating both a kink feature as well as the asymmetry with respect to bias, is plotted in Fig.5.6i. The model indicates that the origin of the kink feature is that as B increases the $D(\uparrow,0) \rightarrow T_+(1,1)$ transition (labeled 2 in Fig.5.6h,i) becomes dimmer while the $D(\uparrow,0) \rightarrow S(2,0)$ transition (labeled 1 in Fig.5.6h,i) becomes brighter. In the model, the dimming and brightening of the transitions is associated with proximity to the interdot resonances that occur at higher bias. The bias asymmetry is associated with the different parities of the left and right dots, the asymmetry flips if the parities are switched, which can be seen in the spin structure of the full 3x3 configurations in Fig.5.7.

In Fig.5.7 we plot the magnetic field behaviors of the subgap resonance for all of the 3x3 configurations. Firstly, along diagonal of the map, bias symmetry is observed as branches at both biases are measured with similar strength. Along off-diagonal, the bias asymmetry is swapped, meaning in (2,0) the resonance at negative bias is strong while that at positive bias it is hardly visible. Across the bias symmetric (1,1) configuration, the resonance strength has an opposite relation with bias in (0,2).

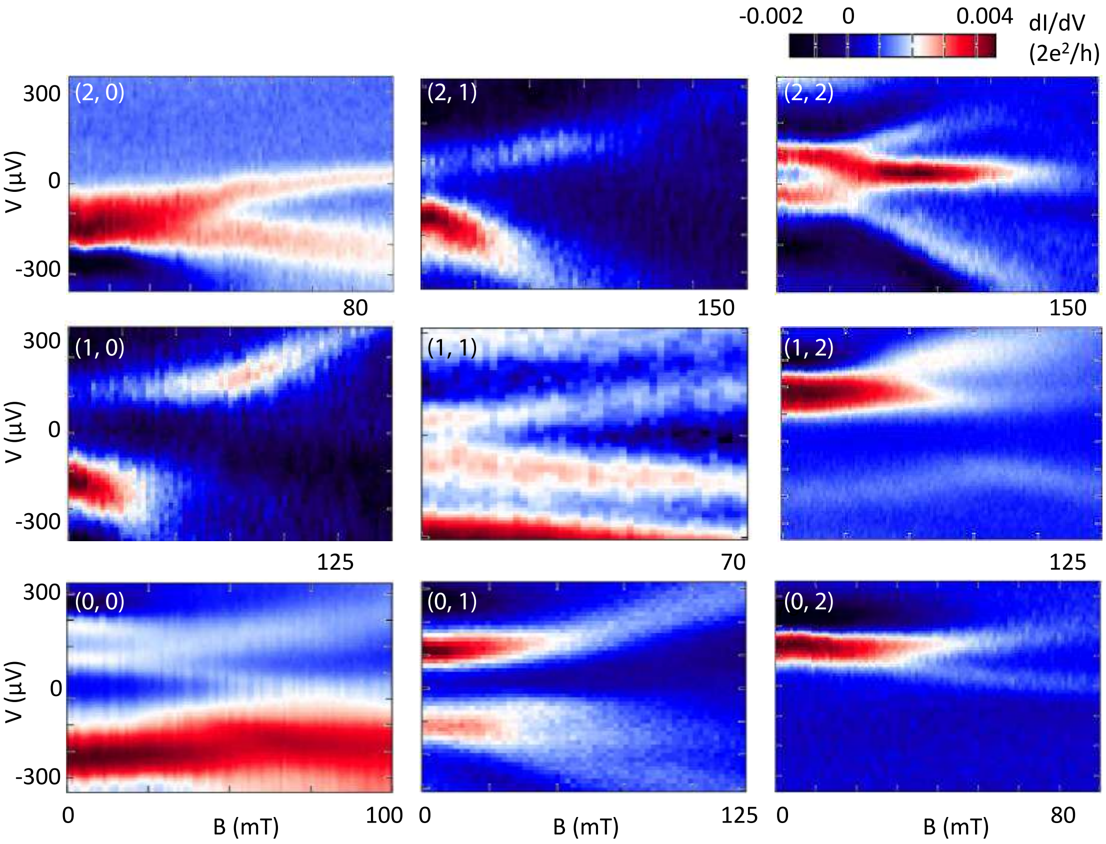

Figure 5.7: Spin map. The magnetic field dependence of the subgap resonances in the 3x3 double dot configurations around (1,1). Within each configuration, the magnetic field dependence of the resonances is measured at a few fixed gate voltages. Scans in each configuration demonstrate consistent magnetic field behavior and one typical scan is presented here. Note that the positive (negative) bias branch in (2,0) ((0,2)) is missing, which is a consequence of spin blockade and asymmetric couplings.

5.4 CONCLUSION

The elucidation of Andreev molecular spectra and of their evolution in magnetic field opens several avenues for future research. Andreev molecule is a building block for the emulation of the Kitaev chain model [18, 17], in which tuning of longer quantum dot chains is to be performed pairwise along the chain. This taps into the largely unexplored potential of semiconductor systems for quantum simulation research [93]. Simulations of quantum dynamics of Andreev states in quantum dots chains can be attempted in hard gap nanowires

[94, 95, 11]. In topological qubits, double quantum dots have been proposed for fusion and readout of Majorana quantum states [75]. These operations transmute topologically protected Majorana states into Andreev molecular states. Andreev molecules with topologically superconducting reservoirs will become building blocks of topological quantum circuits, and can be realized in the same nanowires with longer quantum dots (200 nm or longer) subjected to higher magnetic fields (0.5 Tesla) [11, 13].

5.5 SUPPLEMENTARY INFORMATION

5.5.1 Complimentary data on spectroscopy and magnetic field dependence

In Fig.5.8 we further explore the arcs connecting the current maximal regimes in the stability diagrams. We measure the stability diagrams at V_{bias} = -200 μV at various magnetic field, as shown in Fig.5.8c-g. We then take line cuts through the center of (1,1) depicted in Fig.5.8c and step magnetic field. In Fig.5.8a, for B $\leq$ 100 mT, the high current lines that define the (1,1) region move apart. At higher fields, the lines exhibit kinks. They are consistent with the previously observation in InSb nanowire single quantum dots. The origin is the change of ground states by magnetic field [60]. Based on it, the spins of the electrons added to the dot are depicted by arrows along the high current lines.

Spectroscopy of the molecular device has at least three dimensions: V_L, V_R and V_bias. In the main text, we present bias vs. detuning and bias vs. energy shift plots. In Fig.5.9 we present scans along more directions: Fig.5.9b is obtained by sweeping chemical potential of the left dot when the chemical potential of the right dot is fixed at a degenerate point. Fig.5.9c is obtained by the other way around. When the line cut is along the energy shift direction but through the (1,1) $\leftrightarrow$ (2,0) degenerate points, we observe Fig.5.9d.

Notice that the magnetic field evaluation of the subgap resonance in (even, odd) and (odd, even) are less clear. We thus take a closer look at it by measuring the field evolution at various spots in (2, 1) configuration. Recall in (2,1), the resonance at positive bias is weaker. We measure a series of bias vs. field scans at chemical potential settings farther and

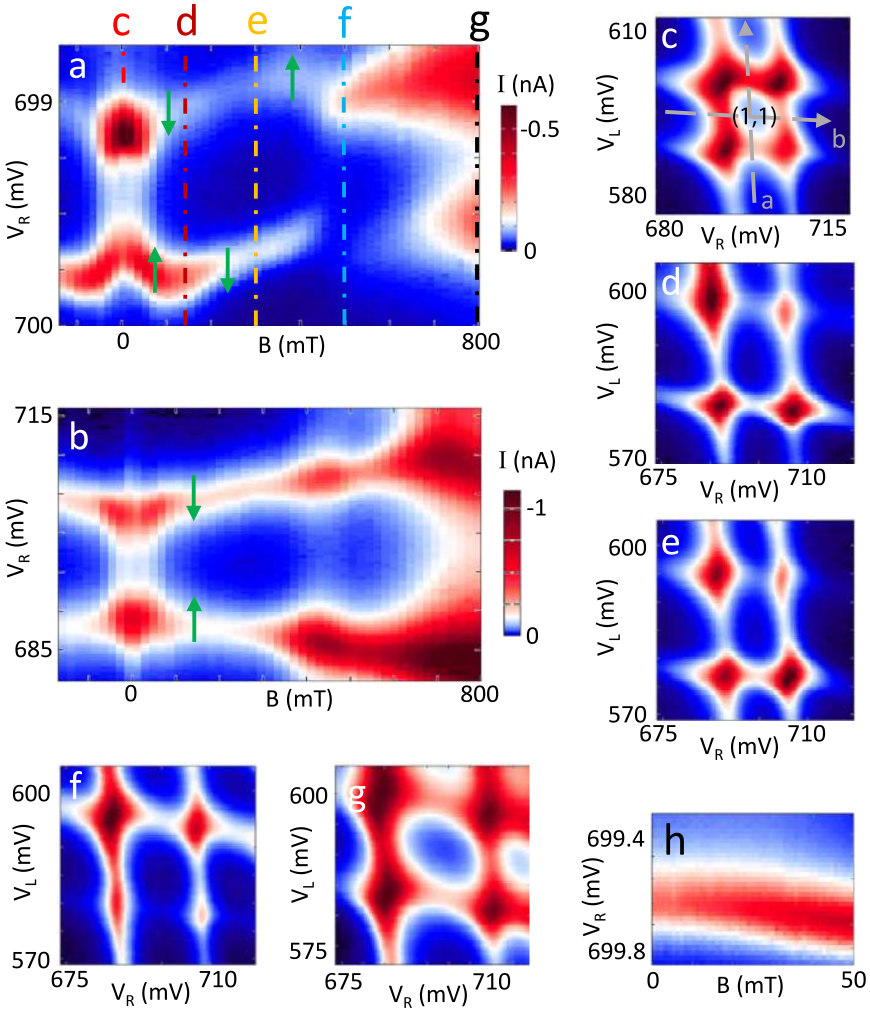

Figure 5.8: Magnetic field evolution of the charge stability diagrams. (**a-b**), The evolution of current along line cuts a and b shown in panel **c**, V_{bias} = -200 μV. **c-g**, Double dot stability diagrams at 0, 140, 300, 500, 800 mT, V_{bias} = -200 μV. We notice that the higher current lines connected the spin blockade points (lower branch of **a** and higher branch of **b**) also have lower current at zero field. It is specially demonstrated with a zoomed-in scan of the lower branch from 0 to 50 mT (**h**). The color bar of **b** is on its right side. The other plots share the color bar on the right side of **a**.

farther away from the degeneracy point, depicted by the yellow diamond, green triangle, blue square and black dot in Fig.5.10a. One can see that the splitting behavior at spots closer to the generate points evolves into very broadened resonance (See Fig.5.10b-e). This shows qualitatively the same features that are observed within the same quadrant of the double

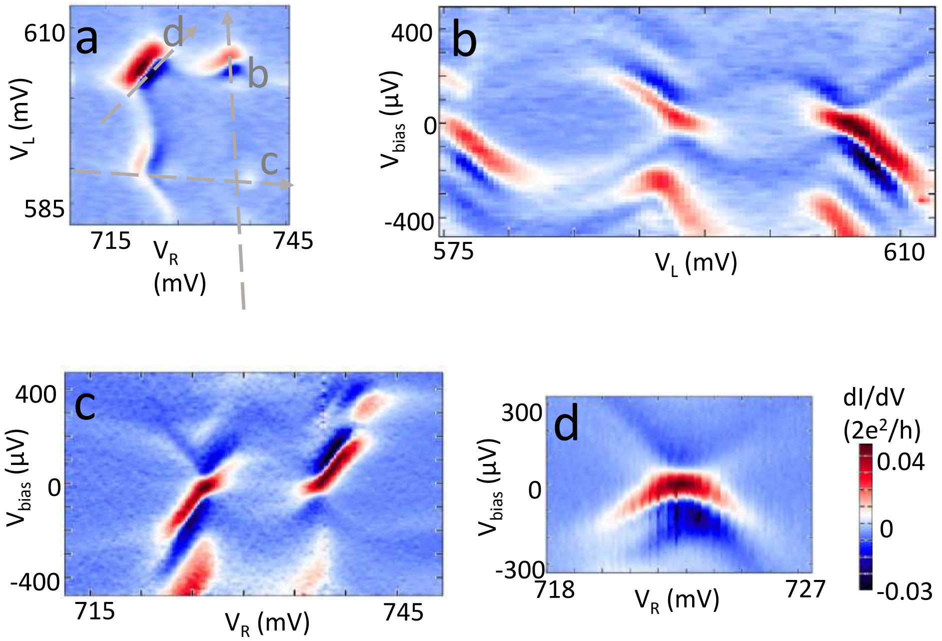

Figure 5.9: Spectroscopy measurements of Andreev molecular resonances along complimentary line cuts. a, Gate vs. gate differential conductance diagrams at the bias of 200 μV. The plot is repeated to illustrate the line cuts used in **b-d**. **b**, With the right dot fixed at its degeneracy point. Here we extend the plot to display adjacent Andreev loops. **c**, With the left dot fixed at its degeneracy point. **d**, Along the symmetric cut through the (1,0)↔(2,1) degeneracy point.

dot stability diagram in Fig.5.7.

Magnetic field behaviors can be also seen in terms of finite field spectroscopy. In Fig.5.11, we plot the spectroscopy of the subgap resonance at 0 and 35 mT. On the left, the bias vs. gate plots along the line cuts depicted in Fig.5.11e are presented. On the right, we plot the associated measurements at a finite field. Clearly for both bias directions, resonances are doubled at finite field in the (even, even) configurations; while in (1,1) a resonance does not split.

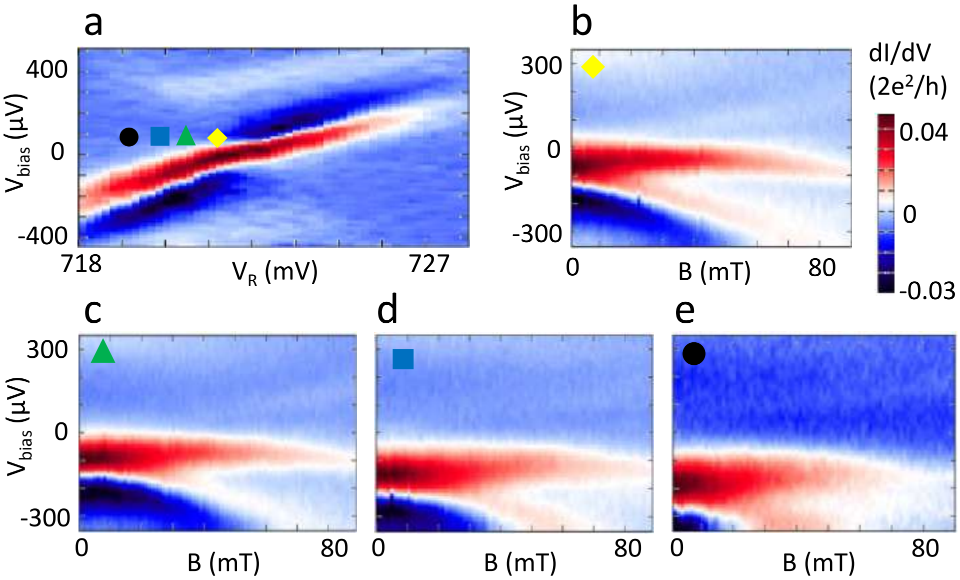

Figure 5.10: Detailed magnetic field data in the (even, odd)/(odd, even) configuration. **a**, The spectroscopy along the detuning cut through the (2,1)↔(1,2) degeneracy point. **b-e**, A series of bias vs. field scans in (2,1) at spots farther and farther away from the degeneracy point, depicted by the yellow diamond, green triangle, blue square and black dot marked in panel **a**.

5.5.2 Strong interdot coupling regime

Remarkably, the theoretical model not only produces the consistent magnetic fields behaviors for the (odd, odd), (even, even), and (odd, even)/(even, odd) configurations individually, it also exhibit inter-configuration pattern which matches the experimental spin structure shown in Fig.5.7. This can be seen by comparing the measured spin map with the full 3x3 simulated spin map plotted in Fig.5.12. First, (0,0) and (2,2) show resonances symmetrically at both biases, while only the negative (positive) branch has high conductance in (2,0) ((0,2)). Then, in (1,0) and (2,1) the kinks occur at the positive bias while in (0,1) and (1,2) the kinks occur at the negative bias. We notice that even with stronger interdot coupling (Fig.5.14), such consistency is still valid.

By increasing interdot coupling, we see stronger hybridization between Andreev bound states in the two dots. For best comparison, we re-tune the device to lower the interdot barrier by adjusting gate V_t from -685 mV to -635 mV, while at the same time all other

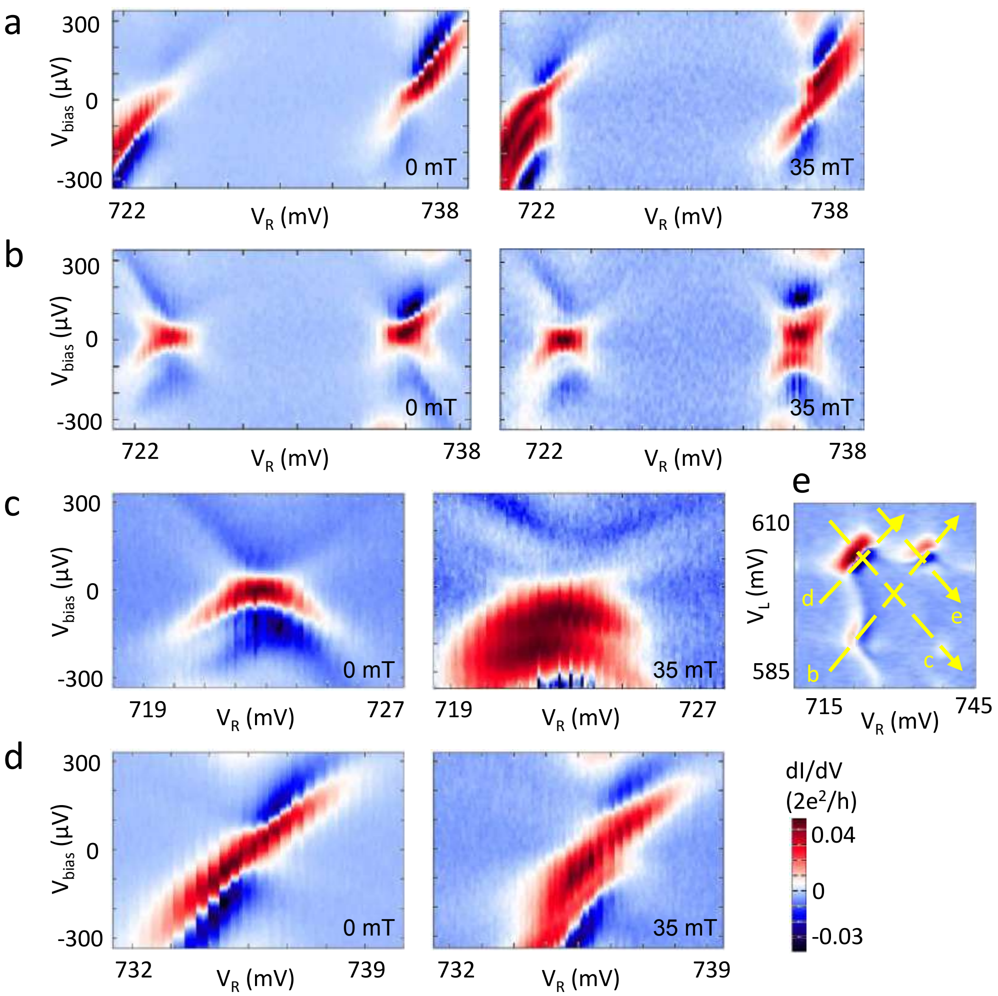

Figure 5.11: Finite field spectroscopy. a-d, The spectroscopy measurements at 0 mT (left) and 35 mT (right) along different cuts depicted by the yellow arrows in **e** which is the same as Fig.5.9**b**. **a-b**, Resonances are doubled at 35 mT in the (0, 0) and (2,2) configurations; while in (1,1) a resonance does not split. **c**, Along the energy shift cut through the (2,0)↔(1,1) degeneracy point. **d**, Along the detuning cuts through (2,1)↔(1,2) degeneracy point.

gates are tuned to keep the same dot occupations. $V_{\Gamma L}$ and $V_{\Gamma R}$ remain almost the same. The measured spectra are qualitatively similar to those in the weaker interdot coupling regime. However, owning to the stronger interdot coupling, a few features which are less clearly resolved in the weaker interdot coupling regime are more pronounced here. First, the resonances away from the degeneracy points are clearly visible. Secondly, we are able to observe the resonances that close to zero bias and within the loop-like resonances clearly.

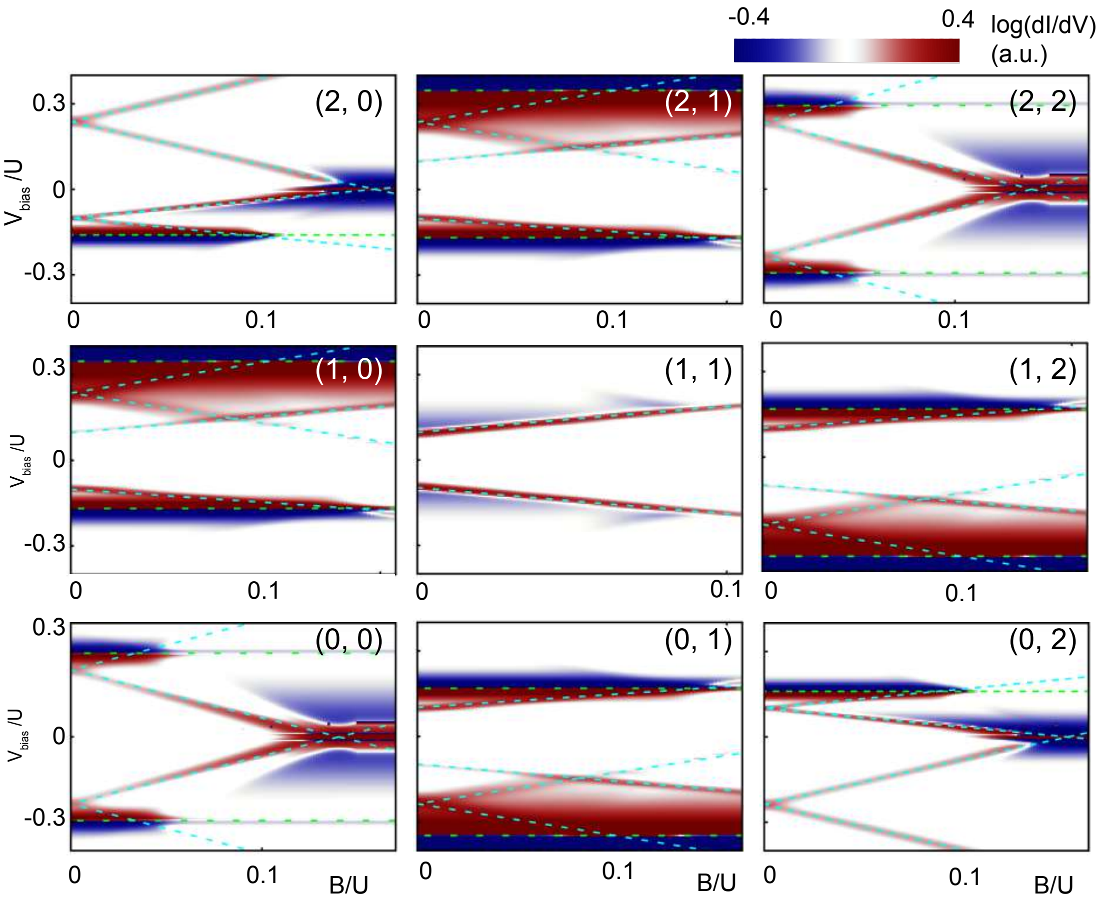

Figure 5.12: Theoretical spin map. Simulated magnetic field dependence of the 3x3 configurations around (1, 1). Besides the good fitting between measurements and simulations in each individual configuration, the experimental (Fig.5.9) and the simulated maps exhibit impressively similar patterns.

These resonances are due to charge degeneracy in the right dot.

Magnetrospectroscopy is performed for the 3x3 double dot configurations around (1,1) in the stronger interdot coupling regime as well. In each configuration a typical example is presented (See Fig.5.14). Although the resonances are more broadened, qualitatively similar magnetic field dependencies are observed: that resonances do not split but move away from zero bias in (1,1), that resonances split in the (even, even) configurations, and that resonances exhibit kinks at positive (negative) bias and broadened structures at negative (positive) bias in (1,0) and (2,1) ((0,1) and (1,2)).

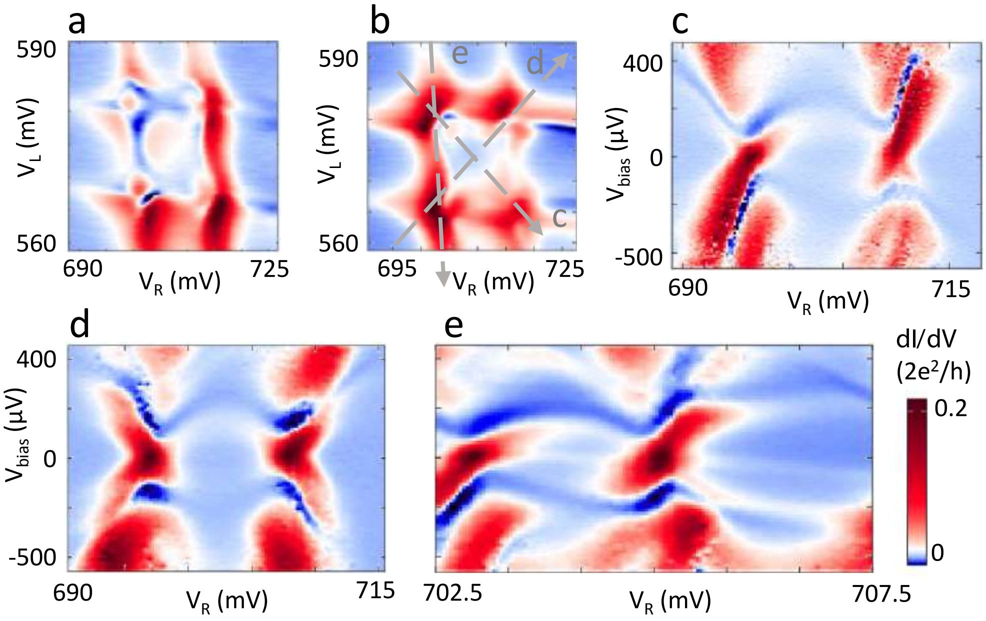

Figure 5.13: Spectroscopy in strong interdot coupling regime. a-b, The gate vs. gate differential conductance diagrams at biases of 200 μV and -200 μV. **c** and **d**, The spectroscopy scans along the detuning and energy shift cuts. **e,** scan the left dot when the right dot is fixed at the degeneracy point. The line cuts of panels **c,d,e** are depicted in **b**.

5.5.3 Strong superconductor-quantum dot coupling regime.

In this strong superconductor-dot coupling regime, the ground state of Andreev bound states in each dot is $|S\rangle$ when the other dot is removed. The ground state of the molecular Andreev bound states also becomes $|S\rangle$ regardless the dot chemical potentials. In Fig. 5.15 we show the spectroscopy of a double dot system with a different device in the strong superconductor-quantum dot coupling regime. The four degeneracy points are broadened due to increased superconducting coupling to the leads (Fig.5.15a). In the bias vs. gate plots where the chemical potential of one dot is scanned when the other is fixed (Fig.5.15**b-c**), the resonances display structures of anti-crossing-like.

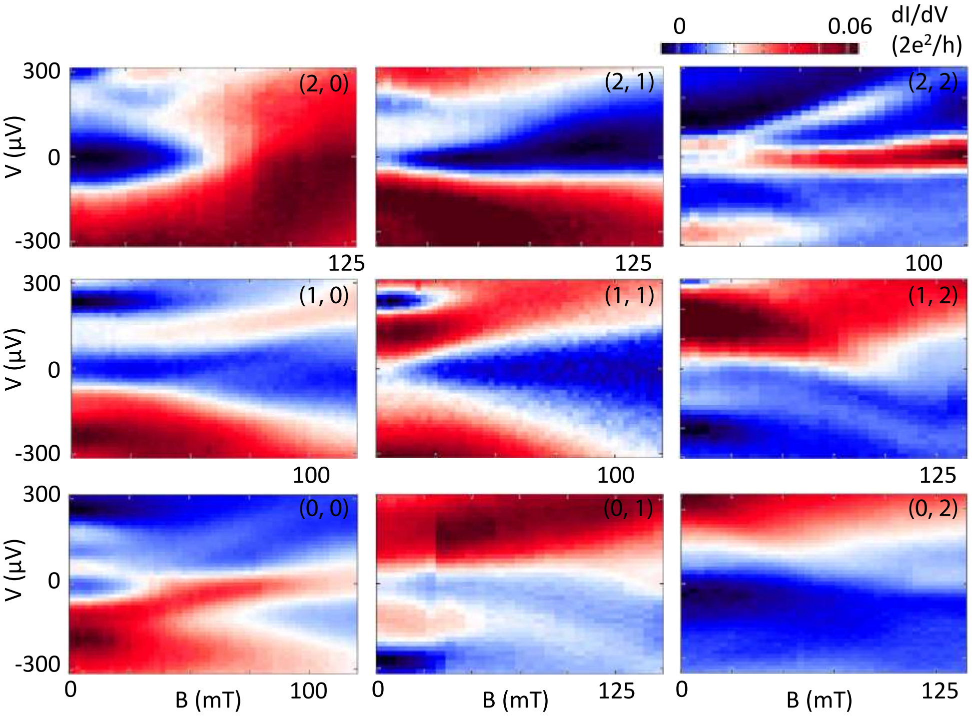

Figure 5.14: Spin map in the stronger interdot coupling regime. The voltage of the barrier gate , V_t is -635 mV.

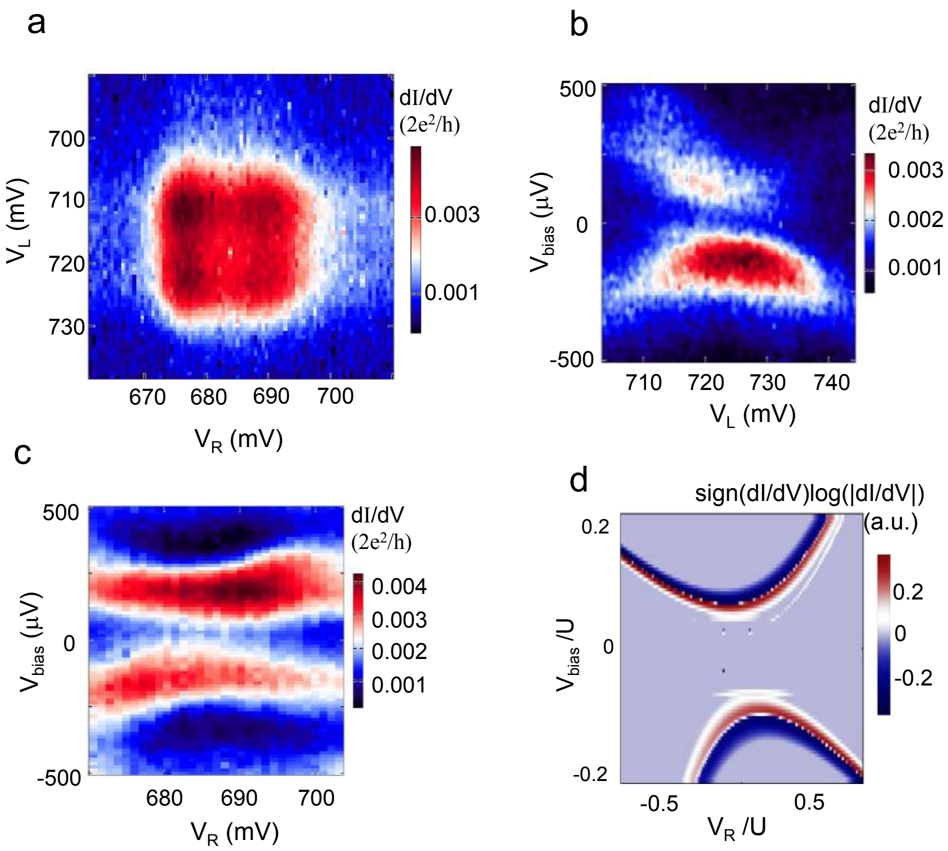

Figure 5.15: Strong superconductor-quantum dot coupling regime. a, dI/dV as a function of V_L and V_R with a fixed bias at -120 μV. **b(c),** the resonances as a function of V_L (V_R) when V_R (V_L) is set to 687 mV (717 mV) respectively. **d,** the simulated plot in the strong coupling regime, when left dot chemical potential is fixed to 0 and right dot chemical potential is swept. The simulation also reproduces the anticrossing observed in experiment.

6.0 ANDREEV BOUND STATES IN INSB TRIPLE QUANTUM DOT CHAINS

In this chapter we implement a triple dot chain. There are three superconductors and each is strongly coupled to a quantum dot. We measure transport resonances through Andreev bound states in the triple dot and explore the magnetic field evolution of the resonances.

6.1 INTRODUCTION

Implementing chains of superconductor-quantum dot structures is important because they are potential platforms for quantum simulation [85, 86, 87] and topological quantum computation. For the latter, a more intensively explored direction to realize the Kitaev model is based on superconductor-nanowire structures [10, 56, 11, 13, 12], where practical challenges lie in nonuniform chemical potential along the nanowires, weak tunability of carrier density in the nanowires covered by the superconductors due to screening effect, and disorder in the semiconductor materials (Topological states break time reversal symmetry thus the superconducting gap, unlike that in s-wave superconductors, is suppressed by disorder [17, 18, 19].). Chains of superconductor-quantum dot structures not only provide an alternative direction for the realization of the Kitaev model [2], but also might avoid these challenges [17, 18, 19].

In addition to circumventing current challenges with the superconductor-nanowire structure, studying the chain structure allows us to explore the Kitaev model deeper, e.g., exploring the effect of Coulomb interactions which are not considered in the Kitaev model.

In the rest of this section, we shall revisit the Kitaev model introduced in Chapter 2, and the Hamiltonian of a chain consisting of superconductors and quantum dots, which would guide us to tune a triple dot chain to the desired topological regime.

The Kitaev model made of N ($N \gg 1$) fermionic sites is given by:

$$H_{\text{Kitaev}} = \sum_{j} \left(-t(c_j^\dagger c_{j+1} + c_{j+1}^\dagger c_j) - \mu(c_j^\dagger c_j - \frac{1}{2}) + (\Delta c_j c_{j+1} + H.C.) \right), \tag{6.1}$$

where j is the number of the site, t is the inter-site hopping amplitude, μ is the chemical potential and $\Delta = |\Delta| e^{i\theta}$ is the superconducting gap [2].

This model is a toy model and it places a few unusual assumptions: (A1) there is no charging energy within each site; (A2) there is only one spin component; (A3) Δ pairs particles of same spin. Two conditions define the topological regime where unpaired Majorana zero modes are present, i.e., (C1) $|\Delta| > 0$ and (C2) $2|t| > |\mu|$ [2].

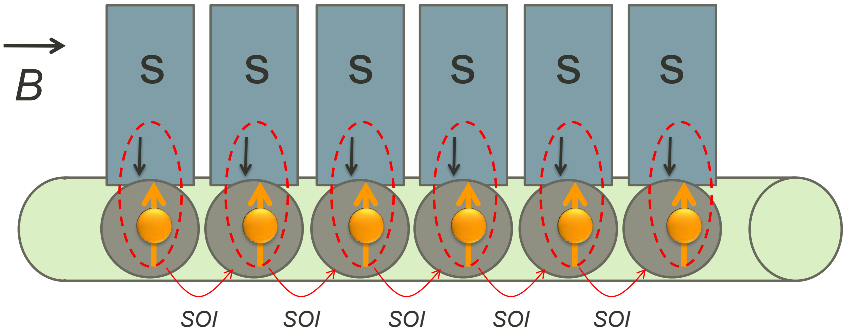

Figure 6.1: Schematic of the realization of the Kitaev chain with quantum dots and superconductors. A building block is a quantum dot strongly coupled to an s-wave superconductor. The chain has a number of building blocks. The quantum dots are defined in a semiconductor nanowire. Each quantum dot has a single electron at its chemical potential. Neighboring quantum dots are tunnel coupled. Spin-orbit interaction (SOI) can make an electron in a dot undergo spin rotation after tunneling to the next dot. Magnetic field parallel to the nanowire axis is applied to polarize the electron spins.

In our implementation, a fermionic site of the Kitaev chain is emulated by a quantum dot coupled to a superconducting reservoir which represents a building block in our scheme (Fig.6.1). The Hamiltonian of a chain having N building blocks consists of several terms:

$$H = \sum_{j=1}^{N} H_{\mathrm{S},j} + \sum_{j=1}^{N} H_{\mathrm{QD},j} + \sum_{j=1}^{N} H_{\text{S-QD},j} + \sum_{j=1}^{N-1} H_{\mathrm{t},j}, \tag{6.2}$$

where $H_{\mathrm{S},j}$ corresponds to the BCS Hamiltonian of the j-th superconducting reservoir, given by (omitting index j)

$$H_{\mathrm{S}} = \sum_{k\sigma} \xi_k d^\dagger_{k,\sigma} d_{k,\sigma v} + \sum_{k} \left(\Delta d^\dagger_{k\uparrow} d^\dagger_{-k\downarrow} + \mathrm{H.C.} \right), \tag{6.3}$$

where $d^\dagger_\sigma$ creates an electron (quasiparticle) with spin σ and momentum k on the level of ξ_k in the superconducting reservoir and Δ is the superconducting order parameter. Importantly, Δ pairs electrons of opposite spins.

$H_{\text{QD},j}$ corresponds to the j-th single uncoupled quantum dot, given by (omitting index j)

$$H_{\text{QD}} = \sum_{\sigma=\{\uparrow,\downarrow\}} \epsilon_\sigma c_\sigma^\dagger c_\sigma + U n_\uparrow n_\downarrow, \tag{6.4}$$

where $c_\sigma^\dagger$ creates an electron with spin σ on the level of ϵ_σ in the quantum dot. Here we include Zeeman energy, i.e., $\epsilon_\uparrow = \epsilon - 1/2 g\mu_B B$ and $\epsilon_\downarrow = \epsilon + 1/2 g\mu_B B$, where g is g-factor, μ_B is Bohr mageton and B is magnetic field. When $B > 0$, level $\epsilon_\uparrow$ has a lower energy and is filled before level $\epsilon_\downarrow$. At last U is the Coulomb interaction between two electrons of opposite spins in the dot;

$H_{\text{S-QD},j}$ corresponds to the coupling between the j-th superconducting reservoir and the j-th quantum dot, given by (omitting index j)

$$H_{\text{S-QD}} = \sum_{k\sigma} \left(V_k d_{k\sigma}^\dagger c_\sigma + \text{H.C.} \right), \tag{6.5}$$

where V_k expresses the superconductor-dot hopping;

$H_{\text{t},j}$ expresses the interdot coupling between the j-th and (j+1)-th quantum dots, given by

$$H_{\text{t},j} = t_j e^{i\boldsymbol{\lambda_i}\boldsymbol{\sigma}} \sum_{\sigma=\{\uparrow,\downarrow\}} d_{j,\sigma}^\dagger d_{j+1,\sigma} + \text{H.C.}, \tag{6.6}$$

where t_j is the interdot hopping amplitude between the j-th and (j+1)-th quantum dots, vector $\boldsymbol{\sigma}$ is the Pauli matrices, and vector $\boldsymbol{\lambda_j}$ characterizes the spin rotation acquired during a hopping between the j-th and (j+1)-th quantum dots due to spin-orbit coupling [18].

Now, let's specifically examine how the three assumptions of the Kitaev model and the two topological conditions can be realized in a superconductor-dot chain. (A1) To reach low charging energy (U) in the dot, the superconductor is strongly coupled to the dot within each building block. (A2) To realize the spinless assumption, an odd number of levels below the Fermi level per dot can be tuned, and a magnetic field is applied to break time-reversal symmetry such that the single electrons in the dots have the same spin polarization. (A3) The superconducting pairing of electrons of same spin can be fulfilled by spin-orbit coupling and induced s-wave superconductivity. Within each building block, the s-wave superconductivity is induced from the superconductor that is strongly coupled to it. Neighboring quantum dots are coupled by tunnel coupling (t), and electrons undergo rotation in spin polarization during hopping from one dot to the other in the presence of spin-orbit coupling. This hopping with spin-orbit coupling leads to some component of spin polarizations in opposite directions, which enables the induced s-wave superconductivity to pair the electrons. This also fulfills the first topological condition: (C1) $|\Delta| > 0$. The second condition, (C2) $2|t| > |\mu|$, can be realized by tuning the dot level close to the Fermi level. Given all assumptions and conditions fulfilled, unpaired Majorana zero modes are expected to appear at the two ends of the chain. In practice, a chain has a finite length thus the two Majorana zero modes at the two ends are coupled. Note that in the Kitaev model, all fermionic sites are coupled to a single superconductor that has a single phase, while in the herein chain discussed, the N superconductors do not necessarily have the same phase. Controlling the phase differences can be performed by applying magnetic field fluxes through superconducting circuits made of these N superconducting leads and is not implemented in this thesis.

6.2 THE TRIPLE DOT DEVICE

In this chapter, we explore a chain made of three dots. The three dots can be created along a nanowire. Two gate tunable barriers located between neighboring dots can be used to control the interdot coupling (t_{LM}, t_{RM}) (Fig.6.2a). Besides, it is necessary to be able to control the dot chemical potentials (μ_L, μ_M, μ_R) and superconductor-quantum dot couplings ($\Gamma_L, \Gamma_M, \Gamma_R$).

This complex quantum device is challenging to implement, because there are at least 8 parameters that must be independently controlled (t's, Γ_S's and μ's). In addition, unlike the double dot where the two superconducting contacts can be made on the two ends of a nanowire, here there are three superconducting terminals involved. To accomplish all of the ingredients based on an InSb nanowire, we design the following geometry (Fig.6.2b): on top of bottomgates that are almost perpendicular to the nanowire, we fabricate three highly transparent NbTiN contacts to the nanowire. Two leads connecting the nanowire from the two ends are labeled superconducting reservoirs L and R. Closely next to reservoir-L, three

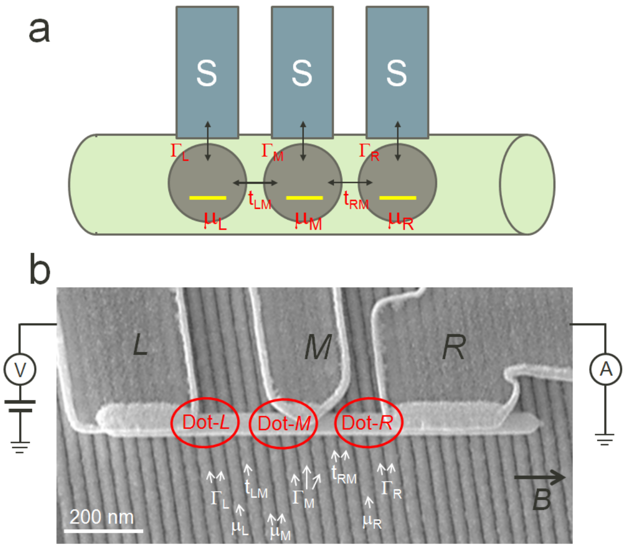

Figure 6.2: Schematic of triple dot chain and device SEM. a, Schematic of triple dot chain based on a nanowire and three superconductors connected from one side. The chemical potential (μ) in each dot is gate tunable. The coupling between each quantum dot and a superconductor above it, Γ_S should be also tunable. t's control the tunnel couplings between neighboring dots. **b,** Device SEM image. The InSb nanowire device is fabricated on top of bottomgates with a dielectric layer in between. Three NbTiN superconductors (L, M and R) are fabricated to make contacts to the nanowire. In a measurement, two of the three contacts are connected into the measurement circuit while the rest is floating. The contact in the middle is carefully fabricated to ensure a contact area of as small as possible. Three quantum dots, depicted by the red circles, can be defined with bottomgates. Note some parameters are tuned with more than a gate in practice. Magnetic fields parallel to the nanowire axis can be applied in the experiment.

gates denoted with Γ_L, μ_L and t_{LM} are used to define dot-L whose chemical potential is tuned by gate μ_L and coupling to reservoir-L is controlled by gate Γ_L. The same for the right end of the nanowire where dot-R is defined.

So far dot-L and dot-R can be made in the typical manner that is used in a double dot chain, which, however, is not suitable to create the third dot in the nanowire. In order to incorporate the third contact, we make a tip-shape superconducting reservoir (M) that is in the middle and is closer to the right lead than to the left lead. It covers the nanowire in a very small area (half-covered or less). The middle dot (dot-M) can be defined on the left side of contact-M by gate Γ_M and gate t_{RM}. Two tunnel barriers gates t_{LM} and t_{RM} are used to tune the interdot couplings between dot-L and dot-M, and between dot-M and dot-R, respectively. Note that we make the contact area of the middle reservoir as small as possible to ensure direct interdot tunnel coupling between dot-M and dot-R, instead of through the middle contact (A wide middle contact can suppress the electronic wavefunction overlap between dot-M and dot-R.). Experimentally, we confirm that superconductivity is induced in dot-M in spite of the small contact area ($\sim 0.002\ \mu\text{m}^2$) by observing Andreev Bound states in dot-M. Importantly, this design allows implementing long chains by fabricating a number of such middle contacts. At last, these three superconducting reservoirs are also used as source and drain for electrical transport studies, i.e., each time two of them are connected to the measurement circuit while the third one is kept floating.

6.3 TUNING UP THE TRIPLE DOT CHAIN

In this device, we create Andreev bound states in a triple dot where each dot is strongly coupled a superconducting reservoir and the three dots in series are coupled via tunnel couplings. This is done in three levels: (1) generating Andreev bound states in individual dots; (2) hybridizing Andreev bound states pairwise in neighboring dots; (3) tuning the entire chain. By the end of the tuning, we aim to adjust the superconductor-quantum dot couplings ($\Gamma_L, \Gamma_M, \Gamma_R$) and interdot couplings (t_{LM}, t_{RM}) to the desired parameter regime defined by the assumptions (A1-A3) and topological conditions (C1, C2). The exploration of the remaining assumptions and conditions, i.e., dot chemical potential (μ_L, μ_M, μ_R) and magnetic field, is presented in the next sections.

Specifically, we create dot-R by first connecting reservoirs M and R to the measurement circuit and keeping reservoir-L floating. Tuning Andreev bound states in a single dot is analogous to the procedure discussed in Chapter 4. More specifically, we employ three gates, V_{TR}, V_R and V_{MR}, to form a well-defined single quantum dot, which is confirmed by the observation of Coulomb diamonds. We then gradually increase the superconductor-dot coupling (Γ_S), which yields loop-like subgap resonances through Andreev bound states in bias vs. V_R scans. Finally, we increase Γ_S until the loop-like resonances evolve into anti-crossing-like, which signals the $|D\rangle/|S\rangle$ phase transition of Andreev bound states. Note that

$t_{MR} \ll \Gamma_R$ and dot-R is strongly coupled to reservoir-R only.

Then we connect reservoirs M and L into the measurement circuit, and keep reservoir-R floating. We create Andreev bound states in single dot-M that is strongly coupled to reservoir-M, by applying a similar procedure as used for defining dot-R.

At this point, Andreev bound states in dot-R and dot-M are created. We then connect reservoirs L and R into the measurement circuit and measure the resonance through hybridized Andreev bound states in dot-M and dot-R. As expected, fine tuning is necessary because the change of configuration by cross coupling between gates of different dots needs to compensate. An analogous procedure has been used in Chapter 5, in the context of double dots.

Next, we connect reservoirs L and M into the measurement circuit, and keep reservoir R floating. We open dot-M, define dot-L and tune Andreev bound states in dot-L using again a similar methodology as employed for dot-R and dot-M. We subsequently form dot-M again and hybridize Andreev bound states in dot-L and dot-R, as previously done for the pair, dot-R and dot-M.

As a last step, we connect reservoirs L and R to the measurement circuit, keep reservoir-M floating, and fine tune the gates for the entire chain. Finally, we obtain three dots in series, where each dot is strongly coupled to a superconductor. The chain will be explored with these five parameters, Γ_L, Γ_M, Γ_R, t_{LM} and t_{RM}, fixed in the following sections.

6.4 TRANSPORT THROUGH TRIPLE DOT ANDREEV BOUND STATES

We explore the Andreev bound states in the triple dot in terms of transport resonances by applying a voltage bias across the triple dot and measuring the differential conductance, dI/dV. We thus first discuss the condition of resonance in the triple dot chain. Because in this triple dot, each dot is tuned to a regime where $\Gamma \gg t$ such that the neighboring dots are weakly coupled, one can naively model the transport through Andreev bound states in the chain as transport through Andreev bound states in three uncoupled dots. As studied in single quantum dots (Chapter 4), in each dot of the triple dot, there are two subgap

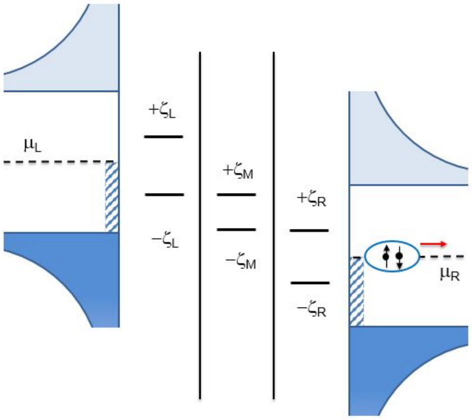

Figure 6.3: Transport cycle through Andreev bound states in a triple dot. a, Schematic of resonance condition in a triple dot in the weak interdot coupling limit: $-\zeta_L$ level is aligned with $+\zeta_M$ level, $-\zeta_M$ level is aligned with $+\zeta_R$ level, and $eV_{\text{bias}} = \zeta_L + 2\zeta_M + \zeta_R$. Reservoir-$L$ and reservoir-R are source and drain, respectively. Reservoir-M is floating. Note that the middle dot also has two resonance levels associated to Andreev bound states because it is coupled to superconducting reservoir-M (floating, not drawn). The blue dashed bars within the gaps are used to approximate subgap density of states.

resonance levels, $\pm\zeta$, associated with Andreev bound states. We can then build the following transport cycle based on these single dot Andreev bound states in a weak interdot coupling regime. Fig.6.3a illustrates the diagram at resonance, i.e., $-\zeta_L$ level is aligned with $+\zeta_M$ level, $-\zeta_M$ level is aligned with $+\zeta_R$ level, and $|eV_{\text{bias}}| = \zeta_L + 2\zeta_M + \zeta_R$. Specifically, the complete cycle to transfer two quasiparticles from reservoir-L to reservoir-R is accomplished in two steps: first transferring two subgap quasiparticles from reservoir-L and form a Cooper pair in reservoir-M, then transferring two subgap quasiparticles from reservoir-M and from a Cooper pair in reservoir-R. The individual steps have the same transport cycle through double dot Andreev bound states discussed in Chapter 5. What is new here is that reservoir-M is floating and its voltage is determined by the resonance condition, i.e., $e(\mu_L - \mu_M) = \zeta_L + \zeta_M$, and $e(\mu_M - \mu_R) = \zeta_M + \zeta_R$. In reservoir-$M$, Cooper pairs can be converted into subgap quasiparticles at its chemical potential without extra energy cost or relaxation. As a result, the energy costs in the first and second steps are $\zeta_L + \zeta_M$, and $\zeta_M + \zeta_R$, receptively, which is compensated by the bias, $|eV_{\text{bias}}|$. Although this naive transport cycle picture does not include hybridization of Andreev bound states in the triple dot, it explains many features in our transport measurements.

Before we discuss the transport plots, we define a notation which would clarify the discussions. As previously discussed in Chapter 4, in the strong Γ_S regime, the minimum distance between the two anticrossing resonance branches appears at the center position of an odd dot occupation. This occupation is defined by two charge degeneracies, i.e, 2n↔2n+1 and 2n+1↔2n+2, where they are numbers of electrons in the dot. If we adapt as a convention that the 2n↔(2n+1) degeneracy corresponds to $\varepsilon = 0$, the minimum distance between the anticrossing branches occurs at $\varepsilon = -U/2$, while the (2n+1)↔(2n+2) degeneracy is at $\varepsilon = -U$, where U is the charging energy of this dot (See a schematic diagram in Fig.6.9). In this way, we can use notation $(\varepsilon_L, \varepsilon_M, \varepsilon_R)$ to denote the triple dot configuration. For example, $(\varepsilon_L = -U_L/2, \varepsilon_M = -U_M/2, \varepsilon_R = -U_R/2)$ corresponds to a triple dot configuration where ζ_L, ζ_M and ζ_R are minimum. Note that in each dot ε is equal to μ with an offset and is also tuned by the plunger gate of the doe, i.e., V_L controls ε_L, V_M controls ε_M, and V_R controls ε_R.

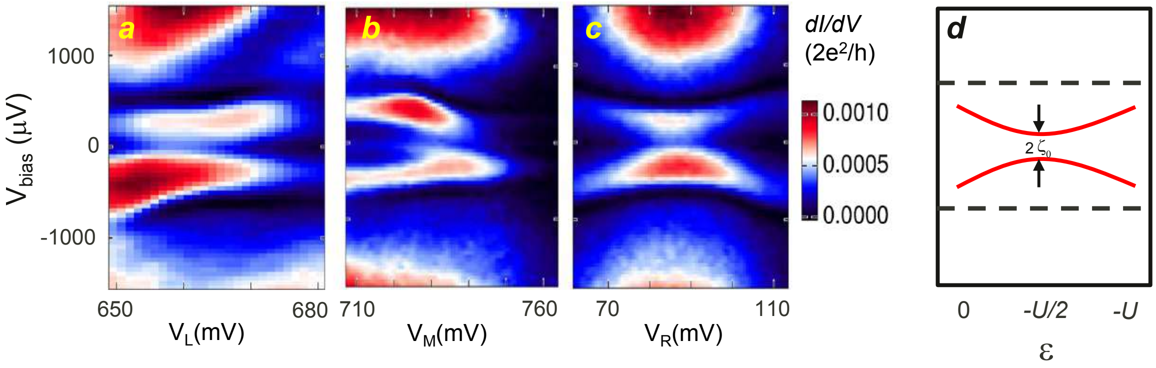

Figure 6.4: Bias spectroscopy of triple dot Andreev bound states as a function of individual chemical potentials. a, Resonances are measured in dI/dV as a function of bias and V_L with $\varepsilon_M = -U_M/2$ and $\varepsilon_R = -U_R/2$. **b,** Resonances are measured in dI/dV as a function of bias and V_M with $\varepsilon_L = -U_L/2$ and $\varepsilon_R = -U_R/2$. **c,** Resonances are measured in dI/dV as a function of bias and V_R with $\varepsilon_L = -U_L/2$ and $\varepsilon_M = -U_M/2$. **d,** Depiction of the resonances in **a-c** as a function of bias and ε. The minimum distance between the two anticrossing branches is at $\varepsilon = -U/2$. Two bias asymmetric anti-crossing branches are presented inside some bias values depicted by the dashed lines.

The following measurements demonstrate the same resonances through the Andreev bound states in the triple dot along different parameter cuts. First, we measure dI/dV as a function of bias and V_L, given $\varepsilon_M = -U_M/2$ and $\varepsilon_R = -U_R/2$ in Fig.6.4a. Anti-crossing-like resonances are observed within $\pm \sim 800$ μV, which appears to be analogous to the resonances through single dot Andreev bound state in the open dot regime in Chapter 4. The minimum distance between the anti-crossing branches (~ 200 μV) is measured at $V_L \approx 675$ mV, which corresponds to $\varepsilon_L = -U_L/2$. Shifting to left or right of 675 mV, the resonance at positive (negative) bias increases (decreases) in bias. Similarly, anticrossing-like structures are observed in the bias vs. V_M scan taken with $\varepsilon_L = -U_L/2$ and $\varepsilon_R = -U_R/2$, and the bias vs. V_R scan measured with $\varepsilon_L = -U_L/2$ and $\varepsilon_M = -U_M/2$, as shown in Fig.6.4b and Fig.6.4c, respectively. In Fig.6.4d we depict a scheme of the anti-crossing of the resonances, analogous to Fig.6.4a-c, where ζ_0 corresponds to the minimum distance between the anticrossing branches expected at ($\varepsilon_L = -U_L/2$, $\varepsilon_M = -U_M/2$, $\varepsilon_R = -U_R/2$).

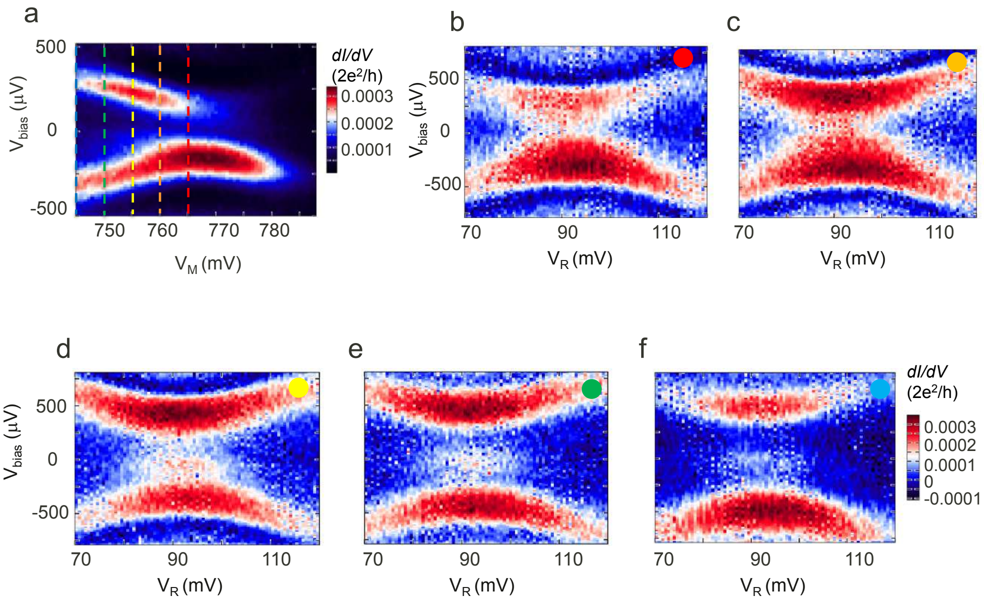

Figure 6.5: Bias vs. V_R scans with various V_M. a, Bias vs. V_M scan with $\varepsilon_L = -U_L/2$ and $\varepsilon_R = -U_R/2$. The dashed lines of various colors denote the V_M values chosen for scans **b-f**. **b-f,** Resonance as a function of bias and V_R with V_M denoted in **a**.

We take a panel from Fig.6.4 and vary the gate of a different dot to investigate its effect on bias spectroscopy. In Fig.6.5b-f, we repeat the bias vs. V_R scan with V_M fixed at various values, as indicated by the dashed lines in Fig.6.5a, and $\varepsilon_L = -U_L/2$. First, Fig.6.5b displays the bias vs. V_R scan, with $\varepsilon_L = -U_L/2$ and $\varepsilon_M = -U_M/2$. We then move V_M away from $\varepsilon_M = -U_M/2$ to a value denoted by the orange dashed line in Fig.6.5a, which yields Fig.6.5c whose minimum distance between the two anticrossing branches grows. As V_M is further decreased and ε_M is increased, the two anticrossing branches move further and further apart(Fig.6.5d,e,f). Eventually, the minimum distance between the two branches is as large as 600 μV and the resonances appear at bias up to ±800 μV (measured from the centers of the broadened resonances). Similar effect is observed when monitoring other pairwise combinations, e.g., monitoring bias vs. V_L scans when V_M is varied. This effect can be explained by the resonance condition ($|eV_{\text{bias}}| = \zeta_L + 2\zeta_M + \zeta_R$), i.e., increasing ζ in any dot yields resonances at higher biases.

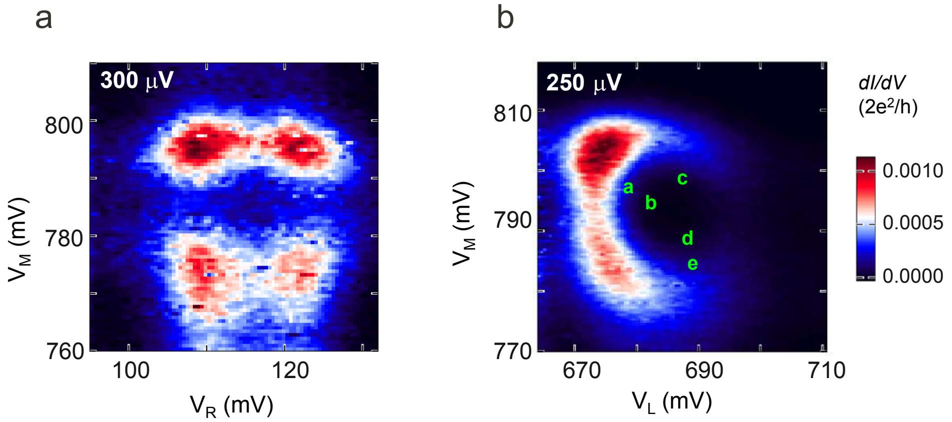

Figure 6.6: Resonances through triple dot Andreev bound states at fixed biases. a, dI/dV as a function of V_M and V_R at a fixed bias of 300 μV, given $\varepsilon_L = -U_L/2$. **b,** dI/dV as a function of V_L and V_M at a fixed bias of 250 μV, given $\varepsilon_R = -U_R/2$. Letters, a-e, mark the gate settings of panels a-e in Fig.6.8.

Finally we measure the resonances as a function of chemical potentials at fixed biases. First, we measure dI/dV as a function of V_M and V_R, with $V_{\text{bias}} = 300$ μV and $\varepsilon_L = -U_L/2$. We observe four strong conductance areas at four corners (Fig.6.6a). The structure is associated with the fixed-bias cuts in the bias vs. gate scans in Fig.6.4b-c. Similar structure is observed in the V_L vs. V_M scan, given $V_{\text{bias}} = 250$ μV and $\varepsilon_R = -U_R/2$ (Fig.6.6b). Notice that the strength of right half of the structure in Fig.6.6b is lower but not zero. Compared to the counterparts of Andreev bound states in double dots (See Fig.5.4 where Andreev bound states have doublet ground states in individual dots), a significant differences is found, i.e., looking from the center of the structures, the arcs connecting the four maximum dI/dV corners are concave here, while the arcs are convex in Fig.5.4. The concave structure here is consistent with the fact that bias resonances are anti-crossing-like. Take Fig.6.6b as an example, when ε_M is close to $-U_M/2$, ζ_M is small, in order to see the resonance at the fixed bias, ζ_L should be large according to the relation, $|eV_{\text{bias}}| = \zeta_L + 2\zeta_M + \zeta_R$, meaning V_L has to be far apart from the gate position that is associated with $\varepsilon_L = -U_L/2$. When ε_M is far apart from $-U_M/2$, ζ_M is large, in order to see the resonance at the fixed bias, ζ_L should be small, meaning V_L has to be close to the gate position that is associated with $\varepsilon_L = -U_L/2$. As a result, the fixed bias resonance is anticipated to exhibit a concave structure. The convex structure in Fig.5.4 can be explained in a similar manner, except that driving ε away from $-U/2$ decreases ζ because the resonances there are loop-like.

The relation of resonance in weak interdot coupling limit, $|eV_{\text{bias}}| = \zeta_L + 2\zeta_M + \zeta_R$, explains a number of transport features in Fig.6.4, Fig.6.5 and Fig.6.6. Taking hybridization of Andreev bound states in individual dots due to interdot couplings into account makes the triple dot spectroscopy complex. Theoretical simulation of the triple dot can be, in principle, accomplished based on the theoretical approach introduced in Chapter 2. In practice, the computation required to simulate coherent transport through such superconductor-quantum dot chains grows exponentially as the number of dot numbers, thus simulation of triple dot chains is not implemented in this thesis (Simulated spectroscopies of a double dot chain are presented in Supplementary Figure 6.10).

At last, the transport measurements in this section not only demonstrate the spectrsocpoy of the triple dot Andreev bound states, but also provide an experimental method to tune the quantum levels in the dots to the regime favored by the Kitaev model. By monitoring the resonances as a function of V_L, V_M and V_R, we can effectively determine the triple dot configuration. For instance, minimizing the minimum distance between the two anticrossing branches adjusts the triple dot configuration to ($\varepsilon_L = -U_L/2$, $\varepsilon_M = -U_M/2$, $\varepsilon_R = -U_R/2$). This is necessary because eventually we want to realize that an odd level is tuned close to the superconductor chemical potential in every dot.

6.5 MAGNETIC FIELD EVOLUTION OF TRIPLE DOT ANDREEV BOUND STATES

In this section, we explore the magnetic field evolution of the resonances through Andreev bound states in the triple dot. The magnetic field that we applied is parallel to the nanowire axis. Among measurements at various chemical potential settings, two distinct types of magnetic field behaviors are observed. The first type is shown in Fig.6.7a. At low magnetic field (< 0.25 T), the resonance at either positive or negative bias splits as magnetic field linearly into two branches with slopes of ± 0.5 mV/T. A short zero bias peak forms at the crossing of split branches at ~ 0.25 T.

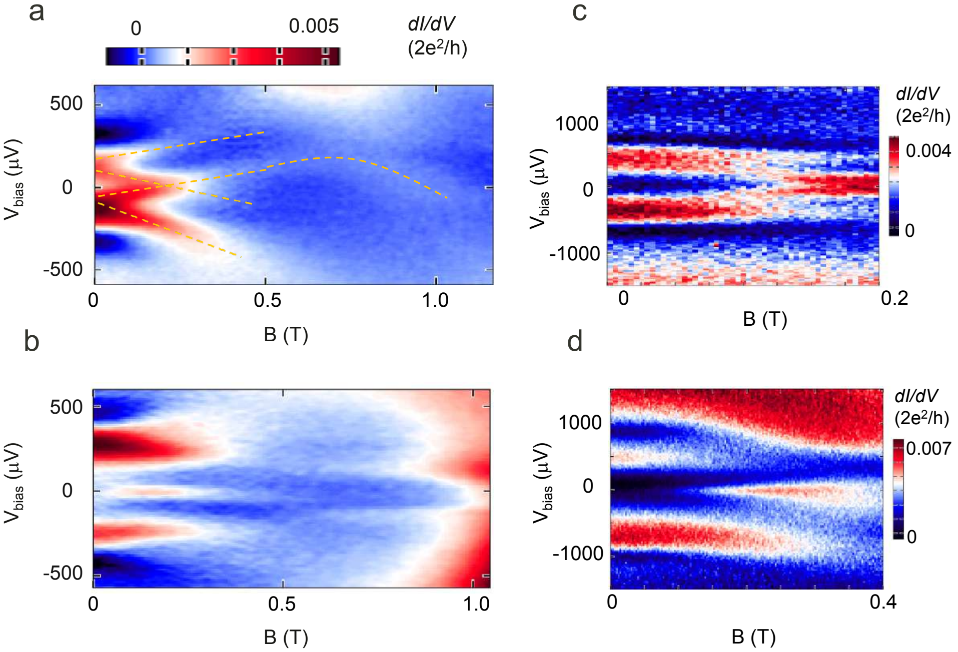

Figure 6.7: Magnetic field evolutions of the resonances through triple dot Andreev bound states. a, Bias vs. field plot at $V_L = 680$ mV, $V_M = 798$ mV, and $V_R = 88$ mV. **b,** Bias vs. field plot at $V_L = 688$, $V_M = 784$ and $V_R = 88$ mV. **c,** Bias vs. field plot at $V_L = 673$, $V_M = 716$ and $V_R = 112$ mV. **d,** Bias vs. field plot at $V_L = 653$, $V_M = 706$ and $V_R = 88$ mV. Note that panels **c-d** are taken after the triple dot is removed and re-created, while all other panels in the main text are taken before the re-creation. The gate settings in **c** and **d** correspond to ($\varepsilon_L > -U_L/2$, $\varepsilon_M > -U_M/2$, $\varepsilon_R > -U_R/2$), and ($\varepsilon_L > -U_L/2$, $\varepsilon_M > -U_M/2$, $\varepsilon_R < -U_R/2$).

The second type of behavior, shown in Fig.6.7b, is dramatically different from the first type. At zero bias, we still observe two bias symmetric resonances at ± 250 μV. As magnetic field is increased, no clear splitting is observed. On the other hand, a zero bias peak emerges at about 60 mT and sustains for more than 0.5 T within visibility. Remarkably, although the strength of the zero bias feature is only 0.002 $(2e^2/h)$, the sharp peak keeps a width of only 50 μV for the entire range of 0.5 T. At last, the zero bias peak does not originate from merging of split branches, which is a stark difference from Fig.6.7a where the zero bias peak is simply a crossing of two split branches. More examples of the two types of magnetic fields behaviors are presented in Fig.6.7c-d focusing on lower field ranges.

More measurements of the field dependence with gradual variations in the dot chemical potentials demonstrate that the two distinct types of magnetic field behaviors evolve from one to the other continuously. In Fig.6.8, we plot the bias vs. field dependence of the resonances at five gate settings depicted in Fig.6.6b. Fig.6.8a (e) plots the same measurement as in Fig.6.7a (b), except that the differential conductance is column normalized here, meaning in each column, pixels have values normalized by the maximum dI/dV value of this column. While in such plots we lose the relative strength of the resonances, the continuous evolution of the two types of magnetic field dependence can be visualized better (The original plots associated with Fig.6.8b-d are in Supplementary Figure 6.11.). The normalized plots, Fig.6.8a and e display the extreme of the two distinct behaviors discussed above, i.e., splitting behavior and emerging of the zero bias peak, respectively. The remaining plots, Fig.6.8b-d, show the gradual crossover between these two behaviors. At finite bias, the splitting behavior starting at zero field becomes less and less pronounced (See Fig.6.8c-d), and finally completely disappear in Fig.6.8e. Specifically, at positive (negative) bias, the branch that moves up (down) remains but with a decreasing slope. More significantly, the branch that moves down (up) grows weaker (Fig.6.8d) and disappears eventually in Fig.6.8e. As a result, the connection between the split branches and the resonances near zero bias also decreases. In other words, the evolution ends up with a zero bias peak that does not evolve from a crossing of the branches and it sticks to zero bias separately from all finite-bias resonances.

Similar splitting magnetic field behavior shown in Fig.6.7a,c has been observed in single quantum dots (Chapter 4) and in double quantum dots (Chapter 5). In both cases, Andreev bound states are associated with $|S\rangle$ ground states and $|D\rangle$ first excited states, and the zero

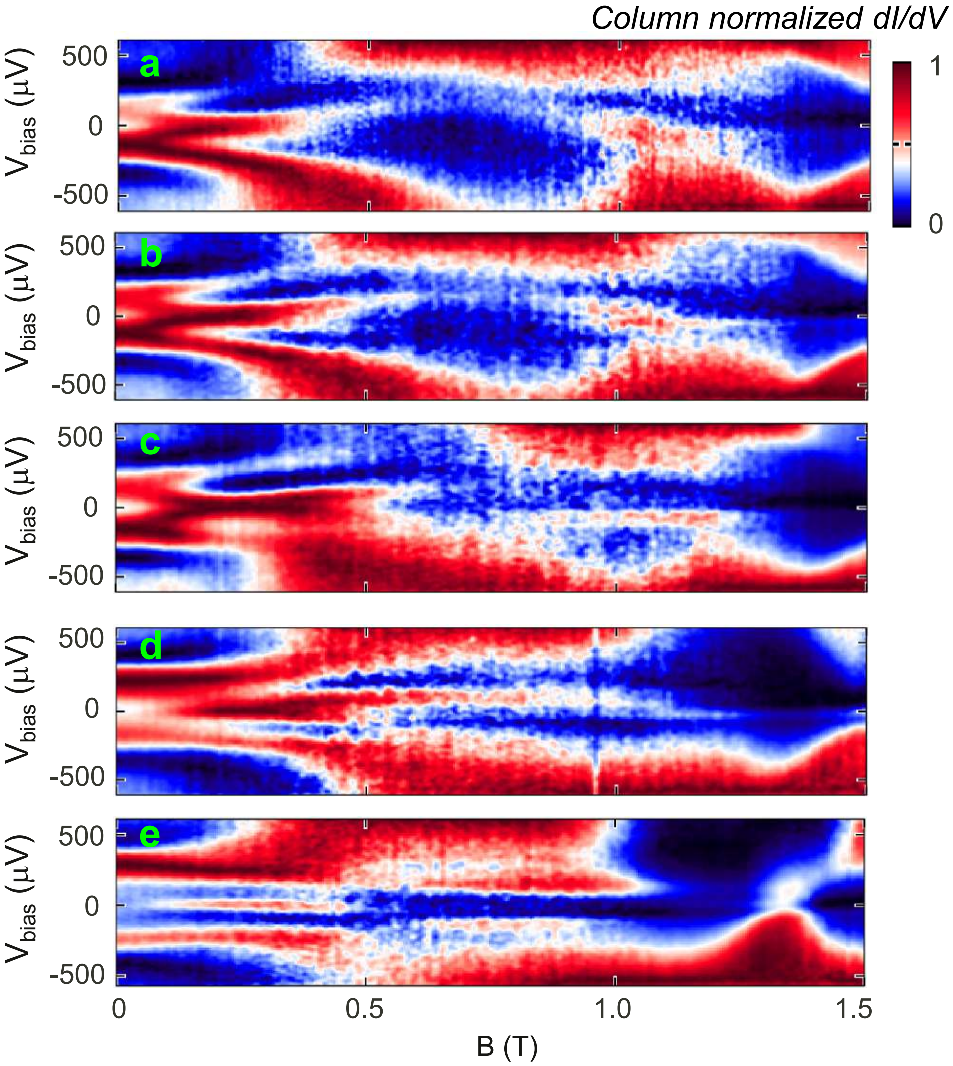

Figure 6.8: Gradual evolution from splitting to zero bias peak. a-e, The magnetic field dependence of the resonances through triple dot Andreev bound states at various triple dot gate settings denoted in Fig.6.6b.

bias crossings simply originate from the degeneracies of distinct spin states, i.e., $|S\rangle$ and $|D\rangle$, at some finite field. Here in the triple dot case, the splitting behavior might have the similar origin, although we have no sufficient evidence to conclude that it is associated with Andreev bound states in part of or the entire triple dot.

The zero bias peak behavior shown in Fig.6.7b,d, however, is hard to understand in terms of Andreev bound states. Here we first discussion a few trivial cases where zero bias peaks can be observed, and then the possibility that the zero bias peak is associated with Majorana zero modes.

Although the gradual crossover shown in Fig.6.8 suggests a strong connection between the zero bias peak and Andreev bound states, the fact that the zero bias peak does not split as a function of field cannot be explained in terms of Andreev bound states alone. Because resonances through Andreev bound states are associated with transitions between states of different spins. If the zero energy mode is associated with degeneracy of Andreev bound states, naively it is expected to split as as a function magnetic field dramatically. For example, if the zero bias resonance is associated with a transition between two states whose spins differ by 1/2, the resonance would move by 1.45 mV in bias after the magnetic field is increased by 0.5 T, given a common g-factor of 50 in InSb nanowires. In stark contrast, here the width of the observed zero bias peak remains at approximately 50 μV irrespective of the large field range. We are aware that, in practice, the zero bias crossings associated with degeneracies of Andreev bound states can be “stretched” into long zero bias peaks, either due to closing of gap [8] or interactions of complex states [79]. In both cases, however, significant splitting at low field is anticipated, which is not observed in our triple dot chain either. Thus, the herein observed zero bias feature cannot be explained in terms of magnetic field behaviors of Andreev bound states that been observed or predicted. Similarly, we should be able to rule out that the zero bias peak is a Kondo peak, because the latter is expected to split as a function of field by the same amount, 1.45 mV.

Another possible origin of the zero bias peak is a supercurrent. As it has been previously observed, supercurrents might appear as a zero bias peak at finite field [96]. We, however, also notice that supercurrent through our device should be highly suppressed because of the potential barriers generated by gates along the nanowire, particularly the high interdot barriers, i.e., low t_{LM} and t_{MR}. Indeed, the differential conductance is only as high as 0.005 $(2e^2/h)$, while in contrast, the conductance in Ref.[96] is $\sim 2e^2/h$. To conclusively rule out the possibility of supercurrent in devices of next generations, normal tunneling probes can be used.

Finally, the herein discussed zero bias feature strongly resembles the zero bias peak that has been interpreted a signature of Majorana zero modes reported in superconductor-nanowire structures [10]. Interestingly, both originate at finite magnetic fields and seem not to result from the merging of split resonances. We thus discuss whether an interpretation of Majorana zero modes in a chain can explain the observed zero bias feature, by examining the assumptions in the Kitaev model and the topological conditions. (A1) As done in Section 6.3, the superconductor-dot coupling is strong therefore charging energy has been tuned to be low. (A2) Here a magnetic field has been applied. (A3, C1) S-wave superconductivity has been induced in InSb where strong spin-orbit coupling is present. (C2) $2|t| > |\mu|$ can be fulfilled at some gate settings where dot levels close to the Fermi levels, i.e., $\varepsilon \sim 0$ at the finite magnetic field. With all assumptions and conditions fulfilled, it is theoretically possible that the zero bias feature is indeed associated with Majorana zero modes in a chain.

However, as always, people should be extreme cautious determining the signature of Majorana zero modes. First of all, we do not have further evidence of Majorana zero modes other than the zero bias peak. Besides, some inconsistencies between the experimental observation and theoretical prediction of Majorana zero modes by ideal models [2, 17, 19] are found. (1) According to the p-wave paring assumption and the topological condition, $2|t| > |\mu|$, the zero bias peak can be present near the regime ($\varepsilon_L = 0$, $\varepsilon_M = 0$, $\varepsilon_R = 0$), and absent far away from it. Experimentally, the evolution of the field behaviors does not follow this relation exactly. Fig.6.7d supports the relation: it has the significant zero bias feature and is taken closer to ($\varepsilon_L = 0$, $\varepsilon_M = 0$, $\varepsilon_R = 0$). Fig.6.7b, however, is a counterexample: it also exhibits the zero bias peak but it is taken when ε_L and ε_R are closer to $-U_L/2$ and $-U_R/2$, respectively. (The exact position of $\varepsilon = -U/2$ can be determined because it is at the minimum distance between the anticrossing branches. However, the exact position of $\varepsilon = 0$ is unknown.). (2) Strength of the zero bias feature is only 0.002 ($2e^2/h$) that is much lower than the predicted value: $2e^2/h$. (3) The triple dot is a short chain therefore considerable coupling is expected between Majorana zero modes at the two ends of the triple dot, if they are present [2]. The coupling leads to oscillating features near zero bias as predicted by the theories. The observed zero bias peak, however, sticks to zero bias and keeps a width of $\sim$ 50 μV. Whether these inconsistencies can be explained and confirming that the zero bias feature is indeed Majorana zero mode require comprehensive modeling of the experiment.

6.6 CONCLUSION

We have implemented a superconductor-quantum dot chain made of three quantum dots based in an InSb nanowire and three NbTiN leads, which importantly, displays an experimentally accessible approach to scale the system to long chains based in nanowires. We demonstrate that the chain structure is a promising platform to emulate the Kitaev model by realizing the assumptions and topological conditions in the model. Various spectroscopy measurements are performed to map out the resonances through Andreev bound states in the triple dot. Furthermore, we explore the magnetic field evolution of resonances. Two distinct magnetic field behaviors are observed. The first, splitting field behavior, can be explained with Andreev bound states, while the second is a zero bias peak starting at a finite field and sustaining for ~ 0.5 T. The zero bias feature is hard to understand in terms of degeneracies of Andreev bound states, the Kondo effect or supercurrent. Theoretical modeling is necessary to understand the measurements and confirm its relation to Majorana zero modes. Chains of next generation, made of hard gap hybrid structures, are desired to rule out trivial states due to subgap density of states, because the zero bias peak might also originate from subgap states with complex interactions. Phase control of the superconductors is another factor to consider for future devices.

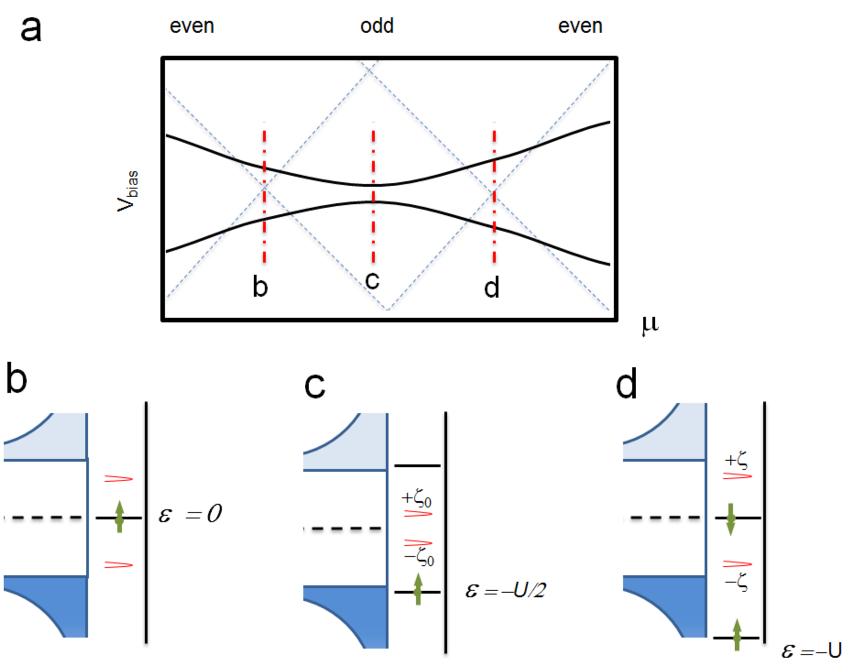

Figure 6.9: Energy diagram in an open dot. a, The anticrossing illustrates resonances through Andreev bound states in a single dot in the open dot regime. The dashed lines depict Coulomb diamonds when the superconductivity in the device is turned off. The dot occupation is even, odd, and even from left to right. The two degeneracies are marked with b and d. The center of them where the minimum distance between the anticrossing branches locates is marked with c. **b-d,** Energy diagram of quantum dot level and resonance levels ($\pm\zeta$) associated with transitions between Andreev bound states in the open dot regime. The levels are relative to the chemical potential of the superconductor (dashed line). Here we trace the single electron quantum dot level, ε. **b,** $\varepsilon = 0$. There are two resonance levels ($\pm\zeta$). **c,** $\varepsilon = -U/2$. Two resonance levels are closest ($\pm\zeta_0$). **d,** $\varepsilon = -U$. There are two resonance levels ($\pm\zeta$).

Fig.6.12 and Fig.6.13 are taken after the triple dot is removed and re-created. Likely they exhibit the same dot occupations as the figures in the main text, however, their gate voltages differ.

Fig.6.14 is taken after a different re-creation. Likely it exhibits the same dot occupations as the figures in the main text, however, its gate voltages differ.

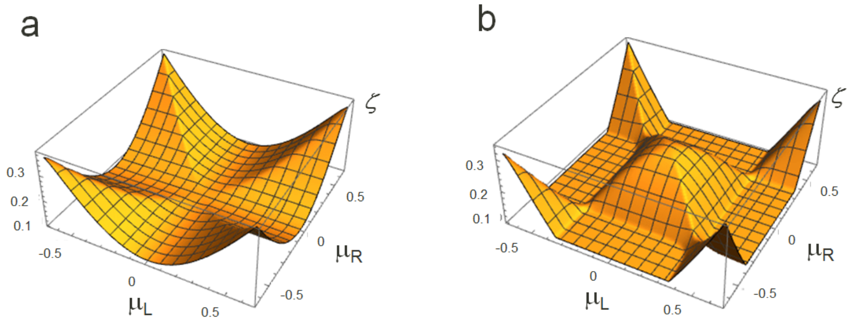

Figure 6.10: Simulated spectroscopies. **a,** Simulation of the transition between ground states and first allowed excited states as a function of bias (vertical axis) and μ_L and μ_R to help picture the spectroscopy, in the strong superconductor-dot coupling regime. $\Gamma_S = 0.6$ **b,** Simulation of the transition between ground states and first allowed excited states as a function of bias (vertical axis) and μ_L and μ_R to help picture the spectroscopy, in the weak superconductor-dot coupling regime. $\Gamma_S = 0.35$. Other simulation parameters are the same for **a** and **b**: $U = 1$, $\Delta\varepsilon = 0.35$, $t = 0.025$, where $\Delta\varepsilon$ is quantum dot level spacing. All parameters and V_{bias} have the same unit, $\hbar$. Note that these are simulations for double dot chains.

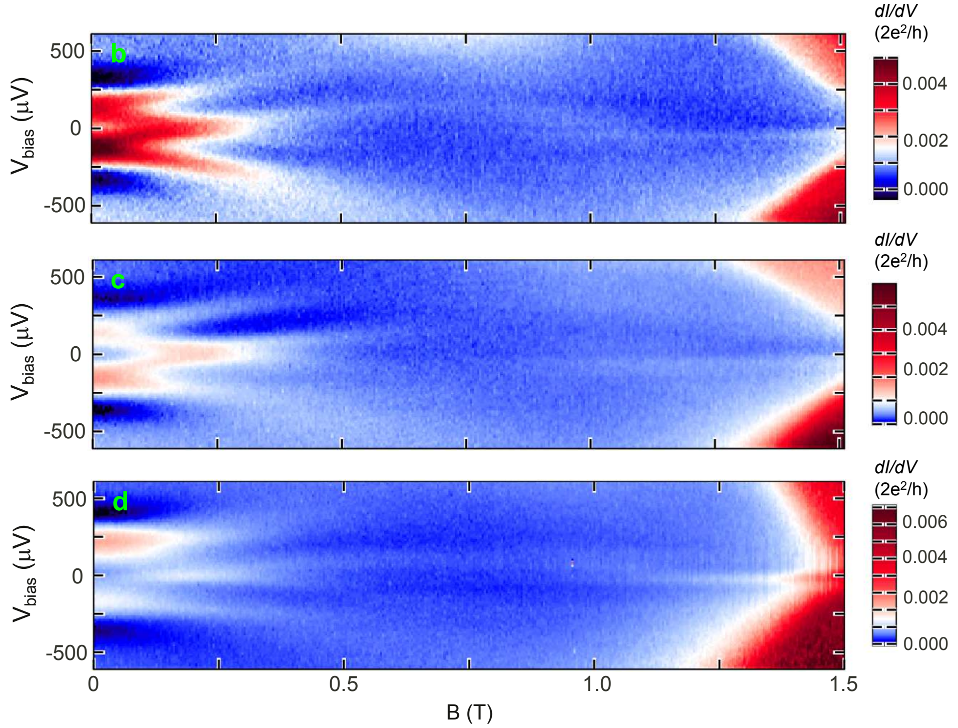

Figure 6.11: Gradual evolution from splitting to zero bias peak: original data. b-d, The magnetic field dependence of the resonances through triple dot Andreev bound states at various triple dot gate settings denoted with letter b-d in Fig.6.6b.

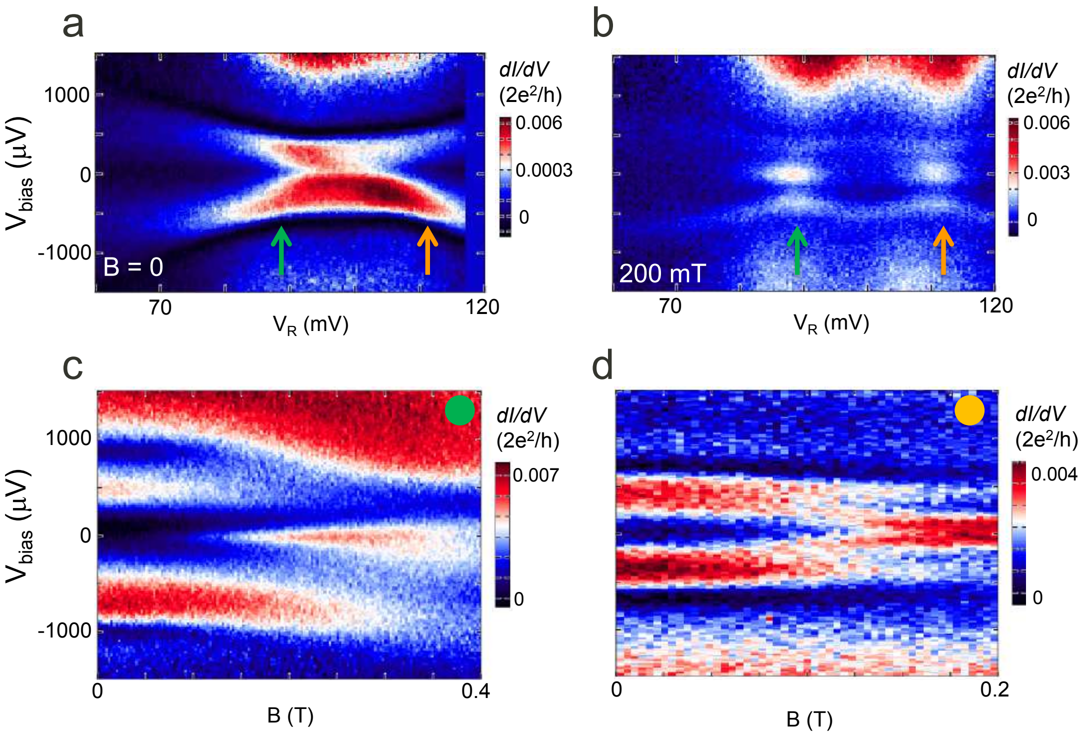

Figure 6.12: Complementary data of magnetic field evolution. **a**(**b**), dI/dV as a function of bias and V_R at 0 mT (200 mT), given $\varepsilon_L > -U_L/2$ and $\varepsilon_M = -U_M/2$. **c**(**d**), bias vs. field with V_M at the position marked by the green (yellow) arrow marked in **a**.

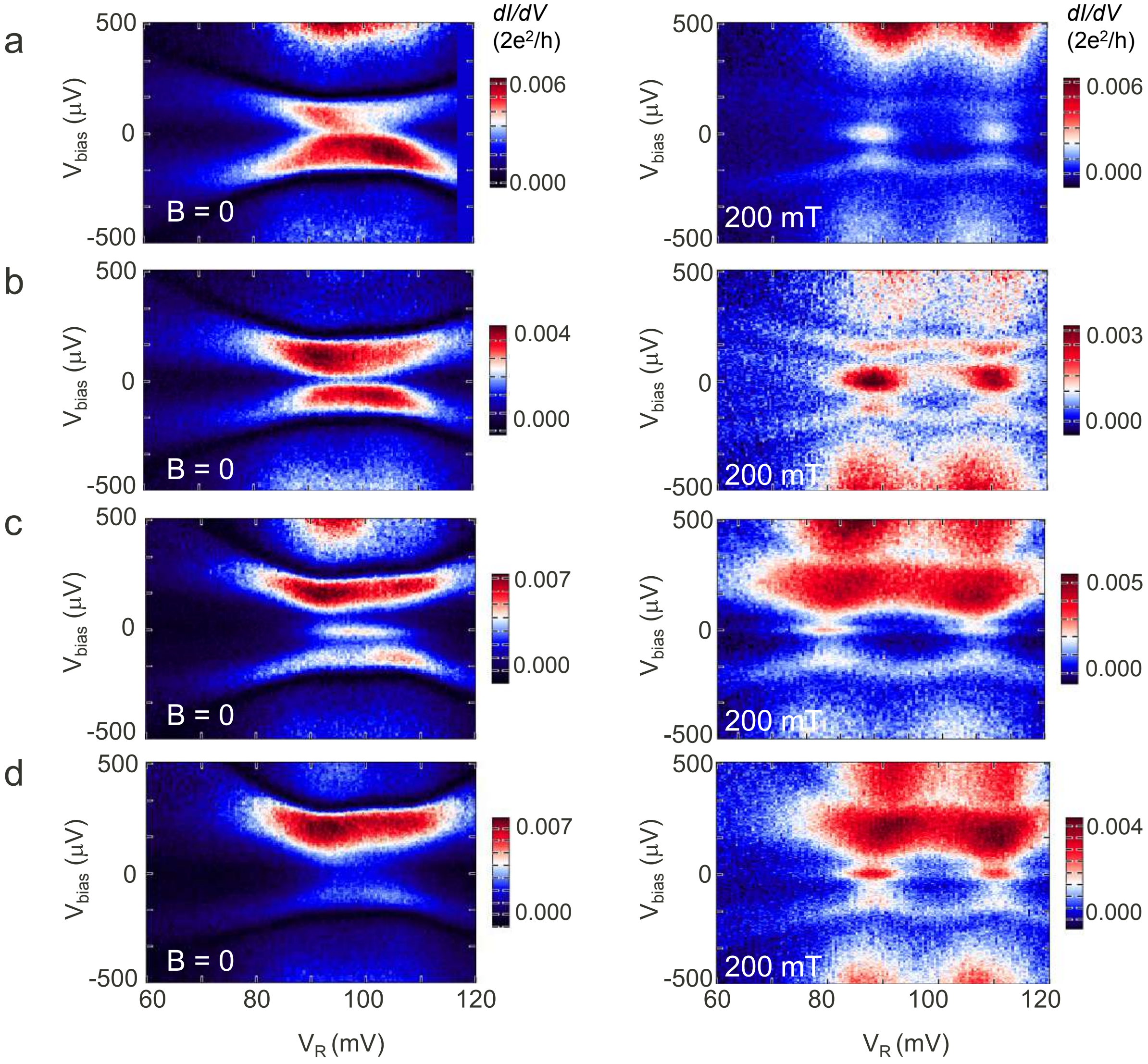

Figure 6.13: Bias spectroscopy at finite magnetic field. **a,** dI/dV as a function of bias and V_R at 0 mT (left) and 200 mT (right), given $\varepsilon_L = -U_L/2$ and $\varepsilon_M = -U_M/2$. $V_L = 676$ mV and $V_M = 740$ mV. **b,** dI/dV as a function of bias and V_R at 0 mT (left) and 200 mT (right), given $\varepsilon_L > -U_L/2$ and $\varepsilon_M = -U_M/2$. $V_L = 672$ mV and $V_M = 712$ mV. **c,** dI/dV as a function of bias and V_R at 0 mT (left) and 200 mT (right), given $\varepsilon_L = -U_L/2$ and $\varepsilon_M > -U_M/2$. $V_L = 662$ mV and $V_M = 700$ mV. **d,** dI/dV as a function of bias and V_R at 0 mT (left) and 200 mT (right), given $\varepsilon_L > -U_L/2$ and $\varepsilon_M > -U_M/2$. $V_L = 672$ mV and $V_M = 700$ mV.

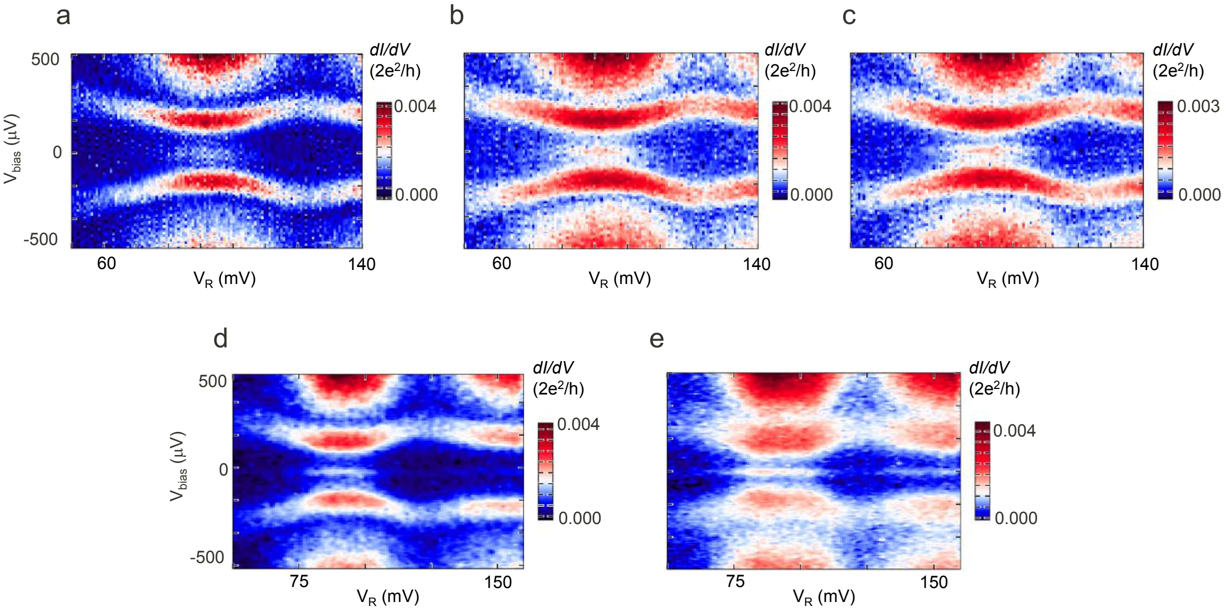

Figure 6.14: More bias spectroscopy at finite magnetic field. a-e, dI/dV as a function of bias and V_R at 0, 30, 60, 100, and 200 mT, given $\varepsilon_L = -U_L/2$ and $\varepsilon_M > -U_M/2$. $V_L = 676$ mV and $V_M = 740$ mV.

7.0 INDUCED SUPERCONDUCTIVITY IN GE/SI NANOWIRE-NBTIN HYBRID STRUCTURES[1]

Transparent contacts between high critical field superconductors and nanowires are crucial in the context of Majorana zero modes based on superconductor-nanowire hybrid structures. In this chapter we achieve such contacts between NbTiN and Ge/Si core/shell nanowires and characterize the induced superconductivity.

---

[1] THIS CHAPTER IS ADAPTED FROM REF.[135].

7.1 INTRODUCTION

Josephson junctions based on semiconductor nanowires have become a fertile research platform in recent years. Charge tunanbility of semiconductors has been used to implement supercurrent transistors [7], Josephson π-junctions [97] and Cooper-pair beam splitters [9]. More recently, theoretical proposals for realizing Majorana zero modes in semiconductor-superconductor hybrid structures [3, 4] have led to a series of experiments that began accumulating evidence for these exotic quantum states [10, 46, 45, 56, 11, 13, 12]. Majorana studies have focused on InAs and InSb nanowires which are characterized by strong spin-orbit interaction, large effective Landé g-factors, ballistic transport along the nanowire, and induced superconductivity in the nanowire.

Ge/Si core/shell nanowires have been proposed for Majorana studies owing to the strong spin-orbit coupling in the valence band [98]. Recent experiments have established the one-dimensional hole gas [99] and ballistic quantum transport [57]. Strong spin-orbit interaction and large effective Landé g-factors have been extracted from both quantum dot and bulk nanowire measurements [100, 101, 102, 57, 103]. The last component, induced superconductivity from high critical magnetic field superconductors, is missing. Although supercurrent is observed in Al-Ge/Si-Al junctions [104], pure Al contacts are not suitable for topological quantum circuits based on Majorana zero modes due to the low bulk critical magnetic field of Al.

In this chapter, we report superconductivity in Ge/Si nanowires induced by niobium titanium nitride (NbTiN) whose critical magnetic field is large. We demonstrate the Josephson supercurrent through NbTiN-Ge/Si-NbTiN junctions to high magnetic fields of order 1 Tesla, as required for Majorana experiments. We evaluate the induced gap in the nanowire through co-tunneling in the pinched-off regime of the junctions.

The devices are fabricated on doped Si substrates which serve as back gates. The substrates are covered by thermal SiO_2 (285 nm) and chemical vapor deposited Si_3N_4 (50 nm) (Fig.7.1**a**). Ge/Si nanowires with core diameters of 20-40 nm and shell thickness of 2 nm [105, 106, 65, 107] are randomly deposited on the substrate. The superconducting leads are patterned by electron beam lithography with nominal spacing of 200 nm followed

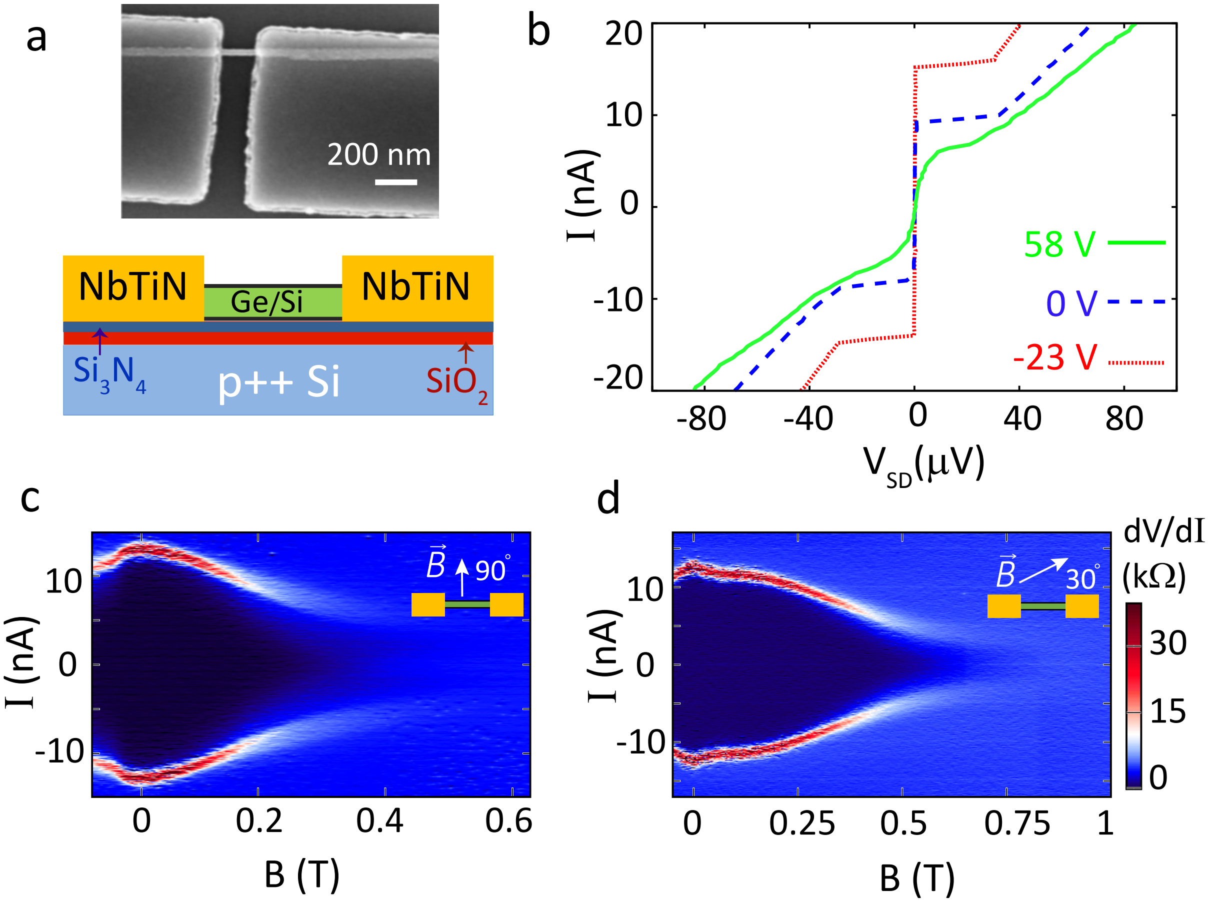

Figure 7.1: NbTiN-Ge/Si-NbTiN devices, Josephson current and the magnetic field dependence. a-Top, Scanning electron micrograph of a Ti/NbTiN-Ge/Si-Ti/NbTiN device. **a-Bottom,** Side view schematic of the device. **b,** IV characteristics of device A at $V_{bg} = -23$ V (red), 0 V (blue) and 58 V (green). **c,d** The differential resistance dV/dI as a function of current bias and magnetic field for device A at $V_{bg} = -10$ V (panel **c**) and device B at $V_{bg} = 0$ V (panel **d**). In-plane magnetic field orientations are indicated by the cartoons.

by magnetron sputtering of NbTiN. One 3 nm interlayer of Ti (devices A and B) or Al (device C) is deposited prior to NbTiN. Before the metal deposition, a 2-second BHF etch is performed to remove the native oxide on the surface of nanowires. Note that substrate has bilayer and the chemical vapor deposited Si_3N_4 is used to protect SiO_2 from being etched quickly. The measurements are performed in a dilution refrigerator at 20-40 mK.

7.2 SUPERCURRENT AND MAGNETIC FIELD DEPENDENCE

Typical current-voltage (IV) characteristics are shown in Fig.7.1**b**. Because the charge carriers in Ge/Si nanowires are holes, a more negative back gate voltage V_{bg} leads to a lower normal state resistance (R_n) and a higher switching supercurrent (I_c). The excess current (I_{exc}) due to Andreev reflection extracted from the IV traces is in the range of $1-4$ nA. Contact transparency of $\sim 50\%$ is estimated using the Octavio-Tinkham-Blonder-Klapwijk theory from the ratio $eI_{\mathrm{exc}}R_n/\Delta \sim 0.05$, where e is the elementary charge and the bulk gap Δ is 1.7 mV given $T_c = 11$ K [108, 109]. Note that this is a lower bound estimate on the contact transparency since the ratio above is reduced for finite length junctions [110]. On the other hand, the eI_cR_n/Δ ratio is 0.03 which is lower than the theoretical limit of π. Finite contact transparency and premature switching out of the supercurrent state caused by thermal activation can contribute to the reduction of the I_cR_n product [31]. The fact that supercurrent in Ge/Si nanowires is carried by holes which have a different momentum J than electrons in the contact superconductor may also contribute to this reduction, though this remains an open question.

Magnetic field evolution of supercurrents in two devices is presented in Figs.7.1**c,d**. The switch out of the supercurrent state and into the finite voltage state corresponds to a peak in dV/dI. It is clearly visible up to 400 mT and 800 mT but can also be traced to higher fields. Both devices demonstrate monotonous decrease in I_c as magnetic field is increased. The fact that supercurrent survives to higher fields in device B is consistent with the field aligned closer to the nanowire axis in this device, which reduces the magnetic flux threading the junction area for a given field. No nodes or oscillations in the switching current are observed up to fields of 1 Tesla, throughout the range of resolved supercurrent features. Assuming purely Fraunhofer-type interference within the junction only (zero field in the leads), the first node is expected at 300 mT for device A and 600 mT for device B. Detailed understanding of the field evolution of supercurrents in few-mode nanowires [111, 112] will be reported in a separate numerical study which includes the effects of geometry, Zeeman splitting, spin-orbit coupling, vector potential and Meissner effect.

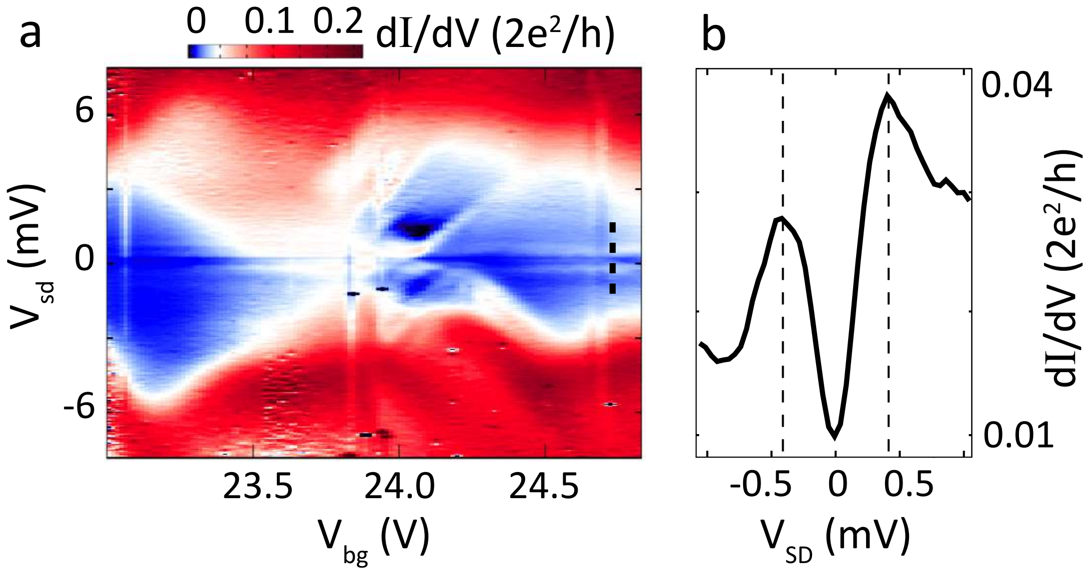

Figure 7.2: Induced superconducting gap measured by co-tunneling transport. a, Coulomb diamond measurements on an accidental quantum dot in device C in the near pinch-off regime, a dashed line marks a line cut shown in panel **b**. **b,** A line cut showing dI/dV as a function of the bias voltage. Peaks separated by $4\Delta_{in}$ are marked by dashed lines.

7.3 INDUCED SUPERCONDUCTING GAP

The induced superconducting gap Δ_{in} is studied in the pinched-off regime through unintentional quantum dots formed in the junctions near pinch-off [80]. Fig.7.2**a** shows differential conductance in device C as a function of back gate voltage. The boundaries of Coulomb diamonds are broadened due to co-tunneling, as the quantum dot barriers remain low. We observe a pair of sharp horizontal resonances of high differential conductance located symmetrically around zero bias at $V_{sd} = 2\Delta_{in} = \pm\ 440\ \mu V$. At biases in between the peaks, conductance is suppressed but remains non-zero. Thus the induced superconducting gap here is of the so-called "soft gap" type (see Fig.7.2**b**). The "soft gap" induced superconductivity has been observed in various experiments and attracted particular attention in the Majorana study. While the underline cause remains mysterious, possible attributes are disorder, quasiparticle poisoning [113, 114] and finite interface transparency. We also notice that the soft gap observed here is of the same magnitude as in the Majorana studies based on InSb nanowires [10, 11, 13]. Since the same NbTiN alloy are used in both InSb and Ge/Si cases, the soft gap measured here indicates that the soft gap is not unique to InSb-NbTiN hybrid structures and the “soft gap” may be associated to the properties of the NbTiN film, such as its granularity and alloy disorder.

7.4 CONCLUSION

We have developed and optimized superconducting contacts to Ge/Si nanowires based on NbTiN and demonstrate gate-tunable supercurrent in NbTiN-Ge/Si-NbTiN junctions and observe supercurrents up to magnetic fields of order 1 Tesla. The induced superconducting gap of 220 μeV is characterized in the co-tunneling regime of transport through quantum dots. The sub-gap conductance remains significant and research on suppressing the subgap conductance is desired [94].

8.0 SPIN-ORBIT COUPLING AND G-FACTORS IN GE/SI DOUBLE DOTS[1]

To measure the spin-orbit coupling and g-factors in Ge/Si core/shell nanowires, we perform transport measurements on double quantum dots defined in Ge/Si core/shell nanowires and focus on Pauli spin blockade. By studying the magnetic field evolution of spin blockade, we estimate a lower bound on the spin-orbit coupling and extract Landé *g*-factors.

---

[1] THIS CHAPTER IS ADAPTED FROM REF.[103].

8.1 INTRODUCTION

Holes in Ge/Si nanowires offer an unexplored platform for the study of Majorana zero modes based on superconductor-nanowires [115]. Particularly, strong spin-orbit interaction is predicted [116] and suggested by experiments [117, 118, 119, 120] to be strong in Ge/Si core/shell nanowires. Strong spin-orbit coupling is desired because it is a key component for implementing Majorana zero modes based on superconductor-nanowires. We use the fact that spin blockade in double dot can be lifted by spin-orbit coupling [121] to extract the spin-orbit coupling in Ge/Si core/shell nanowires. By monitoring the magnetic field dependence of double dot quantum states, we can also measure the g-factor in Ge/Si nanowires that is another key component for realizing Majorana fermions [3, 4, 10, 122].

Besides, the study of spin blockade in quantum dots have a broader perspective as it is also motivated by the proposals to build a spin-based quantum computer [123], as spin blockade can be used for qubit initialization and readout [23, 124]. Firstly, spin blockade and its lifting mechanisms offer a direct insight into spin relaxation and dephasing processes in semiconductors and provide deeper understanding of interactions between spin localized in a quantum dot and its environment, be it the lattice and its vibrations or nuclear spins, spin-orbit interaction, or coupling to spins in nearby dots or in the lead reservoirs [125, 126, 127, 128, 77]. Secondly, the potential of strong spin-orbit coupling offers a path to electrical spin manipulation [129, 27]. Moreover, holes weakly couple to nuclear spins due to their p-wave Bloch wave symmetry. Last and importantly, hyperfine interaction is expected to be greatly reduced owing to the low abundance of nonzero nuclear spin isotopes in the group IV materials [130]. As a result, qubits based on group-IV semiconductors are expected to come with longer spin relaxation times [131].

In this work we perform transport measurements on electrostatically defined double quantum dots [23] made in Ge/Si core/shell nanowires, and detect Pauli spin blockade at several charge degeneracy points. We expand and adapt a previously developed rate equation model to analyze the magnetic-field evolution of the leakage current [121]. We also extract relatively large effective g-factors, up to 8.0 [132, 133, 134], which is promising for Majorana fermion and spin qubit implementations.

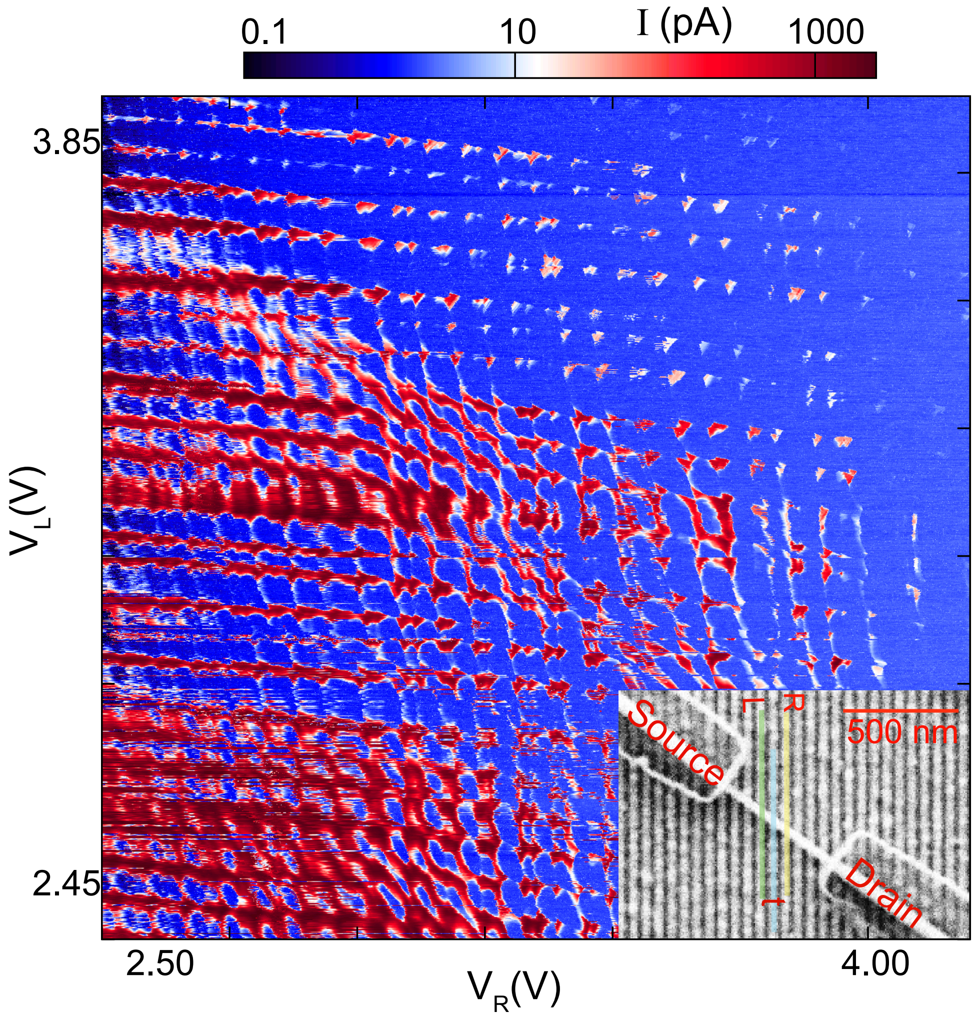

Figure 8.1: Double dot stability diagram in large gate ranges. Current through the double dot as a function of voltage on left gate (V_L) versus voltage on right gate (V_R) at a fixed voltage on barrier gate (V_t). The measurement is taken with a source-drain bias of 4 mV and at zero magnetic field. The inset shows a scanning electron micrograph of a representative Ge/Si nanowire device with Al/NbTiN lithographic contacts (labeled "Source" and "Drain") and tuning gate electrodes labeled L, t and R. The other gates are fixed at zero voltage.

The devices are fabricated with contacts of Al/NbTiN (15/42 nm) on bottomgates of 60 nm pitch. We note that despite the fact that Al and NbTiN are both superconductors the contact between the leads and the nanowire has high resistance and low transparency in these devices, therefore no effects of induced superconductivity are observed on the dots as opposed to nominally the same devices that showed high contact transparency [135]. Furthermore, the applied source-drain bias exceeds the superconducting gap of NbTiN, which remains superconducting at all fields applied here. Thus we do not consider any contribution from the superconductivity of the leads on the leakage current. The measurements are performed in a dilution refrigerator at a base temperature of 30 mK.

The double quantum dot is defined by applying positive voltages to three adjacent gates: V_L and V_R are used to set the outer barriers, and V_t defines the interdot barrier. Since all three gates are in close proximity they all influence the charge occupation of the dots, as well as all three tunneling barriers.

8.2 TRANSPORT THROUGH GE/SI DOUBLE DOTS

The main panel of Fig. 8.1 shows the measured double dot charge stability diagram which consists of a grid of charge degeneracy points connected by co-tunneling lines at higher charge occupations. Many charge degeneracy points are observed before the gate-induced energy barriers to the source and drain get too high to detect the current at the positive gate voltage extremes of the plot. This is in strong contrast with quantum dots defined using similar gates in InAs [27] or InSb [29] nanowires, where only a few charge degeneracy points are visible between complete pinch-off and the open transmission regime. The current is too low to measure at the charge degeneracy points corresponding to the last few holes in both dots, meaning that the tunneling barriers pinch off completely before the dots are emptied. In the regime studied here both dots still contain tens of holes. This is confirmed by asymmetric gate tuning such that as holes are expelled from one dot, the occupation of the other dot is increased and the tunneling barrier is lowered to ensure detectable current. The fact that so many holes fit in a small volume of a double dot (less than 120 nm in length and 30 nm in diameter) is consistent with the large effective hole masses as compared to those of electrons in III-V semiconductors, indicating that the hole wavefunctions are predominantly of a heavy-hole character.

8.3 MEASUREMENTS OF SPIN-ORBIT COUPLING AND G-FACTORS

In double quantum dots with multiple charges per dot, spin blockade does not necessarily occur at each (odd, odd) to (even, even) charge transition as expected for simple few-electron quantum dots [27, 29, 23, 136, 137, 138]. In fact, spin blockade may not occur for multiple transitions in a row [139]. This can be either due to the complex spin structure of the higher orbital states or due to a suppressed energy splitting between the ground state singlet and a higher orbital triplet.

When spin blockade does occur we assume that it can be effectively understood in the same way as the simplest $(1,1) \rightarrow (0,2)$ spin blockade: close to zero detuning, the N_L—th hole in the source dot can only enter the drain dot if it can form a spin-singlet state with the N_R—th hole on the drain dot. Entering an (N_L-1, N_R+1) state in a triplet configuration requires occupation of a higher orbital state which becomes energetically accessible only when an additionally applied interdot energy level detuning ε exceeds the singlet-triplet energy level splitting in the drain dot. For small detuning the system is thus expected to be blocked in one of the three triplet states, which are in principle degenerate and split in energy under the influence of a magnetic field due to the Zeeman effect. For clarity we will refer to the (N_L, N_R) states as $(1,1)$ and to the (N_L-1, N_R+1) states as $(0,2)$. Current through the double dot in the spin blockade regime due to various spin non-conserving processes is referred to as the leakage current.

The primary signature of spin blockade in this study comes from the magnetic field dependence of the leakage current (Fig. 8.2), which can be explained in terms of the simple spin blockade picture described above. We vary the (1,1) to (0,2) energy level detuning, ε by scanning V_L and V_R perpendicular to the base of bias triangles (as indicated in the inset), while stepping the magnetic field. The associated singlet-triplet splitting of ~ 2 meV is representative of the several charge degeneracy points studied (see supplementary information).

A smaller rise in the leakage current at lower detuning, marked with the tilted dashed line in Fig. 8.2, is assigned to a resonance between the lowest $(1,1)$ state T_+ and the singlet $S(0,2)$ state: below this resonance (for smaller ε), $S(0,2)$ is energetically not accessible from the ground state $T_+(1,1)$ and the system is in Coulomb blockade. Since the energy of $S(0,2)$

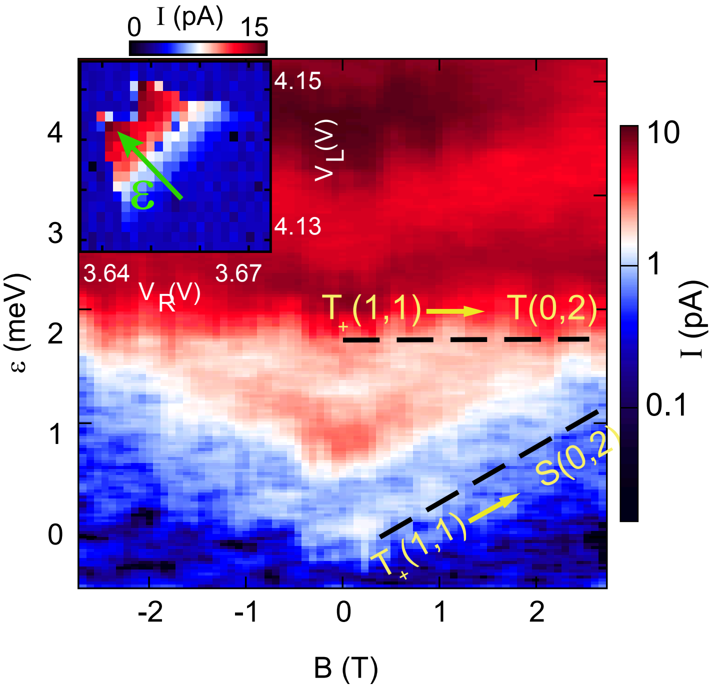

Figure 8.2: Current as a function of detuning and magnetic field. Current through the double quantum dot measured as a function of the detuning ε and the magnetic field B, with an applied source-drain voltage of $V_{SD} = 6.5$ mV. The magnetic field is applied normal to the substrate plane. The resonances associated with $T_+(1,1) \to T_+(0,2)$ and $T_+(1,1) \to S(0,2)$ transitions are marked with dashed lines. From the field dependence of the latter we find $g = 8.0 \pm 0.2$. Inset: the charge degeneracy point at finite bias with the detuning axis used in the main panel indicated by ε.

is not expected to depend on the magnetic field, the B-dependence of this resonance reflects the B-dependence of the energy of $T_+(1,1)$. The pattern formed by two current resonances marked by dashed lines $T_+(1,1) \to T(0,2)$ and $T_+(1,1) \to S(0,2)$ is the main signature of spin blockade in this study. Note that a copy resonance follows the $T_+(1,1) \to S(0,2)$ transition in field, which is not accounted for in the simple spin blockade picture used here.

Using the slope of the resonance labeled $T_+(1,1) \to S(0,2)$, we obtain $g = 8.0 \pm 0.2$ for Fig.8.2. While full g-tensor measurements were not performed, we find lower g-factors for fields deviating from normal to the substrate, in agreement with other studies (see supplemental material) [133, 134]. The highest g-factors extracted here are larger than previously reported for Ge/Si nanowires [118, 133, 134]. One possible reason for this is larger wire diameters used here: indeed, a relevant theory predicts diameter-dependent g-factors [116].

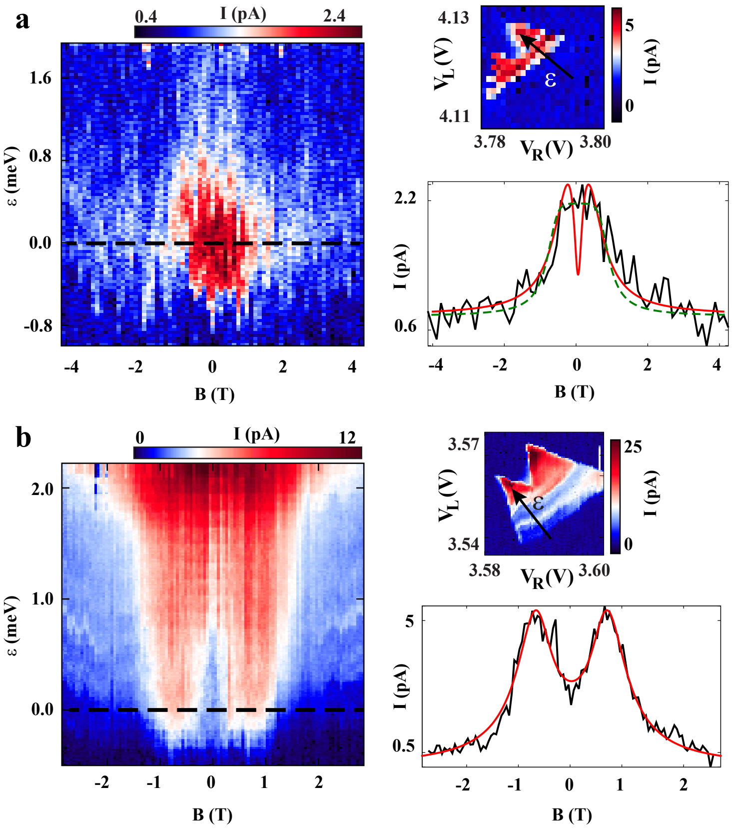

Figure 8.3: Magnetic field evolution of the leakage current in two different spin blockaded transport configurations. In both cases the field is applied in the plane of the nanowire and gates, perpendicular to the gates but making an angle of ∼ 30° with the wire. In the left panels we show the dependence of the leakage current on magnetic field and detuning, and on the right side we show the corresponding charge degeneracy points (top) and a line cut of the data at zero detuning (bottom). The zero-detuning cuts include fits to the theory presented in the main text. **a,** In this configuration, where a bias voltage $V_{SD} = 6.5$ mV is applied, the leakage current has a single-peak structure both as function of the detuning and magnetic field. The corresponding charge stability diagram is taken at $B = 5$ T. In the figure we plot two different theory curves on top of the data, both with $\xi = 0.03$, $g = 4.4$, and an added constant current of 0.8 pA to account for the background signal observed in the data. We further used $\Gamma = 300$ MHz, $t = 50$ μeV, $\gamma = 0.0075$, and $\alpha = 0.4$ (solid red curve) and $\Gamma = 25$ MHz, $t = 150$ μeV, $\gamma = 0.66$, and $\alpha = 0.4$ (dashed green curve). **b,** Leakage current at a different charge degeneracy point, with $V_{SD} = 4$ mV. The corresponding bias triangle is taken at $B = 0$ T. Here the current shows a double-peak structure in the magnetic field, which can also be seen in the zero-detuning cut. The theory curve (red solid line) uses $\xi = 0.03$, $g = 4$, $\Gamma = 256$ MHz, $t = 150$ μeV, $\gamma = 0.061$, and $\alpha = 0.37$.

In Fig.8.3a,b (left panels) we plot the measured leakage current in the spin blockade regime of two representative charge degeneracy points which show a qualitatively different field-dependent behavior. The current in Fig.8.3a shows a single peak centered at zero field, whereas in Fig.8.3b we observe a double-peak structure with a dip at zero magnetic field. We note that beyond the difference in charge numbers, we cannot independently quantify differences in other double dot parameters across the two regimes of Fig.8.3. We speculate that the interdot tunnel coupling as well as the couplings to the leads are not the same in the two regimes.

A zero-field dip in the leakage current is known to occur in double dots hosted in materials with strong spin-orbit interaction [127, 140, 141, 142, 143]. The dip is usually explained in terms of a competition between different types of spin-mixing processes: the combination of spin-orbit interaction and Zeeman splitting due to the applied field enables transitions between triplet and singlet configurations. This mechanism becomes more efficient at higher magnetic field and thus it produces a dip in the leakage current around zero field [121]. Other processes that mix spin states, such as the hyperfine interaction between the electrons or holes and the nuclear spins in the host material [144] or spin-flip co-tunneling processes with the leads [145], can be independent of the magnetic field or even become less efficient with increasing B. If one of such processes provides the dominant spin-mixing mechanism, then there will appear no dip in the current around zero field. Since the spin-orbit-mediated mechanism scales with the interdot tunnel coupling, one can expect to observe a transition from having a zero-field dip to no zero-field dip when changing the tuning of the double dot.

8.4 THEORETICAL MODEL

Ignoring the potentially more complicated nature of spin blockade in the valence band, we assume that in the present case we can describe the leakage current with a model based on the following ingredients: (i) $S(1,1)$, has the same singlet configuration as $S(0,2)$ and is thus strongly coupled to that state, with a coupling energy t. (ii) The state $S(0,2)$ decays to the drain lead with a rate Γ. Immediately after such a transition a new hole enters the system from the source, bringing it in one of the $(1,1)$ states again. (iii) $T_\pm(1,1)$ split off in energy when a magnetic field is applied. (iv) Spin-orbit interaction results in a coherent non-spin-conserving coupling between the $(1,1)$ triplet states and $S(0,2)$. The energy scale characterizing spin-orbit coupling t_{so} is proportional to t. (v) There can be other spin-mixing and spin-relaxation processes causing transitions between the different $(1,1)$ states.

In our data both the dip and the peak are relatively wide: they appear on a field scale of $B \sim 1$ T which is of the order of 3 K. First of all, this rules out hyperfine interaction as the dominant spin-mixing mechanism in the single-peak data of Fig. 8.3a. Hyperfine interaction is known to lift spin blockade around zero field producing a peak in current, but the width of the hyperfine peak is comparable to the typical magnitude of the effective nuclear fields in the dots. We estimate the effective nuclear fields in the present system to be less than 10 mT, which is orders of magnitude smaller than the peak width observed here [146].Secondly, the analytic theory of Ref. [121], which is often used to extract model parameters such as the magnitude of spin-relaxation rates and $\alpha = t_{\mathrm{so}}/t$, is valid for $t, t_{\mathrm{so}}, B \ll \Gamma$ and also assumes the spin-relaxation rates to be isotropic, based on the assumption $B \ll T$, where T is the temperature. From here on we will use $\hbar = k_{\mathrm{B}} = g\mu_{\mathrm{B}} = e = 1$. In the present case, however, we have $B \gg T$ for most fields of interest, and spin relaxation will thus mostly be directed towards the $(1,1)$ ground state instead. Furthermore, the suppression of current at the highest fields could indicate that B exceeds at these fields the effective level width of $S(0,2)$ by such an amount that the system is pushed into a Coulomb blockade in the lowest-lying $(1,1)$ triplet state.

We thus cannot straightforwardly apply the theory of Ref. [121] to model the data shown in Fig. 8.3. Instead we present a modified version of the theory, where we include only spin relaxation to the ground state and do not expand in large Γ. We start from the five-level Hamiltonian

$$H = \begin{pmatrix} 0 & iB & 0 & 0 & i\alpha t \\ -iB & 0 & 0 & 0 & i\alpha t \\ 0 & 0 & 0 & 0 & i\alpha t \\ 0 & 0 & 0 & 0 & t \\ -i\alpha t & -i\alpha t & -i\alpha t & t & 0 \end{pmatrix}, \tag{8.1}$$

written in the basis $\{|T_x\rangle, |T_y\rangle, |T_z\rangle, |S\rangle, |S_{02}\rangle\}$, where $|T_{x,y}\rangle = i^{1/2\mp1/2}\{|T_-\rangle \mp |T_+\rangle\}/\sqrt{2}$ and $|T_z\rangle = |T_0\rangle$ are the three $(1,1)$ triplet levels and $|S\rangle$ and $|S_{02}\rangle$ the $(1,1)$ and $(0,2)$ singlets, respectively. The interdot detuning was set to zero and α parametrizes the strength of the effective spin-orbit interaction in the dots, where $\alpha \sim 1$ corresponds to the strong limit. In principle, the three α's coupling $|T_{x,y,z}\rangle$ to $|S_{02}\rangle$ can be different, constituting a vector $\boldsymbol{\alpha} = (\alpha_x, \alpha_y, \alpha_z)$ (see Ref. [121]). The length of this vector corresponds to the strength of the spin-orbit interaction and its direction is related to the direction of the effective spin-orbit field. In a physical nanowire, the precise orientation of $\boldsymbol{\alpha}$ depends on many details and is hard to predict. We therefore make the simplifying assumption that all three components are of the same magnitude. We diagonalize the Hamiltonian and use its eigenbasis to write a time-evolution equation for the density matrix [121],

$$\frac{d\hat{\rho}}{dt} = -i[H^{\text{diag}}, \hat{\rho}] + \boldsymbol{\Gamma}\hat{\rho} + \boldsymbol{\Gamma}_{\text{rel}}\hat{\rho}. \tag{8.2}$$

The operator $\boldsymbol{\Gamma}$ describes (i) decay of all states $|n\rangle$ (with $n = 0 \dots 4$) to the drain lead with the rates $\Gamma|\langle n|S_{02}\rangle|^2$ and (ii) immediate reload into one of the eigenstates with the probabilities $\{1 - |\langle n|S_{02}\rangle|^2\}/4$. For the relaxation operator $\boldsymbol{\Gamma}_{\text{rel}}$ we take a simple form: We assume that all four excited states relax with the same rate Γ_{rel} to the ground state.

We first discuss this model on a qualitative level, and investigate how it differs from the model of Ref. [121]. For small fields, $B \ll \Gamma$, the different spin relaxation model used here only yields different numerical factors in some of the results. At $B = 0$ we have three blocked states at zero energy that can relax to the hybridized $(1,1)$–$(0,2)$ ground state which quickly decays to the drain lead; this results on average in four holes being transported through the system in a time $3\Gamma_{\text{rel}}^{-1}$, thus yielding a leakage current of $I(0) = \frac{4}{3}\Gamma_{\text{rel}}$. Adding a finite magnetic field induces a coupling of $\sim \alpha B$ between two of the blocked states and $|m\rangle$, which provides an alternative escape route and leads to an increase of the current.

This increase becomes significant only when the rate of this escape $\sim (\alpha B)^2\Gamma/t^2$ becomes comparable to Γ_{rel}, which happens at $B \sim (t/\alpha)\sqrt{\Gamma_{\text{rel}}/\Gamma}$. For larger fields the current tends to its maximum value $I_{\max} = 4\Gamma_{\text{rel}}$, reached when only one truly blocked state is left and on average four holes are transported in a time Γ_{rel}^{-1}. We see that this picture predicts a zero-field dip in the current of width $B_{\text{dip}} \sim (t/\alpha)\sqrt{\Gamma_{\text{rel}}/\Gamma}$ and a maximal suppression of the current, by a factor 3, at $B = 0$. This is, apart from numerical factors, the same result as found in Ref. [121].

Qualitative differences appear when we investigate what happens at even higher fields. Since Γ is finite in the present model and all relaxation is directed toward the ground state, we can enter a situation of Coulomb blockade in the $(1,1)$ ground state $|T_+\rangle$. When we increase B, the current will thus eventually be suppressed to zero, producing in general a double-peak structure in $I(B)$. A naïve guess for the field scale where this suppression sets in would be $\sim \Gamma$: however, the actual field scale of current decay is rather set by the competition of this escape rate with Γ_{rel}: only when the B-induced suppression becomes so strong that escape from $|T_+\rangle$ is the main bottleneck for the leakage current, the decrease in current becomes significant. We thus compare this escape rate $\sim (\alpha t)^2\Gamma/B^2$ with Γ_{rel} and find an estimate for the width of the overall double-peak structure $B_c \sim \alpha t\sqrt{\Gamma/\Gamma_{\text{rel}}}$.

We can also understand how our model could result in an apparent single-peak $I(B)$. Indeed, B_{dip} and B_c show a different dependence on the model parameters, and their ratio $B_{\text{dip}}/B_c \sim \Gamma_{\text{rel}}/\alpha^2\Gamma$ (which determines the relative visibility of the zero-field dip) could be large or small, depending on the detailed tuning of all parameters. For $B_{\text{dip}}/B_c \ll 1$ one could be in the situation where the central dip around zero field is too narrow to be observed.

We will now support these arguments with a more quantitative investigation of the model. We can solve Eq. 8.2 in steady state, $d\hat{\rho}/dt = 0$, and find the current from the resulting equilibrium occupation probabilities $p_n = \hat{\rho}_{nn}$ as $I = \sum_n p_n \Gamma |\langle n|S_{02}\rangle|^2$, yielding

$$I(B) = \Gamma_{\text{rel}} \frac{[w - B^2 + \tau^2][w(1+4\gamma) + B^2 - \tau^2]}{6\gamma w^2 + 2B^2\alpha^2 t^2}, \tag{8.3}$$

where we use the notation $w = \sqrt{(B^2-\tau^2)^2 + 8B^2\alpha^2 t^2}$, the small parameter $\gamma = \Gamma_{\text{rel}}/\Gamma$, and $\tau = t\sqrt{1+3\alpha^2}$ (which is the total tunnel coupling energy). To obtain Eq. 8.3 we assumed $\gamma \ll 1$, which we will also do below.

The current given by Eq. 8.3 indeed shows in general a double-peak structure. At zero field we find $I(0) = \frac{4}{3}\Gamma_{\text{rel}}$, and the current has two maxima at $B = \pm\tau$ where $I = 4\Gamma_{\text{rel}}$. The half-width of the resulting zero-field dip follows as $B_{\text{dip}} = t(\sqrt{\beta^2+2} - \beta)/\sqrt{2}$, where $\beta = \alpha/\sqrt{6\gamma}$. In the limit of large β (small $\sqrt{\gamma}/\alpha$) we find $B_{\text{dip}} \approx t\sqrt{3\gamma}/\alpha$. At high fields, the current drops to zero, and from Eq. 8.3 we find the half-width-half-maximum of the full double-peak structure to be $B_{\text{c}} = t(\sqrt{\beta^2+2} + \beta)/\sqrt{2}$ which reduces to $B_c \approx \alpha t/\sqrt{3\gamma}$ for large β. We see that in the limit of small γ these results agree with the conclusions of our qualitative discussion above. Further study of the two behaviors are presented in Ref.[103] where difference between g-factors in the two dots are introduced. Recent studies on similar materials found g-factors differing by 2–5% between two dots in a double dot [143, 147]. The introduction of such mechanism yields theoretical plots where reasonable agreement is gained.

8.5 CONCLUSION

To conclude, assuming linear Rashba spin-orbit interaction as the dominant relaxation term [116] in these gate-defined double quantum dots with $\alpha = 0.1$–0.4, and a dot-to-dot distance of order 50 nm, we find a spin-orbit length of $l_{\mathrm{so}} = 100$–500 nm. While this corresponds to a substantial spin-orbit interaction, it does not greatly exceed that measured in InAs or InSb nanowires. One possibility for this could be that α is not maximal for the field orientation at which data is obtained here as a consequence of spin-orbit anisotropy [29], although the magnetic field was not oriented in the direction expected for the spin-orbit field. Another factor for lower-than-expected spin-orbit interaction is the low strain between the thin Si shell and relatively thick Ge core. Thus, it is conceivable that spin-orbit interaction can be enhanced by tailoring the nanowire morphology. A more detailed insight into spin-orbit coupling and other double dot parameters could be obtained from electric dipole spin resonance.

8.6 SUPPLEMENTARY INFORMATION

8.6.1 Charge stability diagrams

We have measured three different nanowire devices, A, B, and C, in three different dilution refrigerators all at base temperatures below 30 mK. All three devices have the same fabrication recipe as mentioned in the main text. In this supplemental material we show more data on Device A, the device investigated in the main text, as well as data from the other two devices.

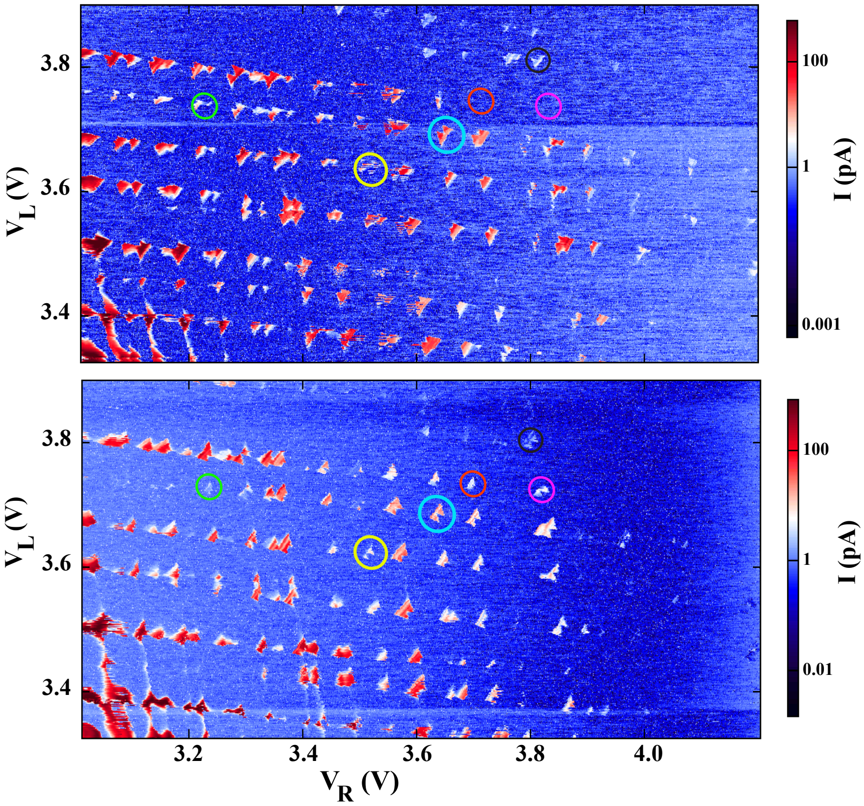

Figure 8.4: Charge stability diagrams in opposite biases. Double quantum dot charge stability diagrams at $V_{SD} = 4$ mV (top) and $V_{SD} = -4$ mV (bottom). The plots show the absolute value of measured leakage current across the dots from one reservoir to the other while scanning V_L vs. V_R at a fixed V_t. Some charge transitions that show bias asymmetric behavior are circled. Measurements are performed at zero magnetic field.

In Fig. 8.4 we show part of the charge stability diagram shown in Fig.8.1, in both source-drain bias directions. We remove parts of the scan with lower gate values from Fig.8.1 to improve the visibility of charge transitions with fewer hole occupation in dots and circle some charge transitions with asymmetric current near the triangles bases to illustrate how we search for spin blockaded transitions. Taking bias asymmetry near zero detuning as an initial signature of a spin blockade candidate charge degeneracy point, we study the magnetic field evolution to determine if spin blockade is present or not.

Fig. 8.5 shows the bias triangle of Fig.8.1b of the main text at zero field where spin blockade is stronger, and at finite magnetic field where the spin blockade is lifted.

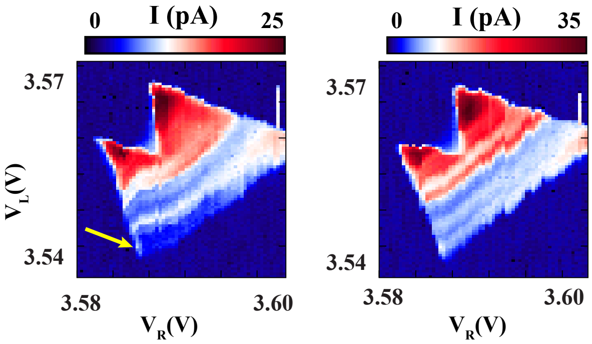

Figure 8.5: Spin blockade lifted at a finite magnetic field. Bias triangle at zero magnetic field (left) and at $B = -0.8$ T (right) at $V_{SD} = 4$ mV. The current is suppressed at the base of the triangle (lower left) at zero field and there is an excess current at the side which can be representative of the hole exchange between the dot and the reservoir where their Fermi energy levels are equal. At finite magnetic field we can see the increase in the leakage current at the base of the triangle associated with lifting the spin blockade.

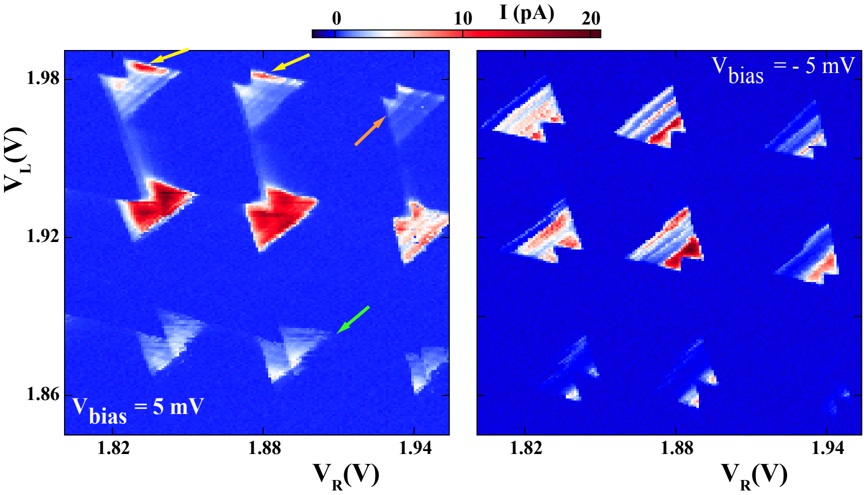

Figure 8.6: Double quantum dot charge stability diagrams of Device B in opposite bias directions. The plots show the absolute value of measured leakage current across the dots from one reservoir to the other while scanning V_L vs. V_R at a fixed V_t at 5 mV (left) and -5 mV (right). The arrows show characteristics of spin blockade explained in the text.

In Fig. 8.6 we see a few charge transitions from Device B in two opposite bias directions. These transitions manifest some indicators of possible spin blockade at zero magnetic field such as suppressed current at the base of the triangles (green arrow), enhanced current on the side of the triangles that can be related to spin exchange with the reservoir leads (yellow arrows), and triplet hats at the triangle tops (orange arrow). However, these features are not conclusive for this set of triangles. In order to accurately identify spin blockade one needs to study the magnetic field dependence of the leakage current, as shown for Device A in the main text and in the supplemental materials.

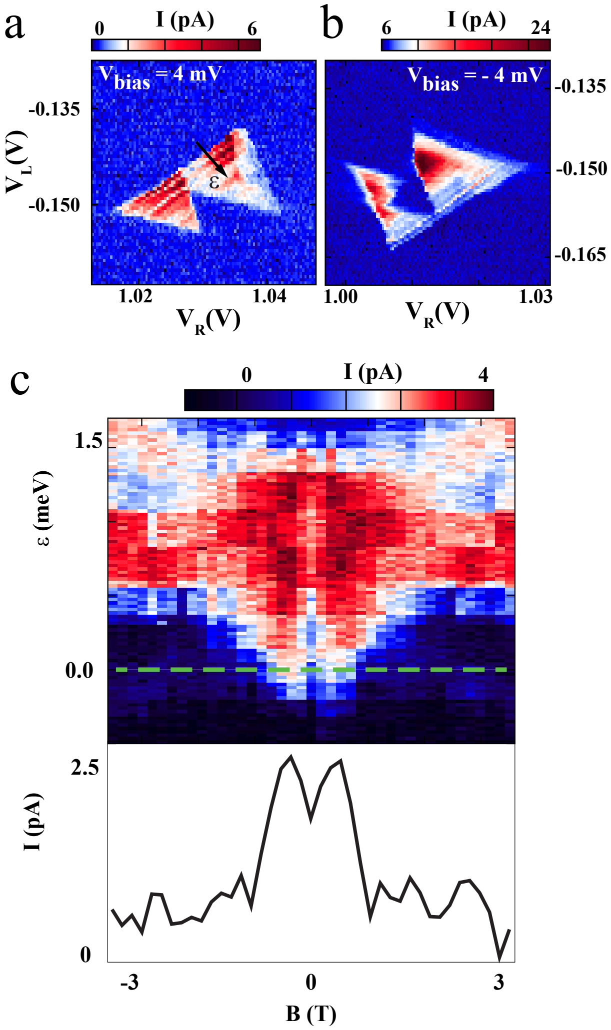

Figure 8.7: Measurements of double dot on Device C. a,b The bias triangles at 4 and -4 mV at zero magnetic field. The colorbar is the absolute value of the leakage current. **c,** The leakage current through the double quantum dot measured as a function of detuning and magnetic field at $V_{SD} = 4$ mV. The double-peak behavior in the bottom panel is highlighted by a line cut in the colorplot.

In Fig. 8.7 we present magnetic field evolution of the leakage current obtained from Device C. A similar pattern is observed here compared with Fig.8.2 of the main text, i.e.

base of the triangle moves to higher detuning with applied magnetic field. The top panel shows a charge degeneracy point studied at bias voltages $V_{SD} = \pm 4$ meV. The bias triangle at positive bias is smaller than the one in opposite bias suggesting the suppression of current at its base, which we attribute to spin blockade. In the middle panel we show the leakage current as a function of detuning ε (as indicated in the top left plot) and the applied magnetic field. In this regime the double-peak structure is observed in the field dependence at low detuning.

8.6.2 Bias asymmetry of spin blockade

For the transition between (1, 1) and (0, 2), spin blockade occurs at one bias direction but not at the opposite bias direction. Fig. 8.8 shows the leakage current as a function of the magnetic field and the gate voltages controlling the detuning, for both bias directions applied across the charge degeneracy points studied in Fig.8.2 (top) and Fig.8.3a (bottom) of the main text. The left panels show a field-dependent behavior of the leakage current, where the detuning at which the current sets on increases with field, whereas in the right panels that are taken at the opposite bias direction the leakage current onsets always at the bottom of the colormap (where zero detuning is located) and the onset voltage does not demonstrate a linear magnetic field dependence. Charge instabilities are responsible for the onset voltage fluctuations, these fluctuations are not symmetric upon magnetic field reversal.

8.6.3 g-factor anisotropy

Remarkable g-factor anisotropy is observed in Ge/Si nanowires. In Figs. 8.9 and 8.10 we show multiple scans of the leakage current through different double quantum dot configurations as a function of magnetic field and detuning for Device A. As we see, not all the scans reveal very sharp steps in the current, but they are still clear enough to read off an effective g-factor from the slope of the resonance associated with $T_+(1,1) \rightarrow S(0,2)$ transition, as shown by dashed lines. When extracting g-factors, we neglect the orbital effect of the magnetic field in the two dots on the energy of the $T_+(1,1) \rightarrow S(0,2)$ transition. The dots are likely occupied with heavy holes with a large effective mass, $m^* = 0.2\, m_e$, for which we estimate a shift

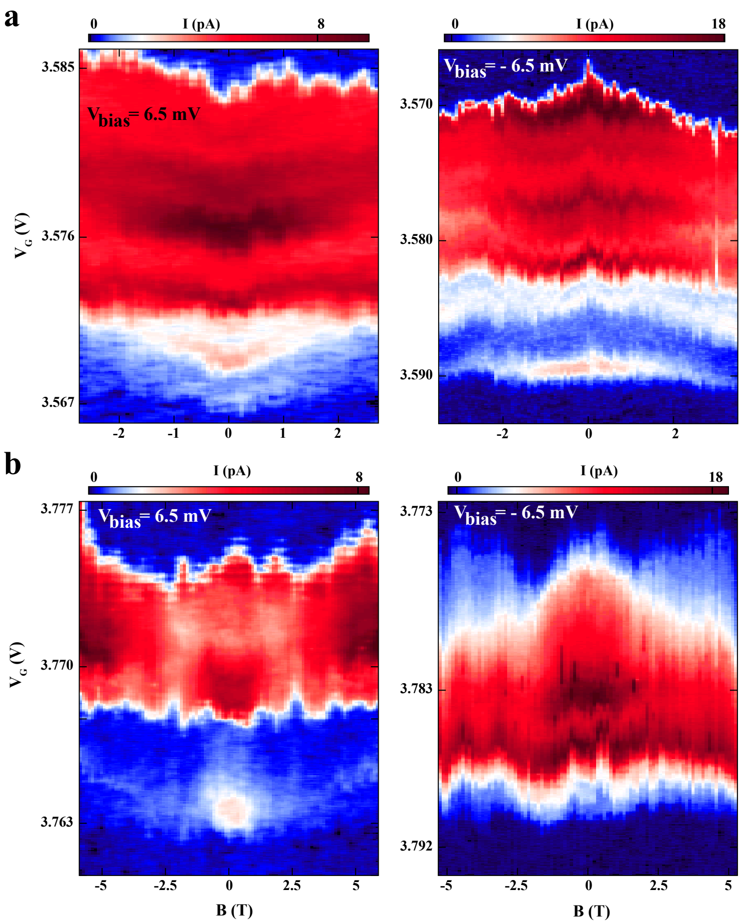

Figure 8.8: Magnetic field evolution of the leakage current in opposite bias directions. Field evolution of the leakage current as a function of detuning controlled by gate voltages V_G. They have opposite bias directions: left panels have positive biases and right panels have negative biases. They are associated with the two double quantum dot configurations shown in Fig.8.2 (top) and Fig.8.3a (bottom), respectively.

of $\approx$ 10% in orbital level splitting using $\Delta E = \hbar\sqrt{\omega_0^2 + \omega_c^2/4} - \hbar\omega_0$ at $B = 3$ T, where $\omega_c = \hbar eB/m^*$ and $\omega_0 \approx 2$ meV. At the same time, Zeeman shifts are comparable to the singlet-triplet energy level spacing in the same field range greatly exceeding the estimated orbital effect for these dots.

We apply magnetic fields in two different directions: (i) normal to the plane of the nanowire and local gates ($B_\perp$) and (ii) in-plane with the nanowire and gates, where the nanowire makes an angle of $\sim 30°$ with the field (B_z).

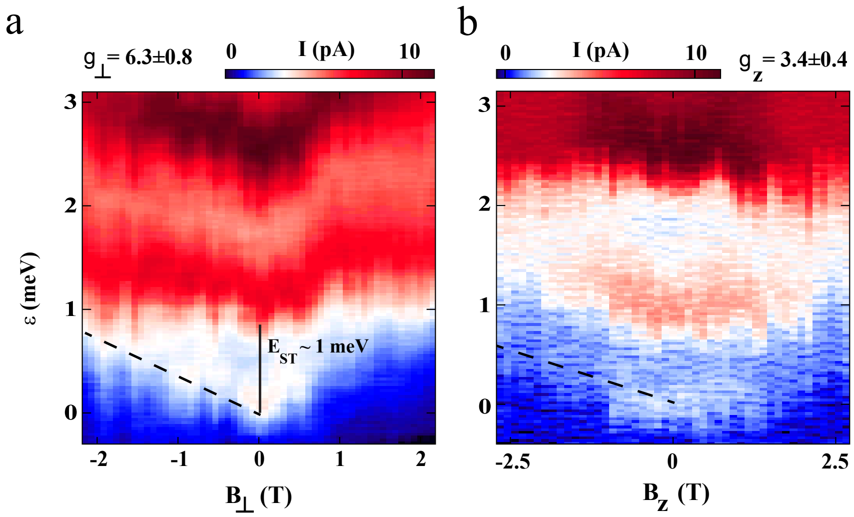

Figure 8.9: Perpendicular and in-plan g-factors. Leakage current is measured as a function of magnetic field and detuning. **a,** Field is applied normal to the substrate. **b,** In-plane magnetic field. The dashed lines show the slope of the resonance line moving as a function of field and detuning from which we extract the effective g-factor.

Fig. 8.9 shows the leakage current through a charge degeneracy point in both directions of applied magnetic field. The slopes from which we can read the effective g-factors are different for the two cases of applied field, larger for the out-of-plane magnetic field and smaller for the in-plane field.

Fig. 8.10 shows more examples of the in-plane magnetic field evolution of the leakage current at two other charge degeneracy points, where g-factor values deviate from those measured in $B_\perp$ shown in Fig.8.9a and Fig.8.2. Also from these scans we extract a singlet-triplet energy splitting $E_{ST} \sim$ 1–2 meV.

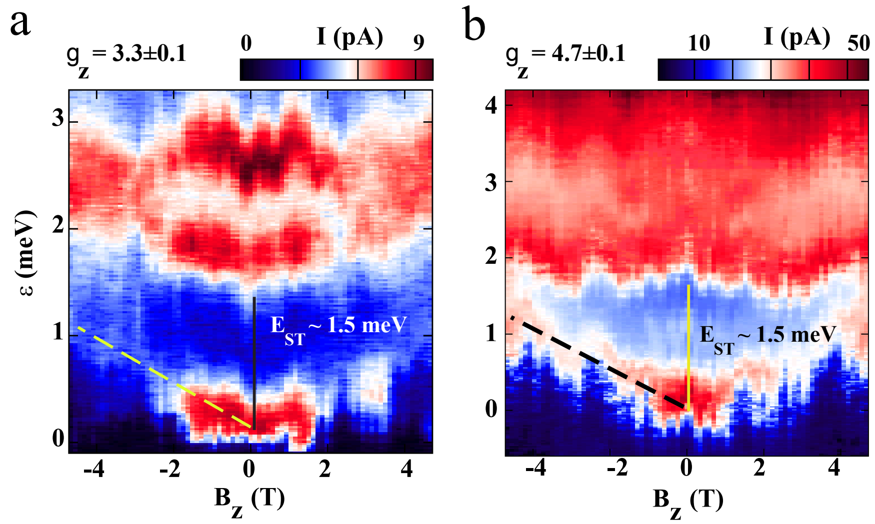

Figure 8.10: In-plane g-factors. Leakage current through two different double dot configurations both as a function of in-plane magnetic field and detuning. Dashed lines are used to extract the effective *g*-factors along the direction of the magnetic field, and the singlet-triplet energy splittings are shown by solid lines.

9.0 CONCLUSIONS

To explore experimental platforms for topological quantum computation and quantum simulation, this thesis studies quantum transport in superconductor-semiconductor hybrid structures, based on two types of semiconductor nanowires, InSb nanowires and Ge/Si core/shell nanowires.

Our experiments based in InSb nanowires explore Andreev bound states in chains that are made of quantum dots coupled to superconductors. These devices have the potential for applications in quantum computation including in the simulation of topological superconductors and Majorana zero modes. On the one hand, the chain structure is predicted to circumvent challenges encountered in common implementation of Majorana zero modes that is based on a single continuous nanowire section covered by a single superconductor. On the other hand, the chain implementation is complex and challenging in device fabrication and measurement. Because a chain contains a number of building blocks, each building block of a chain is already a hybrid structure made of a quantum dot coupled to a superconductor, and three parameters (Γ_S, μ, t) in every building block must be controlled and tuned to the desired parameter regime. We accomplish the chain implementation in the three following steps.

We first achieve individual highly tunable building blocks, NbTiN-single quantum dot in InSb nanowires, by developing local fine gates and highly transparent contacts. In this way, we can tune all of the necessary parameters to create and control Andreev bound states in a single building block independently and in a large parameter space. We explore rich transport features in a number of regimes as Γ_S is increased: from co-tunneling regime to Andreev bounds state regime of $|D\rangle$ and $|S\rangle$ ground states. This is the subgap (superconducting) transport. Transition of above-gap (normal) transport as Γ_S is increased is also investigated:

the quantized charging effect is removed as the dot is tuned to be strongly coupled to the superconductor. Interestingly, we observe that the $|D\rangle/|S\rangle$ transition within the gap and the suppression of quantized charging effect above gap take place simultaneously as the same parameter, Γ_S, is increased. In the open dot regime, we measure the zero bias peaks as a function of μ and magnetic field, which maps out the $|D\rangle/|S\rangle$ phase boundary of Andreev bound states. This phase boundary is found to be similar to the topological phase boundary predicted. Finally, the single dot exhibits two transport anomalies that have not been reported, i.e., high bias replicas and low bias negative differential conductance. We propose a minimum model to explain these anomalies.

As a subsequent step aiming for chains, we study the hybridization of Andreev bound states in two coupled dots. This is realized with a tunnel coupled double dot in an InSb nanowire. The nanowire is connected to two superconducting leads from two ends such that each quantum dot can be tuned to be strongly coupled to a superconductor. We measure the double dot spectra as a function of bias and dot chemical potential (μ_L, μ_R), and also map out the spin structure of the double dot Andreev bound states, meaning the spin states of ground and first excited states in all representative double dot configurations. Importantly, the spectra and the spin state map demonstrate that the Andreev bound states in two dots are hybridized into molecular states, which is essential to the realization of coupled Andreev bound states in chains.

Finally, we implement a superconductor-quantum dot chain made of three quantum dots based on an InSb nanowire and three NbTiN leads. In the chain, we first create Andreev bound states in individual building blocks, then hybridize the Andreev bound states between neighboring building blocks, and finally realize the entire chain. The implementation, importantly, demonstrates an experimentally realizable method to scale these hybrid structures to long chains based in one-dimensional nanowires. We perform spectroscopy measurements to explore the resonances through Andreev bound states in the triple dot as a function of a function of bias and triple dot chemical potentials. Two types of magnetic field behaviors are observed. The first type is splitting and can be explained in terms of Andreev bound states. The second is a zero bias peak appearing from no merging of of split branches. This zero bias peak starts at a finite magnetic field, and sustains for ~ 0.5 T in magnetic field.

This zero bias feature is hard to understand in term of Andreev bound states, the Kondo effect, and supercurrent. Instead, it strongly resembles the previously reported zero bias peak that has been interpreted as Majorana zero modes. Chains of next generation with a few improvements (discussed below), however, are necessary to provide further evidence.

To sum up the experiments based on InSb nanowires, the elucidation of Andreev bound states in single, double and triple dots open doors to future research. Importantly, they lead to a direction of realizing the Kitaev model in terms of quantum dot chains. In addition, the experiments demonstrate high tunability achieved in the chains, which displays the largely unexplored potential of semiconductor systems for quantum simulation.

We suggest future directions starting from these specific experiments based on chains. First, the triple dot devices are still far away from the long chain limit. Hence, the two Majorana zero modes at the two ends of the chain, if present, would be coupled considerably [2]. Therefore, long chains made of a large number of quantum dots is a natural direction in the future. Besides, the phase differences between the three superconductors are not controlled in the triple dot experiment. Controlling the phase differences can be accomplished by fabricating superconducting circuits and applying local magnetic fluxes through the circuits. In addition, although the chain implementation is realized based on 1D nanowires and can be, in principle, scaled to long chains by fabricating multiple-terminal superconducting contacts of small contact areas, it has been shown that incorporating such many components in a 1D nanowire and controlling a large number of parameters independently place great challenges in device fabrication and measurement. Some of these challenges can be solved in 2D semiconductors because more degrees of freedom are present. Two dimensional semiconductors with strong spin-orbit coupling, sufficiently large g-factors and well-developed transparent superconducting contacts, if found, would facilitate easier and more robust fabrication and measurement of such complex chain structures.

More generally, for the entire community that is devoted to realize Majorana zero modes based on superconductor-semiconductor hybrid structure, hard gap induced superconductivity is highly desired. This would eliminate ambiguities in experiments by ruling out trivial states at zero bias caused by subgap quasiparticles. Also simulations of quantum dynamics of Andreev bound states in quantum dot chains can be performed with hybrid structures of hard gap superconductivity [94, 95, 11]. Recently, epitaxial growth has been applied to grow thin superconductor shells on the surface of InAs and InSb nanowires. This gives rise to a significant improvement to the induced gap [94, 148]. Indeed, tunneling experiments show that at zero magnetic field, the subgap density of states in devices with epitaxial superconductors can be 100 times lower than those with evaporated superconductors. This technique, however, may still not be sufficient for the study of Majorana zero modes because even in these nanowires the subgap density of states increases as a magnetic field is applied, which corresponds exactly to the regime where Majorana zero modes are predicted to appear. Further efforts in material engineering are necessary to generate even "harder" induced superconducting gaps. Meanwhile, the search of intrinsic topological superconductors should get attention.

Regarding measurement approaches, most of the current experiments focus on the prime feature of Majorana zero modes: the zero bias feature. There is no doubt that a combination of different signatures would provide stronger evidence of Majorana zero modes. In the short term, non-local measurements should be explored. Because Majorana zero modes form in pairs at the two ends of 1D channels, non-local effects are expected to be observed, if the Majorana zero modes are present. Further experiments directed at investigating braiding could directly test the non-abelian statistics of Majorana zero modes.

Our experiments, based on Ge/Si core/shell nanowires, explore the ingredients required for the study of Majorana zero modes based on superconductor-nanowire hybrid structures: induced superconductivity from superconductors with high critical magnetic fields, strong spin-orbit coupling and sufficiently large g-factors. For the first ingredient, we develop superconducting contacts based on NbTiN and observe supercurrent up to ~ 1 T and induced superconductivity with a soft gap. The induced superconductivity is comparable to that in some devices reported for the study of Majorana zero modes [10, 13], and is worse than that achieved with best current technique [12, 56]. For the other two ingredients, we study quantum transport through hole double dots in Ge/Si nanowires. By implementing spin blockade and examining its magnetic field evolution, we extract a spin-orbit length of 100–500 nm that is similar to those in InSb and InAs nanowires. G-factors up to 8 are measured, which can be sufficient. Therefore, in terms of the three ingredients necessary for the study of Majorana zero modes, Ge/Si nanowires have the potential to implement Majorana zero modes. However, Ge/Si nanowires currently exhibit low feasibility to advanced devices for the study of Majorana zero modes based on superconductor-nanowire structures or quantum dot chains, because the yields of transparent superconducting contacts and high quality nanowires without disorder or impurities are low. Epitaxially grown superconducting shells may improve the former. Developing and optimizing nanowire growth technique and device fabrication can help the latter. Finally, all of the discussion for future improvements discussed previously also applies to Ge/Si nanowires.

9.1 LIST OF PUBLICATIONS

- Mirage Andreev Spectra in superconductor-quantum dot-superconductor structures (manuscript).
- Superconducting and normal transitions in quantum dots coupled to superconducting reservoirs (manuscript).
- Andreev blockade in double quantum dots (manuscript).
- **Z. Su**, A. B. Tacla, M. Hocevar, D. Car, S. R. Plissard, E. P. A. M. Bakkers, A. J. Daley, D. Pekker, and S. M. Frolov. Andreev Molecules in Semiconductor Nanowire Double Quantum Dots. *Nature Communications*, 8, 2017.
- A. Zarassi, **Z. Su (co-first author)**, J. Danon, J. Schwenderling, M. Hocevar, B. M. Nguyen, J. Yoo, S. A. Dayeh, and S. M. Frolov. Magnetic field evolution of spin blockade in Ge/Si nanowire double quantum dots. *Phys. Rev. B*, 95:155416, 2017.
- **Z. Su**, A. Zarassi, B. M. Nguyen, J. Yoo, S. A. Dayeh, and S. M. Frolov. High critical magnetic field superconducting contacts to Ge/Si core/shell nanowires. ArXiv e-prints:1610.03010, 2016.

BIBLIOGRAPHY

[1] P. Yu and M. Cardona. *Fundamentals of Semiconductors: Physics and Materials Properties*. Graduate Texts in Physics. Springer Berlin Heidelberg, 2010.

[2] A. Yu Kitaev. Unpaired majorana fermions in quantum wires. *Physics-Uspekhi*, 44(10S):131, 2001.

[3] Roman M. Lutchyn, Jay D. Sau, and Sankar Das Sarma. Majorana fermions and a topological phase transition in semiconductor-superconductor heterostructures. *Physical review letters*, 105(7):077001, 2010.

[4] Yuval Oreg, Gil Refael, and Felix von Oppen. Helical liquids and majorana bound states in quantum wires. *Physical review letters*, 105(17):177002, 2010.

[5] T. W. Larsen, K. D. Petersson, F. Kuemmeth, T. S. Jespersen, P. Krogstrup, J. Nygård, and C. M. Marcus. Semiconductor-nanowire-based superconducting qubit. *Phys. Rev. Lett.*, 115:127001, Sep 2015.

[6] I. M. Georgescu, S. Ashhab, and Franco Nori. Quantum simulation. *Rev. Mod. Phys.*, 86:153–185, 2014.

[7] Pablo Jarillo-Herrero, Jorden A. van Dam, and Leo P. Kouwenhoven. Quantum supercurrent transistors in carbon nanotubes. *Nature*, 439:953–956, 2005.

[8] Eduardo J. H. Lee, Xiaocheng Jiang, Manuel Houzet, Ramón Aguado, Charles M. Lieber, and Silvano De Franceschi. Spin-resolved andreev levels and parity crossings in hybrid superconductor-semiconductor nanostructures. *Nature nanotechnology*, 9(1):79–84, 2014.

[9] L. Hofstetter, S. Csonka, J. Nygård, and C. Schönenberger. Cooper pair splitter realized in a two-quantum-dot y-junction. *Nature*, 461:690–963, 2009.

[10] Vincent Mourik, Kun Zuo, Sergey M. Frolov, S. R. Plissard, Erik P. A. M. Bakkers, and Leo P. Kouwenhoven. Signatures of majorana fermions in hybrid superconductor-semiconductor nanowire devices. *Science*, 336(6084):1003–1007, 2012.

[11] Hao Zhang, Önder Gül, Sonia Conesa-Boj, Michał P Nowak, Michael Wimmer, Kun Zuo, Vincent Mourik, Folkert K. de Vries, Jasper van Veen, Michiel WA de Moor, et al.

Ballistic superconductivity in semiconductor nanowires. *Nature Communications*, 8, 2017.

[12] M. T. Deng, S. Vaitiekenas, E. B. Hansen, J. Danon, M. Leijnse, K. Flensberg, J. Nygård, P. Krogstrup, and C. M. Marcus. Majorana bound state in a coupled quantum-dot hybrid-nanowire system. *Science*, 354(6319):1557–1562, 2016.

[13] Jun Chen, Peng Yu, John Stenger, Moïra Hocevar, Diana Car, Sébastien R. Plissard, Erik P. A. M. Bakkers, Tudor D. Stanescu, and Sergey M. Frolov. Experimental phase diagram of zero-bias conductance peaks in superconductor/semiconductor nanowire devices. *Science Advances*, 3(9):e1701476, 2017.

[14] Ettore Majorana. Teoria simmetrica dell'elettrone e del positrone. *Il Nuovo Cimento (1924-1942)*, 14(4):171, 2008.

[15] C.W.J. Beenakker. Search for majorana fermions in superconductors. *Annual Review of Condensed Matter Physics*, 4(1):113–136, 2013.

[16] A. Yu. Kitaev. Fault-tolerant quantum computation by anyons. *Annals of Physics*, 303(1):2 – 30, 2003.

[17] Jay D. Sau and S. Das Sarma. Realizing a robust practical majorana chain in a quantum-dot-superconductor linear array. *Nature Communications*, 3:964, 2012.

[18] Ion C. Fulga, Arbel Haim, Anton R. Akhmerov, and Yuval Oreg. Adaptive tuning of majorana fermions in a quantum dot chain. *New Journal of Physics*, 15(4):045020, 2013.

[19] P. Zhang and Franco Nori. Majorana bound states in a disordered quantum dot chain. *New Journal of Physics*, 18(4):043033, 2016.

[20] Immanuel Bloch, Jean Dalibard, and Sylvain Nascimbene. Quantum simulations with ultracold quantum gases. *Nature Phys.*, 8:267–276, 2012.

[21] R. Blatt and C. F. Roos. Quantum simulations with trapped ions. *Nature Phys.*, 8:277–277, 2012.

[22] Andrew A. Houck, Hakan E. Tureci, and Jens Koch. On-chip quantum simulation with superconducting circuits. *Nature Phys.*, 8:292–299, 2012.

[23] R. Hanson, L. P. Kouwenhoven, J. R. Petta, S. Tarucha, and L. M. K. Vandersypen. Spins in few-electron quantum dots. *Rev. Mod. Phys.*, 79:1217–1265, (2007).

[24] Hermann Grabert and Michel H Devoret. *Single charge tunneling: Coulomb blockade phenomena in nanostructures*, volume 294. Springer Science & Business Media, 2013.

[25] Wilfred G. Van der Wiel, Silvano De Franceschi, Jeroen M. Elzerman, Toshimasa Fujisawa, Seigo Tarucha, and Leo P. Kouwenhoven. Electron transport through double quantum dots. *Reviews of Modern Physics*, 75(1):1, 2002.

[26] M. Ciorga, A. S. Sachrajda, Pawel Hawrylak, C. Gould, Piotr Zawadzki, S. Jullian, Y. Feng, and Zbigniew Wasilewski. Addition spectrum of a lateral dot from coulomb and spin-blockade spectroscopy. *Physical Review B*, 61(24):R16315, 2000.

[27] S. Nadj-Perge, S. M. Frolov, E. P. A. M. Bakkers, and L. P. Kouwenhoven. Spin-orbit qubit in a semiconductor nanowire. *Nature*, 468(7327):1084–1087, 2010.

[28] Aurelien Manchon, Hyun Cheol Koo, Junsaku Nitta, SM Frolov, and R. A. Duine. New perspectives for rashba spin-orbit coupling. *Nature materials*, 14(9):871–882, 2015.

[29] S. Nadj-Perge, V. S. Pribiag, J. W. G. van den Berg, K. Zuo, S. R. Plissard, E. P. A. M. Bakkers, S. M. Frolov, and L. P. Kouwenhoven. Spectroscopy of spin-orbit quantum bits in indium antimonide nanowires. *Phys. Rev. Lett.*, 108:166801, 2012.

[30] P. W. Anderson. Localized magnetic states in metals. *Phys. Rev.*, 124:41–53, Oct 1961.

[31] Michael Tinkham. *Introduction to Superconductivity: Second Edition (Dover Books on Physics) (Vol i)*. Dover Publications, second edition edition, June 2004.

[32] Glazman L. I. and Matveev K. A. Resonant josephson current through kondo impurities in a tunnel barrier. *JETP.*, 49:659, 1989.

[33] E. Vecino, A. Martín-Rodero, and A. Levy Yeyati. Josephson current through a correlated quantum level: Andreev states and π junction behavior. *Physical Review B*, 68(3):035105, 2003.

[34] J. C. Hammer, Juan Carlos Cuevas, F. S. Bergeret, and Wolfgang Belzig. Density of states and supercurrent in diffusive sns junctions: Roles of nonideal interfaces and spin-flip scattering. *Physical Review B*, 76(6):064514, 2007.

[35] Christoph Karrasch, Akira Oguri, and Volker Meden. Josephson current through a single anderson impurity coupled to bcs leads. *Physical Review B*, 77(2):024517, 2008.

[36] F. Siano and R. Egger. Erratum: Josephson current through a nanoscale magnetic quantum dot [phys. rev. lett. 93, 047002 (2004)]. *Physical Review Letters*, 94(3):039902, 2005.

[37] A. Martín-Rodero and A. Levy Yeyati. Josephson and andreev transport through quantum dots. *Advances in Physics*, 60(6):899–958, 2011.

[38] Alexander Cyril Hewson. *The Kondo problem to heavy fermions*, volume 2. Cambridge university press, 1997.

[39] Yoichi Tanaka, Norio Kawakami, and Akira Oguri. Andreev transport through side-coupled double quantum dots. *Physical Review B*, 78(3):035444, 2008.

[40] Eduardo J. H. Lee, Xiaocheng Jiang, Ramón Aguado, Georgios Katsaros, Charles M. Lieber, and Silvano De Franceschi. Zero-bias anomaly in a nanowire quantum dot coupled to superconductors. *Phys. Rev. Lett.*, 109:186802, Oct 2012.

[41] R. S. Deacon, Y. Tanaka, A. Oiwa, R. Sakano, K. Yoshida, K. Shibata, K. Hirakawa, and S. Tarucha. Tunneling spectroscopy of andreev energy levels in a quantum dot coupled to a superconductor. *Phys. Rev. Lett.*, 104:076805, Feb 2010.

[42] Eduardo J. H. Lee, Xiaocheng Jiang, Rok Žitko, Ramón Aguado, Charles M. Lieber, and Silvano De Franceschi. Scaling of subgap excitations in a superconductor-semiconductor nanowire quantum dot. *Phys. Rev. B*, 95:180502, May 2017.

[43] A. V. Balatsky, I. Vekhter, and Jian-Xin Zhu. Impurity-induced states in conventional and unconventional superconductors. *Rev. Mod. Phys.*, 78:373–433, May 2006.

[44] W. Chang, V. E. Manucharyan, T. S. Jespersen, J. Nygård, and C. M. Marcus. Tunneling spectroscopy of quasiparticle bound states in a spinful josephson junction. *Phys. Rev. Lett.*, 110:217005, 2013.

[45] M. T. Deng, C. L. Yu, G. Y. Huang, M. Larsson, P. Caroff, and H. Q. Xu. Anomalous zero-bias conductance peak in a nbinsb nanowirenb hybrid device. *Nano Letters*, 12(12):6414–6419, 2012.

[46] Anindya Das, Yuval Ronen, Yonatan Most, Yuval Oreg, Moty Heiblum, and Hadas. Shtrikman. Zero-bias peaks and splitting in an al-inas nanowire topological superconductor as a signature of majorana fermions. *Nature Phys.*, 8:887–895, 2012.

[47] J-D. Pillet, C. H. L. Quay, P. Morfin, C. Bena, A. Levy Yeyati, , and P. Joyez. Andreev bound states in supercurrent-carrying carbon nanotubes revealed. *Nature Phys.*, 6:965–969, 2010.

[48] A. Eichler, M. Weiss, S. Oberholzer, C. Schönenberger, A. Levy Yeyati, J. C. Cuevas, and A. Martín-Rodero. Even-odd effect in andreev transport through a carbon nanotube quantum dot. *Phys. Rev. Lett.*, 99:126602, 2007.

[49] A. Kumar, M. Gaim, D. Steininger, A. Levy Yeyati, A. Martín-Rodero, A. K. Hüttel, and C. Strunk. Temperature dependence of andreev spectra in a superconducting carbon nanotube quantum dot. *Physical Review B*, 89(7):075428, 2014.

[50] Travis Dirks, Taylor L. Hughes, Siddhartha Lal, Bruno Uchoa, Yung-Fu Chen, Cesar Chialvo, Paul M. Goldbart, and Nadya Mason. Transport through andreev bound states in a graphene quantum dot. *Nature Phys.*, 7:386–390, 2011.

[51] Alexander Cyril Hewson. *The Kondo problem to heavy fermions*, volume 2. Cambridge university press, 1997.

[52] Sara M. Cronenwett, Tjerk H. Oosterkamp, and Leo P. Kouwenhoven. A tunable kondo effect in quantum dots. *Science*, 281(5376):540–544, 1998.

[53] Sebastian Pfaller, Andrea Donarini, and Milena Grifoni. Subgap features due to quasiparticle tunneling in quantum dots coupled to superconducting leads. *Physical Review B*, 87(15), April 2013.

[54] C. W. J. Beenakker. Theory of coulomb-blockade oscillations in the conductance of a quantum dot. *Phys. Rev. B*, 44:1646–1656, Jul 1991.

[55] Stevan Nadj-Perge, Ilya K. Drozdov, Jian Li, Hua Chen, Sangjun Jeon, Jungpil Seo, Allan H. MacDonald, B. Andrei Bernevig, and Ali Yazdani. Observation of majorana fermions in ferromagnetic atomic chains on a superconductor. *Science*, 346(6209):602–607, 2014.

[56] S. M. Albrecht, A. P. Higginbotham, M. Madsen, F. Kuemmeth, T. S. Jespersen, J. Nygård, P. Krogstrup, and C. M. Marcus. Exponential protection of zero modes in majorana islands. *Nature*, 531:206–209, 2016.

[57] Dharmraj Kotekar-Patil, Binh-Minh Nguyen, Jinkyoung Yoo, Shadi A Dayeh, and Sergey M. Frolov. Quasiballistic quantum transport through ge/si core/shell nanowires. *Nanotechnology*, 2017.

[58] Jakob Kammhuber, Maja C. Cassidy, Hao Zhang, nder Gl, Fei Pei, Michiel W. A. de Moor, Bas Nijholt, Kenji Watanabe, Takashi Taniguchi, Diana Car, Sbastien R. Plissard, Erik P. A. M. Bakkers, and Leo P. Kouwenhoven. Conductance quantization at zero magnetic field in insb nanowires. *Nano Letters*, 16(6):3482–3486, 2016. PMID: 27121534.

[59] Yennai Wang, Junhong Chi, Karan Banerjee, Detlev Grutzmacher, Thomas Schapers, and Jia G. Lu. Field effect transistor based on single crystalline insb nanowire. *J. Mater. Chem.*, 21:2459–2462, 2011.

[60] H. A. Nilsson, P. Samuelsson, P. Caroff, and H. Q. Xu. Supercurrent and multiple andreev reflections in an insb nanowire josephson junction. *Nano Letters*, 12(1):228–233, 2012.

[61] Zhaoen Su, Alexandre B Tacla, Moïra Hocevar, Diana Car, Sébastien R Plissard, Erik PAM Bakkers, Andrew J Daley, David Pekker, and Sergey M Frolov. Andreev molecules in semiconductor nanowire double quantum dots. *Nature Communications*, 8, 2017.

[62] Philippe Caroff, Jakob B. Wagner, Kimberly A. Dick, Henrik A. Nilsson, Mattias Jeppsson, Knut Deppert, Lars Samuelson, L. Reine Wallenberg, and Lars-Erik Wernersson. High-quality inas/insb nanowire heterostructures grown by metalorganic vapor-phase epitaxy. *Small*, 4:878–882, 2008.

[63] Sbastien R. Plissard, Dorris R. Slapak, Marcel A. Verheijen, Mora Hocevar, George W. G. Immink, Ilse van Weperen, Stevan Nadj-Perge, Sergey M. Frolov, Leo P. Kouwenhoven, and Erik P. A. M. Bakkers. From insb nanowires to nanocubes: Looking for the sweet spot. *Nano Letters*, 12(4):1794–1798, 2012.

[64] V. S. Pribiag, S. Nadj-Perge, S. M. Frolov, J. W. G. van den Berg, I. van Weperen, PlissardS. R., E. P. A. M. Bakkers, and L. P. Kouwenhoven. Electrical control of single hole spins in nanowire quantum dots. *Nat Nano*, 8:170–174, 2013.

[65] Shadi A. Dayeh, Wei Tang, Francesca Boioli, Karen L. Kavanagh, He Zheng, Jian Wang, Nathan H. Mack, Greg Swadener, Jian Yu Huang, Leo Miglio, King-Ning Tu, and S. Tom Picraux. Direct measurement of coherency limits for strain relaxation in heteroepitaxial core/shell nanowires. *Nano Letters*, 13(5):1869–1876, 2013. PMID: 23030346.

[66] O. P. Pchelyakov, Yu B. Bolkhovityanov, A. V. Dvurechenskii, L. V. Sokolov, A. I. Nikiforov, A. I. Yakimov, and B. Voigtländer. Silicon-germanium nanostructures with quantum dots: Formation mechanisms and electrical properties. *Semiconductors*, 34(11):1229–1247, 2000.

[67] Christoph Kloeffel, Mircea Trif, and Daniel Loss. Strong spin-orbit interaction and helical hole states in ge/si nanowires. *Phys. Rev. B*, 84:195314, Nov 2011.

[68] G. E. Blonder, M Tinkham, and T. M. Klapwijk. Transition from metallic to tunneling regimes in superconducting microconstrictions: Excess current, charge imbalance, and supercurrent conversion. *Physical Review B*, 25(7):4515, 1982.

[69] D. B. Suyatin, C. Thelander, M. T. Bj́'ork, I. Maximov, and L. Samuelson. Sulfur passivation for ohmic contact formation to inas nanowires. *Nanotechnology*, 18(10):105307, 2007.

[70] J. Hölzl, F. K. Schulte, and H. Wagner. *Solid Surface Physics.* Springer Berlin Heidelberg, 1979.

[71] William M. Haynes and David R. Lide. *CRC Handbook of Chemistry and Physics : A Ready-reference Book of Chemical and Physical Data.* Raton, Fla.: CRC, 2011.

[72] C. Henkel, S. Abermann, O. Bethge, P. Klang, and E. Bertagnolli. Impact of sputter deposited tan and tin metal gates on zro2/ge and zro2/si high-k dielectric gate stacks. In *2009 10th International Conference on Ultimate Integration of Silicon*, pages 197–200, March 2009.

[73] Wenjuan Lu, Yuehua Dai, Feifei Wang, and Bo Jin. Impact of native defects and impurities in mhfo2 and si3n4 on charge trapping memory devices: A first principle hybrid functional study. *physica status solidi (b)*, pages n/a–n/a, 2016.

[74] Matsunaga T., H. Maezawa, and T. Noguchi. Characterization of nbtin thin films prepared by reactive dc-magnetron sputtering. *IEEE Transactions on Applied Superconductivity*, 13(2):3284–3287, June 2003.

[75] David Aasen, Michael Hell, Ryan V. Mishmash, Andrew Higginbotham, Jeroen Danon, Martin Leijnse, Thomas S. Jespersen, Joshua A. Folk, Charles M. Marcus, Karsten Flensberg, and Jason Alicea. Milestones toward majorana-based quantum computing. *Phys. Rev. X*, 6:031016, 2016.

[76] D. Chevallier, P. Simon, and C. Bena. From andreev bound states to majorana fermions in topological wires on superconducting substrates: A story of mutation. *Phys. Rev. B*, 88:165401, Oct 2013.

[77] S. Nadj-Perge, I. K. Drozdov, B. A. Bernevig, and Ali Yazdani. Proposal for realizing majorana fermions in chains of magnetic atoms on a superconductor. *Phys. Rev. B*, 88:020407, Jul 2013.

[78] Jelena Klinovaja, Peter Stano, Ali Yazdani, and Daniel Loss. Topological superconductivity and majorana fermions in rkky systems. *Phys. Rev. Lett.*, 111:186805, Nov 2013.

[79] Chun-Xiao Liu, Jay D Sau, Tudor D Stanescu, and S Das Sarma. Andreev bound states versus majorana bound states in quantum dot-nanowire-superconductor hybrid structures: Trivial versus topological zero-bias conductance peaks. *arXiv preprint arXiv:1705.02035*, 2017.

[80] K. Grove-Rasmussen, H. I. Joddrgensen, B. M. Andersen, J. Paaske, T. S. Jespersen, J. Nygård, K. Flensberg, and P. E. Lindelof. Superconductivity-enhanced bias spectroscopy in carbon nanotube quantum dots. *Phys. Rev. B*, 79:134518, Apr 2009.

[81] J. C. Cuevas, A. Levy Yeyati, and A. Martin-Rodero. Kondo effect in normal-superconductor quantum dots. *Physical Review B*, 63(9):094515, 2001.

[82] Wenjie Liang, Marc Bockrath, Dolores Bozovic, Jason H. Hafner, M. Tinkham, , and Hongkun Park. Fabry - perot interference in a nanotube electron waveguide. *Nature*, 411:665–669, 2001.

[83] B. M. Andersen, K. Flensberg, V. Koerting, and J. Paaske. Nonequilibrium transport through a spinful quantum dot with superconducting leads. *Phys. Rev. Lett.*, 107:256802, Dec 2011.

[84] Cristina Bena. Metamorphosis and taxonomy of andreev bound states. *The European Physical Journal B-Condensed Matter and Complex Systems*, 85(6):1–11, 2012.

[85] Tim Byrnes, Na Young Kim, Kenichiro Kusudo, and Yoshihisa Yamamoto. Quantum simulation of fermi-hubbard models in semiconductor quantum-dot arrays. *Phys. Rev. B*, 78:075320, 2008.

[86] A. Singha, M. Gibertini, B. Karmakar, S. Yuan, M. Polini, G. Vignale, M. I. Katsnelson, A. Pinczuk, L. N. Pfeiffer, K. W. West, and V. Pellegrini. Two-dimensional mott-hubbard electrons in an artificial honeycomb lattice. *Science*, 332(6034):1176–1179, 2011.

[87] Pierre Barthelemy and Lieven M. K. Vandersypen. Quantum dot systems: a versatile platform for quantum simulations. *Annalen der Physik*, 525:808–826, 2013.

[88] A. Eichler, R. Deblock, M. Weiss, C. Karrasch, V. Meden, C. Schönenberger, and H. Bouchiat. Tuning the josephson current in carbon nanotubes with the kondo effect. *Phys. Rev. B*, 79:161407, 2009.

[89] D. Sherman, J. S. Yodh, S.M. Albrecht, J. Nygård, P. Krogstrup, and C. M. Marcus. Normal, superconducting and topological regimes of hybrid double quantum dots. *Nature nanotechnology*, 12(3):212–217, 2017.

[90] Torsten Karzig, Christina Knapp, Roman M Lutchyn, Parsa Bonderson, Matthew B Hastings, Chetan Nayak, Jason Alicea, Karsten Flensberg, Stephan Plugge, Yuval Oreg, et al. Scalable designs for quasiparticle-poisoning-protected topological quantum computation with majorana zero modes. *Physical Review B*, 95(23):235305, 2017.

[91] Stephan Plugge, Asbjoddrn Rasmussen, Reinhold Egger, and Karsten Flensberg. Majorana box qubits. *New Journal of Physics*, 19(1):012001, 2017.

[92] Tobias Meng, Serge Florens, and Pascal Simon. Self-consistent description of andreev bound states in josephson quantum dot devices. *Phys. Rev. B*, 79:224521, Jun 2009.

[93] T. Hensgens, T. Fujita, L. Janssen, X. Li, C. J. Van Diepen, C. Reichl, W. Wegscheider, S. Das Sarma, and L. M. K. Vandersypen. Quantum simulation of a Fermi-Hubbard model using a semiconductor quantum dot array. *ArXiv e-prints*, February 2017.

[94] W. Chang, S. M. Albrecht, T. S. Jespersen, F. Kuemmeth, P. Krogstrup, J Nygärd, and Charles M. Marcus. Hard gap in epitaxial semiconductorsuperconductor nanowires. *Nat Nano*, 10:232–236, 2015.

[95] T. W. Larsen, K. D. Petersson, F. Kuemmeth, T. S. Jespersen, P. Krogstrup, J. Nygård, and C. M. Marcus. Semiconductor-nanowire-based superconducting qubit. *Phys. Rev. Lett.*, 115:127001, Sep 2015.

[96] Kun Zuo, Vincent Mourik, Daniel B Szombati, Bas Nijholt, David J van Woerkom, Attila Geresdi, Jun Chen, Viacheslav P Ostroukh, Anton R Akhmerov, Sebastién R Plissard, et al. Supercurrent interference in few-mode nanowire josephson junctions. *arXiv preprint arXiv:1706.03331*, 2017.

[97] Jorden A. van Dam, Yuli V. Nazarov, Erik P. A. M. Bakkers, Silvano De Franceschi, and Leo P. Kouwenhoven. Supercurrent reversal in quantum dots. *Nature*, 442:667–670, 2006.

[98] Jelena Klinovaja and Daniel Loss. Composite majorana fermion wave functions in nanowires. *Phys. Rev. B*, 86:085408, Aug 2012.

[99] Wei Lu, Jie Xiang, Brian P. Timko, Yue Wu, and Charles M. Lieber. One-dimensional hole gas in germanium/silicon nanowire heterostructures. *Proceedings of the National Academy of Sciences of the United States of America*, 102(29):10046–10051, 2005.

[100] Yongjie Hu, Ferdinand Kuemmeth, Charles M. Lieber, and Charles M. Marcus. Hole spin relaxation in ge-si core-shell nanowire qubits. *Nat Nano*, 7:47–50, 2012.

[101] A. P. Higginbotham, F. Kuemmeth, T. W. Larsen, M. Fitzpatrick, J. Yao, H. Yan, C. M. Lieber, and C. M. Marcus. Antilocalization of coulomb blockade in a ge/si nanowire. *Phys. Rev. Lett.*, 112:216806, May 2014.

[102] Matthias Brauns, Joost Ridderbos, Ang Li, Erik P. A. M. Bakkers, and Floris A. Zwanenburg. Electric-field dependent g-factor anisotropy in ge-si core-shell nanowire quantum dots. *Phys. Rev. B*, 93:121408, Mar 2016.

[103] A. Zarassi, Z. Su, J. Danon, J. Schwenderling, M. Hocevar, B. M. Nguyen, J. Yoo, S. A. Dayeh, and S. M. Frolov. Magnetic field evolution of spin blockade in ge/si nanowire double quantum dots. *Phys. Rev. B*, 95:155416, Apr 2017.

[104] Jie Xiang, Vidan A., TinkhamM., WesterveltR. M., and Charles M. Lieber. Ge/si nanowire mesoscopic josephson junctions. *Nat Nano*, 1:208–213, 2006.

[105] S. A. Dayeh, A. V. Gin, and S. T. Picraux. Advanced core/multishell germanium/silicon nanowire heterostructures: Morphology and transport. *Applied Physics Letters*, 98(16), 2011.

[106] Shadi A. Dayeh, Nathan H. Mack, Jian Yu Huang, and S. T. Picraux. Advanced core/multishell germanium/silicon nanowire heterostructures: The au-diffusion bottleneck. *Applied Physics Letters*, 99(2), 2011.

[107] Binh-Minh Nguyen, Yuan Taur, S Tom Picraux, and Shadi A Dayeh. Diameter-independent hole mobility in ge/si core/shell nanowire field effect transistors. *Nano letters*, 14(2):585–591, 2014.

[108] M. Octavio, M. Tinkham, G. E. Blonder, and T. M. Klapwijk. Subharmonic energy-gap structure in superconducting constrictions. *Phys. Rev. B*, 27:6739–6746, Jun 1983.

[109] K. Flensberg, J. Bindslev Hansen, and M. Octavio. Subharmonic energy-gap structure in superconducting weak links. *Phys. Rev. B*, 38:8707–8711, Nov 1988.

[110] Simon Abay, Daniel Persson, Henrik Nilsson, Fan Wu, H. Q. Xu, Mikael Fogelström, Vitaly Shumeiko, and Per Delsing. Charge transport in inas nanowire josephson junctions. *Phys. Rev. B*, 89:214508, Jun 2014.

[111] D. Averin and A. Bardas. ac josephson effect in a single quantum channel. *Phys. Rev. Lett.*, 75:1831–1834, Aug 1995.

[112] J. C. Cuevas, A. Martín-Rodero, and A. Levy Yeyati. Hamiltonian approach to the transport properties of superconducting quantum point contacts. *Phys. Rev. B*, 54:7366–7379, Sep 1996.

[113] So Takei, Benjamin M. Fregoso, Hoi-Yin Hui, Alejandro M. Lobos, and S. Das Sarma. Soft superconducting gap in semiconductor majorana nanowires. *Phys. Rev. Lett.*, 110:186803, Apr 2013.

[114] Tudor D. Stanescu, Roman M. Lutchyn, and S. Das Sarma. Soft superconducting gap in semiconductor-based majorana nanowires. *Phys. Rev. B*, 90:085302, Aug 2014.

[115] W. Lu, J. Xiang, B. P. Timko, Y. Wu, and C. M. Lieber. One-dimensional hole gas in germanium/silicon nanowire heterostructures. *Proc. Natl Acad. Sci. USA*, 102(29):10046–10051, (2005).

[116] C. Kloeffel, M. Trif, and D. Loss. Strong spin-orbit interaction and helical hole states in ge/si nanowires. *Phys. Rev. B*, 84:195314, (2011).

[117] X. J. Hao, T. Tu, G. Cao, C. Zhoe, H. O. Li, G. C. Guo, W. Y. Fung, Z. Ji, G. P. Guo, and W. Lu. Strong and tunable spin-orbit coupling of one-dimentional holes in ge/si core/shell nanowires. *Nano Lett.*, 10:2956 – 2960, (2010).

[118] Y. Hu, F. Kuemmeth, C. M. Lieber, and C. M. Marcus. Hole spin relaxation in ge-si core-shell nanowire qubits. *Nature Nanotech.*, 7:47 – 50, (2012).

[119] A. P. Higginbotham, T. W. Larsen, J. Yao, H. Yan, C. M. Lieber, C. M. Marcus, and F. Kuemmeth. Hole spin coherence in a ge/si heterostructure nanowire. *Nano Lett.*, 14:3582 – 3586, (2014).

[120] A. P. Higginbotham, F. Kuemmeth, T. W. Larsen, M. Fitzpatrick, J. Yao, H. Yan, C. M. Lieber, and C. M. Marcus. Antilocalization of coulomb blockade in a ge/si nanowire. *Phys. Rev. Lett.*, 112:216806, (2014).

[121] J. Danon and Yu V. Nazarov. Pauli spin blockade in the presence of strong spin-orbit coupling. *Phys. Rev. B*, 80:041301, (2009).

[122] F. Maier, J. Klinovaja, and D. Loss. Majorana fermions in ge/si hole nanowires. *Phys. Rev. B*, 90:195421, (2014).

[123] D. P. DiVincenzo and D. Loss. Quantum information is physical. *Superlattices and Microstructures*, 23(3):419 – 432, (1998).

[124] J. R. Petta, A. C. Johnson, J. M. Taylor, E. A. Laird, A. Yacoby, M. D. Lukin, C. M. Marcus, M. P. Hanson, and A. C. Gossard. Coherent manipulation of coupled electron spins in semiconductor quantum dots. *Science*, 309(5744):2180–2184, (2005).

[125] F. H. L. Koppens, J. A. Folk, J. M. Elzerman, R. Hanson, L. H. Willems van Beveren, I. T. Vink, H. P. Tranitz, W. Wegscheider, L. P. Kouwenhoven, and L. M. K. Vandersypen. Control and detection of singlet-triplet mixing in a random nuclear field. *Science*, 309(5739):1346–1350, (2005).

[126] A. C. Johnson, J. R. Petta, J. M. Taylor, A. Yacoby, M. D. Lukin, C. M. Marcus, M. P. Hanson, and A. C. Gossard. Triplet-singlet spin relaxation via nuclei in a double quantum dot. *Nature*, 435:925 – 928, (2005).

[127] A. Pfund, I. Shorubalko, K. Ensslin, and R. Leturcq. Suppression of spin relaxation in an inas nanowire double quantum dot. *Phys. Rev. Lett.*, 99:036801, (2007).

[128] A. Pfund, I. Shorubalko, K. Ensslin, and R. Leturcq. Spin-state mixing in inas double quantum dots. *Phys. Rev. B*, 76:161308, (2007).

[129] K. C. Nowack, F. H. L. Koppens, Yu V. Nazarov, and L. M. K. Vandersypen. Coherent control of a single electron spin with electric fields. *Science*, 318(5855):1430–1433, (2007).

[130] Y. Hu, H. O. H. Churchill, D. J. Reilly, J. Xiang, C. M. Lieber, and C. M. Marcus. A ge/si heterostructure nanowire-based double quantum dot with integrated charge sensor. *Nature Nanotech.*, 2:622 – 625, (2005).

[131] J. Fischer, W. A. Coish, D. V. Bulaev, and D. Loss. Spin decoherence of a heavy hole coupled to nuclear spins in a quantum dot. *Phys. Rev. B*, 78:155329, (2008).

[132] F. Maier, C. Kloeffel, and D. Loss. Tunable g factor and phonon-mediated hole spin relaxation in ge/si nanowire quantum dots. *Phys. Rev. B*, 87:161305, (2013).

[133] S. Roddaro, A. Fuhrer, P. Brusheim, C. Fasth, H.Q. Xu, L. Samuelson, J. Xiang, and C.M. Lieber. Spin states of holes in Ge/Si nanowire quantum dots. *Phys. Rev. Lett.*, 101:186802, (2008).

[134] M. Brauns, J. Ridderbos, A. Li, E.P.A.M. Bakkers, and F. A. Zwanenburg. Electric-field dependent g-factor anisotropy in ge-si core-shell nanowire quantum dots. *Phys. Rev. B*, 93:121408, (2016).

[135] Z. Su, A. Zarassi, B. M. Nguyen, J. Yoo, S. A. Dayeh, and S. M. Frolov. High critical magnetic field superconducting contacts to Ge/Si core/shell nanowires. *ArXiv e-prints:1610.03010*, (2016).

[136] A. C. Johnson, J. R. Petta, C. M. Marcus, M. P. Hanson, and A. C. Gossard. Singlet-triplet spin blockade and charge sensing in a few-electron double quantum dot. *Phys. Rev. B*, 72:165308, Oct (2005).

[137] H. W. Liu, T. Fujisawa, Y. Ono, H. Inokawa, A. Fujiwara, K. Takashina, and Y. Hirayama. Pauli-spin-blockade transport through a silicon double quantum dot. *Phys. Rev. B*, 77:073310, Feb (2008).

[138] N. Shaji, C. B. Simmons, M. Thalakulam, L. J. Klein, H. Qin, H. Luo, D. E. Savage, M. G. Lagally, A. J. Rimberg, R. Joynt, M. Friesen, R. H. Blick, S. N. Coppersmith, and M. A. Eriksson. Spin blockade and lifetime-enhanced transport in a few-electron si/sige double quantum dot. *Nat Phys*, 4:540 – 544, (2008).

[139] H. O. H. Churchill, A. J. Bestwick, J. W. Harlow, F. Kuemmeth, D. Marcos, C. H. Stwertka, S. K. Watson, and C. M. Marcus. Electron-nuclear interaction in 13c nanotube double quantum dots. *Nat Phys*, 5:321 – 326, (2009).

[140] S. Nadj-Perge, S. M. Frolov, J. W. W. van Tilburg, J. Danon, Yu. V. Nazarov, R. Algra, E. P. A. M. Bakkers, and L. P. Kouwenhoven. Disentangling the effects of spin-orbit and hyperfine interactions on spin blockade. *Phys. Rev. B*, 81:201305, May 2010.

[141] G. Yamahata, T. Kodera, H. O. H. Churchill, K. Uchida, C.M. Marcus, and S. Oda. Magnetic field dependence of pauli spin blockade: A window into the sources of spin relaxation in silicon quantum dots. *Phys. Rev. B*, 86:115322, (2012).

[142] R. Li, F. E. Hudson, A. S. Dzurak, and A. R. Hamilton. Pauli spin blockade of heavy holes in a silicon double quantum dot. *Nano Lett.*, 15:7314 – 7318, (2015).

[143] H. Bohuslavskyi, D. Kotekar-Patil, R. Maurand, A. Corna, S. Barraud, L. Bourdet, L. Hutin, Y.M. Niquet, X. Jehl, S. De Franceschi, M. Vinet, and M. Sanquer. Pauli blockade in a few-hole PMOS double quantum dot limited by spin-orbit interaction. *ArXiv e-prints:1607.00287*, (2016).

[144] O. N. Jouravlev and Yu V. Nazarov. Electron transport in a double quantum dot governed by a nuclear magnetic field. *Phys. Rev. Lett.*, 96:176804, (2006).

[145] W. A. Coish and F. Qassemi. Leakage-current line shapes from inelastic cotunneling in the pauli spin blockade regime. *Phys. Rev. B*, 84:245407, (2011).

[146] W. J. Childs and L. S. Goodman. Hyperfine structure of ge^{73} in the $^3p_1$ and $^3p_2$ atomic states and the nuclear magnetic dipole moment of ge^{71}. *Phys. Rev.*, 141:15–21, (1966).

[147] B. Voisin, R. Maurand, S. Barraud, M. Vinet, X. Jehl, M. Sanquer, J. Renard, and S. De Franceschi. Electrical control of g-factor in a few-hole silicon nanowire mosfet. *Nano Lett.*, 16:88 – 92, (2016).

[148] Sasa Gazibegovic, Diana Car, Hao Zhang, Stijn C Balk, John A Logan, Michiel WA de Moor, Maja C Cassidy, Rudi Schmits, Di Xu, Guanzhong Wang, et al. Epitaxy of advanced nanowire quantum devices. *arXiv preprint arXiv:1705.01480*, 2017.